Validation of three-dimensional finite element model for critical velocity

THE UNIVERSITY of EDINBURGH

HERIOT WATT UNIVERSITY

Proceedings of the
INFRASTRUCTURE AND ENVIRONMENT SCOTLAND
3rd POSTGRADUATE CONFERENCE

9 December 2015
Heriot-Watt University
Edinburgh

INFRASTRUCTURE AND ENVIRONMENT SCOTLAND
3rd POSTGRADUATE CONFERENCE

9 December 2015
Heriot-Watt University
Edinburgh, UK

ISBN 978-0-9565951-4-0

Heriot-Watt University

First Published 2015 by Heriot-Watt University, Riccarton, Edinburgh, United Kingdom, EH14 4AS

ISBN 978-0-9565951-4-0

This publication is part of the proceedings of the Infrastructure and Environment Scotland 3rd Postgraduate Conference, held at Heriot-Watt University, Edinburgh on 9 December 2015.

Organising Committee:

PREFACE

Infrastructure and Environment Scotland (IES), the joint research Institute combining the Institutes of Infrastructure and Environment (I&E) at the University of Edinburgh and Heriot Watt University, was formally launched in December 2012. The aim of the joint Institute is to foster collaboration between researchers working in I&E and related areas.

The IES Postgraduate Conference is a major event on the calendar of the Institute and is now the 3rd in the series. The Conference draws together researchers from both Institutes and constitutes a forum for PhD students to present their work in a relatively informal, friendly and sympathetic setting.

These Proceedings contain 24 papers presented by PhD students at the Infrastructure and Environment Scotland 3rd Postgraduate Conference held at Heriot-Watt University in Edinburgh on the 9th December 2015. The Conference also includes poster presentations given by first year PhD students.

The success of any event depends upon dedicated individuals so the Committee would like to express its thanks to the academic and support staff at both Universities in making this event happen.

Wishing you all an enjoyable conference.

W John McCarter

Edinburgh
December 2015

CONTENTS

Infrastructure and Environment Scotland 3rd Postgraduate Conference
9th December 2015
Heriot-Watt University, Edinburgh

Assessing the effect of steel fibres on the load bearing capacity of RC Beams through the use of Artificial Neural Networks

Ahmad Afaq, Demitrios M. Cotsovos, Heriot-Watt University, Edinburgh, UK
Nikos D. Lagaros, National Technical University of Athens, Athens, GR

Abstract:

Current work sets out to investigate the effect of steel fibres on the behaviour of simply supported reinforced concrete (RC) beam specimens approaching their ultimate limit state (ULS) through the use of appropriately trained Artificial Neural Networks (ANNs). The training process of the ANNs is based on the use of four databases, which are formed from the available test data. Each database is associated with a specific type of beam specimen: (i) with no stirrups or fibres, (ii) with stirrups but no fibres, (iii) with fibres but no stirrups and (iv) with both fibres and stirrups. The ANNs are employed to directly assess the available test data. The input parameters are selected on the basis of the physical models adopted by the current design codes for describing the mechanisms underlying RC structural response at the ULS and are associated with the specimen design details. For each specimen-type considered a different combination of input parameters is used. The validated ANNs are then employed in order to conduct a parametric investigation to determine the effect of various parameters associated with the steel fibres, the material properties as well as the geometry and reinforcement details of the beams on the exhibited load-bearing capacity. Based on the analysis of the predictions it is concluded that the ANNs are capable of realistically quantifying the effect of the above parameters on the load carrying capacity of RC beams.

LIST OF NOTATIONS

b	Width of the RC beam cross-section
d	Effective depth of the RC beam cross-section
a_v	Shear Span
a_v/d	Shear Span to depth Ratio
f_c	Compressive strength of concrete
ρ_l	Longitudinal reinforcement ratio
f_y	Yield strength of the longitudinal reinforcement
ρ_w	Transverse reinforcement ratio
f_{yw}	Yield strength of the transvers reinforcement
l_f	Fibre length
d_f	Fibre Diameter
l_f/d_f	Fibre Aspect Ratio
V_f	Volumetric percentage of steel fibres
V_u	Ultimate Shear capacity
SFRC	Steel fibre reinforced concrete

1. INTRODUCTION

Structural concrete is a brittle material with significant strength in compression but a low load-bearing capacity in tension (approximately 10% of fc) (Kotsovos & Pavlović, 1995). In order to compensate for this disadvantage it is combined with steel reinforcement bars to form reinforced concrete (RC) structural elements in which the reinforcement bars mainly undertake tensile stresses. The majority of the available codes (ACI, 2008, EC2, 2004, JSCE, 2007) employed for the design of RC members are based on the use of physical models (i.e. truss-analogy and strut & tie models) which assume that an RC member, after crack-formation, behaves essentially as a truss, with concrete and reinforcement bars acting in compression forming struts and the reinforcement bars acting in tension forming ties (Figure.1). In an attempt to enhance the material properties of structural concrete – especially in tension – and to address problems associated with reinforcement congestion often observed in certain critical regions of RC members (e.g. beam-column joint) (Cotsovos, 2013) fibres are introduced into the concrete mix, to improve the load bearing capacity and reduce the amount of conventional reinforcement required (Abbas et al., 2014a, Abbas et al., 2014b). To date different types of fibres have been used (steel, glass, polypropylene, carbon etc.) however, those most commonly employed are steel fibres. Present work forms part of a more general study aiming to assess the potential benefits stemming from the use of steel fibres on RC structural response.

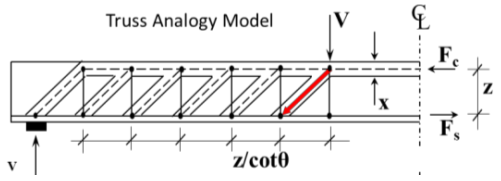

Figure 1. Truss Analogy Model of RC member

In the present article a concise review is initially conducted of the relevant published test data describing the effect of steel fibres on the load bearing capacity and mode of failure exhibited by simply supported RC beam specimens under concentrated static loads applied at specific points along their span. For this purpose four databases (DBs) are formed (see Table 1). Each database is associated with a specific type of beam specimen with certain characteristics.

Artificial Neural Networks (ANNs) do not strictly adhere to the principles of theoretical mechanics and have been frequently employed as the basis for the development of powerful and computationally efficient numerical tools capable of successfully replacing time-consuming structural analysis procedures based on the

finite element method. Such tools are lately being successfully employed to predict RC structural response at the ULS (Abdalla et al., 2007, Jeyasehar, 2006, Mansour et al., 2004). In the present study four different ANNs are developed for predicting the load-bearing capacity of the beams considered in Table 1. It should be pointed out that the development of the latter ANNs is directly based on the available test data without considering the mechanics underlying RC structural response at ULS or the associated physical models. The accuracy of the resulting ANN depends heavily on the validity of the experimental data employed.

Table 1. The four types of RC beams considered

DB	Beam characteristics	Name	Samples
DB-1	No Stirrup, No Fibers.	CL	643
DB-2	Stirrup, No Fibers.	CLT	222
DB-3	No Stirrup, Fibers.	CLF	200
DB-4	Stirrup, Fibers.	CLTF	101

The ANNs developed are presently used to quantify the effect of various parameters associated with the steel fibres, the material properties as well as the geometry and reinforcement details of the RC beams on the exhibited load-bearing capacity. Based on the predictions obtained it is concluded that the ANNs are capable of realistically and objectively quantifying the effect of the above parameters on the specimen load carrying capacity.

2. EXPERIMENTAL BACKGROUND

To date, a large number of experiments have been carried out in order to investigate RC structural response at ULS (Cucchiara et al., 2004, Slater et al., 2012, Dinh, 2009). The vast majority of these tests have been carried on simply supported RC beam specimens under concentrated static loads applied at specific points along their span. The available test data is presently employed for the development of the four databases mentioned earlier. These DBs describe the effect of a wide range of parameters associated with the steel fibres (i.e. fibre length l_f, aspect ratio l_f/d_f, fibre content V_f), the material properties (compressive strength of concrete f_c, yield strength of steel f_y) as well as the geometry and reinforcement details of the beams (i.e. depth d, width b, transverse and longitudinal steel ratios (ρ_w, ρ_l), shear span ratio a_v/d,) on the load-bearing capacity of RC beams.

When considering flexure behaviour the experimental evidence clearly indicates that the introduction of fibres into the concrete mix can result in an increase in stiffness, load carrying capacity and ductility. The databases reveal that the effect of fibres increases with increasing values of V_f, l_f/d_f, l_f and the bond developing between the fibres and the surrounding concrete. Furthermore, it has been observed that as the amount of ρ_l increases the effect of the fibres on the flexural capacity reduces (Mertol et al., 2015, Yoo et al., 2015).

Considering that ρ_w is considerably less than ρ_l, the contribution of fibres to shear capacity is more profound than in the case of flexural capacity. This is in agreement with findings of published relevant studies (Abbas et al., 2014a, Abbas et al., 2014b). Based on the available data the shear capacity of SFRC beams can be affected by a range of additional parameters such as a_v/d, V_f, d, f_c (Furlan, 1997, Mansur et al., 1986, Mondo, 2011). The present work forms part of a more general study aiming to study and quantify the effect of fibres on the response exhibited by RC beams approaching ULS in relation to the parameters mentioned above, by employing ANNs.

3. EXPERIMENTAL DATABASES

The databases presently formed incorporate test data that describe the relationship between a range of parameters associated with the design details of the RC specimens considered and the load-bearing capacity. These DBs form the basis of the parametric study mentioned earlier. Table 2 provides the statistical information concerning the variation of the parameters considered.

Table 2. Variation of the parameters considered

	Units	Min	Max	Mean	St.Dev	COV
CL (643)						
b	(mm)	50	500	169.02	67.62	0.4
d	(mm)	65	483	253.85	73.15	0.29
a_v/d		0.38	11.42	3.55	1.59	0.45
f_c'	(Mpa)	12.2	110.9	38.38	21.08	0.55
ρ_l	(%)	0.25	7.46	2.14	1.1	0.51
f_y	(Mpa)	35	1779	418.02	160.53	0.38
CLT (222)						
b	(mm)	85	307	178.18	49.6	0.28
d	(mm)	113	466	295.6	115.13	0.39
a_v/d		1	6.97	3.45	1.58	0.46
f_c'	(Mpa)	13.8	108.7	41.47	20.97	0.51
ρ_l	(%)	0.17	5.86	2.28	1.02	0.45
f_y	(Mpa)	250	910	433.81	98.65	0.23
ρ_w	(%)	0.06	14.13	0.53	1.21	2.28
f_{yw}	(Mpa)	224	716	389.13	91.9	0.24
CLF (200)						
b	(mm)	52	200	131.45	47.41	0.36
d	(mm)	122	460	238.24	99.96	0.42
a_v/d		0.4	6	2.99	1.07	0.36
f_c'	(Mpa)	24.4	93.3	48.34	17.22	0.36
ρ_l	(%)	0	5.72	1.93	1.02	0.53
f_y	(Mpa)	0	670	481.88	78.64	0.16
l_f/d_f		40	133.3	74.94	25.04	0.33
V_f	(%)	0.22	3	0.89	0.51	0.57
CLTF (101)						
b	(mm)	100	200	147.23	36.77	0.25
d	(mm)	122	275	191.65	43.03	0.22
a_v/d		1.90	9.28	4.36	1.73	0.40
f_c'	(Mpa)	18.9	111.4	50.17	25.61	0.51
ρ_l	(%)	0.17	3.29	1.63	0.68	0.42
f_y	(Mpa)	250	716	465.88	99.48	0.21
ρ_w	(%)	0.08	0.94	0.4	0.15	0.38
f_{yw}	(Mpa)	250	716	451.31	118.65	0.26
l_f/d_f		38	127.7	72.83	19.29	0.26
V_f	(%)	0.4	2	0.95	0.37	0.39

***C**oefficient **of V**ariance
+ **S**tandard **D**eviation

4. ARTIFICIAL NEURAL NETWORKS

ANNs mimics the biological neural networks in the central nervous system and the brain of animals and humans (Fig.2) (Basheer 2000). They are used to estimate or approximate functions that depend on a large number of input parameters the effect of which is not clearly established or quantified. ANNs have the ability to learn, generalize, categorize and predict values due to their adaptive nature and their ability to remember information introduced to them during their training. They consist of a number of layers. Each layer consists of a system of interconnected "neurons". Each link (forming between two neurons) has a specific weight. These weights are multiplied by the input values generated by the neurons. The values obtained from all neurons of a specific layer during the latter process are then transferred through the links and summed with the bias (see Fig.2).

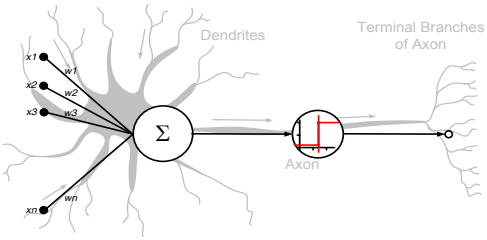

Figure 2. Function of Artificial Neuron

This latter sum is then introduced into a predefined activation function representing the relationship between layers and is described by Eq. (1). The outputs of the activation function form the input value for the neurons of the next layer (see Fig.4). The weights are initially randomly assigned and their final values are obtained through the training process and use of the available data.

$$O = f(\sum x_i w_i + b) \quad (1)$$

where O is the output from neural network,
x_i = input values,
w_i = weight coefficients and
b = bias value.

In the present study ANNs are used to predict the load-bearing capacity of four types of simply-supported RC beam specimens (CL, CLT, CLF and CLTF) mentioned above. Figure 3 describes the process through which this is achieved. Based on past experience (Svozil 1997, Saxén, 2006, Wilson, 2003) multilayer feed-forward NNs (MLFNNs) (see Fig. 4) are considered to be the most appropriate for the type of problem presently studied. The later type of ANN typically consists of an input layer, two hidden layers and an output layer. Each layer has its own predefined activation function which affects the overall performance of the ANN. Signals are generated by the neurons and travel from left to right through the path described earlier (see Fig. 4).

In the present investigation the logistic activation function is used between the input and hidden layers and hyperbolic activation function is employed between the second hidden layer and output layer of the ANN. The resulting error is calculated by Eq. (2);

$$\mathrm{E(w)} = \frac{1}{2}\sum_i (T - O)^2 \quad (2)$$

where T and O are the target (defined in the database) and output (predicted by the ANN) value respectively.

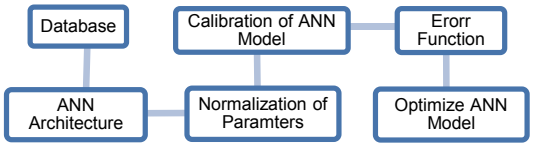

Figure 3. Flow Chart of ANN developing

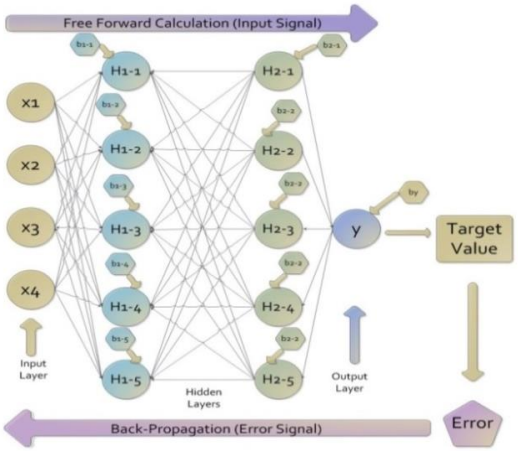

Figure 4. Multi-layer Feed Forward NN (MLFFNN)

To minimize the error obtained from Eq.(2) the back-propagation technique (DETA RULE) (Wilson, 2003) is employed. This process is carried out from right to left of the ANN (Fig. 4) and makes use of the information included in the databases. Its aim is to adjust the values of the weights (of the links connecting the neurons) and bias, which are initially randomly selected, so that the output values of the ANN realistically agree with target values defined in the database. The ANN then employs the adjusted weights in order to obtain more accurate predictions which in turn result in smaller errors. This iterative process is repeated until the errors become closer to that a predefined value.

4.1. NORMALIZATION OF DATABASE

The performance of an ANN depends upon the quality of the database. The normalization of the parameters considered in the database has significant impact on the ANN procedure. Considering that the various input combinations are associated with different units the normalization process allows their conversion to unitless parameters. To avoid problems associated with low learning rates of the ANN (Papadokonstantakis et al., 2005) it is better to normalize the values of the parameters between an appropriate upper and lower limits. In this work all parameters are normalised between [0.1, 0.9] instead of [0, 1], by using following Eq. (3).

$$\mathrm{X} = \left(\frac{0.8}{\mathrm{x_{max} - x_{min}}}\right)\mathrm{x} + \left[09 - \left(\frac{0.8}{\mathrm{x_{max} - x_{min}}}\mathrm{x_{max}}\right)\right] \quad (3)$$

4.2. CALIBRATION OF ANN MODEL

The calibration of the ANN is achieved through the multi-layer free forward back-propagation process (MLFFBP) (Saxén, 2006) and the use of the available test data. To avoid the over-fitting and enhance the performance of the ANN, the latter normalised data is initially divided into three sub-sets: each of these sub-sets is employed for training, validation and testing purposes.

Table 3. Input and Output parameters for each type of RC Beams

Name	Input Parameter	Output Parameter
CL	$b, d, a_v/d, f'_c, \rho_l, f_y = \mathbf{6}$	$V_u = \mathbf{1}$
CLT	$b, d, a_v/d, f'_c, \rho_l, f_y, \rho_w, f_{yw} = \mathbf{8}$	$V_u = \mathbf{1}$
CLF	$b, d, a_v/d, f'_c, \rho_l, f_y, l_f/d_f, V_f = \mathbf{8}$	$V_u = \mathbf{1}$
CLTF	$b, d, a_v/d, f'_c, \rho_l, f_y, \rho_w, f_{yw}, l_f/d_f, V_f = \mathbf{10}$	$V_u = \mathbf{1}$

Matlab (Beale et al., 2015) is used to develop the ANNs and to randomly divide the database into the previously mentioned sub-sets: **70%** of the database is used for training, **15%** for validation and another **15%** for testing purposes. Each ANN model is trained for ***100 epochs*** (iterations including the full MLFFBP process). This process is stopped when one of the following conditions is met: (i) a maximum of ***25 validation failures*** are exhibited (validation failure is exhibited when the NN performance during each iteration fails to improve or remains constant), (ii) the value of ***performance goal is 0.0001*** (expressing the difference between the target and output values) and (iii) the ***minimum performance gradient*** (related to the rate at which the weights are adjusted through the MLFFBP process) becomes $\mathbf{10^{-10}}$. These conditions are proposed by the Levenberg-Marquardt back-propagation method which is currently adopted (Beale et al., 2015).

4.3. OPTIMIZED ANN MODEL

Table 4. Number of Neurons in hidden layer of ANN

Name	No of Input Neurons	No of Hidden Neurons	Output Neurons
CL-1	6	6	1
CL-2	6	12	1
CLT-1	8	8	1
CLT-2	8	16	1
CLF-1	8	8	1
CLF-2	8	16	1
CLTF-1	10	10	1
CLTF-2	10	20	1

Table 3 describes the different input and output parameters considered for each one of the four type of RC beams considered (CL, CLT, CLF & CLTF). For each case, two different ANN models are developed, with different number of hidden neurons in each hidden layer, as described in table 4. By using Tables 3 & 4 two ANN models are trained for each four type of RC beams.

Figure 5 and Table 5 show the prediction of ANNs associated with specimen for each type of RC beams (CL, CLT, CLF & CLTF) in relation to their experimental counterparts. From figure 5 and table 5 it is observed that the shear strength predictions for all types of beams obtained by both ANN models are in good agreement with the available test data. However, the predictions related to CL-1 and CLT-1 are characterised a COV similar to that of their experimentally established shear strength values V_u-CL and V_u-CLT respectively. Similar conclusions can be derived for the predictions obtained for the case of specimen-types CLF-2 and CLTF-2.

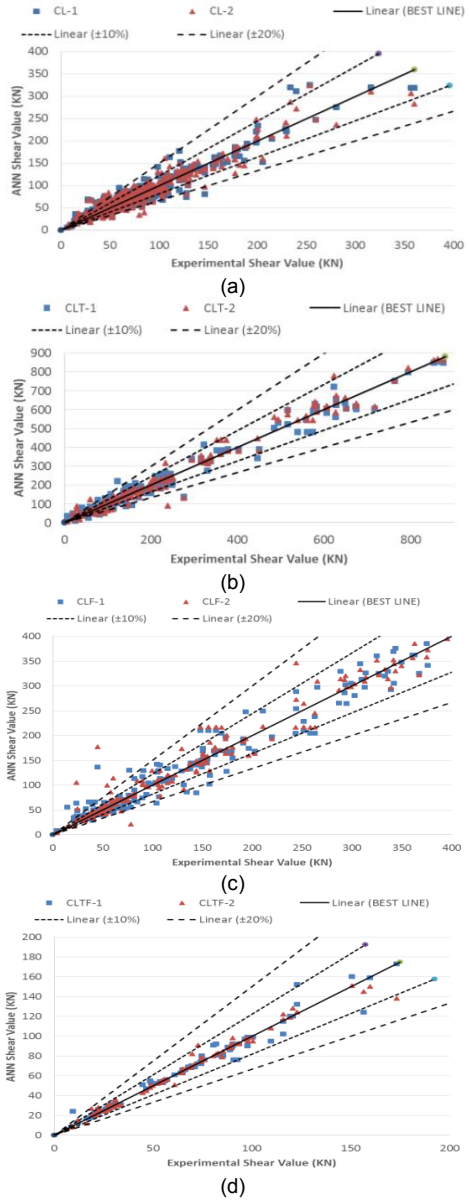

Figure 5. Comparison of ANN & Experimental V_u for RC beams (a) CL (b) CLT (c) CLF (d) CLTF

Table 5. Statistical Analysis of Pred. & Exp. V_u

(KN)	Min	Max	Mean	St.Dev.	CoV
V_u-CL	7	360	67.40	46.94	0.70
CL-1	5	325	68.04	46.9	0.69
CL-2	5	323	66.78	45.38	0.68
V_u-CLT	7	876	199.72	199.63	1.00
CLT-1	10	854	197.47	194.81	0.99
CLT-2	7	867	200.94	202.95	1.01
V_u-CLF	4.2	454	133.9	106.66	0.80
CLF-1	5	430	133.88	104.89	0.78
CLF-2	3	429	136.63	107.46	0.79

V_u-CLTF	8.9	173.3	61.7	36.6	0.59
CLTF-1	8	173	61.3	36.08	0.57
CLTF-2	8	151	61.44	35.4	0.58

5. PARAMETRIC STUDY

The ANN models CL-1, CLT-1, CLF-2 and CLTF-2 are used to perform a parametric study to assess the ability of ANN models in predicting the effect of various parameters on load-bearing capacity of RC beams. The parameters considered are presented in Table 6. For each case study two parameters vary while the rest remain constant as shown in Table 6.

Table 6. Statistical Information of the parameters use in Parametric Studies

Parameters		Constant Values	Varying Values
b	(mm)	125	125
d	(mm)	200	150,175,**200**,225,250
a_v/d		2.0	**2.0**,3.0,4.0,5.0,6.0
f_c	(Mpa)	40	20,**40**,60,80,100
ρ_l	(%)	1.5	1.0,**1.5**,2.0,2.5,3.0
f_y &f_{yw}	(Mpa)	450	250,350,**450**,550,650
ρ_w	(%)	0.2	0.2
l_f/d_f		80	40,60,**80**,100,120
V_f	(%)	1.0	0.25,0.5,**1.0**,1.5,2.0

Figures 6 & 7 provide the 3D representation of the predictions of the parametric studies for the case of beams (without fibres), by employing trained optimized ANNs models. Figure 6a, shows that increasing values of f_y and ρ_l result in an increase in V_u. Figure 6b reveals that with constant value of a_v/d, V_u increases with larger values of d. Finally, figure 6c shows that increasing values of f_c and d result in higher values of V_u. Figure 7a, shows that for constant value of f_y, V_u increase with the increase in ρ_l. Figure 7(b,c) reveal similar trends to those described in figure 6(b,c), respectively.

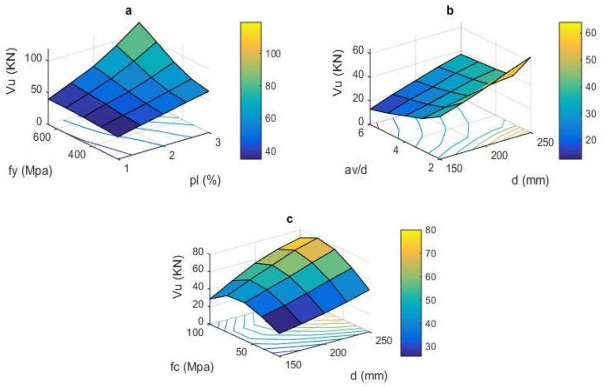

Figure 6. Parametric studies for CL-1

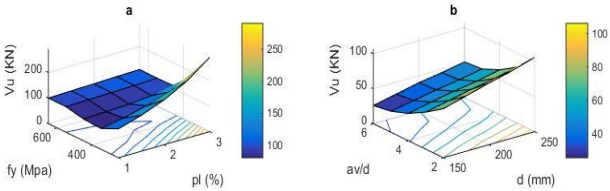

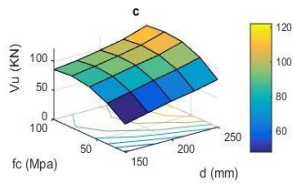

Figure 7. Parametric studies of CLT-1

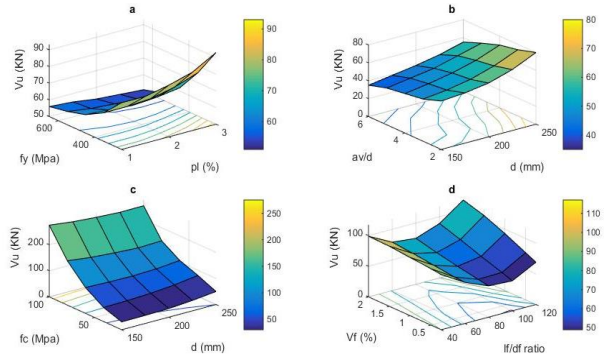

Figure 8. Parametric studies of CLF-2

Figures 8 & 9 provide the 3D representation of the predictions of the parametric studies for the case of beams (with fibres), by employing trained optimized ANNs models. Figure 8a, shows that increasing values of f_y and ρ_l result in an increase in V_u. Figure 8b reveals that with constant value of a_v/d, V_u increases with larger values of d. Figure 8c shows that increasing values of f_c and d result in higher values of V_u. Finally, figure 8d shows that for minimum and maximum l_f/d_f ratios with constant V_f, result in an increase in V_u. For higher V_f ratio, V_u shows higher values, against constant value of l_f/d_f.

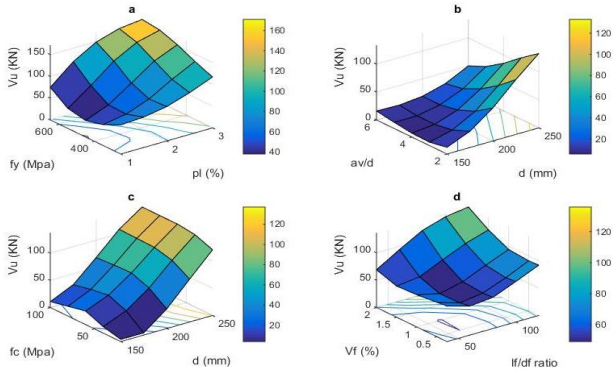

Figure 9. Parametric studies of CLTF-2

Figure 9a, shows that increasing values of f_y and ρ_l result in an increase in V_u. Figure 9b reveals that with constant value of a_v/d, V_u increases with larger values of d. Figure 9c shows that increasing values of f_c and d result in higher values of V_u. Finally, figure 9d shows that V_u increase with increasing values of l_f/d_f and V_f.

6. CONCLUSIONS

The objective of the present work is to investigate, through the use of appropriately trained ANNs, the effect of various parameters associated with the design

of different types of RC beams on the exhibited load-bearing capacity. The most important conclusions derived are:

- ANN models appear to be capable of providing predictions which provide a close fit to the available test data, for all types of RC beams considered herein.
- The number of hidden neurons affects the performance and stopping criteria of ANN models.
- The parametric study reveals that the V_u increases with larger l_f/d_f ratio for given fiber content V_f. The ANN model also shows that the V_u increases with f_c and decrease with a_v/d for given value of depth d.

It should be noted that additional work is currently being conducted in order to further validate the predictions obtained from the parametric investigation presented in the present article through the use of nonlinear finite element analysis and additional experimental data.

REFERENCES

ABBAS, A. A., SYED MOHSIN, S. M. & COTSOVOS, D. M. 2014a. Seismic response of steel fibre reinforced concrete beam–column joints. *Engineering Structures,* 59**,** 261-283.

ABBAS, A. A., SYED MOHSIN, S. M., COTSOVOS, D. M. & RUIZ-TERAN, A. M. 2014b. Shear behaviour of steel-fibre-reinforced concrete simply supported beams. *Proceedings of the ICE - Structures and Buildings,* 167**,** 544-558.

ABDALLA, J. A., ELSANOSI, A. & ABDELWAHAB, A. 2007. Modeling and simulation of shear resistance of R/C beams using artificial neural network. *Journal of the Franklin Institute,* 344**,** 741-756.

ACI 2008. Building Code Requirements for Structural Concrete (ACI 318-08) and Commentary. *aci-318-08*. American Concrete Institute 38800 Country Club Drive Farmington Hills, MI 48331.

BEALE, M. H., HAGAN, M. T. & DEMUTH, H. B. 2015. *Neural Network Toolbox™-User's Guide,* The MathWorks, Inc. 3 Apple Hill Drive Natick, MA 01760-2098, The MathWorks, Inc.

COTSOVOS, D. M. 2013. Cracking of RC beam/column joints: Implications for the analysis of frame-type structures. *Engineering Structures,* 52**,** 131-139.

CUCCHIARA, C., LA MENDOLA, L. & PAPIA, M. 2004. Effectiveness of stirrups and steel fibres as shear reinforcement. *Cement and Concrete Composites,* 26**,** 777-786.

DINH, H. H. 2009. *Shear Behavior Of Steel Fiber Reinforced Concrete Beams Without Stirrup Reinforcement*. Doctor of Philosophy, The University of Michigan.

EC2 2004. Eurocode 2: Design of concrete structures - Part 1-1: General rules and rules for buildings. *EN 1992-1-1* Management Centre: Avenue Marnix 17, B-1000 Brussels.

FURLAN, S. J. H., J.B. 1997. Shear Behaviour of Fiber Reinforced Concrete Beams. *Cement and Concrete Composites,* 19**,** 359-366.

I.A. BASHEER , M. H. 2000. Artificial neural networks: fundamentals, computing, design, and application. *Journal of Microbiological Methods* 43**,** 3-31.

JEYASEHAR, C. A. S., K. 2006. Damage assessment of prestressed concrete beams using artificial neural network (ANN) approach. *Computers & Structures,* 84**,** 1709-1718.

JSCE 2007. Standard Specifications for Concrete Structures -2007. *JSCE Guideline for Concrete No. 15*. Yotsuya 1-chome, Shinjuku-ku, Tokyo 160-0004, JAPAN.

KOTSOVOS & PAVLOVIĆ 1995. *Structural Concrete: Finite-element analysis and design,* Thomas Telford, London.

MANSOUR, M. Y., DICLELI, M., LEE, J. Y. & ZHANG, J. 2004. Predicting the shear strength of reinforced concrete beams using artificial neural networks. *Engineering Structures,* 26**,** 781-799.

MANSUR, M. A., ONG, K. C. G. & PARAMASIVAM, P. 1986. Shear Strength of Fibrous Concrete Beams Without Stirrups. *JOURNAL OF STRUCTURAL ENGINEERING,* 112**,** 2066-2079.

MERTOL, H. C., BARAN, E. & BELLO, H. J. 2015. Flexural behavior of lightly and heavily reinforced steel fiber concrete beams. *Construction and Building Materials,* 98**,** 185-193.

MONDO, E. 2011. *Shear Capacity of Steel Fibre Reinforced Concrete Beams without Conventional Shear Reinforcement*. M.Sc, Royal Institute of Technology (KTH)

PAPADOKONSTANTAKIS, S., MACHEFER, S., SCHNITZLEIN, K. & LYGEROS, A. I. 2005. Variable selection and data pre-processing in NN modelling of complex chemical processes. *Computers & Chemical Engineering,* 29**,** 1647-1659.

SAXÉN, H., PETTERSSON, F. 2006. Method for the selection of inputs and structure of feedforward neural networks. *Computers & Chemical Engineering,* 30**,** 1038-1045.

SLATER, E., MONI, M. & ALAM, M. S. 2012. Predicting the shear strength of steel fiber reinforced concrete beams. *Construction and Building Materials,* 26**,** 423-436.

SVOZIL , D., KVASNIEKA ,V., JIE POSPICHAL, J. 1997. Introduction to multi-layer feed-forward neural networks. *Chemometrics and Intelligent Laboratory Systems***,** 43-62.

WILSON, D. R., MARTINEZ, TONY R. 2003. The general inefficiency of batch training for gradient descent learning. *Neural Networks,* 16**,** 1429-1451.

YOO, D.-Y., YOON, Y.-S. & BANTHIA, N. 2015. Flexural response of steel-fiber-reinforced concrete beams: Effects of strength, fiber content, and strain-rate. *Cement and Concrete Composites,* 64**,** 84-92.

Infrastructure and Environment Scotland 3rd Postgraduate Conference
9th December 2015
Heriot-Watt University, Edinburgh

Towards a Better Understanding of the Factors Affecting the Prediction of Shear Buckling Coefficients of Steel Plate Girders

Z. Al-Azzawi, T. Stratford, M. Rotter, L. Bisby
Institute for Infrastructure and Environment,
University of Edinburgh
(Corresponding author e-mail: z.al-azzawi@ed.ac.uk)

ABSTRACT

In the design of plate girder web panels, according to AISC, AASHTO and EN 1993-1-5 specifications, the post-buckling strength is added to the elastic buckling strength. To calculate the elastic buckling strength, the boundary conditions of the web panel that is stiffened by transverse intermediate stiffeners must be determined. In current practice, the elastic shear buckling stress of a web panel with transverse stiffeners is estimated using the conservative assumption that the web panel has simply supported boundary conditions at the junctions with the flange and the stiffener. This study explores this assumption using a more realistic approach, both numerically, through approximately 5000 finite element models, and experimentally using a novel picture frame testing rig, designed for testing thin-walled plates for shear buckling. A design equation is proposed for estimating the shear bucking coefficients for plate girders loaded mainly in shear having both transverse and diagonal stiffeners.

1. INTRODUCTION

The two essential functions of the web plate in a plate girder are to maintain a relative distance between the top and bottom flanges and to resist shear stresses. In most practical ranges of plate girder bridge spans, the shear stresses are relatively low compared to bending stresses in the flanges induced by flexure. As a result, the web plate is typically much thinner than the flanges. The web panel is therefore prone to buckling at comparatively low shear forces. To enhance the web's buckling strength, it is often reinforced with transverse stiffeners. The web design then involves a selection of plate thickness and stiffener spacing to provide optimum economy in terms of the material and fabrication costs.

It is generally assumed that transverse stiffeners are sufficiently stiff to form nodal lines of the sinusoidal buckling waves on the web. This assumption is well justified, since the transverse stiffeners are designed to meet this condition. On the other hand, the web panel is elastically restrained at the junction between the web and flanges. The degree of the elastic restraint depends on many geometric parameters, such as a_w/h_w , h_w/t_w , b_f/h_w , t_f/t_w , and t_s/t_w , where a_w is the transverse stiffener spacing, h_w is the girder depth, b_f is the flange width, t_f is the flange thickness, t_s is the stiffener thickness, and t_w is the web thickness. Although the notion of the real boundary condition at the junction of the web and flanges to be somewhere between simple and fixed has been recognized for some time, it has always been idealized, mainly due to lack of means to evaluate it in a rational manner. For example, Basler (1963) and Porter et al. (1975) assumed that the web panel was simply supported at the junction, while Chern and Ostapenko (1969) obtained the ultimate strength by assuming that the junction was a fixed support. AISC and AASHTO specifications follow Basler's procedure just like the Euro standards follows Porter et al., in which the boundary condition at the junction is conservatively assumed to be simply supported.

2. ELASTIC SHEAR BUCKLING STRESS

The elastic buckling strength in Basler's approach as well as in the Cardiff method (Porter et al., 1975) is calculated considering the web panel simply supported on all sides. According to Timoshenko (1961):

$$\tau_{cr} = \frac{k_s \pi^2 E}{12(1-\nu^2)} \left(\frac{t_w}{h_w}\right)^2 \quad (1)$$

where

- τ_{cr} : elastic b uckling shear stress of web panel
- t_w : web plate thickness
- h_w : web plate height
- E : Young's modulus
- ν : Poisson's ratio
- k_s : shear buckling coefficient

$$k_s = 5.34 + \frac{4.0}{(a_w/h_w)^2} \qquad a_w/h_w \geq 1 \quad (2.a)$$

$$k_s = 4.0 + \frac{5.34}{(a_w/h_w)^2} \qquad a_w/h_w < 1 \quad (2.b)$$

where a_w is the space between vertical stiffeners.

According to Bulson (1970), Fujii, recommended fixed condition for the web sides along the flanges.

The shear buckling coefficient for this condition is given in graphical form by Fujii and as regression formula derived by Bulson (1970) as follows:

$$k_{sf} = 8.98 + \frac{5.61}{(a_w/h_w)^2} - \frac{1.99}{(a_w/h_w)^3} \quad a_w/h_w \geq 1 \qquad (3.a)$$

$$k_{sf} = \frac{5.34}{\left(\frac{a_w}{h_w}\right)^2} - \frac{2.31}{\left(\frac{a_w}{h_w}\right)} + 8.39\left(\frac{a_w}{h_w}\right) - 3.44 \quad a_w/h_w \geq 1 \qquad (3.b)$$

Based on over 300 numerical results, Lee et al. (1996) proposed the following two simple equations:

$$k = k_s + \frac{4}{5}\left(k_{sf} - k_s\right)\left[1 - \frac{2}{3}\left(2 - \frac{t_f}{t_w}\right)\right] \quad \frac{1}{2} < \frac{t_f}{t_w} < 2 \quad (4.a)$$

$$k = k_s + \frac{4}{5}\left(k_{sf} - k_s\right) \quad \frac{t_f}{t_w} > 2 \qquad (4.b)$$

where k_s is the simply supported buckling coefficient (Equation 2) and k_{sf} is given in Equation 3.

Al-Azzawi et al. (2015) found that Lee's equation is not safe for some range of their data, especially when $t_f / t_w \leq 3$, and proposed a similar modified equation as follows:

$$\mathrm{k} = \mathrm{k_s} + \frac{4}{5}(\mathrm{k_{sf}} - \mathrm{k_s}) \times \left[1 - \frac{1}{1.5}\left(3 - \frac{\mathrm{t_f}}{\mathrm{t_w}}\right)\right] \; 1.5 < \frac{\mathrm{t_f}}{\mathrm{t_w}} < 3 \quad (5.a)$$

$$\mathrm{k} = \mathrm{k_s} + \frac{4}{5}(\mathrm{k_{sf}} - \mathrm{k_s}) \quad \frac{\mathrm{t_f}}{\mathrm{t_w}} > 3 \quad (5.b)$$

3. EXPERIMENTAL WORK

In order to start the project with certain limits for the geometrical boundary conditions of the web plate, we needed to verify first whether there is a possibility to reach the fixed boundary conditions experimentally or not. To achieve this goal, a new testing rig (Picture Frame) is introduced. This Picture Frame is capable of holding the steel plate, applying fixed boundary conditions and in-plane shear load as can be seen in Figure 1. This Frame is capable of moving only in-plane using a 4-hinge beam chain mechanism and thus applying shear force upon the steel plate. This in-plane movement is achieved by 8 hinges instead of 4 to avoid cutting the plate corners which will affect the stress distribution and to make sure that the loads are applied throughout the plate corners as well. The figure shows the shear buckling curve for the tested specimen as well.

The tested plate dimensions were 500x500x2mm with an aspect ratio of 1.0 and a slenderness ratio of 250. The experimental value of the critical buckling shear stress was 42.5 MPa corresponding to 42.54 MPa in theory for fixed boundary condition. The plate had an initial imperfection of 0.4mm and it was tested using a 1000 kN Instron actuator with a stroke of 1.0 mm/min. The data were recorded using Microlink 3000 data acquisition system at a rate of 1.0 Hz.

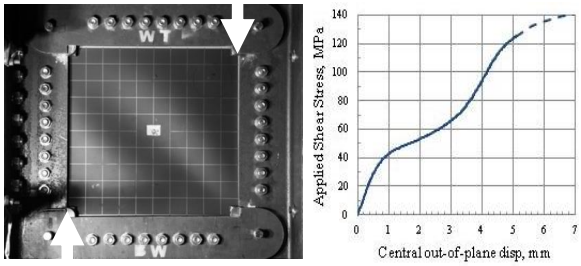

Figure 1. Picture frame testing rig and buckling curve.

4. FINITE ELEMENT ANALYSIS OF GIRDERS WITH TRANSVERSES STIFFENERS

4.1 *Analytical and Finite Element Model*

Figure 2 shows the plate girder analytical model adopted in this study. In studying the critical buckling shear stresses, the researchers usually model one panel from the plate girder, but in this study, two panels were modelled to take the stiffener effect on the buckling shear stress into account in addition to the usual flange effect. The stiffener effect is usually neglected in the calculations and simply supported boundary conditions in the junction between the web plate and the stiffener is assumed. In this study, single one sided whole height stiffener was used with three different projected widths (b_s) of 70, 110, and 140mm. This was done to take the effect of rigidity of the stiffener and its second moment of area on the geometrical boundary conditions at the junction with the web plate. Figure 2 also shows the load pattern which was necessary to simulate the case of pure shear in order to compare it with theory. The width of the flange (b_f) was chosen to be 340 mm which satisfies most of the available standards for plate girder design, but with minimum requirements, this is to ensure that worst-case scenario is taken into account in this study, and hence it is safely applicable for other range of flange widths. The yield strength (f_y), Poisson's ratio (v), and the modulus of elasticity (E) were taken as 355MPa, 0.3, and 200 GPa, respectively, and were kept constant in this study.

Figure 3 shows the buckled shape of one of the finite element models in this study where S9R5 elements are used to model the web plate and analysed using buckling analysis available in Abaqus software. Full details of the finite element model and a detailed convergence study can be found in Al-Azzawi et al. (2015).

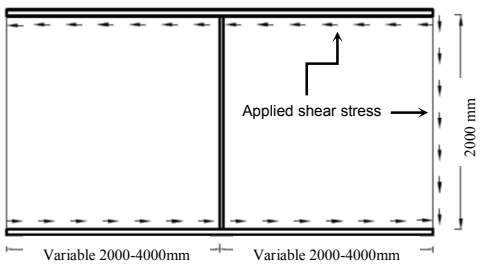

Figure 2. Plate girder analytical model.

4.2 *Parametric Study*

An extensive parametric study with approximately 5000 numerical analyses has been performed. The key variables were the aspect ratio (a_w /h_w), the slenderness ratio (h_w /t_w), the stiffener projected width (b_s), the flange thickness (t_f), the stiffener thickness (t_s), and the effect of initial imperfection (***ii***). The range of variables was as follows:

a_w/h_w =	1.0- 2.0	: a_w = 2000- 4000 mm
h_w/t_w =	125- 250	: t_w = 8- 16 mm,
ii =	$h_w/125000$-$h_w/100$	: a_w/h_w = 1.0
b_s =	70- 150 mm	
t_f =	2- 50 mm	
t_s =	2- 50 mm	

4.3 *Analysis of Numerical Results*

Figures 4.a-4.c show how the calculated critical buckling shear stress coefficient varies with the non-dimensional parameter (t_f /t_w) for an aspect ratio (a_w/h_w) of 1.0, 1.5, and 2.0, respectively.

A more sophisticated, conservative and continuous equation covering the whole range of data with better correlation with data, as shown in Figure 4 can be stated as follows:

$$k = k_s + \frac{0.9(k_{sf} - k_s)}{1 + e^{-\alpha\left(\frac{t_f}{t_w} - \beta\right)}} \qquad (6.a)$$

Where:

$\alpha = 2.5$ and $\beta = \frac{a_w}{h_w} + 0.5$

In addition, the following constraints should be taken into consideration:

- The effect of stiffener rigidity on the critical buckling shear stress coefficient for specimens with an aspect ratio a_w /h_w ≤1.0 may be taken as follows:

$$k_{Stiffener\ Effect} = k + 0.5\ ln\left(\frac{t_s}{t_w}\right) \qquad (6.b)$$

- k must be reduced for specimens with slenderness ratio h_w/t_w≤125 and t_f/t_w≤1.5 by the following factor:

$$k_{Slenderness\ Effect} = k - \left(\frac{a_w}{h_w} - 1\right) \qquad (6.c)$$

As a matter of fact, to the authors' knowledge, this reduction factor due to the slenderness ratio effect of the web plate is not mentioned elsewhere. This could lead to unconservative design in cases where shear buckling is significant.

4.4 *Validation of the Proposed Design Equation*

Table 1 illustrate the predictions of the proposed equation along with its constraints in comparison to Lee et al. and Al-Azzawi et al. equations where, *Sum* e^2, *e. sd.*, R^2, and *Rd* refer to the sum of the squared errors, the absolute error standard deviation, the R-squared, and ratio of the design equation to the numerical analysis value, respectively. *Rd* value <1 and >1 refer to safe and unsafe estimation, respectively.

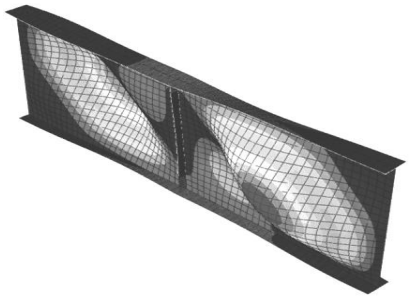

Figure 3. Finite element model buckling mode.

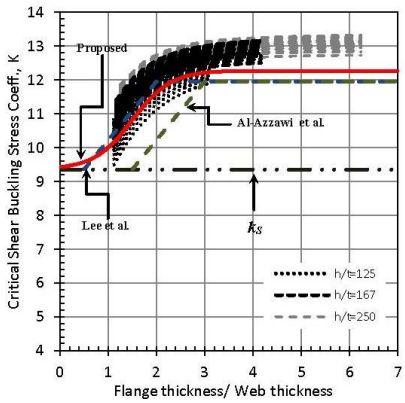

Figure 4-a. a_w /h_w=1.0

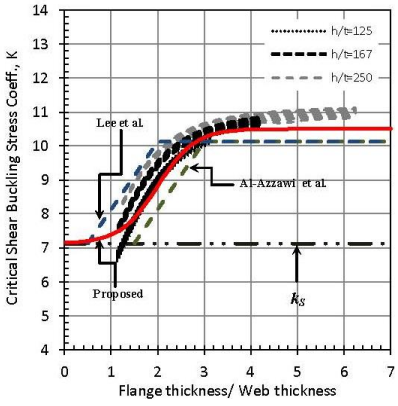

Figure 4-b. a_w /h_w=1.5

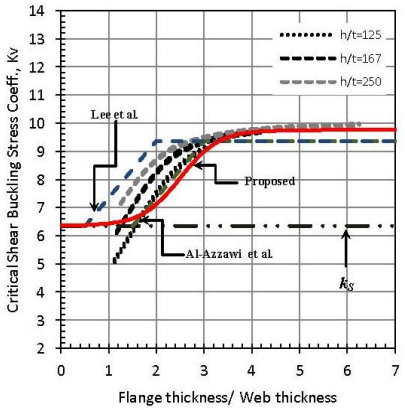

Figure 4-c. a_w /h_w=2.0

Figure 4. Design envelops for the critical buckling shear stress coefficient.

From Table 1 it can be seen that the proposed Equation (6) shows a better correlation with the data and much more accurate and conservative estimation for the critical shear buckling stress coefficients. The data in Table 1 is based on 2718 point out of a total of 4563 numerical analysis after excluding the unpractical range of data where the thickness of the flange and stiffener is less than the thickness of the web.

5. DIAGONALLY STIFFENED PLATES

In this section the critical shear buckling stress of diagonally stiffened plates will be introduced. Figure 5 shows the proposed analytical model. The model depends on the diagonally symmetric properties of plates subjected to pure shear stress. The assumption made was to divide the plate into two equal triangles by applying the appropriate boundary conditions on the plate perimeter and solving it numerically using finite element analysis. This model requires providing a diagonal stiffener sufficiently strong to form nodal lines of sinusoidal mode shapes, which implies that the stiffener will not deform during buckling. Both simply supported and clamped boundary conditions are investigated.

5.1 *Cox and Klein Isosceles Plate Model*

Cox and Klein model of isosceles triangle plates was recreated using finite element modelling having the same loading and boundary conditions, see Figure 6. For the sake of comparison, the loading in this model was a compression shear loading which is in the reverse direction of the usual tension shear loading of diagonally stiffened shear panels. This was done for the sake of comparison between the finite element and the analytical model which provides the solution for this case only. Table 2 compares the critical buckling shear stress results of the finite element model with Cox and Klein model. From this table it can be seen that the numerical and the analytical model are in good agreement.

5.2 *Rectangular versus Triangular Models*

The plate in Figure 5 was modelled numerically using commercial finite element software (Abaqus 6.10). In the first case the whole plate was modelled with the boundary conditions applied to the plate perimeter and the compression diagonal-model-I. In the second case, the rule of symmetry was exploited and only one half (triangle) of the plate was modelled with twice the applied load-model-II. In either case, both simply supported and clamped boundary conditions were investigated. In addition to that, three aspect ratios, namely, 1.0, 1.5, and 2.0, were taken into consideration.
Figure 7 shows the model for specimens having an aspect ratio of 1.0 with clamped boundary conditions on the plate perimeter and compression diagonal. Table 3 illustrates the results of the numerical models.

Table 1. Comparison of design methods

Method	a_w/h_w	Sum e^2	e. sd.	R^2	Rd
Lee et al.	**1.0**	4.21	3.39	0.69	0.94
	1.5	5.76	7.89	0.79	1.01
	2.0	22.33	13.76	0.76	1.06
Al-Azzawi et al.	**1.0**	8.99	5.3	0.83	0.92
	1.5	9.32	4.89	0.91	0.91
	2.0	4.93	5.77	0.89	0.95
Proposed Equation 6	**1.0**	0.7	2.34	0.87	0.98
	1.5	1.98	3.16	0.93	0.97
	2.0	4.75	5.75	0.89	0.96

Table 2. Comparison of the numerical results with Cox & Klein model.

	Analytical	Numerical	Error
S. S. B.C's	36.1	34.3	5%
Clamped B.C's	79.5	84.8	6%

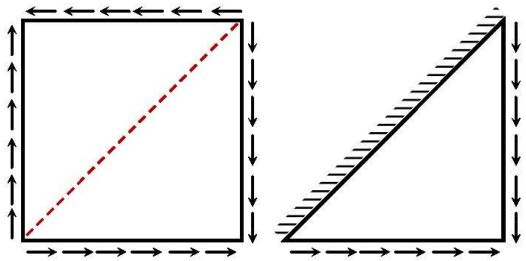

Figure 5. Analytical model adopted for diagonally stiffened plates.

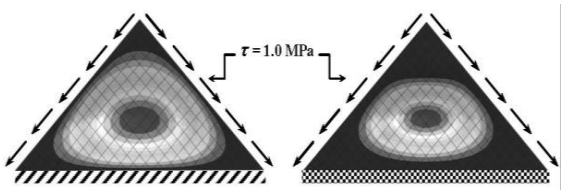

(a) Simply supported B.C's (b) Clamped B.C's

Figure 6. Cox and Klein model using finite element analysis.

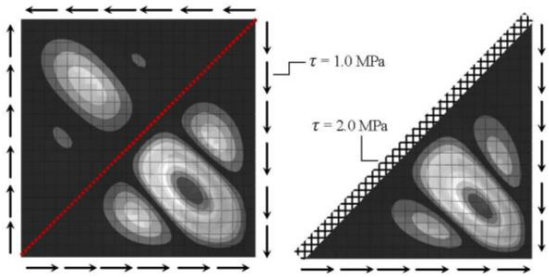

(a) Model-I (a) Model-II

Figure 7. Buckling modes of square and triangular plates.

Table 3. Critical buckling shear stresses, MPa.

S.S. B.C's		Aspect ratio (a_w/h_w)	Clamped B.C's	
Model-I	Model-II		Model-I	Model-II
89.9	89.0	**1.0**	124.9	124.6
63.4	58.6	**1.5**	86.6	82.5
52.4	44.0	**2.0**	70.0	62.4

From Table 3 it can be seen that the hypothesis of using a triangular plate with twice the applied shear stress instead of the diagonally stiffened square plate works perfectly for plates having an aspect ratio of 1.0. However, the accuracy of this assumption declines with increasing the aspect ratio from 1.0 with an average accuracy of 99% to 1.5 and 2.0 with an average accuracy of 94% and 87%, respectively. This lack of accuracy can be justified by the fact that triangle is not an isosceles anymore and the applied shear stress must be corrected accordingly. A geometrical correction factor can be suggested to be multiplied by the critical buckling shear stress for the non-isosceles triangular plates. This non-dimensional factor can be expressed as follows:

$$GNCF = \sqrt[4]{\frac{a_w}{h_w}} \quad (7)$$

where *GNCF* is the geometrical non-dimensional correction factor. Re-analyzing Model-II (the triangular palate model) with the proposed correction factor increased the accuracy of the model significantly to reach an average accuracy of 96.5% and 97% for plates with aspect ratios of 1.5 and 2.0, respectively.

The critical buckling shear stress coefficient for diagonally stiffened plates can be calculated using a reverse form of Equation 1 and the critical buckling shear stress determined using model-I, these values are shown in Table 4. The simply supported boundary conditions were imposed by restraining only the out of plane displacement of the plate perimeter and compression diagonal while the clamped boundary conditions refer to fixing all degrees of freedom in the plate perimeter and compression diagonal except for the in-plane displacement (*Ux*,*Uy*) of the plate simulating a diagonal stiffener strong in the major axis and weak in the minor one. The fully fixed boundary conditions refer to the same as above except that in-plane displacement of the plate was restrained in the compression diagonal to simulate an infinitely stiff diagonal stiffener. In all cases, the *x*,*y* displacement was restrained in the left hand side perimeter of the plate in Figure 7 for stability requirements.

The calculated buckling coefficient values form the minimum and maximum envelopes for shear buckling analysis of diagonally stiffened plates. Yet, these theoretical conditions are unlikely to be fulfilled and further investigation is needed for the practical cases where the diagonal stiffener provides neither simply supported nor fixed boundary conditions in the junction with the plate compression diagonal, which will be provided via finite element analysis in the next section.

Table 4. Critical shear buckling coefficients.

a_w/h_w	S.S. B.C's	Clamped B.C's	Fully Fixed B.C's
1.0	31.09	43.18	62.18
1.5	21.92	29.93	46.66
2.0	18.13	24.20	32.56

6 DIAGONALLY STIFFENED PLATE GIRDERS

6.1 Analytical and Finite Element Model

Figure 8 shows the analytical model adopted in this section for the diagonally stiffened plate girders. Typical two-span plate girder having an aspect ratio ranging from 1.0 to 2.0 was considered for simplicity. The dimensions, sectional and material prosperities were kept the same as in section (4) for the sake of comparison. However, in order to reduce the variables in this parametric study, the flange thickness (t_f) and the transverse stiffener thickness (t_s) were kept relative to the thickness of the web plate at a ratio of ($3\times t_w$) to insure the consistency of the outcomes and to estimate the effect of the diagonal stiffener independently. In addition to that, the projected width b_s of all stiffeners was kept constant at 110mm, which is the average stiffener width we had in the previous parametric study.

The adopted finite element model for studying the effect of diagonal stiffeners on the critical buckling shear stress of plate girders was built using the same procedures adopted in the previous parametric study (section 4.1) except for adding two external stiffeners to relieve the stress concentration at the diagonal stiffeners external junctions. The load was applied at the middle of the plate girder and simply supported boundary conditions were imposed at the two supports- Figure 8. The buckled shape of a specimen with an aspect ratio of 1.0, slenderness ratio of 167, and a diagonal stiffener thickness of 12mm is shown in Figure 9.

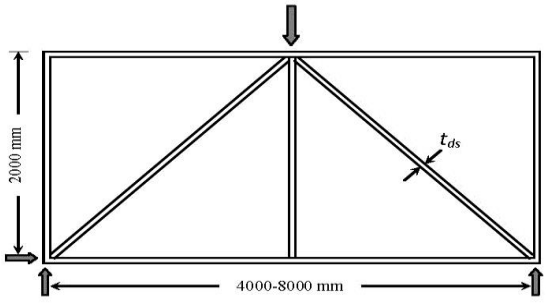

Figure 8. Analytical model adopted in the diagonal stiffener study.

6.2 *Parametric Study*

The parametric study was performed with the following range of variables:

a_w/h_w = 1.0- 2.0 with a_w = 2000- 4000 mm,
h_w/t_w = 125- 250 with t_w = 8- 16 mm,
$t_{ds} = t_w$ - 50 mm,

where t_{ds} is the diagonal stiffener thickness.

Figure 10 shows the critical buckling shear coefficients for the whole data range of this parametric study. It can be seen that the data is mostly affected by the aspect ratio of the web (a_w/h_w) with minor effect of slenderness ratio (h_w/t_w); mostly with an aspect ratio of 1.0 and then its effect descends with increasing the aspect ratio.

6.3 *Analysis of Numerical Results*

From Figure 10, it can easily be shown that there is a limiting factor which allows reaching the simply supported boundary condition buckling coefficient for diagonally stiffened steel plate girders, this factor can be expressed as follows:

$$\frac{t_{ds}}{t_w} \geq \frac{a_w}{h_w} + 2.0 \qquad (8)$$

In another word, the ratio of the diagonal stiffener thickness to the web thickness must be greater or equal to the aspect ratio plus two. Beyond this limit the buckling coefficients may be increased even more to a specific value, however, reducing this limit will reduce the buckling coefficient as well.
For the whole range of data, the following general equation can be proposed:

$$k = \alpha \left(\frac{t_{ds}}{t_w}\right)^{\beta} \qquad 1.0 \leq \frac{t_{ds}}{t_w} \leq 6.25 \qquad (9)$$

where:

$$\alpha = 1.5k_s - 0.5k_{sf}$$
$$\beta = 0.1\left(3 - \frac{a_w}{h_w}\right)$$

k_s and k_{sf} represent the simply supported and clamped boundary condition buckling coefficients predicted in Table 4.

7. CONCLUSIONS

The assumption for the boundary conditions represented by the elastic restraint at the junction of the web, flange, and stiffener of steel plate girders was revisited and investigated using finite element analysis. Approximately 5000 numerical model were implemented in an extensive parametric study covering wide range of variables affecting the prediction of shear buckling coefficients. It was shown that calculating the shear buckling coefficients using the assumption of simply supported boundary conditions adopted in most codes of practice is rather conservative and that the effect of transverse stiffener can be taken into consideration in calculating the shear buckling coefficients for plate girder webs having an aspect ratio of 1.0 or less. A more reliable general equation for determining the shear buckling coefficients is proposed. This new equation is more general, correlates better with the available data, and proved to be more conservative as well.
A mixed approach between theoretical and numerical analysis was adopted to calculate the theoretical shear buckling coefficients of diagonally stiffened plate girders both for simply supported and clamped boundary conditions and a parametric study was performed to investigate the more practical case of hybrid boundary conditions at the junction between the diagonal stiffener and the web plate. A novel equation was proposed to estimate the shear buckling coefficients of diagonally stiffened plate girders.

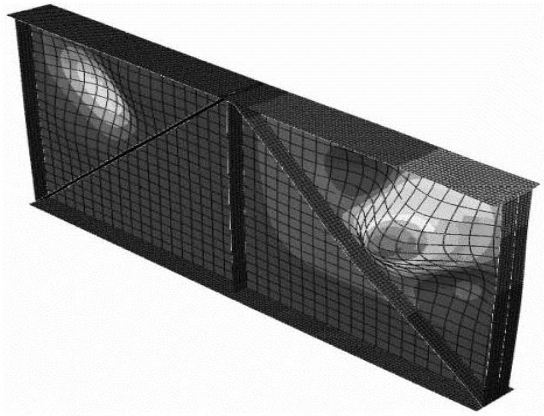

Figure 9. Finite element model buckling mode.

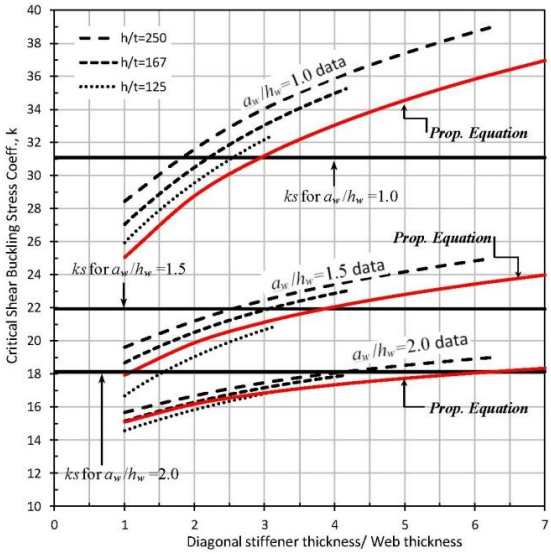

Figure 10. Critical buckling shear coefficients for diagonally stiffened plate girders.

REFERENCES

AASHTO, LRFD-SI Units (2007). “Standard Specifications for Highway Bridges,” 4th Ed., Washington, D.C, USA.

AISC, LRFD (1994). “Manual of Steel Construction, Load and Resistance Factor Design,” 2nd Ed., Vol. I and II, Chicago, Illinois, USA.

AL-AZZAWI, Z., STRATFORD, T., ROTTER, M., and BISBY, L. (2015) “Effect of flange and stiffener rigidity on the boundary conditions and shear buckling stress of plate girders,” European Bridge Engineering Conference, Edinburgh, 23-25rd June, 12 pp.

BASLER K. (1963). “Strength of plate girders in shear,” Trans. ASCE 128, pp. 683-719.

BULSON P. S. (1970). “Stability of Flat Plates,” Elsevier, New York.

CHERN C. and OSTAPENKO A. (1969). “Ultimate strength of plate girder under shear,” Fritz Engineering Laboratory. Report No. 328.7, Lehigh University.

COX H. L. and KLEIN B. (1955). “The buckling of isosceles triangular plates,” J. Aero. Sci., Vol. 22, No. 5, pp. 321 -325.

EUROPEAN COMMITTEE FOR STANDARDISATION (EC3 2006). Eurocode 3: Design of Steel Structures-Part 1-5: Plated Structural Elements. EN 1993-1-5: 2006. Brussels: CEN.

LEE S.C., DAVIDSON J.S., and YOO C. H. (1996). “Shear buckling coefficients of plate girder web panels,” Computers & Structures, Vol. 59, No 5, pp. 789-795.

PORTER D.M., ROCKEY K.C., and EVANS H.R. (1975). “The collapse behaviour of plate girders in shear,” Journal of The Structural Engineer, Vol. 53, No. 8, pp. 313-325.

TIMOSHENKO S. and GERE J.M. (1989). “Theory of elastic stability,” Second renewed edition, Dover Publications Inc., Mineola, New York, originally published: New York, McGraw-Hill Book, 1961, 541 pp.

Infrastructure and Environment Scotland 3rd Postgraduate Conference
9th December 2015
Heriot-Watt University, Edinburgh

Elastic-Plastic hardening buckling of axially compressed imperfect cylinders with different material properties

Hussain Al-Lawati and J. Michael Rotter
Institute for Infrastructure and Environment,
University of Edinburgh
(e-mail: H.Al-Lawati@ed.ac.uk and m.rotter@ed.ac.uk)

ABSTRACT

This paper presents a comprehensive exploration of the non-linear buckling and collapse strength of thin axially compressed medium length imperfect cylindrical shells made of elastic-plastic-hardening materials. The predictions are obtained using specialist finite element program NEPAS. The well-established circumferential weld depression imperfection form is used and the parameters of the European Standard on Shell Buckling (EN-1993-1-6, 2007) are extracted to give a clear description of the complex range of behaviour discovered. The study explored a very wide range of the many parameters involved. Some significant unexpected outcomes were discovered, giving new insights into the complex buckling behaviour involved. The new findings will very probably be adopted into the next edition of EN 1993-1-6.

1. INTRODUCTION

Shell structures are considered to be a major challenge to the analyst and the designer. The designer should guarantee the safety of the structure against a wide range of possible failure modes that may occur during severe incidents. As a result, a huge number of studies of shell structures, including linear elastic, plastic, stability, imperfection sensitivity and collapse analyses have been undertaken to explore the many possible issues (Rotter, 2004). Although, certain of these analyses can be used immediately to estimate the shell strength, most of them lead to poor evaluations. Consequently, some cautious interpretation is needed in order to obtain a shell structure that is safe against catastrophic events. As a result, few organized standards for shell structures are currently available (e.g. ACI-334.1R (2002), API-620 (2002), and EN-1993-1-6 (2007) and its commentary in ECCS (2008)).

Shell structures most commonly fail either by buckling, by excessive deformation or by rupture. The most intensively researched aspect is the buckling behaviour, partly because it presents the most challenging problems mathematically, partly because the buckling strength is extremely sensitive to small deviations of geometry, and partly because thin shells that are susceptible to buckling offer the most efficient structural form for many conditions (Rotter, 2007). Because of its complexity the understanding of shell buckling phenomena developed rather slowly during the 20th century and it remains a field in which many new discoveries can be made. Knowledge of shell buckling was gained from experiments, from algebraic theory and from computational assessments, but these three are not often easy to correlate with each other: this has consequently led to the slow development.

The earliest design methods for shell structures were based empirically on experiments. This continues to be the case to a significant extent, though the relationship between laboratory tests and full scale construction is not close. The causes of huge discrepancy between the first shell theory (e.g. Southwell (1914)) and the first shell test outcomes (Robertson, 1928) were not sorted out until to the work of Koiter (1945), who examined the effect of the geometric imperfections on the cylindrical shell buckling resistance. Following researchers, like Donnell and Wan (1950), Hoff and Soong (1967), Flügge (1973), Budiansky and Hutchinson (1966), Hutchinson et al. (1971), Muggeridge and Tennyson (1969) and Yamaki (1984) had also contributed exceedingly in resolving the mismatch between theory and experimental results. Indeed, the history of shell buckling is governed by the buckling of cylinders subjected to axial compression.

Axial compression in a cylinder arises from different sources (e.g. self-weight, wind, earthquake, roof loads, stored solids …etc.). The buckling behaviour of a cylindrical shell under axial compression, such as tanks and silos is thoroughly investigated compared to other shell buckling problems (Rotter, 2005). It is well known that the axially compressed cylinder is extremely sensitive

to the geometric imperfections shape and amplitude. Therefore, the credible strength of such structure under this particular loading condition is complicated to evaluate in safe manner (Rotter, 2008). Due to the enormous range of potential imperfection forms, and the poor connection of basic shapes to measured imperfections, there has long been an argument with regard to the worst shape of imperfection and the practically pertinent shape. In the current study, the circumferential weld depression imperfection form (Rotter and Teng, 1989) is implemented (Figure 1).

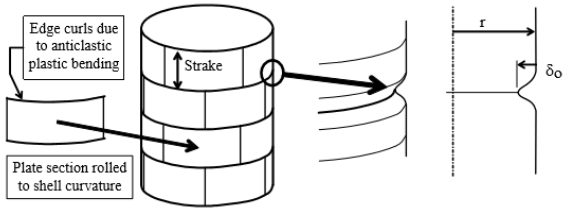

Figure 1. Weld depression imperfection and its causes (Rotter, 2011).

The advantageous of this type of imperfection can be summarized as follows: has a strong basis in full scale shell measurements, has been extensively studied in the literature and has shown to be either the worst or near to the worst when measured using allowed stick measurements. Moreover, this specific imperfection shape is readily defined, local, continuous over the height, and around the circumference of the shell and can be utilized in studies of a wide range of multiple problems for comparison, since its impact on the elastic buckling carrying capacity of cylinders have been precisely and comprehensively authenticated in the past.

A lot of previous studies on the axially compressed cylinder has concentrated to find the elastic buckling resistance, rather than inelastic buckling strength, which is true for both experimental and numerical approaches (ECCS, 2008). Generally speaking, the majority of research on elastic-plastic shell buckling has been done utilizing numerical methods. There are far fewer laboratory tests on elastic-plastic shell buckling than on elastic buckling, and for this reason the complete database is limited to some extent. Also, a few analytical studies are available for discovering the impact of material non-linearity on bifurcation buckling. Rotter (2008) has accomplished an important work in exploring the elastic-plastic imperfection sensitivity of axially compressed cylinders with weld depressions by changing material properties (without covering the effect of the strain hardening on the buckling strength as shown in Figure 2 and Figure 3). In his study, the analysis has been done using Finite Element calculations (FE).

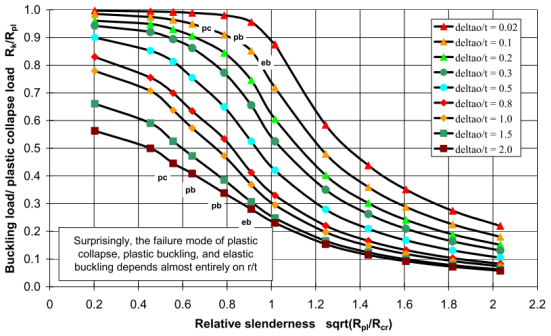

Figure 2. Elastic-plastic buckling and collapse strengths of imperfect cylinders (Rotter, 2008).

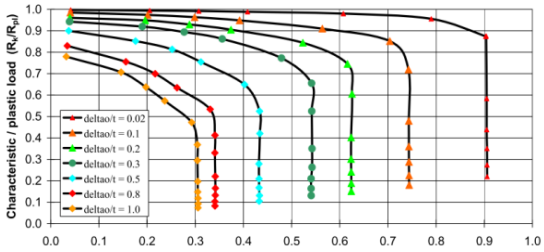

Figure 3. Buckling and collapse curves for parameter extraction (Rotter, 2008).

In view of this, this paper is targeting to expand the study of Rotter (2008) by involving the strain hardening influence that is results in an increase in buckling strength. Actually, the results will be interpreted in the context of the most advanced shell buckling standard (EN-1993-1-6, 2007) that is mainly relied on empirical fits to tests data and its commentary (ECCS, 2008). In other words, this paper is seeking a match between codified rules concerning the elastic-plastic buckling strength of cylinders under axial compression and the FE estimations.

2. THE EN 1993-1-6 (2007) CAPACITY CURVE FOR SHELL BUCKLING

The general capacity curve (Figure 4) illustrates the relationship between the buckling resistance and the relative slenderness. The relative slenderness is determined in terms of the plastic limit reference resistance *Rpl* and the elastic critical resistance *Rcr* (Equation 1).

$$\lambda_x = \sqrt{R_{pl}/R_{cr}} \quad (1)$$

The plastic limit reference resistance is obtained from the small displacement theory ideal elastic-plastic analysis, whereas the elastic critical resistance is found from the linear bifurcation analysis. The normalized buckling strength χ is defined in the matter of the characteristic resistance *Rk* and the plastic limit reference resistance *Rpl* (Equation 2).

$$\chi = R_k / R_{pl} \quad (2)$$

The characteristic strength is indicated by experiment or from a geometrically and materially non-linear analysis of the imperfect structure.

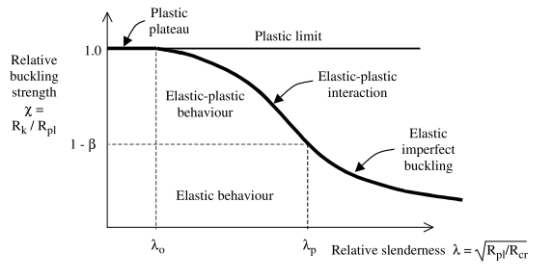

Figure 4. The traditional capacity curve in EN 1993-1-6 (2007) (Rotter, 2005).

The entire capacity curve is consists of three segments in respect of the slenderness ratio: slender (elastic buckling), stocky (plastic collapse) and intermediate structures (elastic-plastic buckling). The formulation of the EN-1993-1-6 (2007) general capacity curve is given by.

$$\chi = 1 \qquad \text{when } \lambda x \le \lambda o \quad (3)$$

$$\chi = 1 - \beta \left[\frac{\lambda_x - \lambda_o}{\lambda_p - \lambda_o}\right]^{\eta} \qquad \text{when } \lambda o < \lambda x < \lambda p \quad (4)$$

$$\chi = \alpha / \lambda^2 \qquad \text{when } \lambda p \le \lambda x \quad (5)$$

In which

$$\lambda_p = \sqrt{\frac{\alpha}{1-\beta}} \quad (6)$$

The background to these equations can be found in Rotter (2005).

The elastic-plastic interaction capacity curve is strictly dominated by the key parameters α, β, λo and η, each of which defines a distinguish aspect of the behaviour. For elastic buckling regime ($\lambda x \ge \lambda p$), the reduction of strength because of geometric non-linearity and imperfection sensitivity is controlled by the elastic imperfection reduction factor α, which it-self relies on the imperfection shape and amplitude. The plastic range factor β is capturing the load level at which plasticity first influences the buckling resistance ($\lambda x = \lambda p$). The squash limit relative slenderness λo is defining the slenderness at which the plastic reference resistance Rpl is overtaken ($\lambda x \le \lambda o$). The interaction exponent η controls the curvature of the elastic-plastic buckling curve, allowing the full relationship to vary from about no interaction between the elastic and plastic buckling to very strong interaction ($\lambda o < \lambda x < \lambda p$). Each of these parameters is always depends on the geometry, load case and boundary conditions.

From Figure 4 it is not simple to extract the controlling parameters directly and therefore Rotter (2002) has devised an alternative form (Figure 5) that authorize these parameters for general structural system to be rigorously earned with proportional simplicity. In this alternative capacity curve the ratio of failure load to plastic reference load (Rk/Rpl) is plotted versus the ratio of the failure load to linear elastic bifurcation critical load (Rk/Rcr). An example of such interaction curve is displayed in Figure 3.

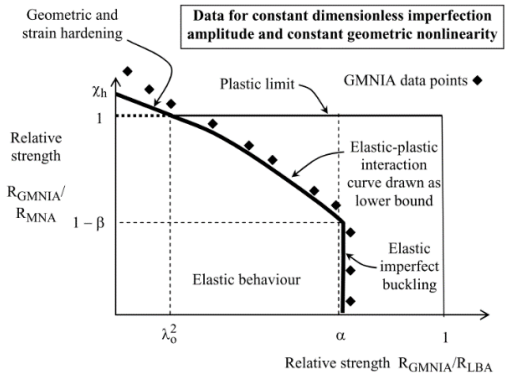

Figure 5. The alternative capacity curve for extracting parameters (Rotter, 2005).

3. MODELLING OF ELASTIC-PLASTIC HARDENING CYLINDERICAL SHELL

In this study, non-linear elastic-plastic buckling analysis, including strain hardening effect of the medium length cylindrical shell is conducted using the program NEPAS (Teng and Rotter, 1989). The reason behind the selection of the medium length cylinder is to ensure that there is no critical role of boundary conditions in determining the buckling strength. Thus, a cylinder with a dimensionless length ω (Equation 7) equal to 271.895 is used to achieve this purpose.

$$\omega = \frac{L}{r}\sqrt{\frac{r}{t}} = \frac{L}{\sqrt{rt}} \quad (7)$$

The cylinder radius to thickness ratio r/t is assumed to be 1000. The geometric imperfections with amplitudes in the range of $0.01 < \delta o/t < 1.0$ are used in this work.

Imperfection shape of a single circumferential weld depression Type A (Rotter and Teng, 1989) is assumed throughout the analysis (Figure 1), although multiple imperfections (closely placed) of the same amplitude has been proved to drop the buckling strength dramatically (Rotter, 1996). The imperfection form is represented by Equation 8.

$$\delta = \delta_o e^{-\pi x/\lambda_i}(\sin \pi x/\lambda_i + \cos \pi x/\lambda_i) \quad (8)$$

where δ is the local amplitude at the axial distance x from the center of the imperfection and λi is the half wavelength of the imperfection, taken here as the linear bending half wavelength of the cylinder λ (Equation 9).

$$\lambda = 2.444\sqrt{rt} \quad (9)$$

This assumption is considered because it gives buckling strength that is close to the lowest buckling resistance as well as it is of practical relevance (Rotter, 1997).

For pre-buckling stage, the upper edge is free to displace radially and axially, whereas it is restrained circumferentially and rotationally. At lower edge, all the displacements are restrained, except the radial displacement. This boundary condition is implemented to produce a uniform membrane stress state, and so ignoring any bending stresses arise near the boundary. For buckling phase, both of roof and base are constrained to move radially and circumferentially, but are free to rotate and displace axially. This boundary condition is assumed to be in line with the assumptions made for the classical medium cylinder under uniform axial compression buckling strength (Equation 10).

$$\sigma_{cl} = 0.605\, E\, \frac{t}{r} \quad (10)$$

For plasticity, the deformation theory is chosen during the analysis because it has demonstrated previously reasonable results compared to the experiments (Galletly et al., 1990).

A mild steel cylinder with Young's modulus E = 200000 MPa and Poisson's ratio v = 0.3 is utilized in this study. Different strain hardening modulus are involved in this study (1% ≤ Es/E ≤ 5%). A wide range of yield stress σy is applied with a view to get different material properties. This may produce data points, which are affected by the geometric imperfection amplitude and the geometric nonlinearity to the same extent (i.e. attaining invariable elastic buckling strength ratio α, making its value easy to extract as clear in Figure 5).

4. ELASTIC-PLASTIC HARDENING BUCKLING PREDICTIONS OF AXIALLY COMPRESSED CYLINDER

Figure 6 to Figure 9 shows the effect of strain hardening (1% ≤ Es/E ≤ 5%) on the axially compressed imperfect cylinder buckling strength. This is offered through plotting both, the classical and the alternative buckling capacity curves, for two different imperfection amplitudes, $\delta o/t$ = 0.01 (almost perfect cylinder) and 1.0.

As obvious from Figure 7 and Figure 9, the elastic buckling ratio α is decreases with higher imperfection amplitude. For $\delta o/t$ = 0.01, α is near 1.0, whilst it is declined by roughly 70 per cent at imperfection just of one wall thickness. It is clear that α is independent of Es.

In addition, neither λp nor β are impacted by Es, regardless of imperfection amplitude (Figure 6 to Figure 9).

Of-course, η and λo are changing due to the strain hardening existence, but with wider influence for larger imperfections.

The cylinder will suffer from plasticity with greater level at smaller ratios of Es/E, where lower $\sigma k/\sigma y$ is found, irrespective of $\delta o/t$ (but the effect is more pronounced at higher $\delta o/t$) as revealed in Figure 6 to Figure 9.

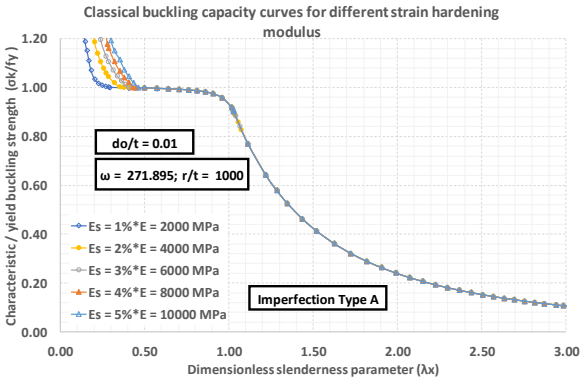

Figure 6. Traditional e-p buckling capacity curve for axially compressed imperfect cylinder ($\delta o/t$ = 0.01) with different Es.

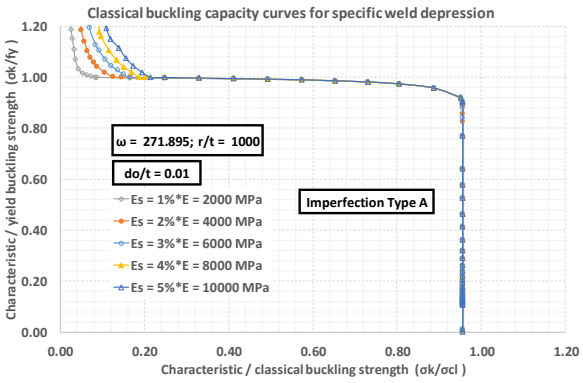

Figure 7. Alternative e-p buckling capacity curve for axially compressed imperfect cylinder ($\delta o/t$ = 0.01) with different Es.

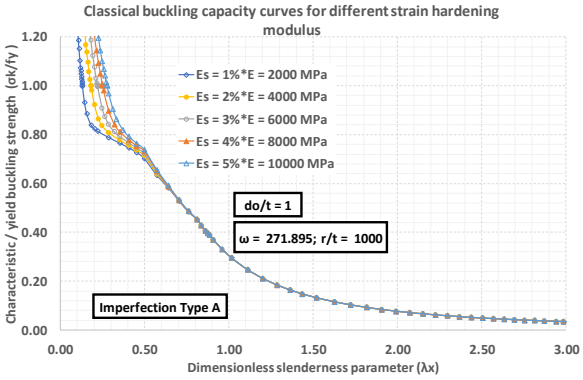

Figure 8. Traditional e-p buckling capacity curve for axially compressed imperfect cylinder ($\delta o/t$ = 1.0) with different Es.

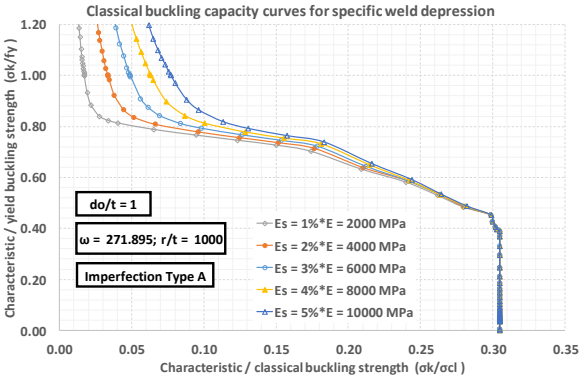

Figure 9. Alternative e-p buckling capacity curve for axially compressed imperfect cylinder ($\delta o/t$ = 0.01) with different Es.

The variation of the relative buckling resistance because of different imperfection amplitudes is demonstrated via Figure 10 to Figure 13. This is presented for two disparate Es/E values, 1 and 5 per cent.

The elastic buckling factor α is reduced considerably as the imperfection amplitude increases. However, it is remained stable (unchanged with different σy values for any $\delta o/t$) for both Es/E ratios.

The plastic limit relative slenderness λp is decreased and the plastic range factor β is raised when the cylinder wall subjected to bigger depressions at its mid-height. This implies stronger interaction between stability and plasticity (and thus lesser η) as a result of deeper inward imperfections. Actually, this case becomes more critical for Es/E = 1%, compared with Es/E = 5% as evidently viewed in Figure 10 to Figure 13.

The squash limit relative slenderness λo is dropped over higher $\delta o/t$ values. This drop is more serious if smaller strain hardening modulus is accounted into the design process.

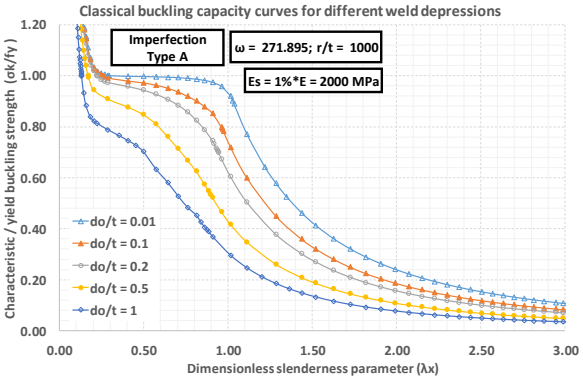

Figure 10. Traditional e-p buckling capacity curve for axially compressed imperfect cylinder (Es/E = 1%) with different $\delta o/t$.

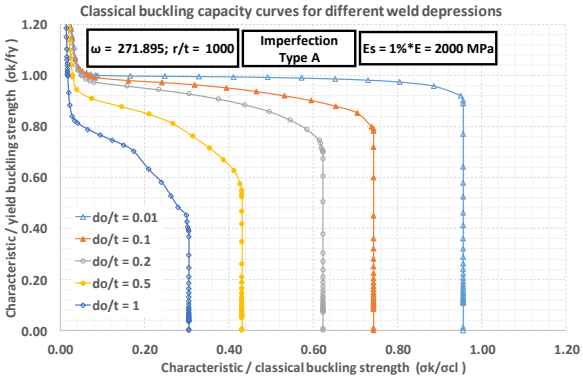

Figure 11. Alternative e-p buckling capacity curve for axially compressed imperfect cylinder (Es/E = 1%) with different $\delta o/t$.

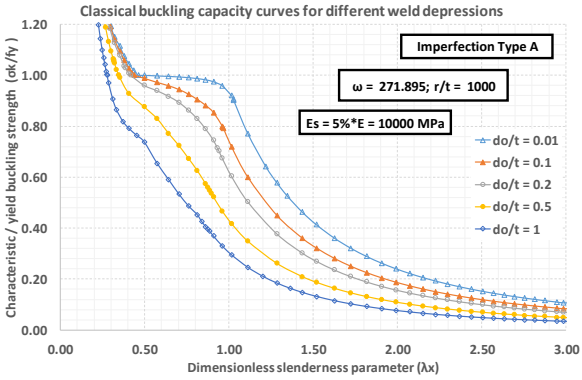

Figure 12. Traditional e-p buckling capacity curve for axially compressed imperfect cylinder (Es/E = 5%) with different $\delta o/t$.

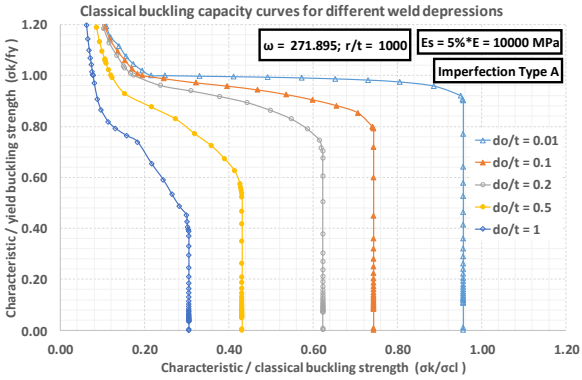

Figure 13. Alternative e-p buckling capacity curve for axially compressed imperfect cylinder (Es/E = 5%) with different $\delta o/t$.

4.1 The elastic imperfection reduction factor α

Figure 14 displays the variation of the elastic buckling resistance ratio α of an imperfect medium uniformly axially compressed cylindrical shell over a practical range of imperfection amplitude $\delta o/t$.

The cylindrical shell under uniform axial compression is quite sensitive to imperfections as illustrated in Figure 14. For example, the buckling

strength ratio is decreased drastically to about 30 per cent of the classical elastic buckling stress σ_{cl} when the circumferential weld depression is just one wall thickness.

In fact, there is no any impact on the elastic buckling carrying capacity of the cylinder due to the change in strain hardening as presented in Figure 14.

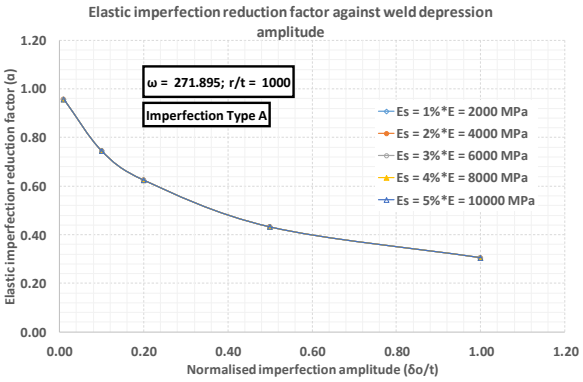

Figure 14. The imperfection sensitivity curve for axially compressed cylinder with different *Es*.

The traditional elastic buckling capacity curve of axially compressed cylinder is exhibited in Figure 15.

Since, the cylinder is medium in length and the loading is uniform around the circumference, then the classical elastic buckling stress and the yield stress are used in place of *Rpl* and *Rcr* respectively.

Here it is confirmed again the sensitivity of axially compressed thin cylinder to the imperfections. Smaller imperfections will maintain the elastic behavior of the cylinder until higher σ_k/σ_y, while bigger imperfections tends to change the failure mode from elastic to elastic-plastic buckling earlier.

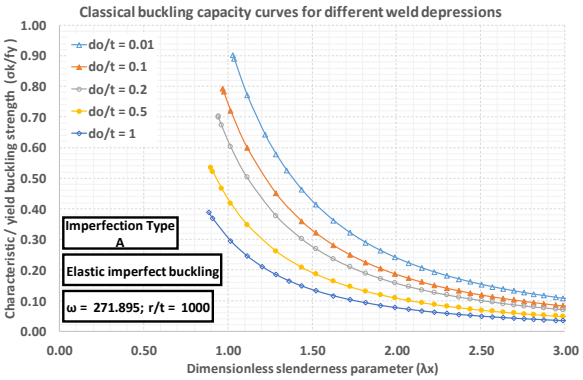

Figure 15. Traditional elastic buckling capacity curve for axially compressed cylinder with different *δo/t*.

CONCLUSION

The first wide ranging study of the axial compression buckling of thin imperfect cylindrical shells made of elastic-plastic-hardening material has been undertaken. It has covered the full range of geometries, imperfection amplitudes and material properties to produce a comprehensive description for wide applications in tanks, silos, turbine towers, biodigesters and many other structural forms.

The results have been expressed in terms of the shell buckling capacity curve of EN-1993-1-6 (2007) to give a comprehensive but relatively simple description of the very complex overall behaviour.

Most computational studies of shell buckling have used an ideal elastic-plastic material model, which has led to seriously underestimated resistances for both thick and thin shells. The present study is consequently able to justify classical empirical rules that had no justification theoretically.

Many unexpected aspects were discovered in this study, making it a ground-breaking first exploration of vitally important phenomena for practical design.

REFERENCES

ACI-334.1R 2002. Concrete Thin Shell Design and Construction. Detroit, USA: American Concrete Institute.

API-620 2002. Design and Construction of Large Welded, Low-Pressure Storage Tanks Washington, D.C.: American Petroleum Institute.

BUDIANSKY, B. & HUTCHINSON, J. W. 1966. A Survey of Some Buckling Problems. *AIAA Journal*, 4**,** 1505-1510.

DONNELL, L. H. & WAN, C. C. 1950. Effect of imperfections on buckling of thin cylinders and columns under axial compression. *Applied Mechanics, Transaction of the ASME,* 17**,** 73-83.

ECCS 2008. European Recommendations for Steel Construction: Buckling of Shells. Brussels: CEN.

EN-1993-1-6 2007. Eurocode 3, Part 1.6: Strength and Stability of Shell Structures. Brussels: CEN.

FLUGGE, W. 1973. *Stresses in shells,* Berlin, Springer-Verlag.

GALLETLY, G. D., BLACHUT, J. & MORETON, D. N. 1990. Internally pressurised machined domed ends - a comparison of the plastic buckling predictions of the deformation and flow theories. *Proceedings of the Institution of Mechanical Engineers Part C-Journal of Mechanical Engineering Science,* 204**,** 169-186.

HOFF, N. J. & SOONG, T. C. Buckling of axially compressed cylindrical shells with non-uniform boundary conditions. In Symposium

on Thin Walled Steel Structures, 1967 University College, Swansea. 61-80.

HUTCHINSON, J. W., MUGGERIDGE, D. B. & TENNYSON, R. C. 1971. Effect of a local axisymmetric imperfection on the buckling behaviorof a circular cylindrical shell under axial compression. *AIAA Journal,* 9**,** 48-52.

KOITER, W. T. 1945. *On the Stability of Elastic Equilibrium*. PhD Thesis, Delft University.

MUGGERIDGE, D. B. & TENNYSON, R. C. 1969. Buckling of axisymmetric imperfect circular cylindrical shells under axial compression. *AIAA Journal,* 7**,** 2127-2131.

ROBERTSON, A. 1928. The Strength of Tubular Struts. *Proceedings of the Royal Society of London A: Mathematical, Physical and Engineering Sciences,* 121**,** 558-585.

ROTTER, J. M. Elastic plastic buckling and collapse in internally pressurised axially compressed silo cylinders with measured axisymmetric imperfections: interactions between imperfections, residual stresses and collapse. Proc. International Workshop on Imperfections in Metal Silos: Measurement, Characterisation and Strength Analysis, 1996 Lyon, France. CA-Silo, 119-140.

ROTTER, J. M. Design standards and calculations for imperfect pressurised axially compressed cylinders. Proceedings of the International Conference on Carrying Capacity of Steel Shell Structures, 1–3 October 1997 Brno. 354–360.

ROTTER, J. M. 2002. Shell Buckling and Collapse Analysis for Structural Design. *In:* DREW, H. R. & PELLEGRINO, S. (eds.) *New Approaches to Structural Mechanics, Shells and Biological Structures*. Springer Netherlands.

ROTTER, J. M. 2004. Buckling of cylinderical shells under axial compression. *In:* TENG, J. G. & ROTTER, J. M. (eds.) *Buckling of Thin Metal Shells*. Spon, London: Taylor & Francis.

ROTTER, J. M. The practical design of shell structures exploiting different methods of analysis. Proceedings of SSTA8: Eighth Conference on Shell Structures: Theory and Applications, 12-14 October 2005 Gdansk-Jurata, Poland.

ROTTER, J. M. A framework for exploiting different computational assessments in structural design. Proc. Sixth International Conference on Steel and Aluminium Structures, 6th ICSAS 07, June 2007 Oxford.

ROTTER, J. M. The elastic-plastic imperfection sensitivity of axially compressed cylinders with weld depressions. Proc., Eurosteel Conference, 3-5 September 2008 Graz, Austria. 1497-1502.

ROTTER, J. M. 2011. Shell buckling design and assessment and the LBA-MNA methodology. *Stahlbau,* 80**,** 791-803.

ROTTER, J. M. & TENG, J. G. 1989. Elastic Stability of Cylindrical Shells with Weld Depressions. *Journal of Structural Engineering,* 115**,** 1244-1263.

SOUTHWELL, R. V. 1914. On the General Theory of Elastic Stability. *Philosophical Transactions of the Royal Society of London A: Mathematical, Physical and Engineering Sciences,* 213**,** 187-244.

TENG, J. G. & ROTTER, J. M. 1989. Non-symmetric bifurcation of geometrically nonlinear elastic-plastic axisymmetric shells under combined loads including torsion. *Computers & Structures,* 32**,** 453-475.

YAMAKI, N. 1984. *Elastic stability of circular cylindrical shells,* Amsterdam, North-Holland.

Infrastructure and Environment Scotland 3rd Postgraduate Conference
9th December 2015
Heriot-Watt University, Edinburgh

Modelling the Structural Fire Response of Two-Way Spanning Simply Supported Reinforced Concrete Slabs

Emran Baharudin, Luke Bisby
Institute for Infrastructure and Environment,
University of Edinburgh
(e-mail: e.baharudin@ed.ac.uk,Luke.Bisby@ed.ac.uk)

ABSTRACT

Finite element (FE) modelling has become an important tool in studying the structural behaviour of fire-exposed structures. Various FE codes, both bespoke and commercial are available and have been widely applied for the analysis and performance-based design of steel structures for fire. However, for the case of reinforced concrete structures there has been much less work, and numerous studies conducted so far are lacking in substantial validation for practical cases due to limited experimental test data reported in the literature. This paper presents a study on the structural response of a 6600×5000×120mm two way spanning reinforced concrete slab exposed to an ISO 834 standard fire, from below for 220minutes, to gauge the ability of the currently available finite element codes to treat this relatively simple case. The developed finite element models are based on experiments carried out previously by Zhang et al. (2014). A smeared cracking concrete model implemented in commercial FE codes LS-Dyna and SAFIR is adopted. Formulation of constitutive material models for both concrete and steel are based on Eurocode 2. It is demonstrated that the response of concrete elements under thermal exposures is highly sensitive to the assumed concrete tensile strength behavior, which is not well characterised for elevated temperature analysis.

1. INTRODUCTION

Numerous investigations using numerical methods or finite element models to study concrete structures exposed to fires lack substantial validation against experimental results, due to only limited data being available. Bailey (2002) reported a full-scale fire test on a concrete building frame at the Building Research Establishment (BRE) laboratories in Cardington, UK. To the authors' knowledge, this was the most comprehensive test ever conducted to study the behaviour of a real reinforced concrete building structure, however the data from even this test are somewhat limited.

A number of other researchers have performed individual element tests on instrumented reinforced concrete elements, typically in furnaces. Zhang et al. (2014) and Lim and Wade (2002) tested simply-supported two-way slabs, and these tests have provided valuable information for studying full-scale, single span concrete slab behaviour under standard fires. Both tests provide insights into the behaviour of two-way simply-supported concrete slab under realistic thermal gradients through the thickness of the slab as a result of thermal exposure. Bailey and Toh (2007) tested forty eight small-scale two-way concrete slabs. These tests provide valuable information on the effect of various parameters on the behaviour of the slabs that are useful for numerical validation in understanding the behaviour of fire-exposed concrete slabs. All of these studies show that concrete slabs can carry greater loads than calculated using conventional yield-line theory, by mobilising tensile membrane action.

Gales (2013), Aimin et al. (2013), and Bailey and Ellobody (2009) have tested prestressed concrete slabs. With the advance development in the prestressed concrete technology where slabs are designed to be thinner and have longer span, knowledge on its behavior under fire exposures is still very limited. For instance, Bailey and Ellobody (2009) from their study concluded that the fire resistance specified in the current codes of practice are generally conservative for bonded post-tensioned one way spanning concrete slabs. In general all of the above test were conducted with the intention to provide data, which will allow validation of any computer models.

Choi and Shin (2011) and Dwaikat and Kodur (2009) tested single span reinforced concrete beam while Abrams et al. (1976) tested a continuous reinforced concrete beam. Despite the above tests, issues such as spalling, temperature distribution in the concrete, effects of restraint at supports and/or continuity at supports and redistribution of moment are still not fully understood. Redistribution of moment can enhance the fire resistance of continuous reinforced concrete beams (Abrams et al., 1976).

Among the earliest researchers, Terro (1998) modelled concrete slabs and a columns under fire exposures. Huang (1999; 2009; 2010; 2010), Lim et al. (2004), and Bailey and Ellobody (2009) have all numerically studied the behaviour of concrete structures under fires. All models mentioned above are developed for the elements exposed to standard time-temperature curve specified by the relevant codes such as Eurocode 1 (CEN, 2002) and ISO 834 (ISO, 1999). Their behavior under more realistic fires, for example natural fire and localised fires, has not been studied so far. One of the reasons might be because of the belief that the fire scenario specified by the standard fire curve is the worst possible thermal exposure that the elements under consideration might experience.

Despite the above fire tests and attempts to model the response of concrete during fire, the behaviour of concrete structures under real fire exposures is not yet well understood. Concrete is a mixture of cement, sand, aggregates, and water; the resulting structural material is complex and variable, thus complicating attempts to understand the response of concrete structures under fire. Composite action between steel reinforcing bars and concrete, with different thermo-mechanical properties, further complicates the structural response.

Lim et al. (2004) concluded through computational studies that concrete slabs have excellent fire resistance when deforming in double curvature with tensile membrane action. Huang (2010) investigated the response of slabs with different degrees of spalling and concluded that the compressive membrane force could reduce the impact of spalling might have on the structural behavior of floor slabs when exposed to fires.

This paper presents computational studies on the structural behaviour of a two-way spanning fire-exposed 6660×5000×120mm reinforced concrete slab tested by Zhang et al. (2014). The slab was exposed to an ISO 834 (ISO, 1999) fire for 220 minutes with 2kN/m^2 of superimposed applied load. The deformation behavior of the slab and stresses through the thickness are investigated in an attempt to better understand the structural behavior of reinforced concrete slabs in fire.

2. EXPERIMENTAL DETAILS

A two-way, simply-supported slab denoted as Slab 1 by Zhang et al. (2014) was selected for study. The slab dimensions were 6600×5000×120mm and it was reinforced with 8mm Ø ribbed reinforcing bars with a nominal yield strength of 400MPa. The clear concrete cover to the reinforcement was 15mm.

The measured yield strength and ultimate strength of the steel rebars were 435MPa and 580MPa, respectively. Normal weight concrete was used, with crushed limestone aggregate with a maximum size of 30mm. The compressive strength of the concrete was 31.5MPa at the time of testing.

The slab was simply-supported on all edges, with no restraint against horizontal movement, and heated according to ISO 834 (ISO, 1999) from below for 3hrs. Full details are given by Zhang et al. (2014).

3. THERMO-MECHANICAL ANALYSIS

3.1 Heat transfer analysis

Heat transfer analysis for concrete elements heated in a furnace is not always straightforward. Assuming constant thermal properties in predicting the thermal response is rarely accurate. Eurocode 2 (CEN, 2004) suggests thermal properties that are variable with temperature, so that the moisture evaporation and other factors are adequately accounted for in heat transfer analyses.

However, prediction of temperatures through the thickness of the slab is not core to the current study. Thus, the temperature history recorded from the tests at the exposed (soffit) surface of the slab were assumed as boundary conditions for the heat transfer analysis, and the temperatures through the thickness of the slab were predicted using the FE codes. Loss of heat through convection and radiation at the un-exposed surface, the thermal and physical properties of materials (i.e. specific heat, thermal conductivity, density) were all assumed following the Eurocodes (CEN, 2002; 2004). A comparison of the resulting predicted and measured temperatures is shown in Figure 1. It is clear that the predicted temperatures are in good agreement with the test data, and these were thus assumed as input temperatures for the mechanical analysis.

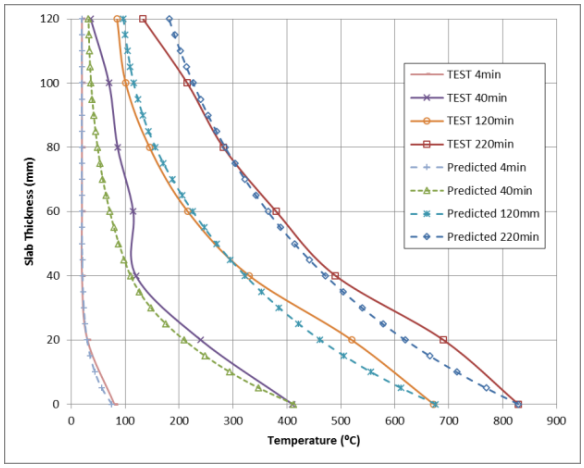

Figure 1. Comparison of predicted and measured temperatures through the slab's thickness.

3.2 Structural model

One quarter of the slab was modelled. The mesh used is shown in Figure 2. A general purpose FE package, LS-Dyna, as well as a special purpose structural fire analysis FE package, SAFIR, were chosen to develop the models. A shell element formulation was adopted for both models. Information on the elements and material models in SAFIR are explained by Lim (2003) and Wang (2006); these are not repeated here.

The *'Fully Integrated'* shell element formulation available in LS-Dyna (LSTC, 2013) was adopted in the current study. This element has 4 in-plane integration points and 28 integration points through its thickness (refer to Figure 3). Steel reinforcing bars within the slab are approximated as a smeared steel layer with thicknesses of 0.279mm and 0.251mm to represent a steel reinforcement area equivalent to 279mm^2/m (8mm Ø at 180c/c) and 251mm^2/m (8mm Ø at 200 c/c) in the long and short directions, respectively. Steel reinforcement and concrete were defined to have their own integration points. The '**Part_Composite'* card (LSTC, 2013) was used to realize the FE model.

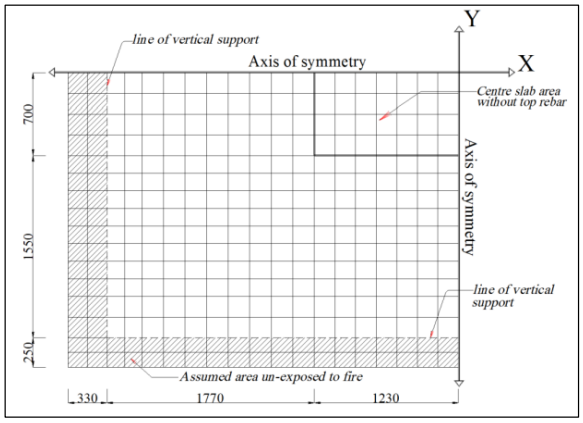

Figure 2. Finite element mesh used.

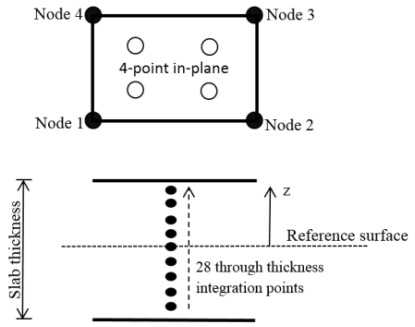

Figure 3. Graphical illustration of the shell elements adopted in the LS-Dyna model.

3.2.1 Explicit dynamic approach

For the model developed in LS-Dyna, an explicit dynamic approach was implemented. The explicit dynamic approach is an alternative to the (more common) implicit static approach adopted for most numerical studies on the response of structures in fire. Despite the fact that the results produced must be carefully checked for instabilities and inertial effects, the efficiency of this approach is worth considering since there are fewer convergence issues such as commonly experienced in implicit solvers (Lim, 2003). Instabilities are particularly problematic when sudden deflections occur such as during snap-through. Explicit dynamic solvers also require less computational effort.

3.3 Constitutive material behaviour of concrete

The assumed concrete material properties for the finite element model are given in Table 1. f_{ck} is the specified compressive strength, f_t is the tensile strength, v is the Poisson's ratio, while α is the coefficient of thermal expansion (CTE).

Table 1. Concrete material properties assumed.

f_{ck} (MPa)	f_t (MPa)	V	α ($^0C^{-1}$)	Aggregate
31.5	3.0	0.3	EC2	Calcareous

3.3.1 Compressive behaviour

The constitutive behaviour given by Eurocode 2 (CEN, 2004) was implemented in the models. The value of peak strain, ε_{c1}, failure strain, ε_{cu}, and the variation of strength with temperature for concrete compressive properties were scaled based on a softening factor as suggested by the code.

3.3.2 Tensile behaviour

The stress-strain behavior of concrete in tension was assumed to follow a linear relationship until peak tensile strength. Peak strength was defined as $0.3(f_{ck})^{2/3}$ following CEB-FIP(2010). The post-peak tensile behaviour of concrete was modelled with a bilinear relationship suggested by Rots et al. (1984). The reduction of peak strength with temperature followed Eurocode 2 (CEN, 2004). The strength at ambient was constant to 100^{0}C and reduced linearly to zero at 600^{0}C; beyond 600^{0}C, it was assumed to have no strength.

At ambient temperature, the strain to fully open crack, ε_u, was defined as 0.0016. This was defined based on $\varepsilon_u = \alpha\varepsilon_{cr}$, where ε_{cr} is the peak tensile strain or cracking strain. The multiplier factor, α, has been reported by Barzegar-Jamshidi and Schnobrich (1986). These are in the range of 5 to 25. With an increase in temperature, tensile strain will also increase such that the fracture energy to open the crack remains constant. Up to 500^{0}C, tensile strains increase with an increase in temperature. Beyond 500^{0}C the tensile strain no longer increases (LSTC, 2013).

3.4 Steel material behaviour

The formulation of the constitutive material model for the steel reinforcement also followed Eurocode 2 (CEN, 2004). This formulation applies for steel in both tension and compression. Under loading, steel response starts with linear elastic range, follows with proportional limit, straining at maximum stress level and finally linear descending branch to total failure. Strain hardening is not considered. Table 2 shows the assumed properties for the steel, where E is the elastic modulus and σ_u is the ultimate stress.

Table 2. Material properties assumed for steel.

E (GPa)	σ_u (MPa)	V	α ($^0C^{-1}$)
210	580	0.3	EC2

4. RESULTS

The predicted vertical mid-span displacement of the slab is shown in Figure 4. The test result is plotted together with the predictions using both LS-Dyna and SAFIR. The predictions are in reasonably good agreement with the test result, both in terms of the trend and the values. However both predicted plots show that the model was unable to precisely capture the rate of deflection during the early stages of heating. With 3.0MPa concrete tensile strength defined, the model predicted a rate of deflection less than that observed in the test. Only after 20 minutes of exposure to fire did the rate of deflection increase rapidly as in the test. At 210 minutes of fire exposure, the magnitude of displacement reported in the test was 272mm. LS-Dyna predicted 224mm vertical deflection while SAFIR estimated 216mm at the same time of fire exposure.

To further investigate the deformation behaviour of the slab, stresses along the thickness for an element near the centre of the slab were plotted (Figures 5 and 6). Figure 5 shows the plot of X-stress profile along the thickness of the slab while Figure 6 shows similar plot for stress in Y direction (Y-stress). On the Y-axis in the plots, 0mm denotes the surface exposed to fires while 120mm denotes the un-exposed face of the slab. Three instants in time are shown i.e. ambient, 18 minutes of fire exposure, and 20 minutes of fire exposure to further illustrate how the stresses over the thickness of the slab influence the vertical displacement trends shown in Figure 4. As can be seen from Figure 5 and Figure 6, stresses in the middle section of the concrete gradually increase in tension until the first tensile crack initiates. Crack opening then occurs for the element due to the stresses in the Y-direction (transverse) first and then followed by the stress in X-direction (longitudinal). At approximately 20minutes of fire exposure, tensile cracks open in both X and Y directions. This behaviour partly explains why the rate of deflection increases from 20 mins.

In the test, as soon as the heating takes place, the slab deflects at a higher rate during the first 10 minutes of exposure and then deflects at lower rate thereafter. Zhang et al. (2014) reported that for the first 97 minutes, their slab deflected at 1.67 mm/min, and then at approximately 0.84 mm/min until the test ended.

Figure 5 and Figure 6 show that concrete sections that are closest to the fires (i.e. the concrete cover) immediately goes into compression as soon as the heating commences, when it was initially in tension due to mechanical loads at ambient temperature. The expansion of concrete cover due to heating was restrained by the cool internal concrete. This behaviour partly explains why concrete cover immediately goes into compression as soon as the heating commences. It is noteworthy that the rebar stress both in the X and Y directions are not included in figures 5 and 6 for clarity, since these are much higher than those in the concrete. It must also be emphasized that the formulation of shell element in the current study cannot capture some factors that could influence this behaviour, such as bond degradation between concrete and rebars.

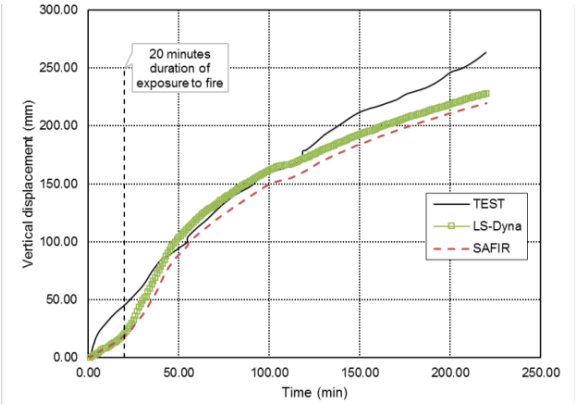

Figure 4. Vertical mid-span displacement.

In general, the structural fire engineering community is in agreement that tensile membrane action enhances the load bearing capacity of two way reinforced concrete slabs, either if the slab is restrained at its support or free to move (i.e. simply-supported). Figure 7 shows a plot of membrane forces for the slab under consideration at 220 minutes of exposure. It can be seen that a compressive ring has formed and surrounds the tensile zone at the centre of the slab (Taylor, 1965). It is noteworthy that the formulation of tensile membrane action at the centre of the slab is slightly affected by the lack of top reinforcement. Tensile membrane force has not fully developed and can be seen in a rectangular area at the centre of the slab (Figure 7). However it is unclear whether this would have any effect to the overall structural stability of

the slab in fire, and further investigation is required on this issue.

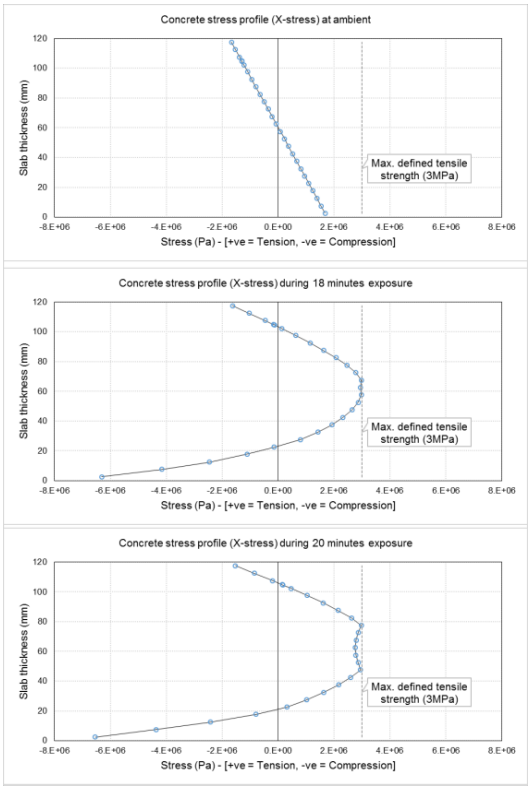

Figure 5. Concrete X-stress profile along the thickness of the slab (rebar stress omitted).

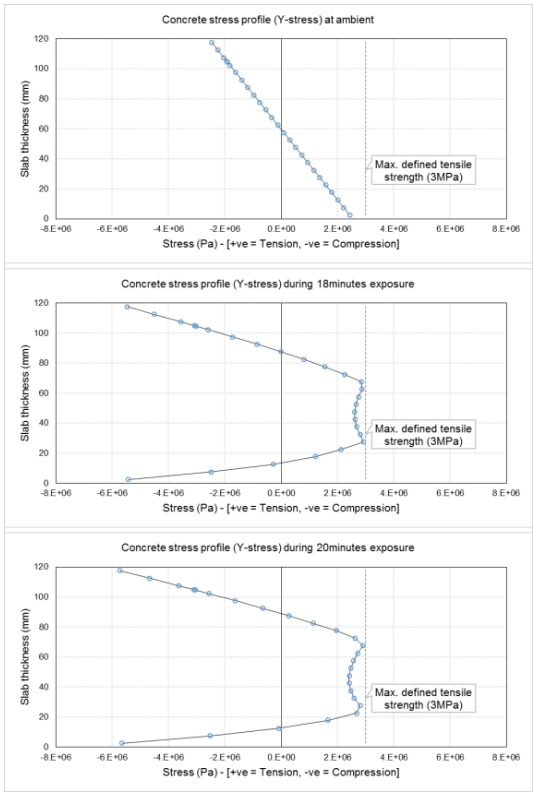

Figure 6. Concrete Y-stress profile along the thickness of the slab (rebar stress omitted).

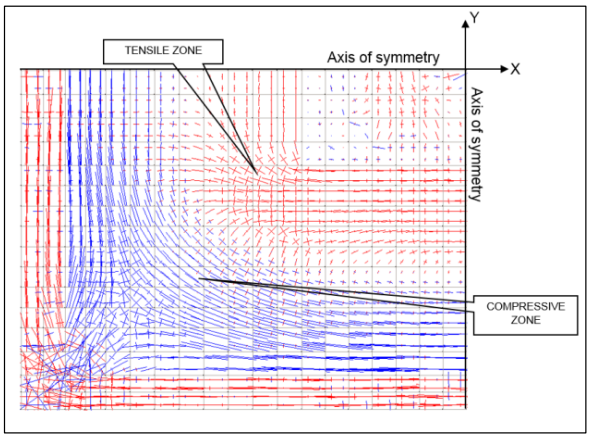

Figure 7. Membrane forces in the slab at 220 minutes of fire exposure.

5. CONCLUSION

Finite element models using an explicit dynamic approach (in LS-Dyna) or a static implicit approach (in SAFIR) were developed to predict the structural response of a two-way, simply-supported reinforced concrete slab under standard fire exposure for 220 minutes. In general, the predicted displacement trend matched reasonably well with the test results. In addition, the slab also survived during the exposure to fire, without structural failure and sustaining large deformations. The following preliminary conclusions can be drawn from this study:

1. Results from this study concur with the current consensus among the structural fire engineering community that concrete slabs can withstand fire exposures longer than that estimated based on conventional yield line theory. Considering reduction of load carrying capacity of the slab due to degradation of reinforcing steel strength at elevated temperature, Zhang et al (2014) predicted the slab would fail during 150 minutes of exposure to fire but the slab survived until at the end of test i.e. 220 minutes.
2. Vertical displacement behaviour of the slab under consideration is influenced by the formation of tensile cracking at the internal section of the concrete during heating. Among other factors, it was found that the rate of vertical mid-span displacement increased rapidly as the crack opened in the internal section of the concrete depth. Properly defining concrete tensile behaviour is therefore important in predicting the structural fire response of reinforced concrete slabs using FE methods.

REFERENCES

Abrams, M.S., Gustaferro, A.H., and Lin, T.D. (1976)" Fire endurance of continuous reinforced

concrete beams." *IABSE Congress Report*, 10(1976).
Aimin, Y., Yuli, D., and Litang, G., (2013)"Behaviour of unbonded prestressed continuous concrete slabs with the middle and edge span subjected to fire in sequence." *Fire Safety Journal*, 56:20-29.
Bailey, C., (2002)" Holistic behaviour of concrete buildings in fire." *Proceedings of the Institution of Civil Engineers*, Structures and Buildings 152, Issue 3,pp 199-212.
Bailey, C. and Toh, W.S. (2007)"Behaviour of concrete floor slabs at ambient and elevated temperatures "*Fire Safety Journal,* 42:425-436.
Bailey, C. and Toh, W.S. (2007)"Small scale concrete slab tests at ambient and elevated temperatures "*Engineering Structures,* 29(2007)2775-2791.
Bailey, C., and Ellobody, E., (2009)" Comparison of unbonded and bonded post-tensioned concrete slabs under fire conditions." The Structural Engineer,87(19).
Bailey, C., and Ellobody, E., (2009)" Whole-building behaviour of bonded post-tensioned concrete floor plates exposed to fire." *Engineering Structures*, 31:1800-1810.
CEN (2002) BS EN 1991-1-2:2002 – Eurocode 1: Action on structures – Part 1.2: General actions – Actions on structures exposed to fire. *European Committee for Standardization*, Brussels
CEN (2004) BS EN 1992-1-2:2004 – Eurocode 2: Design of concrete structures – Part 1.2: General rules – Structural fire design. *European Committee for Standardization*, Brussels
Choi, E.G., and Shin, Y.S. (2011)"The structural behaviour and simplified thermal analysis of normal strength and high-strength concrete beams under fire." *Engineering Structures*, 33:1123-1132.
Deeny, S., (2010)"The implications of compartment fire non-uniformity for the membrane action of reinforced concrete slabs" PhD. Thesis, University of Edinburgh, Edinburgh, UK.
Dwaikat, M.B., and Kodur, V.K.R.(2009)" Response of restrained concrete beams under design fire exposure." *Journal of Structural Engineering*, 135:1408-1417.
Gales, J.A., (2013) "Unbonded post-tensioned concrete structures in fire. "PhD. thesis, University of Edinburgh., Edinburgh, UK.
Huang, Z., Burgess, I.W., and Plank, R.J. (1999)"Nonlinear analysis of reinforced concrete slabs subjected to fire." *ACI Structural Journal*, N 96, January-February 1999, 127-135.
Huang, Z., Burgess, I.W., and Plank, R.J. (2009)"Three-dimensional analysis of reinforced concrete beam-column structures in fire." *Journal of Structural Engineering*, 135:1201-1212.
Huang, Z. (2010)" Modelling of reinforced concrete structures in fire." *Proceedings of the Institution of Civil Engineers, Engineering and Computational Mechanics* 163(1): 43-53
Huang, Z. (2010)" The behaviour of reinforced concrete slabs in fire." *Fire Safety Journal*, 45:271-282.
International Federation for Structural Concrete (2010) 'fib Bulletin 55: Model Code 2010, First complete draft – Volume 1' *International Federation for Structural Concrete*, Lausanne, Switzerland.
ISO (1999) ISO 834-1. Fire resistance tests – elements of building construction. Part 1: general requirement. International Organization for Standardization, Geneva
Joint Fire Research Organization, FROSI (1972)" A standard fire resistance test on a gravel aggregate concrete column (reference B1)." FROSI No.5510.FRO/118/010.
Lim, L., and Wade, C., (2002)"Experimental fire tests of two-way concrete slabs." *University of Canterbury Fire Engineering Research Report 02/12*
Lim, L., (2003) "Membrane action in fire exposed concrete floor systems. "PhD. thesis, University of Canterbury., Christchurch, New Zealand.
Lim, L., Buchanan, A., Moss, P., and Franssen, J.M. (2004)" Numerical modelling of two-way reinforced concrete slabs in fire." *Engineering Structures*, 26:1081-1091
LSTC (2013)"LS-Dyna keyword user's manual." *Livermore Software Technology Corporation(LSTC*), California
Rots, J.G. et al (1984)"The need for fracture mechanics option for finite element models for concrete structures."*Proc. Int. Conf. on Computer Aided Analysis and Design of Concrete Structures*, F. Damjanic et al., Pineridge Press, Part 1, 19-32.
Taylor, R. (1965) "A note on a possible basis for a new method of ultimate load design of reinforced concrete slabs." *Magazine of Concrete Research*, Vol. 17 Issue 53.pp 183-186.
Terro, M.J. (1998)" Numerical modelling of the behaviour of concrete structures in fire." *ACI Structural Journal*, N 95, March-April 1998, 183-193.
Warrington Fire Research Centre, WFRC (1987)"Ad-hoc fire test using the heating conditions of BS 476:Part 8:1972 on two 150mm thick normal weight concrete slabs." *Fire Research Station*, WARRES No. 40728
Zhang, D., Fang, Y., and Dong, Y., (2014)"Behaviour of full-scale two-way simply supported concrete slabs in fire." *Magazine of Concrete Research*, Volume 66 Issue 16.

Infrastructure and Environment Scotland 3rd Postgraduate Conference
9th December 2015
Heriot-Watt University, Edinburgh

Dual Seismic-Resistant Steel Frame with High Post-Yield Stiffness Braces for Residual Drift Reduction: Numerical Evaluation

M. Baiguera, G. Vasdravellis,
Institute for Infrastructure and Environment,
Heriot-Watt University
(e-mail: mb311@hw.ac.uk)

ABSTRACT

A dual seismic-resistant steel frame, which consists of a moment-resisting frame equipped with high post-yield stiffness energy-dissipative braces, is proposed and numerically evaluated. Replaceable hourglass shape pins made of duplex stainless steel with high post-yield stiffness and large energy dissipation and fracture capacity are in series connected to conventional steel braces. Moreover, replaceable fuses are introduced in the beams at the locations where plastic hinges are expected to develop. The seismic performance of the dual frame is evaluated with advanced numerical simulations using experimentally validated shell-solid finite element models and simplified beam element models. The numerical results show that the dual frame has adequate stiffness and energy dissipation capacity to control peak storey drifts (i.e. non-structural damage), while plastic deformations (i.e. structural damage) are isolated within the replaceable pins of the braces and the beam fuses. In addition, the high post-yield stiffness of the pins, combined with the appreciable elastic deformation capacity of the moment-resisting frame, results in significant reduction of residual storey drifts, which are found to have a mean value of 0.06% under the design earthquake and a mean value of 0.12% under the maximum considered earthquake. These values indicate a superior residual storey drift performance compared to steel frames equipped with buckling restrained braces, and highlight the potential of the proposed dual frame to help steel buildings to return to service within an acceptable short time in the aftermath of a strong earthquake.

1. INTRODUCTION

Conventional seismic-resistant steel frames designed according to current seismic provisions, e.g. Eurocode 8 (CEN, 2004), prevent collapse and ensure life safety under the design earthquake. However, two major drawbacks of conventional systems are that they experience significant inelastic deformations (i.e. damage) in main structural members and residual storey drifts after a strong seismic event. Socio-economic losses associated with repairing damage in structural members include high repair costs and excessive disruption to building use or occupation. Residual storey drifts may pose further complications: a recent study on the economic impact of residual drifts showed that direct and indirect repair costs are not financially viable when residual drifts are greater than 0.5% (McCormick et al., 2008).

Braced frames represent a system with enhanced seismic performance due to their high initial stiffness, which can effectively reduce storey drifts. However, conventional braced frames, such as concentrically braced frames (CBFs), exhibit a degrading hysteretic behaviour, which results in damage concentration to certain stories, fracture, and increased collapse potential. Buckling-restrained braced frames (BRBFs) represent an improved class of braced frames (Watanabe et al., 1988). The buckling-restrained braces (BRBs) exhibit a stable hysteretic response and the ability to withstand significant ductility demands. However, they may be susceptible to large residual drifts and damage concentrations due to their low post-yield stiffness (Bruneau et al., 2011). Previous analytical studies have shown that BRBFs designed according to current seismic codes do not meet the immediate occupancy performance level under the design-basis earthquake (10% probability of occurrence in 50 years; denoted as DBE), due to residual drifts greater than 0.5% (Erochko et al., 2011). Simple approaches to mitigate residual drifts have been studied in (Pettinga et al., 2008). Among these, providing high post-yield stiffness is recognized as an effective strategy to reduce residual drifts.

To overcome the issue of reparability of structural members, an innovative design approach is to concentrate damage in carefully designed replaceable elements, typically named in the literature as structural fuses. This concept was first presented by Balut and Gioncu (2003) as an

alternative to dog-bone connections in MRFs. The fuses are detailed to dissipate energy and to be easily replaced if damaged, whereas the main structural members are designed to be elastic. In addition, the removal and replacement of fuses allows the structure to recenter (Bruneau et al., 2011). Replaceable nonlinear links in steel MRFs were proposed by Shen et al. (2011).

This paper proposes an MRF equipped with concentric braces, denoted as dual CBF-MRF, which uses simple structural details to provide enhanced seismic performance, i.e.: a) energy-dissipative hourglass shape pins made of duplex stainless steel (SSD) with high post-yield stiffness, designated as SSD-WHPs, are placed in series with the concentric braces; and b) replaceable fuses are placed at the locations of the beams where plastic hinges are expected to develop.

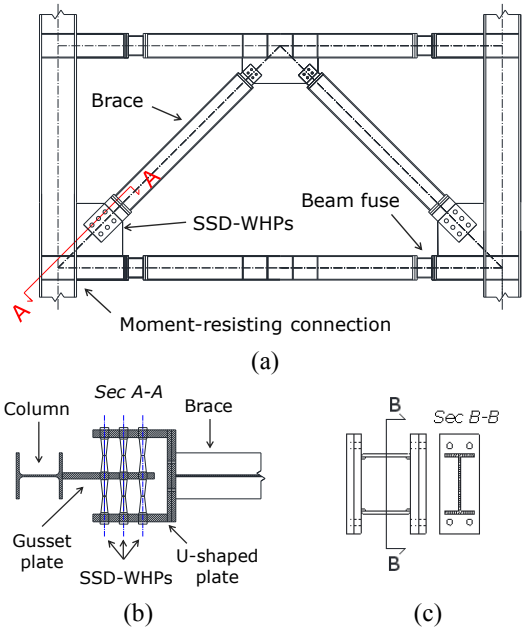

Figure 1. Geometry of the proposed dual CBF-MRF: a) overview; (b) brace-WHP connection detail; and (c) beam fuse detail

2. STEEL DUAL CBF-MRF

Fig. 1a shows the configuration of the proposed CBF-MRF. The SSD-WHPs are installed only at one end of the braces and pass through aligned holes between the gusset plate and a strong U-shaped plate, which is connected by either welding or bolting to the brace member (Fig. 1b). WHPs are hourglass-shape steel yielding devices that dissipate energy due to bending inelastic deformations. The geometric properties of the bending part of a WHP are shown in Fig. 2. The internal parts have length L_{WHP}, external diameter D_e, and mid-length diameter D_i. The internal part is assumed to have fixed boundary conditions as it bends. The hourglass shape promotes a constant curvature profile and a uniform distribution of plastic deformations to delay fracture and increase energy dissipation. WHPs have been previously used by Vasdravellis et al. (2013) in a post-tensioned connection. A further experimental evaluation of the cyclic behaviour of WHPs (Vasdravellis et al., 2014) made of high-strength steel and two grades of stainless steel (i.e. austenitic grade 304 and SSD) showed that they have stable hysteresis and high fracture capacity. In that study, SSD-WHPs showed excellent energy dissipation capacity and high post-yield stiffness, indicating the potential benefits of using them in bracing systems.

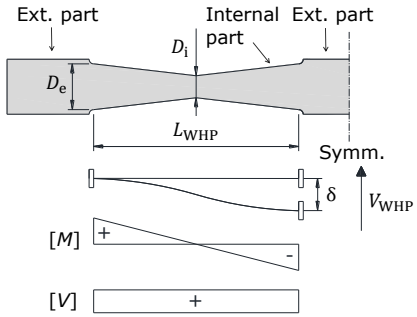

Figure 2. Web-hourglass shape steel pin (WHP).

Replaceable fuses are placed in the main beams immediately after the gusset plates, where plastic hinges are expected to develop, as shown in Fig. 1a. They are designed following the same concept of the replaceable link proposed by Shen et al. (2011). The fuses are smaller than the main beam steel I-sections, welded on strong end plates, which in turn are bolted on the main beam (Fig. 1c).

A 6-storey prototype building with three equal bays in each direction is designed according to the provisions of Eurocodes 3 (CEN, 2003) and 8 (CEN, 2004) using as seismic-resistant system either a BRBF coupled with an MRF (BRBF-MRF) or the proposed CBF-MRF. The bay width and the storey height are 6 m and 3 m, respectively. A performance-based seismic design procedure is used to design the dual frames as described in detail in Baiguera et al. (2015).

3. NUMERICAL MODELLING

The seismic performance of the proposed CBF-MRF is studied by means of nonlinear finite element (FEM) analyses using the Abaqus software (Hibbit et al., 2013). A detailed three-dimensional model (Fig. 3), based on the use of solid and shell elements, is constructed to study both the local and global behaviour of the system and to identify all possible failure modes through nonlinear cyclic pushover analyses. Beams, columns and bracing members are modelled using shell elements with reduced integration, namely S4R in Abaqus. The SSD-WHPs, gusset plates, U-

shaped plates and beam fuses are modelled using solid elements with reduced integration, namely C3D8R. Solid-shell coupling constraints are used to allow for the correct transition of stresses between shell and solid elements. To account for P-Δ effects from the gravity frame of the building, a lean-on column is added and truss elements are used to link it to the frame. The hysteretic behaviour of the key components, i.e. the SSD-WHPs and the beam fuses, is calibrated using available experimental results.

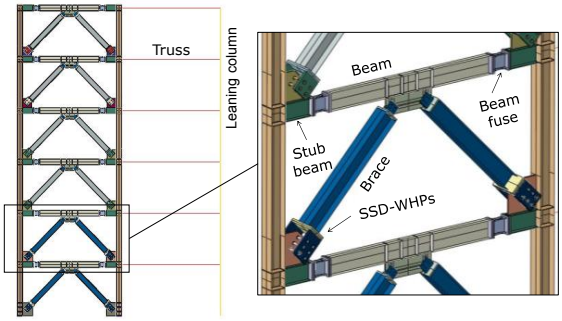

Figure 3. View of the detailed FEM model.

SSD-WHP fracture is not modelled explicitly; however, the experiments conducted by Vasdravellis et al. (2014) showed that WHPs can achieve a ratio of fracture displacement to yield displacement, i.e. cyclic ductility, at least equal to ten under the standard seismic loading protocols. Fracture of SSD-WHPs is crucial for the proposed frame, since it may result in a sudden drop of strength, accelerating the collapse of the frame. However, more tests are needed in order to take into account the appropriate boundary conditions and the expected loading history in a braced frame. For this initial evaluation study, it is assumed that an SSD-WHP fractures when the cyclic ductility demand reaches a value of ten.

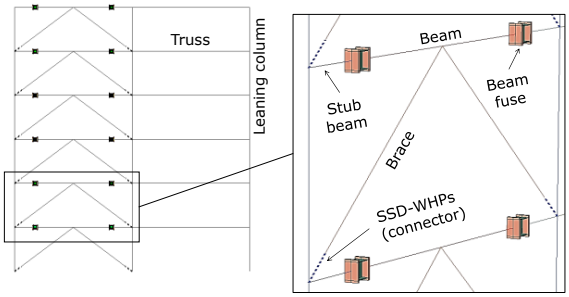

Figure 4. View of the simplified FEM model.

A simplified version of the detailed model (Fig. 4), based on the use of beam elements, is created to evaluate the global seismic response of the structure through nonlinear dynamic analyses. To capture the local buckling and the strength and stiffness deterioration due to cycling inelastic loading, the fuses are modelled using C3D8R solid elements. The SSD-WHPs are modelled using nonlinear connector elements. Connectors are spring-like elements with an elastoplastic force-displacement law whose cyclic hardening parameters are calibrated based on tests and additional FEM analyses, as described in detail in Baiguera et al. (2015).

To compare the seismic performance of the proposed CBF-MRF with that of the BRBF-MRF, a simplified model of the dual BRBF-MRF is also constructed. The geometry is identical to the beam-solid model of the dual CBF-MRF, but the SSD-WHPs are removed and concentric BRBs are used to resist the lateral force. The BRBs are modelled as connector elements with elastoplastic behaviour, assigning a post-yield stiffness ratio of 0.01 based on component test results reported in Fahnestock et al. (2007).

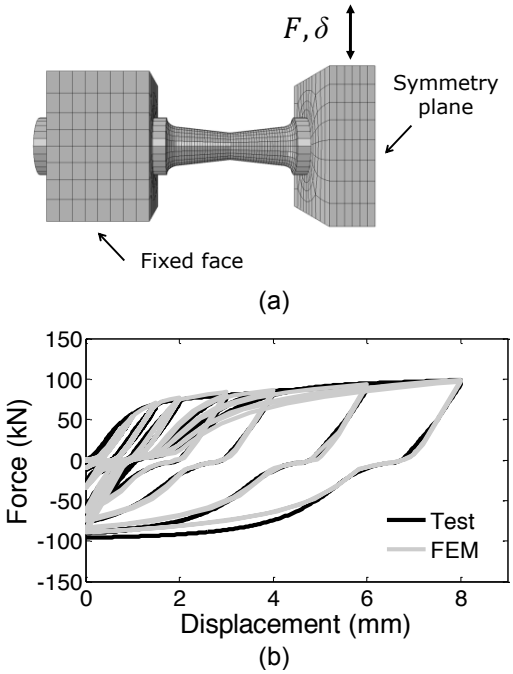

Figure 5. (a) FEM model of half of a WHP. (b) Experimental and numerical hysteresis of a WHP under cyclic loading.

3.1 Calibration of cyclic hardening parameters for SSD-WHPs

The material properties of the SSD-WHPs are calibrated using the experimental results reported in Vasdravellis et al. (2014). In that study, several cyclic tests on SSD-WHPs were carried out. Fig. 5a shows the three-dimensional FEM model that was used to simulate the hysteretic response of WHPs made of high-strength steel in Vasdravellis et al. (2013). Those models are modified in this study to capture the behaviour of SSD material. Only half of the WHP is modelled due to its symmetric geometry. Both the WHP and the supporting plates are discretized using C3D8R elements. In order to capture the pinching behaviour at zero force observed in the experimental curve (Fig. 5b) due to the slip of WHPs within the surrounding holes, a small

clearance, equal to 0.1 mm, is left between the cylindrical external surfaces and the holes of the U-shaped plates.

The hysteretic behaviour of SSD-WHPs is simulated by an elastoplastic material model with combined isotropic and kinematic hardening, as described in detail in Baiguera et al. (2015). Fig. 5b shows that a good agreement is found between the numerical and the experimental cyclic force-displacement curves

3.2 Calibration of cyclic hardening parameters for the beam fuse

To ensure that the numerical model for the fuse is reliable and capable of capturing the deterioration of stiffness and strength due to buckling phenomena, the material parameters are calibrated against the experimental results of full-scale tests on a beam-column connection with a replaceable link reported by Shen et al. (2011). The tested specimen is reproduced in Abaqus using the same modelling features as for the whole frame model. Similar to the calibration procedure presented in the previous section, the constitutive material parameters of the fuse are identified iteratively by conducting several simulations. Fig. 6 shows that a good correlation between the experimental and the numerical results is achieved.

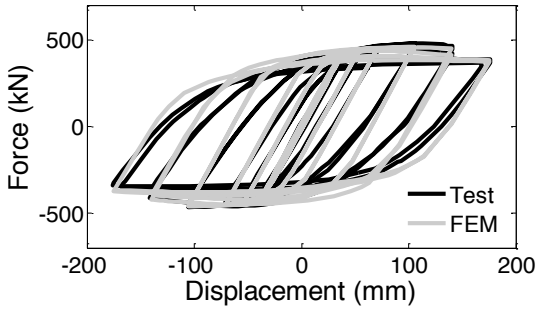

Figure 6. Experimental and numerical results of the replaceable link (Shen et al., 2011).

4. NONLINEAR CYCLIC ANALYSES

Nonlinear cyclic static (push-pull) analyses on the dual CBF-MRF are performed using both the detailed model and the simplified model. Displacement-controlled analyses are performed using a triangular force distribution. Both models are subjected to three cycles up to the FOE, DBE and MCE target drifts (0.5%, 1% and 1.5%, respectively). The results show that the beams, columns and braces are damage-free under the MCE, whereas the SSD-WHPs and beam fuses are the only elements that experience plastic deformations. The base shear coefficient, i.e. the base shear (V) normalised by the seismic weight (W) of the building, versus the roof drift, i.e. the roof horizontal displacement over the height of the building denoted as θ_r, responses of the two models are compared in Fig. 7a. A good agreement is observed with a slightly lower base shear strength showed by the simplified model. Therefore, the simplified FEM model can be reliably used for nonlinear dynamic analyses.

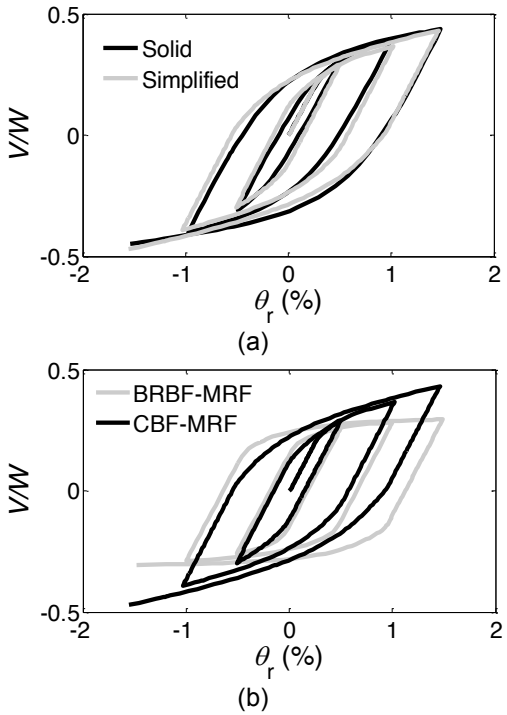

Figure 7. Cyclic pushover response: a) detailed and simplified FEM models; and (b) dual CBF-MRF and conventional BRBF-MRF.

The V/W-θ_r responses of the conventional BRBF-MRF and the dual CBF-MRF are shown in Fig. 7b. Both frames show large energy dissipation capacity. The cyclic inelastic behaviour of the two systems is noticeably different: the proposed frame possesses a significantly higher post-yield stiffness than the conventional frame as a result of the SSD material used for the WHPs. In addition, the nonlinear cyclic static analyses curves show that the residual drifts of the proposed dual CBF-MRF are smaller than those of the BRBF-MRF. The nonlinear dynamic analyses, however, will provide a more realistic estimation of the expected seismic response and residual drifts of the two systems.

5. NONLINEAR DYNAMIC ANALYSES

Nonlinear dynamic analyses are conducted to evaluate the seismic performance of the dual CBF-MRF and the BRBF-MRF. A set of 22 ground motions selected from FEMA P695 (2008) is used. The ground motion records are scaled to the FOE, DBE and MCE seismic hazard levels, according to the procedure based on the recommendations of FEMA P695 (2008).

Table 1. Storey drift summary.

		$\theta_{s,max}$ (%)			$\theta_{s,res,max}$ (%)		
		m	***m+σ***	**Median**	***m***	***m+σ***	**Median**
CBF-MRF	FOE	0.47	0.56	0.49	0.02	0.04	0.01
	DBE	0.88	1.11	0.88	0.06	0.10	0.05
	MCE	1.27	1.62	1.19	0.12	0.23	0.10
BRBF-MRF	DBE	1.02	1.38	0.96	0.27	0.49	0.23
	MCE	1.52	2.06	1.38	0.44	0.80	0.37

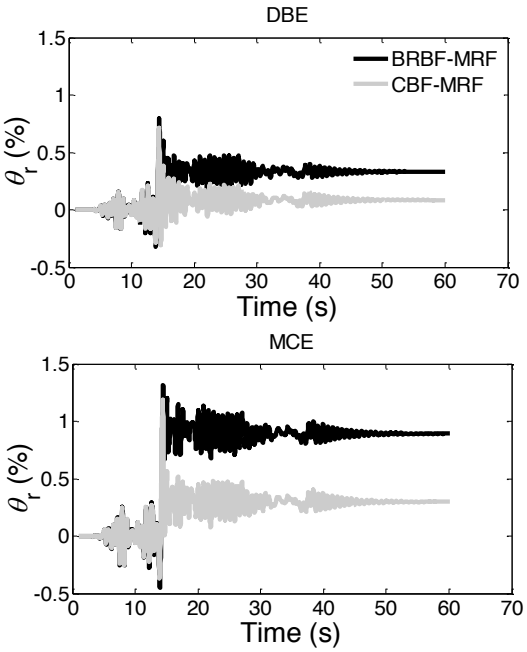

Figure 8. Roof drift time histories under n.16 ground motion scaled to the DBE and MCE seismic hazard levels.

Fig. 8 shows θ_r time histories of the dual CBF-MRF and BRB-MRF under the no. 16 record scaled to the DBE and MCE ground motions. A significant difference in the residual drift values is observed between the two systems: the BRBF-MRF oscillates and finds static equilibrium with appreciable residual drifts, whereas the dual CBF-MRF has a clear tendency to re-centre. Under the DBE ground motion, both systems experience a $\theta_{s,max}$ approximately equal to 1%. At the end of the imposed time history, the BRBF-MRF has a maximum residual drift ($\theta_{s,res,max}$) equal to 0.4%, whereas the proposed CBF-MRF has a negligible $\theta_{s,res,max}$= 0.09%. Under the MCE ground motion, the BRBF has $\theta_{s,max}$= 1.88% and $\theta_{s,res,max}$= 1.07%. The corresponding values of the dual CBF-MRF are 1.56% and 0.38%. It is concluded that, under this particular accelerogram, even though the two systems experience similar peak storey drifts, the higher post-yield stiffness of the proposed frame results in a drastic reduction of residual drifts.

Table 1 provides a summary of the statistics of $\theta_{s,max}$ and $\theta_{s,res,max}$ values for the two systems, in terms of mean (*m*), median, and mean plus standard deviation (*m+σ*) values. The proposed dual frame has mean $\theta_{s,max}$ equal to 0.47% under the FOE, 0.88% under the DBE and 1.27% under the MCE. These values are slightly lower than the design target values (i.e. 0.48%, 0.96%, and 1.44%). The BRBF-MRF has slightly greater mean $\theta_{s,max}$ than the CBF-MRF, i.e. 1.02% and 1.52% under the DBE and MCE, respectively. The mean $\theta_{s,res,max}$ for the dual CBR-MRF is 0.02% under the FOE, 0.06% under the DBE and 0.12% under the MCE. The BRBF-MRF exhibited nearly five times larger mean $\theta_{s,res,max}$ under the DBE (0.27%) and almost four times larger mean $\theta_{s,res,max}$ under the MCE (0.44%). The *m+σ* of $\theta_{s,res,max}$ for the dual CBF-MRF are 0.10% and 0.23% under the DBE and MCE, respectively, i.e. still very low. The corresponding values for the BRBF-MRF are 0.49% and 0.80%, demonstrating a much higher scatter in the results.

The results of this study are compared to the results of previous research studies concerning experimental or numerical nonlinear dynamic analyses on prototype BRBFs (Fahnestock et al, 2007; Sahoo et al., 2015). They show that BRBFs can exhibit mean $\theta_{s,res,max}$ in the range of 0.3-1.3% and 1.2-3.9% under DBE and MCE ground motions, respectively. These values suggest that significant permanent deformations may occur in BRBFs under strong seismic excitations, resulting in non-reparable damage. In the study conducted by Kiggins and Uang (2006) on a 6-storey building with BRBs, $\theta_{s,res}$ were reduced by using a backup MRF, i.e. from 0.29% to 0.13% under the DBE. However, the proposed dual CBF-MRF achieves an even more drastic reduction of residual drifts, i.e. from 0.27% in the BRBF-MRF to 0.06% (see Table 1), thus enabling repair without significant disruption to the building use.

The maximum displacement demands on the SSD-WHPs under the ground motion records in each storey resulted below the assumed fracture value of ten times the yield displacement. The mean values of maximum displacement demand under the FOE and DBE are 8.4 mm and 17 mm, respectively. For the MCE hazard level, SSD-WHPs reach displacements with a mean value equal to 23 mm in the third storey. Therefore, there is a very small likelihood of fracture for seismic events up to MCE.

6. CONCLUSIONS

In this work, a dual seismic-resistant system (denoted as CBF-MRF) consisting of a steel moment-resisting frame equipped with high post-yield stiffness braces and replaceable beam fuses was presented and numerically evaluated. The seismic performance of the CBF-MRF was evaluated by means of advanced numerical simulations. Based on the results presented herein, the following conclusions are drawn:

- A simplified model of the CBF-MRF using beam elements for the main structural members, nonlinear connector elements for the SSD-WHPs and solid elements for the beam fuses, is found to provide a similar level of accuracy with a detailed FEM model using shell and solid elements.
- The proposed frame can be designed to have stiffness and strength comparable with a conventional buckling-restrained braced moment frame (BRBF-MRF), but exhibits a much higher post-yield stiffness owing to the properties of the duplex stainless steel material used for the SSD-WHPs.
- Nonlinear dynamic analyses performed using the simplified FEM model show that the proposed CBF-MRF and the conventional BRBF-MRF experience comparable peak storey drifts. However, the combined effects of the high post-yield stiffness and the appreciable elastic displacement capacity of the MRF drastically reduce the maximum residual drift of the dual CBF-MRF. The maximum residual drift experienced by the BRBF-MRF is five times larger under the DBE and nearly four times larger under the MCE.
- The SSD-WHPs are designed in such a way that they have a large yield displacement, and therefore, a reduced likelihood of fracture based on observations from previous tests. However, further experiments need to be carried out on the fracture capacity of SSD-WHPs installed in brace members in order to reliably account for their fracture capacity and its effect on the collapse capacity of the proposed frame.

REFERENCES

Baiguera, M., Vasdravellis, G., Karavasilis, T.L. (2015). Seismic-resistant steel frame with high post-yield stiffness braces for residual drift reduction: numerical evaluation. *J. Constr. Steel Res.*, under review.

Balut, N., Gioncu, V. (2003). Suggestion for an improved 'dog-bone' solution. In: *4th International Conference STESSA*. Naples, Italy.

Bruneau, M., Uang, C.M., Sabelli, R. (2011). *Ductile design of steel structures*. New York, NY: McGraw-Hill.

CEN (2003). *Eurocode 3: design of steel structures - part 1-1: general rules and rules for building*. Brussels: European Commitee for Standardization.

CEN (2004). *Eurocode 8: design provisions for earthquake resistance of structures - part 1: general rules, seismic actions and rules for building*. Brussels: European Committee for Standardization.

Erochko, J., Christopoulos, C., Tremblay, R., Choi, H. (2011). Residual drift response of SMRFs and BRB frames in steel buildings designed according to ASCE 7-05. *J. Struct. Eng.*, 137(5):589-99.

Fahnestock, L.A., Sause, R., Ricles, J.M. (2007). Seismic response and performance of buckling-restrained braced frames. *J. Struct. Eng.*, 133(9):1195-1204.

FEMA P695 (2008). *Quantification of building seismic performance factors*. *ATC-63 Project*. CA: Applied Technology Council.

Hibbit, D., Karlsson, B., Sorensen, P. (2013). *ABAQUS/Standard analysis user's manual, version 6.13*. Providence, RI: Dassault Systèmes/Simulia.

Kiggins, S., Uang, C.M. (2006). Reducing residual drift of buckling-restrained braced frames as a dual system. *Eng. Struct.,* 28(11):1525-32.

McCormick, J., Aburano, H., Ikenaga, M., Nakashima, M. (2008). Permissible residual deformation levels for building structures considering both safety and human elements. In: *14th World Conference on Earthquake Engineering*. Beijing, China.

Pettinga, D., Christopoulos, C., Pampanin, S., Priestley, N. (2008). Effectiveness of simple approaches in mitigating residual deformations in buildings. *Earthq. Eng. Struct. Dyn.*, 36(12):1763-83.

Sahoo, D.R., Chao, S. (2015). Stiffness-based design for mitigation of residual displacements of buckling-restrained braced frames. *J. Struct. Eng.*,141(9):04014229.

Shen, Y., Christopoulos, N., Mansour, C., Tremblay, R. (2011). Seismic design and performance of steel moment-resisting frames with nonlinear replaceable links. *J. Struct. Eng.*, 137(10):1107-17.

Vasdravellis, G., Karavasilis, T.L., and Uy, B. (2014). Design rules, experimental evaluation, and fracture models for high-strength and stainless steel hourglass shape energy dissipation devices. *J. Struct. Eng.*,140(11):04014087.

Vayas, I., Thanopoulos, P. (2005). Innovative dissipative (INERD) pin connections for seismic resistant braced frames. *Int. J. Steel. Struct.*, 5(5):453-464.

Watanabe, A., Hitomi, Y., Saeki, E., Wada, A., Fujimoto, M. (1988). Properties of brace encased in buckling-restraining concrete and steel tube. In: *9th World Conference on Earthquake Engineering*. Tokyo-Kyoto, Japan.

Infrastructure and Environment Scotland 3rd Postgraduate Conference
9th December 2015
Heriot-Watt University, Edinburgh

Overcoming the Fire Barrier to Tall Timber Construction

Alastair Bartlett, Kuba Gajewski, Sean Lineham, Daniel Thomson, Rory Hadden, Luke Bisby, Neal Butterworth
Institute for Infrastructure and Environment,
University of Edinburgh
(e-mail: alastair.bartlett@ed.ac.uk)

ABSTRACT

Architects' aspirations of tall buildings formed predominantly from exposed, structural timber elements are currently limited in part due to fire safety concerns, and a lack of available knowledge and understanding of the fire performance of such a structure. This paper presents some of the key areas of uncertainty, and highlights recent and ongoing research on engineered timber elements' fire behaviour. The pyrolysis, charring, structural performance in fire, flame spread, auto-extinction, and delamination processes are explored, and the key research priorities identified. Auto-extinction in particular is identified as an area requiring further research to be able to apply the existing knowledge in design. Delamination is also a key concern, due to its propensity to affect all the other phenomena discussed herein, and uncertainty as to its cause(s).

1. INTRODUCTION & BACKGROUND

Cross-laminated timber (CLT) is an engineered mass timber product which is gaining popularity in the construction industry due to its aesthetic, structural, sustainability, and constructability appeal. It is engineered with adjacent lamellae glued together with their grain directions perpendicular, as shown in Fig. 1, thus providing significant structural capacity in both directions. Primarily used as structural wall and floor slabs, CLT offers bending strengths competitive with concrete, creating the opportunity for multi-storey, architecturally unique buildings composed predominantly of exposed structural timber. A significant factor preventing its widespread uptake is uncertainty as to its performance in the event of a fire.

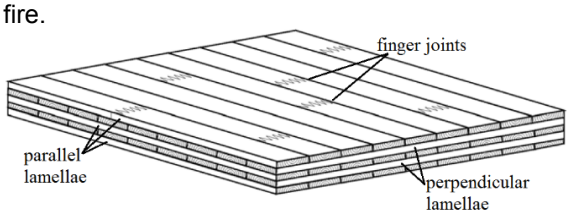

Figure 1. Illustration of cross-laminated timber showing alternating grain directions and finger joints (from (CEN, 2004))

To enable safe, sustainable, resilient and efficient performance-based design of mass timber structures, a detailed understanding of the structural behaviour of CLT at elevated temperatures, and additional understanding of how to apply the existing knowledge of pyrolysis, ignition, and combustion processes is essential. Current design guidance (CEN, 2004) defines the fire resistance of timber as the duration it can withstand furnace exposure to a standard temperature-time curve without its loadbearing, insulation, or integrity abilities being compromised. These depend on three factors: (1) the contribution of any fire protection applied to the exterior of the structural timber, such as plasterboard, (2) heating and charring of the timber, and (3) the residual loadbearing capacity of the timber section, its integrity, and insulation performance (White, 2002). Whilst the fire resistance of timber can be relatively easily increased by adding gypsum plasterboard (Schmid et al., 2010), this does not allow the desired architectural vision of exposed mass timber to be realised. Sacrificial protection through charring is thus the preferred method of providing so called "fire resistance".

2. PYROLYSIS OF TIMBER

When timber is heated, it undergoes thermal degradation (pyrolysis), producing both flammable and inert gases, liquid tars, and a rigid carbonaceous char. The process of char formation is typically assumed to occur at temperatures close to 300°C, with pyrolysis of wood typically commencing around 200°C (Friquin, 2011, Buchanan, 2001, Drysdale, 2011), with temperatures varying slightly for the three constituent polymers. Woods typically comprise about 50% cellulose, 25% hemicellulose, and 25% lignin (Drysdale, 2011, Inghelbrecht, 2014, Lautenberger, 2014), with considerable variations between species. Pyrolysis and the subsequent combustion of wood has been observed to consist of four distinct stages (Browne, 1958):

(1) Up to 200°C a mostly inert heating stage is observed, during which free water evaporates.

Pyrolysis in this temperature range, if it occurs, is very slow, increasing slightly after the sample has dehydrated (Yang et al., 2003). Production of flammable gases is low during this stage – the main products, in addition to water vapour, being small amounts of carbon dioxide and carbon monoxide, as well as formic and acetic acids (Browne, 1958). Structural changes in the complex lignin molecules have been observed at temperatures as low as 65°C (White and Dietenberger, 2001) to 100°C (Reszka and Torero, 2008) which may result in a reduction of structural strength. Below 200°C char production is dominated by hemicellulose decomposition, with prolonged heating to these temperatures producing hemicellulose char whilst leaving cellulose largely unreacted (Browne, 1958, Lautenberger, 2014).

(2) At about 200°C to 300°C pyrolysis reactions remain slow, and most evolved gases remain non-combustible (Browne, 1958). The primary pyrolysis reactions occur in this range (Inghelbrecht, 2014), with the onset of combustion following in the presence of oxygen. Cellulose may break down in two modes, one favouring production of char and the other the production of volatiles (Drysdale, 2011). Due to the slower reaction rates in this temperature range, break down of cellulose will favour the former, exothermic reaction, yielding more char than at higher temperatures (Browne, 1958, Milosavljevic et al., 1996).

(3) At about 300°C to 500°C pyrolysis reaction rates significantly increase (Friquin, 2011, Inghelbrecht, 2014, Browne, 1958, White and Dietenberger, 2001) as chain scissions occur in the cellulose producing levoglucosan molecules (tar) (Drysdale, 2011); these then rapidly decompose further to produce volatiles (Browne, 1958) such as methane, formaldehyde, hydrogen, and methanol, providing the main pyrolysis gases supporting flaming combustion (White and Nordheim, 1992). Char is formed rapidly in this temperature range (Friquin, 2011, Inghelbrecht, 2014, White and Dietenberger, 2001), creating a layer which has a lower effective thermal conductivity than the virgin timber, and thus serves as insulation for the underlying wood. Once a char layer is formed the rate of additional char formation decreases to a lower, quasi-constant, value (Drysdale, 2011, Bartlett et al., 2015b) which serves to slow the progress of in-depth heating and delays further pyrolysis reactions (Browne, 1958). It should be noted that depths up to 40mm beneath the char layer experience temperatures considerably above ambient (Buchanan, 2001). The char yield is largely dependent on the chemical makeup of the wood, with different species with different ratios of polymers giving different char yields.

(4) At temperatures above 500°C, rapid secondary oxidation of char occurs (Friquin, 2011, Inghelbrecht, 2014, Browne, 1958), although the temperature for this to occur has been quoted as low as 300°C (Spearpoint and Quintiere, 2000, Ohlemiller et al., 1987) to 400°C (Ohlemiller et al., 1987, König, 2006) and as high as 700°C with increased external heat flux (Ohlemiller et al., 1987, Kashiwagi et al., 1987); it also depends on oxygen concentration (Ohlemiller et al., 1987). Secondary oxidation reduces the thickness of the insulating char layer, thus allowing additional in-depth heating of the sample and further pyrolysis.

The rate at which pyrolysis occurs is well known to be dependent on numerous material and system properties, such as density, moisture content, species, permeability, sample size and orientation, grain direction, external heat flux, and oxygen concentration (Bartlett et al., 2015b), with external heat flux having the greatest significance in design.

A knowledge of the basic pyrolysis processes and the effects of the resultant insulating char layer form the basis of current prescriptive design methodologies for timber in fire.

3. CHARRING BEHAVIOUR

Current design guidance for charring behaviour of timber assumes a constant value of 0.65mm/min, to standard fire exposure. In order to explore the true charring response of timber under various heating scenarios a series of intermediate-scale tests were run on 300mm x 200mm x 120mm thick softwood CLT samples (Bartlett et al., 2015b).

The heating scenarios tested were: constant heat fluxes of 30kW/m^2 and 50kW/m^2; quadratically increasing heat fluxes from 10kW/m^2 at rates of 8.33W/m^{2}min^2, 12.5W/m^{2}min^2, and 16.7W/m^{2}min^2; and simulated standard cellulosic (ISO, 1999) and slow heating fire curves (CEN, 1999). The external heat flux was applied using a mobile radiant panel array capable of imposing time-varying heat fluxes, developed at the University of Edinburgh known as the Heat Transfer Rate Inducing System (H-TRIS) (Maluk and Bisby, 2012). Samples were protected on the sides by ceramic board to limit heat losses through the sides and promote one-dimensional heat transfer. Type K thermocouples (TCs) were inserted through the sides of the samples at 5mm depth increments from the exposed surface to 40mm depth, with an additional TC at 60mm. Curve fitting was used to locate the position of the 300°C isotherm on the resulting thermal profile at each time-step; this was used to calculate char depth, and thus instantaneous charring rate. Charring rate as a function of time is shown in Fig. 2. It shows that, far from a constant rate of 0.65mm/min, the charring rate is subject to an initial peak before dropping off to a lower, quasi-steady value. Whilst the post-peak behaviour of all tests are similar, tending towards the Eurocode's value of 0.65mm/min, the differences in peak behaviour show a strong dependence on external heat flux, thus yielding

significantly different time-average charring rates. Taking an average charring rate over the whole test is thus not an accurate way of representing charring; the effect of charring peaks must be considered due to typical durations of compartment fires.

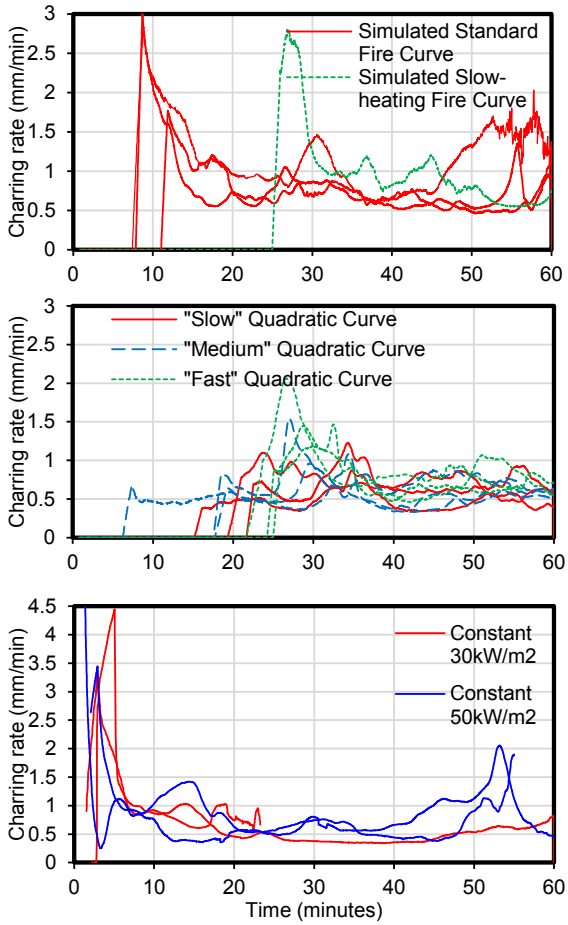

Figure 2. Charring rate plots for heating curves tested herein.

4. STRUCTURAL RESPONSE

The current structural design guidance for CLT assumes the abovementioned constant 0.65mm/min charring rate, and adds an additional, 7mm "zero-strength" layer to attempt to account for the additional 40mm heated zone beyond the char layer. Previous work (Schmid et al., 2012, Schmid et al., 2014) has suggested that this 7mm value is unsuitable, and that alternative values should be adopted.

In order to verify, or otherwise this approach, CLT slab strips of length 2000mm, width 300mm, and depth 100mm were prepared with lay-ups of either of three or five lamellae of uniform thickness. Load was applied using a servo-hydraulic actuator at 2mm/min in 4-point bending until failure (Bartlett et al., 2015c). It was found (with testing in duplicate) that the 3-layer slabs failed at an average load of 52.6±0.2kN by a 'rolling shear' failure mode, and the 5-layer beams failed at an average load of 40.4±2.3kN in a flexural (tension) mode (see Fig. 3).

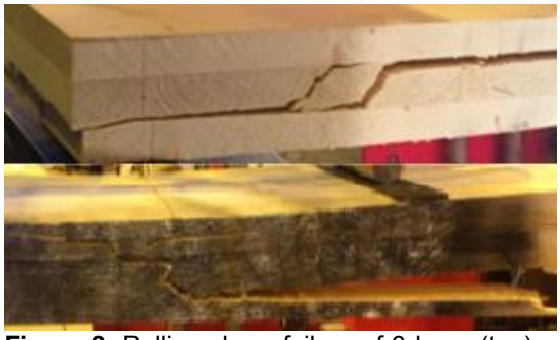

Figure 3. Rolling shear failure of 3-layer (top) and flexural failure of 5-layer samples (bottom).

Eight further tests (in duplicate) were performed under sustained load and radiant heating on samples loaded to 10 or 20% of ultimate ambient strength. Only the constant moment region was heated (with an incident heat flux of 25 to 30kW/m^2) to investigate the effects of loss of section on structural capacity and failure modes. Eurocode methods were used to predict the residual cross-section, from which the reductions in structural capacity during heating were also predicted (see Fig. 4).

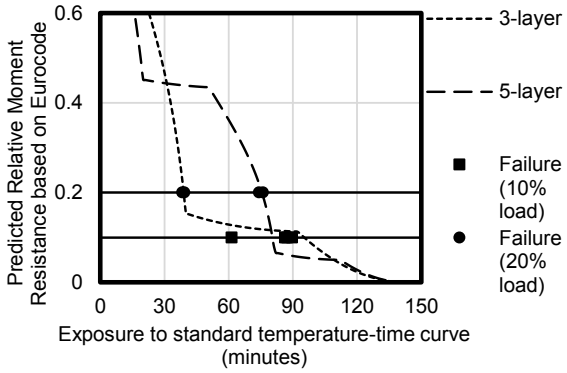

Figure 4. Relative flexural capacity during exposure to fire for 3- and 5-layer CLT samples

Whilst it was observed that failures were predicted with a high level of accuracy, a lower than assumed charring rate of about 0.5mm/min was calculated from in-depth temperatures; resulting in experimental char depths of approximately 20mm and 35mm at failure for the 3- and 5-lamellae samples respectively. This would correspond to zero-strength layer depths of 13mm or 21mm using the Eurocode's effective cross-section approach. Predictive models of the time-deflection response showed that the zero-strength layer fails to capture the true physics of the problem, and that the concept of a zero-strength layer applied to CLT is fundamentally flawed due to the grain-dependent strength parameters. Instead, the possibility of applying a thermomechanical sectional analysis is being explored, in which temperature-dependent mechanical properties are mapped onto the

temperature profile to give a true representation of the strength throughout the cross-section.

5. FLAME SPREAD

Whilst the Eurocode guidance focuses on charring and structural behaviour, other aspects of timber's response to fire, such as flame behaviour, also require investigation.

Eight flame spread tests were carried out on 885mm x 270mm x 220mm thick softwood CLT samples. Samples were set at an angle of around 15° to H-TRIS, to achieve a heat flux distribution over the sample length as shown in Fig 5.

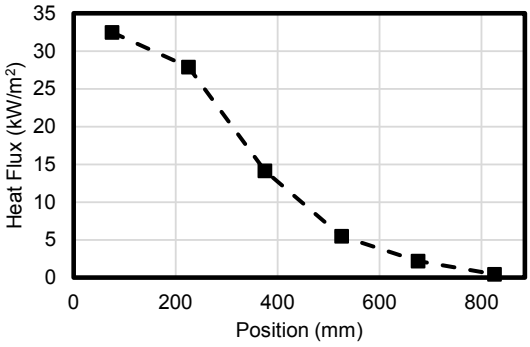

Figure 5. Heat flux distribution in flame spread tests

Samples were tested both parallel and perpendicular to the grain; somewhat surprisingly, no key difference was observed based on grain direction. When samples were pre-heated as in (Quintiere, 1981), a flame spread parameter of 10.2±3.5kW/m^3 was observed, and a critical heat flux for flame spread of 3.8±1.3kW/m^2. At heat fluxes below about 9kW/m^2, flames passed without sustained, continuous flaming. This critical heat flux for flame spread is very low, suggesting that in standard compartments, the majority of the timber surfaces will quickly become involved in the fire.

6. AUTO-EXTINCTION

Another important design consideration is the concept of auto-extinction; it is well known that wood as a material will only sustain flaming if there is an incident external heat flux (Drysdale, 2011). In a structural system with multiple exposed CLT surfaces, a fire will result in the ignition of the exposed timber. The heat produced by the burning of each surface will radiate to the others potentially allowing sustained burning of the timber after the compartment fire load has burnt out. This radiative exchange can be estimated using configuration factors and surface temperatures. If this heat flux is less than the critical heat flux for sustained flaming, then auto-extinction should occur (i.e. the timber will cease burning), otherwise flaming would continue most likely resulting in collapse in the absence of fire service intervention.

A series of tests on 85mm x 85mm x 100mm thick softwood CLT samples have been undertaken in the FM Global Fire Propagation Apparatus (FPA) to explore the conditions under which flame extinction occurs. These consisted of constant heat flux tests, and two-phase tests in which the sample was exposed to a "high" heat flux for a prescribed time before reducing the heat flux to a "low" value to simulate heating from another burning CLT surface. Mass loss and temperature distribution data within the timber were collected. Whilst the time to extinction was clearly affected, with samples typically extinguishing within 2 minutes of reducing the heat flux due to a greater char thickness, the critical mass loss rate was consistent with uniform heat flux tests, thus confirming that the mass loss rate is the governing mechanism (Drysdale, 2011).

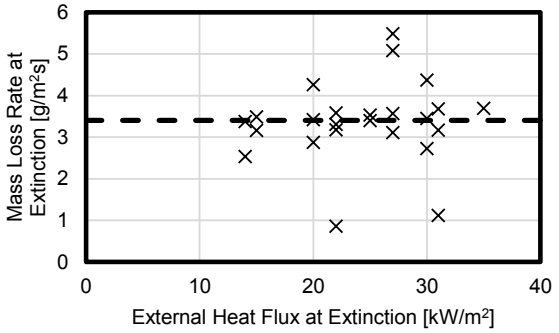

Figure 6. Mass loss rate at extinction as a function of heat flux

Initial investigations have found a critical heat flux for ignition in this configuration to be about 13kW/m^2, with a critical heat flux for sustained flaming of about 31kW/m^2, consistent with (Hottel, 1942). The critical mass loss rate for extinction was found to be around 3.4g/m^{2}s, as shown in Fig. 6.

Based on these data it can thus be theorised that if the incident heat flux to exposed timber in a compartment from all the other surfaces is such that the mass flux of volatiles is less than 3.4g/m^{2}s, then auto-extinction of flaming combustion will occur. Hence consideration of the compartment geometry at the design stage can be used as a basis for calculating if auto-extinction occurs in a compartment.

Further research is needed to verify the auto-extinction criteria under realistic configurations, and to identify additional variables (e.g. delamination, sample orientation, oxygen concentration, and smouldering) that might affect combustion behaviour and extinction mechanisms/criteria.

7. DELAMINATION

All of these phenomena can be affected by delamination – a phenomenon in which the fire-exposed lamella (or part thereof) detaches from the

rest of the member. When the charred layer falls off, the layer beneath is suddenly exposed to the fire and it has been observed that this results in faster burning and pyrolysis until the char layer has been re-established (Frangi et al., 2009). This in turn affects the structural response, due to the pyrolysis front and subsequent loss of mechanical properties propagating further into the sample upon delamination.

It has been observed in flame spread tests (Bartlett et al., 2015a) that as the front lamella starts to detach, a significant increase in temperature occurs, followed by flaming ignition of the second lamella. This resulted in a significant increase in flame height, shown in Fig. 7, and a 5kW increase in heat release rate, comparable to that of initial ignition. As well as affecting charring rates and mechanical properties, this has significant impact on auto-extinction; (Crielaard, 2015) found in miniature compartment tests that after auto-extinction, delamination caused a transition from smouldering back to flaming.

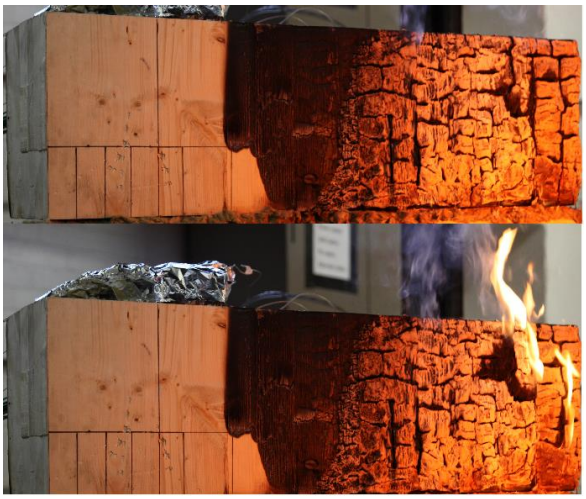

Figure 7. Flaming before and during delamination of a flame spread sample

Previous work on delamination (Frangi et al., 2009) had suggested that CLT panels bonded with a polyurethane (PU) adhesive (used for the flame spread tests in this paper) are susceptible to delamination, whereas those bonded with melamine urea formaldehyde (MUF) adhesives are not.

Tests were carried out on softwood CLT samples 300mm wide, 400mm high, and 100mm thick, consisting of three uniform lamellae bonded with a melamine formaldehyde (MF) adhesive. Samples were wrapped in foil and protected with vermiculite insulation on their sides so as to reduce heat losses through the sides and to promote one-dimensional heat transfer within the samples. Samples were subjected to a constant external heat flux of 100kW/m^2 from H-TRIS.

In these tests, contrary to the conclusions in previous work, delamination occurred. In agreement with observations from previous researchers, it was observed that delamination occurred not by entire lamellae falling off at once, but rather by small pieces of charred timber, generally 2 to 5 centimetres in length, actively detaching from the lamella below. This suggests that delamination is not limited to PU adhesives, however no general conclusions can be drawn regarding the underlying physical/controlling mechanisms.

8. FURTHER WORK

All of the above areas require further research in order to confidently allow safe, optimised, performance-based design guidance.

Of the areas discussed, the pyrolysis and charring behaviour are the best understood, with plentiful data available in the literature. The next step to apply these data in design is to understand the likely heat fluxes experienced in a timber compartment fire, in order to be able to select suitable charring rates for the initial fire stages.

It is clear that the existing zero-strength method is unsuitable for application to CLT, and thus further work is needed to determine accurate temperature-dependent mechanical properties to use as an input parameter in a thermomechanical sectional analysis method for structural design. Whilst data are available in the literature, agreement between different researchers is poor, and highly apparatus-dependent.

Further testing is ongoing to better understand auto-extinction criteria. In particular, the effects of reduced oxygen concentrations and apparatus require further understanding in order to apply the knowledge in the context of compartment fires.

As delamination can affect all the phenomena under study, it is vital that its cause(s) and effects be better understood. To this end, small scale shear testing at the glue-line will be undertaken at elevated temperatures to gain a preliminary understanding of glue failure.

If all the above knowledge can be gained and applied in the form of rational design guidance, then a significant barrier to architects' aspirations of tall, exposed timber buildings can be removed.

ACKNOWELDEGEMENT

The authors gratefully acknowledge generous support from Arup, partly through EPSRC iCASE Studentship 14220013.

REFERENCES

Bartlett, A., Gajewski, K., Hadden, R., Bisby, L. & Butterworth, N. Fire-Induced Delamination of Cross-Laminated Timber. *In:* Werther, N. & Winter, S., eds. 1st European Workshop on Fire Safety of Green Buildings, 6-7 October 2015a Berlin, Germany. Shaker Verlag, 17-20.

Bartlett, A., Hadden, R., Bisby, L. & Law, A. 2015b. Analysis of cross-laminated timber charring rates upon exposure to non-standard heating conditions. *Fire and Materials.* San Francisco, CA: Interscience Communications Ltd.

Bartlett, A., Lineham, S., Thomson, D., Hadden, R., Bisby, L. & Butterworth, N. Flexural Behaviour of Cross-Laminated Timber under Radiant Heating. *In:* Forero, M. P. G. & Palacio, A. M. L., eds. First Working Group Meeting of the COST Action FP 1404, 20-21 April 2015c Barcelona, Spain. Centre Tecnologic Forestal de Catalunya, 77-78.

Browne, F. L. 1958. Theories of the combustion of wood and its control.

Buchanan, A. H. 2001. *Structural design for fire safety*, Wiley New York.

CEN 1999. EN 1363-2 Fire resistance tests. *Part 2: Alternative and additional procedures.* Brussels, Belgium: European Committee for Standardization.

CEN 2004. Eurocode 5. Design of timber structures. . *Part 1-2: General. Structural fire design.* Brussels: European Committee for Standardisation.

Crielaard, R. 2015. *Self-extinguishment of Cross-Laminated Timber.* Master of Science in Civil Engineering MSc, Delft University of Technology.

Drysdale, D. 2011. *An introduction to fire dynamics*, John Wiley & Sons.

Frangi, A., Fontana, M., Hugi, E. & Jöbstl, R. 2009. Experimental analysis of cross-laminated timber panels in fire. *Fire Safety Journal,* 44**,** 1078-1087.

Friquin, K. L. 2011. Material properties and external factors influencing the charring rate of solid wood and glue-laminated timber. *Fire and Materials,* 35**,** 303-327.

Hottel, H. C. 1942. Report on "wood flammability under various conditions of irradiation". National Defense Research Committee of the Office of Scientific Research and Development.

Inghelbrecht, A. 2014. *Evaluation of the burning behaviour of wood products in the context of structural fire design.* International Master of Science in Fire Safety Engineering MSc, The University of Queensland, Ghent University.

ISO 1999. ISO 834-1: Fire resistance tests. Elements of building construction. *Part 1: General Requirements.* Geneva, Switzerland: Internatinal Organisation for Standardization.

Kashiwagi, T., Ohlemiller, T. & Werner, K. 1987. Effects of external radiant flux and ambient oxygen concentration on nonflaming gasification rates and evolved products of white pine. *Combustion and flame,* 69**,** 331-345.

König, J. 2006. Effective thermal actions and thermal properties of timber members in natural fires. *Fire and materials,* 30**,** 51-63.

Lautenberger, C., Sexton, S., & Rich, D. 2014. Understanding Long Term Low Temperature Ignition of Wood. *International Symposium on Fire Investigation Science and Technology.* College Park, MD.

Maluk, C. & Bisby, L. 2012. 120 years of structural fire testing: Moving away from the status quo.

Milosavljevic, I., Oja, V. & Suuberg, E. M. 1996. Thermal effects in cellulose pyrolysis: relationship to char formation processes. *Industrial & Engineering Chemistry Research,* 35**,** 653-662.

Ohlemiller, T., Kashiwagi, T. & Werner, K. 1987. Wood gasification at fire level heat fluxes. *Combustion and Flame,* 69**,** 155-170.

Quintiere, J. 1981. A simplified theory for generalizing results from a radiant panel rate of flame spread apparatus. *Fire and Materials,* 5**,** 52-60.

Reszka, P. & Torero, J. 2008. In-depth temperature measurements in wood exposed to intense radiant energy. *Experimental Thermal and Fluid Science,* 32**,** 1405-1411.

Schmid, J., Just, A., Klippel, M. & Fragiacomo, M. 2014. The Reduced Cross-Section Method for Evaluation of the Fire Resistance of Timber Members: Discussion and Determination of the Zero-Strength Layer. *Fire Technology***,** 1-25.

Schmid, J., König, J. & Just, A. 2012. The Reduced Cross-Section Method for the Design of Timber Structures Exposed to Fire—Background, Limitations and New Developments. *Structural Engineering International,* 22**,** 514-522.

Schmid, J., König, J. & Köhler, J. Design model for fire exposed cross-laminated timber. Proc of the sixth International conference Structures in Fire, Lancaster, US, 2010.

Spearpoint, M. & Quintiere, J. 2000. Predicting the burning of wood using an integral model. *Combustion and Flame,* 123**,** 308-325.

White, R. H. 2002. Analytical methods for determining fire resistance of timber members. *The SFPE handbook of fire protection engineering. 3rd ed. Quincy, MA: National Fire Protection Association*.

White, R. H. & Dietenberger, M. 2001. Wood products: thermal degradation and fire.

White, R. H. & Nordheim, E. V. 1992. Charring rate of wood for ASTM E 119 exposure. *Fire Technology,* 28**,** 5-30.

Yang, L., Chen, X., Zhou, X. & Fan, W. 2003. The pyrolysis and ignition of charring materials under an external heat flux. *Combustion and Flame,* 133**,** 407-413.

Infrastructure and Environment Scotland 3rd Postgraduate Conference
9th December 2015
Heriot-Watt University, Edinburgh

High order Finite Element Formulations for solving Helmholtz problems

K. Christodoulou, O. Laghrouche, M.S. Mohamed
Institute for Infrastructure and Environment,
Heriot Watt University
(email: kc328@hw.ac.uk)

ABSTRACT

The aim of the paper is to accurately model a two-dimensional wave problem using high order finite element formulations. These include the high-order finite element method (*p*-FEM) and the Partition of Unity Finite Element Method (PUFEM). In particular, both methods are used to solve a diffracted wave problem by a rigid cylinder. Numerical experiments are carried out on a bounded domain for which the analytical solution of the problem is imposed on its boundary. The performance of both methods is considered in terms of accuracy and conditioning. It is shown that both schemes have their positive and negative features.

1. INTRODUCTION

The finite element method has been a powerful technique for obtaining approximate solutions to wide variety of engineering problems, especially when solution domains have complex geometries. However, the finite element method based on linear or quadratic polynomial functions is not an effective tool for solving high frequency Helmholtz problems. The accuracy of the numerical solution becomes rapidly worse with increasing the wave number even if the number of elements per wavelength is kept constant. For reliable results, the method requires a considerable computational effort due to the requirement of dense discretization.

In comparison with low-order finite element methods, the use of plane wave based methods has been shown to reduce computation time and memory requirements associated with the numerical approximation of Helmholtz problems at high wave numbers. The enriched methods offer an easy way to include special functions into the finite element space which can approximate the solution even better than the classical polynomials functions. These include the Partition of Unity Finite Element Method (PUFEM), the generalized finite element method (GFEM), the Partition of Unity Boundary Element Method (PUBEM), the Ultra Weak Variational Formulation (UWVF) and finally, the Discontinuous Enrichment Method (DEM).

Despite the fact that these methods are very promising and have proven their efficiency for solving acoustic problems, they still suffer from a number of drawbacks. For instance, the enrichment methods often require high order quadrature schemes or special integration techniques due to the evaluation of oscillatory integrals. The methods also yield ill-conditioned matrices which prevents the use of efficient iterative solvers.

For these reasons, a considerable amount of research has been focused to the use of high-order polynomial element methods. In the literature, several families of polynomial basis functions has been proposed, such as high-order Lagrange polynomials with special nodal distributions, the normalized integrals of the Legendre polynomials, basis functions derived from Bernstein polynomials and Non-Uniform Rational B-Spline polynomials known as NURBS.

The current work compares numerical solutions of the PUFEM against the polynomial high-order finite element method (*p*-FEM) for Helmholtz problems at high wave numbers. The PUFEM has been thoroughly investigated for acoustics and elastic wave problems and it was shown that the method provides high quality results with a significant smaller number of degrees of freedom in comparison to low order finite element methods. In this work, we compare the performance of PUFEM and *p*-FEM in terms of accuracy and conditioning as have it never been done before.

This paper is organized as follows: Section 2 presents the formulation of the Helmholtz model problem which we consider. It recalls the weak form of the equation and its numerical approximation by either, the high-order polynomial element method and the partition of unity finite element method. Section 3 presents numerical experiments whereas in section 4 we give some concluding remarks.

2. FORMULATION OF THE PROBLEM

In this section we first formulate the Helmholtz model problem with Robin boundary conditions and then we present the finite element formulations, namely the *p*-FEM and PUFEM.

2.1 Weak formulation and numerical approximation

Let $\Omega \subset \mathbb{R}^2$ be an open bounded domain with a smooth boundary Γ. We consider finite element discretizations for the following Helmholtz problem:

$$\Delta u + k^2 u = 0, \qquad \text{in } \Omega \tag{1a}$$

$$\nabla u.\boldsymbol{n} + ik\phi = g. \qquad \text{on } \Gamma \tag{1b}$$

Here, $u = u(x, y)$ is the unknown function, Δ is the Laplace operator and the coefficient $k \in \mathbb{R}$ is the wavenumber of the considered problem. The term g represents a boundary source on Γ and $\boldsymbol{n}$ denotes the outward normal unit vector defined everywhere on Γ.

The Galerkin finite element approximation is applied to the weak variational formulation of the Helmholtz problem. The weak formulation is obtained by multiplying the Helmholtz equation (1a) by a smooth test function $v = v(x, y)$ and integrating the resulting equation over the domain Ω such as

$$\int_\Omega (\Delta u + k^2 u) v \, d\Omega = 0. \tag{2}$$

Equation (2) involves second derivatives of u. By applying the integration by parts to the integrand with second derivatives, we obtain

$$\int_\Omega (-\nabla u.\nabla v + k^2 uv) d\Omega + ik \oint_\Gamma (\nabla u.\boldsymbol{n}) \boldsymbol{v} \, d\Gamma = 0. \tag{3}$$

Finally, by introducing the Robin boundary condition from the expression (1b), the system of equations to solve is then

$$\int_\Omega (\nabla u.\nabla v - k^2 uv) d\Omega + ik \oint_\Gamma u\boldsymbol{v} \, d\Gamma = \oint_\Gamma g\boldsymbol{v} \, d\Gamma. \tag{4}$$

Problem (5) is referred to as a variational problem and as the variational form of the Helmholtz equation (1a)-(1b).

2.1 Element interpolation functions

Let $M = \{\Omega_1, \Omega_2, \ldots\ldots, \Omega_K\}$ be a partition of Ω into N uniform non-overlapping elements $\Omega_e, e = 1,2, \ldots . K$. The field unknown variable u is approximated over each element Ω as follows

$$u \approx u_h = \sum_{j=1}^{N} u_j N_j(x, y) \tag{5}$$

where $u_j = u(x_j, y_j)$ are the specified or presumed function values at each nodal point (x_j, y_j) and $N_j(x, y)$ are the interpolation polynomial functions used to describe the behaviour of the exact solution. In this work, high order Lagrange polynomial functions (*p*-FEM) are used to solve the considered problems.
The one dimensional Lagrange *p*-order polynomials functions denoted by $L_j(x)$ (for j=0:*p*) are defined on *p*+1 nodal points and are given explicitly by

$$L_j(x) = \frac{(x - x_0)}{(x_j - x_0)} \cdot\cdot \frac{(x - x_{j-1})}{(x_j - x_{j-1})} \frac{(x - x_{j+1})}{(x_j - x_{j+1})} \cdot\cdot \frac{(x - x_p)}{(x_j - x_p)}$$

$$\Longrightarrow \quad L_j(x) = \prod_{\substack{k=0 \\ k \neq j}}^{p} \frac{(x - x_k)}{(x_j - x_k)}. \tag{6}$$

Lagrange polynomials also satisfiy the property

$$L_j(x) = \begin{cases} 1, & j = k \\ 0, & j \neq k \end{cases}$$

for all $0 \leq j, k \leq p$. In two-diimensional problems, Lagrange polynomial functions are easily defined by

$$N_j(x, y) = L_j(x) L_j(y), \;\; j = 0,1,2,.,(p \times p). \tag{7}$$

To create Lagrange polynomials a certain grid of nodes in the considered domain is required. Besides the trivial choice of an equi-spaced distribution of nodes, in this paper we also examine the Chebyshev-Gauss Lobatto nodal distribution. Both nodal distributions are given respectively by the following schemes:

- Equi-spaced (EQ)

$$x_i^{EQ} = \frac{2(i-1) - p}{p} \tag{8a}$$

- Chebyshev-Gauss Lobatto (CGL)

$$x_i^{CGL} = -\cos\left(\frac{(i-1)\pi}{p}\right) \tag{8b}$$

for $i = 0,1, \ldots\ldots, p$. Lastly, the number of degrees of freedom of the *p*-FEM approximation depends on the number of nodal points per element.
To implement the PUFEM approximation, we first define the local space of bases functions, $W_{loc}^{k:m}$,

which includes all the linear combination of *m* plane waves traveling in a range of $[0,2\pi]$. The local space is given by

$$W_{loc}^{k:m} = \text{span}\{\psi_l = e^{ik(x\cos\theta_l + y\sin\theta_l)}, l = 1,..,m\}. \quad (9)$$

The idea of PUFEM is to construct an approximation space which consists of the classical piecewise linear basis functions $N_j(x,y)$ multiplied with plane waves come from the local space (9). The PUFEM approximation is then given by

$$u \approx u_h = \sum_{j=1}^{N} N_j \left(\sum_{l=1}^{m} A_j^l \, e^{ik(x\cos\theta_l + y\sin\theta_l)} \right). \quad (10)$$

The unknowns of the problem are no more the coefficients u_j but the amplitude factors $A_j^l \in \mathbb{R}^2$ of the enrichment functions. Hence, the number of degrees of freedom of the PUFEM approximation depends on the number of enrichment functions included in the local approximation space.

3. NUMERICAL EXPERIMENTS

In this section, we illustrate the performance of both finite element formulations, *p*-FEM and PUFEM, by solving a scattering wave problem by a rigid cylinder.

For all the experiments we choose a quadrilateral mesh grid. In the case of *p*-FEM, the unknown field variable over each element is approximated by Lagrange polynomial interpolations of order *p*. In the case of the PUFEM approximation, we use piecewise bilinear shape functions multiplied by a set of [plane waves] enrichment functions.

To compare the results we focus on the relative error, in percent, using the L_2 norm defined as:

$$\frac{\left(\int_\Omega |u - u_h|^2 d\Omega\right)^{1/2}}{\left(\int_\Omega |u|^2 d\Omega\right)^{1/2}} \times 100 \quad (11)$$

with u being the exact solution of the considered problem and u_h the approximate solution using either, *p*-FEM or PUFEM.

We also define a parameter τ which indicates the discretization level in terms of degrees of freedom per wavelength. It is given by

$$\tau = \lambda \sqrt{\frac{totdof}{\Omega_{area}}} \quad (12)$$

where λ is the wavelength of the considered problem, *totdof* is the global number of degrees of freedom in the whole domain and Ω_{area} is the total area of the computational domain.

Finally, the conditioning of the stiffness matrix, denoted by $\kappa(A)$, is estimated using the 1-norm such as

$$\kappa(A) = ||A||_1 ||A^{-1}||_1. \quad (13)$$

To conclude with, all the elementary integrals are evaluated numerically in a straight forward way by using Gauss-Legendre quadrature. The number of integration points is chosen to be enough so that the results are not affected by the integration errors.

3.1 Problem of interest

The problem of a horizontal plane wave scattered by a rigid cylinder in an infinite domain is considered. This problem has analytical solution given by

$$u = \sum_{n=0}^{\infty} i^n \varepsilon_n \frac{j_n'(k\alpha)}{H_n'(k\alpha)} H_n(kr)\cos(n\theta). \quad (14)$$

where a is the radius of the cylinder, r and θ are the polar co-ordinates of any considered point of the domain, $H_n(kr)$ and $J_n(kr)$ are respectively the Hankel and Bessel functions of the first kind and order n, and ε_n is defined by $\varepsilon_0 = 1, \varepsilon_n = 2$ for all $n \geq 1$. For simplicity, the radius α is taken equal to unity.
The scattered wave u which satisfies the 2D Helmholtz equation (1a) is studied in a square domain which is chosen to be in the vicinity of the scattering cylinder such that

$$\Omega = [\alpha, \alpha] \times [2\alpha, 2\alpha].$$

Finally, the analytical solution (14) is imposed on the boundary Γ through the Robin boundary condition given in expression (1b) with the aim to quantify the error solely due to our approximations.

We start our study by solving the scattered problem with the *p*-FEM approximation. High-order Lagrange polynomials defined on the equi-spaced distribution (EQ) and on the Chebyshev-Gauss Lobatto distribution (CGL) are used to solve the problem for the wave number $k\alpha = 2\pi$. We fix a spatial mesh of 100 elements and we vary the polynomial degree over each element from 1 up to 20. The performance of both distributions is compared in terms of accuracy and conditioning. The results are presented in Fig.1.

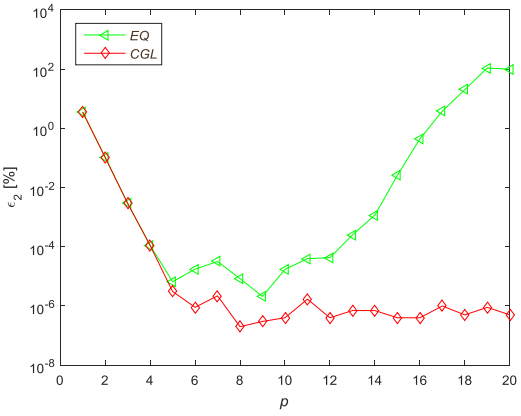

(a)

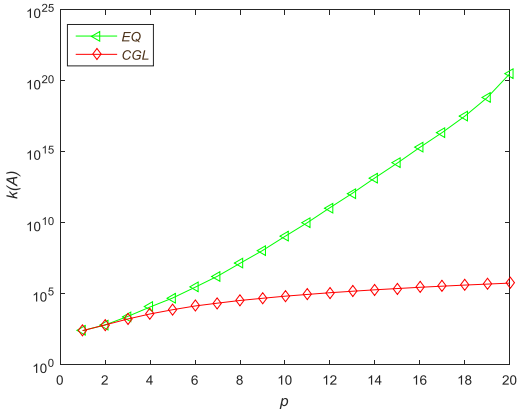

(b)

Figure 1. Obtained results with *p*-FEM at $k\alpha = 2\pi$. (a) Relative L_2-error with respect to polynomial order p; (b) conditioning $\kappa(A)$ of the stiffness matrix with respect to polynomial order *p*.

The approximation error and conditioning of both distributions are plotted as functions of the polynomial degree *p*. First, we consider plot (a) which compares the obtained L_2 error. As can be seen from the graph, both nodal distributions give almost the same accuracy for polynomials up to and including the 5th order (*p*=5). As *p* increases, the obtained error with the EQ-grid deteriorates, reaching to an error of 100% for the case of *p*= 20. On the other hand, the CGL-grid improves the accuracy and provides errors of magnitude up to 10^{-6}% of order of magnitude. Once the CGL-grid solution reaches a certain level of accuracy, the error stagnates even if we keep increasing the order of the polynomial functions. The conditioning $\kappa(A)$ is also presented. As shown in figure (b), the conditioning for the EQ-grid increases with *p,* resulting in very high condition numbers at high polynomial orders. On the other hand, the condition values obtained from the CGL-grid remain very low even for high polynomial orders.

More numerical experiments are carried out to further investigate high order polynomial element approximations. The scattered wave problem is now solved for the wave number $k\alpha = 40\pi$ which corresponds to the wavelength $\lambda/\alpha = 0.05$. Once again, both distributions are compared in terms of accuracy and conditioning. The results are plotted in Figure 2.

Considering the error plots (a) and (b), one can easily see the bad performance shown from high order EQ-grids in comparison to those with CGL-grids. Indeed, the EQ-grid can provide acceptable results for polynomial approximations up to and including the 16th order. However, for the same order of polynomial approximations, we can clearly see that CGL-grids lead to high quality results with minimum errors of 10^{-4}% of order of magnitude.

Moreover, the graphs (c) and (d) of Figure 2 show that the EQ-grid suffers from ill-conditioning if high order elements are used. In particular, the condition number deteriorates dramatically when the polynomial degree *p* over each element is increased from 10 to 20. On the other hand, the condition numbers obtained for the CGL distribution are much lower and remain approximately unchanged with increasing *p*.

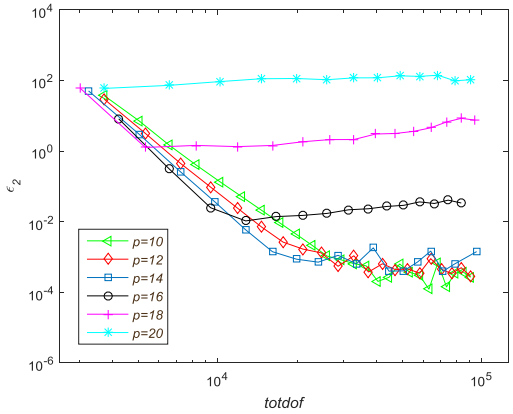

(a) EQ nodal distribution

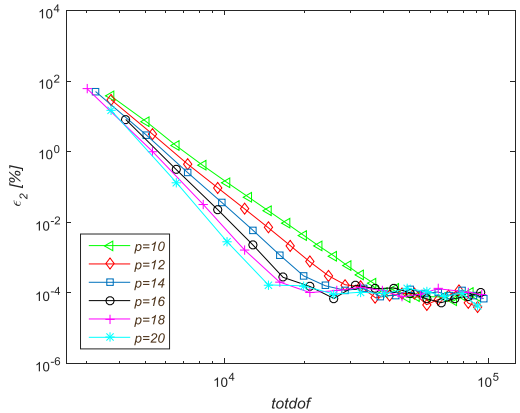

(b) CGL nodal distribution

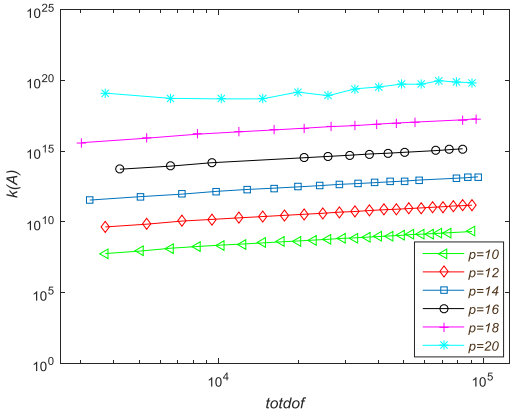

(c) EQ nodal distribution

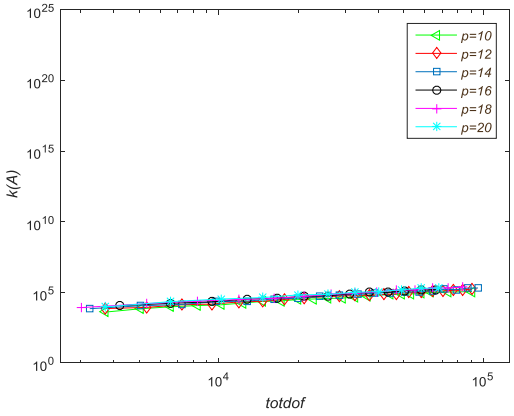

(c) CGL nodal distribution

Figure 2. Relative L_2-error and conditioning against the total number of degrees of freedom, *totdof,* for the wave number $k\alpha = 40\pi$.

Finally, we examine the efficiency of the proposed PUFEM compared to high order elements. Since the previous experiment indicated that high order elements based on Chebyshev-Gauss Lobatto distribution are the most reliable and efficient ones, only this family is compared with the proposed PUFEM approximation. Both formulations are investigated for the wave number $k\alpha = 100\pi$ and their performance is considered in terms of accuracy and conditioning. In the case of the *p*-FEM approximation, polynomial elements of order *p*=10, *p*=20, *p*=30 and *p*=50 are used in the analysis. In the case of the enriched element method, we fix a coarse spatial mesh of 16 elements and we vary the number of enrichment functions in such a way that $m = 70, 80, , 200$. The results are given in Figure 3.

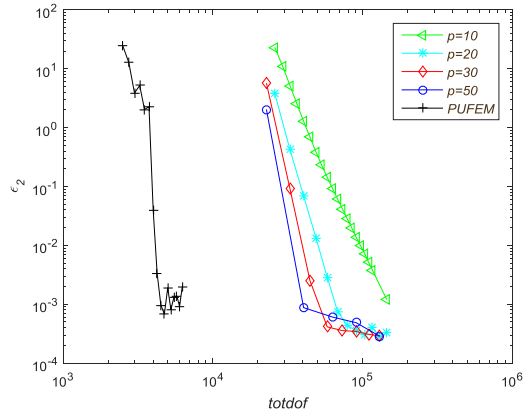

(a)

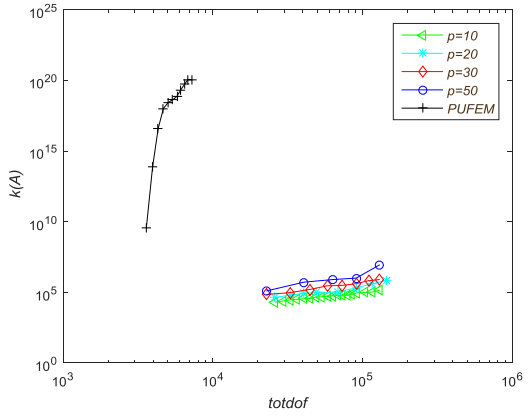

(b)

Figure 3. PUFEM and *p*-FEM results for the wave number $k\alpha = 100\pi$. (a) L_2-error against *totdof* ; (b) conditioning against *totdof.*

There are several important features to observe from Figure 3(a). First of all, the results show that both methods perform very well in high frequency problems. However, PUFEM is clearly the most efficient approximation due to high convergence behaviour. The PUFEM solution exhibits the fastest rate of convergence in comparison to high order elements, and therefore, less degrees of freedom are needed in order to reach a certain level of accuracy. On the other hand, it has to be noted that the PUFEM solution presents unsteady behaviour before it reaches 1% error. It is also experiences high oscillations at low error levels, i.e, at a level of 10^{-4}% of order of magnitude. This is simply a consequence of the fact that PUFEM solutions are influenced by rounding errors due to high condition numbers. The conditioning of both approximations is graphed in plot (b). Considering the *p*-FEM approximation, we see that the method performs better on a fine mesh grid. Furthermore, it is noticeable that higher order polynomial elements improve significantly the efficiency of the FEM solution. As can be seen, all polynomial element

solutions converge faster for higher *p*. Concerning minimum errors, we clearly see that the *p*-FEM approximation provides the highest accuracy. Lastly, by considering the conditioning plot, it would be reasonable to conclude that the PUFEM simulations are, in general, ill-conditioned whereas the *p*-FEM simulations appear to be more consistent and significantly better than those of the PUFEM. In particular, the condition numbers obtained with *p*-FEM remain below 10^7 of order of magnitude even for the case of *p*=50. In contrast to p-FEM, the conditioning of the PUFEM deteriorates with increasing the number of plane waves and it reaches up to a number of 10^{20} of order of magnitude.

3. CONCLUSIONS

In this work, two high order finite element formulations have been used to solve a 2D Helmholtz problem. The methods chosen are the high order polynomial finite element method (*p*-FEM) and the partition of unity finite element method (PUFEM). We investigated the performance of both methods for solving a diffracted problem in a bounded domain.
From the numerical tests, it is shown that high order polynomial elements are very effective and efficient for solving high frequency Helmholtz problems. They provide high quality results with significantly reduced number of degrees of freedom than those obtained by the conventional finite element method (FEM). In addition, it is shown that finite element solutions are strongly affected by the nodal distribution. In fact, polynomial interpolations defined on Chebyshev-Gauss Lobatto nodal distribution provide better accuracies with low conditioning in comparison to polynomial interpolation solutions on uniform distribution

The comparison between the two numerical formulations show that the enriched method (PUFEM) offers superior accuracies with even lower number of degrees of freedom than those obtained with *p*-FEM. In particular, for cases where the wavelength is much smaller compared to the dimension of the problem, the PUFEM approximation obtain errors with a low number of degrees of freedom. Similar error levels could be also obtained with *p*-FEM, however, this happens at a higher number of degrees of freedom. In general, the enrich element method offers the highest convergence rate and therefore it requires the least number of degrees of freedom for achieving a desire relative error.

On the other hand, it has to be noted that the PUFEM approximation suffers from ill-conditioning in comparison to *p*-FEM. For instance, the discrete system of the method becomes ill-conditioned as the number of the enrichment functions [plane waves] increases. As shown from the results, the error of the PUFEM ceases to improve at a lower level of accuracy than the minimum error obtained with *p*-FEM. This is simply a consequence of the fact that PUFEM solutions affected form rounding errors due to high condition numbers. Unlike PUFEM, the *p*-FEM approximation provides consistent and low in magnitude condition numbers. In summary, every scheme has it positive features and drawbacks.

REFERENCES

Melenk, J.M, Babuška, I. (1996). The partition of unity finite element method, *Comput Meth Appl Mech Eng.* 139: 289-314.

Babuška, I.M., Sauter, S.A. (2000). Is the Pollution Effect of the FEM Avoidable for the Helmholtz Equation Considering High Wave Numbers? *J Numer Anal,* 34(6):2392-2423.

Laghrouche, O., Bettess, P. (2000). Short wave modelling using special finite elements. *J Comput Acoust.* 8(1): 189-210.

Petersen, S., Dreyer, D., & von Estorff, O. (2006). Assessment of finite and spectral element shape functions for efficient iterative simulations of interior acoustics. *Computer methods in applied mechanics and engineering*, 195(44): 6463-6478.

Laghrouche, O., and M. S. Mohamed. (2010). Locally enriched finite elements for the Helmholtz equation in two dimensions. *Computers & structures* 88.23: 1469-1473.

Willberg, C., Duczek, S., Perez, J. V., Schmicker, D., & Gabbert, U. (2012). Comparison of different higher order finite element schemes for the simulation of Lamb waves. *Computer Methods in Applied Mechanics and Engineering*, 241(1): 246-261.

Infrastructure and Environment Scotland 3rd Postgraduate Conference
9th December 2015
Heriot-Watt University, Edinburgh

UV LED photocatalytic degradation of bisphenol-A: Technical & economic feasibility study

Konstantina Davididou, Robin Nelson, Efthalia Chatzisymeon
Institute for Infrastructure and Environment,
University of Edinburgh
(e-mail: K.Davididou@ed.ac.uk)

ABSTRACT

A UVA light emitting diode (LED) was used as illumination source for the TiO_2 photocatalytic degradation of bisphenol A (BPA). The effects of initial BPA and TiO_2 concentration on BPA removal were assessed. Increase of BPA, from 2.5 to 10 mg/L, resulted in removal decrease from 99.9 to 80% due to depletion of TiO_2 active sites for BPA adsorption. 250 mg/L TiO_2 was proved to be the optimal catalyst dosage being able to breakdown 99% of BPA in 45 minutes. Furthermore, the energy consumption was calculated and compared with other advanced oxidation processes (AOPs) used for BPA degradation. UV LED demonstrated great energy efficiency; the electric energy per order, E_{EO}, was found to be 15.75 and 26.41 kWh m^{-3}, for the optimal initial BPA and P25 concentration, respectively. LED driven photocatalysis exhibited an exceptional performance in terms of mass removal, treatment time and energy efficiency; three crucial parameters that affect directly the performance, the economy and subsequently the sustainability of the process.

1. INTRODUCTION

In recent years, endocrine disrupting compounds (EDCs) receive considerable academic and public attention due to their widespread occurrence and potential impact on human health and wildlife. EDCs have been detected at trace levels, i.e. <1 μg/L, in wastewater treatment plant (WWTP) effluents, surface water, as well as drinking water (Zhang and Zhou, 2008, Benotti et al., 2009, Liu et al., 2009). Major routes in the aquatic environment are through municipal sewage treatment plants (STP) effluent discharge, agricultural and urban runoff, landfill leachates and concentrated animal feeding operations (Benotti et al., 2009). These emerging micropollutants are subclasses of organic contaminants with estrogenic and androgenic activity at trace level concentrations (Liu et al., 2009) and can be either natural substances or xenobiotics. Various health cases, such as female breast cancer, testicular and thyroid cancer in male adults, have been attributed to EDCs exposure while it was proven that EDCs cause altered sex ratios, feminization and reproductive abnormalities in wildlife (Zhang and Zhou, 2008, Tijani et al., 2013). These compounds are known for their persistent, recalcitrant, non-biodegradable and toxic character (Klavarioti et al., 2009) fact that explains their wide distribution in waterways.

Various chemical substances have been identified as potential EDCs including pharmaceuticals and personal care products (PPCPs), pesticides, industrial chemicals, heavy metals and recently artificial sweeteners (Liu et al., 2009, Sang et al., 2014). Bisphenol-A (BPA), a listed EDC, is used extensively in the plastic industry (Tijani et al., 2013, Tsai et al., 2009), and receives considerable attention as it is highly abundant in water environment (Zhang and Zhou, 2008).

The present physical and biological treatment methods are ineffective in terms of complete degradation of these micropollutants (Tijani et al., 2013, Tsai et al., 2009). In the conventional activated sludge system the majority of the compounds is absorbed in the sludge produced (and a big percentage of them will be released in water during dewatering process) or remains soluble in the effluent (Belgiorno et al., 2007). Technologies such as granular activated carbon (GAC) adsorption and membranes are effective for the removal of EDCs, however both of them only transfer the micro contaminants from one medium (water) to another by accumulating EDCs in the GAC or concentrate respectively (Benotti et al., 2009, Belgiorno et al., 2007). Consequently, an advanced treatment technology is sought, combining high performance and cost effectiveness.

Advanced oxidation processes (AOPs) are attractive alternatives due to their ability of mineralizing completely EDCs (Tijani et al., 2013, Tsai et al., 2009). The processes of this category follow the same pathway; highly reactive species, mainly free hydroxyl radicals (•OH), are formed and attack non-selectively refractory organic pollutants

by their subsequent conversion to CO_2 and inorganic ions. Heterogeneous TiO_2 photocatalysis holds a unique position among other AOPs as it has demonstrated its high efficiency in degrading and finally mineralizing bio-recalcitrant organic compounds (Xu et al., 2014). It is chemically stable, inexpensive, versatile, operates in ambient conditions and catalyst itself features outstanding properties such as long-term photostability, chemical inertness, low cost and environmentally friendly nature (Xu et al., 2014, Ibhadon and Fitzpatrick, 2013). To increase process sustainability, solar or light emitting diode (LED) - photocatalysis can be used. In this direction, considerable attention has been drawn to optimize process efficiency for water treatment applications (Malato et al., 2009). Sunlight driven photocatalysis makes use of the UV band of solar spectrum for the photoexcitation of catalysts in an economical and ecological way without the high operating cost of the artificial photon generation. LEDs in contrast with traditional mercury UV lamps feature significant advantages such as narrower emission spectra, higher light output, lower energy consumption, extended life time, smaller environmental footprint and are free of the toxic mercury (Leblebici et al., 2015).

In light of this, the present study investigated the technical and economic feasibility of UV LED photocatalysis for BPA removal from aqueous solutions.

2. MATERIALS AND METHODS

2.1 Chemicals

BPA (CAS No: 80-05-7) was obtained from Sigma Aldrich in purity ≥99% and used without further modification. BPA solutions, 2.5-10 mg/L, were prepared in deionized water (18.2 ΩM cm, Elga Labwater). Aeroxide® TiO2 P25 (P25), supplied by Evonic, was used as the photocatalyst.

2.2 Photocatalytic experiments

The photocatalytic experiments were carried out in a batch reactor, applying a working volume of 150 mL. For LED driven photocatalysis a quartz plate was placed above the reactor where the LED was fixed on it emitting at 365 nm (UVA) and at light intensity of 11W.

BPA solution was loaded in the photoreactor and the accurate pre-weighted amount of P25 was added. The slurry solution in the reactor was continuously stirred with a magnetic stirrer to achieve uniform mixing and to promote dispersion of the photocatalyst. The solution was stirred for thirty minutes in the dark allowing for an adsorption-desorption equilibrium of BPA on TiO_2 surface at the beginning of each experiment (adsorption phase). During this time, the reactor was covered with aluminum foil to prevent irradiation losses. Then the lamp was switched on and the suspension was irradiated for 45 minutes. During the experimental procedure samples were withdrawn at scheduled times and filtered through 0.45 μm syringe filters (CM Scientific) to separate catalyst's particles. The filtrate was analysed for BPA residuals by applying chromatographic and spectrophotometric analysis. All the experiments were conducted in room temperature and at a neutral pH. The effect of key operational parameters on treatment performance was assessed and evaluated in terms of BPA removal.

2.3 Analysis

BPA concentration was measured by HPLC method obtained by (Frontistis, 2011). HPLC (C18 Luna 5u, 250 x 4.6 mm, Phenomenex) with a UV-DAD detector at a wavelength of 225 nm was used. The mobile phase was a mixture of water (35 vol. %) and acetonitrile (65 vol. %) at a flow rate of 1mL·min^{-1}. The solvents were eluted isocratically and the injection volume was at 40 μL. Additionally, calibration curve for the determination of BPA was established for the UV- Visible spectrophotometer (Varian, Cary 100 Scan) at λ_{MAX}=193 nm.

3. RESULTS AND DISCUSSION

3.1 Photocatalytic degradation of BPA

For the better understanding of the operating parameters' effect on BPA photodegradation various initial BPA concentrations, 2.5-10 mg /L, and P25 dosages, 0-250 mg/L, were applied in a series of experiments.

3.1.1 Effect of initial BPA concentration

To investigate the effect of initial BPA concentration on photocatalytic performance, 2.5, 5, 7.5 and 10 mg/L were applied at a constant catalyst load of 125 mg/L. The results revealed that increase of initial organic load resulted in decrease of BPA removal. This trend is in agreement with literature; higher organic concentration leads to depletion of the hydroxyl radicals (Sin et al., 2012).

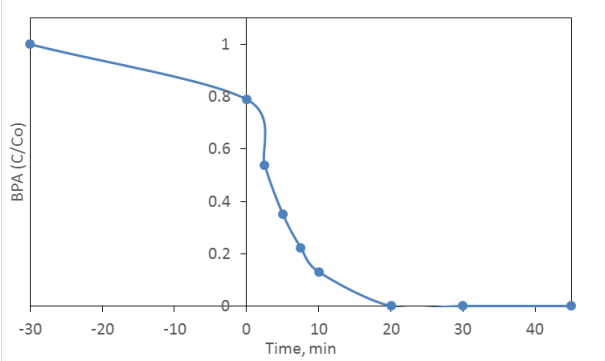

Figure 1. Removal profile of BPA. Photocatalytic

conditions: $[BPA]_0$=2.5 mg/L, [P25]=125 mg/L, irradiation source: LED, light intensity: 11W, irradiation time=45 min. and room temperature ≈ 25°C

In the present study, 20 minutes proved adequate for the 99.9% degradation of 2.5 mg/L BPA (Figure 1). However, when concentration of 10 mg/L BPA applied, 45 minutes of irradiation were not sufficient to remove more than 80% of the BPA.

3.1.2 Effect of catalyst dosage

The effect of TiO_2 dosage on the photocalytic degradation of BPA was the next to be studied. In this direction, 100, 125 and 250 mg/L P25 were tested while the initial BPA concentration was held at 5 mg/L. The optimal dosage was found to be 250 mg/L P25 that was able to remove 99 % of the BPA in less than 40 min as shown in Figure 2.

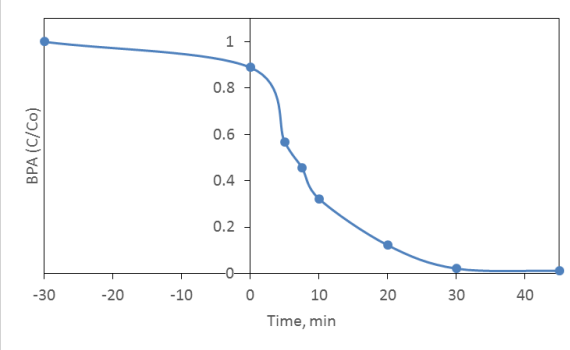

Figure 2. Removal profile of BPA. Photocatalytic conditions: $[BPA]_0$=5 mg/L, [P25]=250 mg/L, irradiation source: LED, light intensity: 11W, irradiation time=45 min. and room temperature ≈ 25°C

Principally, efficiency is increased linearly with catalyst concentration, since more active sites are available. However, in the case of TiO_2 overloading the turbidity formed by the catalyst's particles, limits the amount of the UV light that reaches the catalyst's surface (Sin et al., 2012).

3.2 Economic evaluation

High operational costs associated with electric energy driven AOPs hinder their commercialisation, so it is crucial for every feasibility study to involve an estimation of the cost efficiency. Figures of merit as developed by (James R. Bolton, 2001) were used to calculate the electric energy per order, E_{EO} - energy required for 90% degradation of pollutants in a unit volume (m^3) of contaminated water:

$$E_{EO} = \frac{Pt1000}{Vlg\left(c_i/c_f\right)} \quad (1)$$

Where, P is the rated power (kW) of the AOP system, V is the volume (L) of water treated in the time t (h) and c_i, c_f are the initial and final concentrations (M) of the compound under study.

For idealised batch reactor, a perfectly mixed reactor, Eq. 1 is simplified into Eq.2:

$$E_{EO} = \frac{38.4\,P}{Vk_1'} \quad (2)$$

Where, k'_1 is the first-order rate constant (min^{-1}). E_{EO} is an informative tool in situations where the initial concentration of the pollutant is low and the removal follows a first-order reaction model, like the present study.

As can be seen from Table 1, UV LED photodegradation of BPA was amongst the AOPs with the greatest energy efficiency with E_{EO}= 15.75 and 26.41 kWh m^{-3}, for the optimal initial BPA and P25 concentration, respectively. Compared to the systems used in (Hansen and Andersen, 2012), (Sharma et al., 2015) and (Torres et al., 2007), the LED based AOP, used in the present study, achieved higher BPA mass removal. Furthermore, LED driven photocatalysis resulted in up to 10 times shorter treatment time for the 90% removal of BPA compared to UV/$S_2O_8^{2-}$, UV/H_2O_2, US/Fe^{2+}, US/UV and US/UV/Fe^{2+}.

Table 1. Energy consumption for BPA degradation by various AOPs

Process	Power, W	Time, min	E_{EO}, kWh m^{-3}	Ref.
UVA/TiO_2	11	20	15.75	*(1)[1]*
UVA/TiO_2	11	30	26.41	*(1)[2]*
UV	700		16.1±1.	*(2)*
UV/H_2O_2	700		8.7±1.2	*(2)*
UV/$S_2O_8^{2-}$	40	240	307.45	*(3)*
UV/H_2O_2	40	240	509.49	*(3)*
US/Fe^{2+}	80	300	6010	*(4)*
US/UV	105	300	3735	*(4)*
US/UV/Fe^{2+}	105	300	1033	*(4)*

(1) Present study, (1)[1]-$[BPA]_0$=2.5 mg/L, [P25]=125 mg/L, (1)[2]-$[BPA]_0$=5 mg/L, [P25]=250 mg/L
(2)(Hansen and Andersen, 2012) -$[BPA]_0$=1μg/L
(3)(Sharma et al., 2015)-$[BPA]_0$=50mg/L
(4)(Torres et al., 2007)-$[BPA]_0$=27μg/L

4. CONCLUSIONS

A new trend was adopted in heterogeneous photocatalysis aiming to optimize this advanced oxidation process in terms of performance and sustainability for EDCs removal from water and wastewater. In this direction, a UVA-LED was employed as irradiation source for the photocatalytic removal of BPA. Results revealed that LED driven photocatalysis achieved high performance in degrading BPA. 99.9% removal was achieved in 20 min at initial BPA concentration of 2.5 mg/L. Under the optimal catalyst dosage, 250 mg/L P25, BPA was completely degraded in less than 40 min. Apart from the outbalanced performance, LED

exhibited energy efficiency as well, compared with other AOPs.

REFERENCES

BELGIORNO, V., RIZZO, L., FATTA, D., DELLA ROCCA, C., LOFRANO, G., NIKOLAOU, A., NADDEO, V. & MERIC, S. 2007. Review on endocrine disrupting-emerging compounds in urban wastewater: occurrence and removal by photocatalysis and ultrasonic irradiation for wastewater reuse. *Desalination,* 215**,** 166-176.

BENOTTI, M. J., TRENHOLM, R. A., VANDERFORD, B. J., HOLADY, J. C., STANFORD, B. D. & SNYDER, S. A. 2009. Pharmaceuticals and Endocrine Disrupting Compounds in U.S. Drinking Water. *Environmental Science & Technology,* 43**,** 597-603.

FRONTISTIS, Z. 2011. Removal of endocrine disruptors from aqueous phase by advanced oxidation processes. *PhD thesis*. *University of Crete*.

HANSEN, K. M. S. & ANDERSEN, H. R. 2012. Energy Effectiveness of Direct UV and UV/H2O2 Treatment of Estrogenic Chemicals in Biologically Treated Sewage. *International Journal of Photoenergy,* 2012**,** 9.

IBHADON, A. & FITZPATRICK, P. 2013. Heterogeneous Photocatalysis: Recent Advances and Applications. *Catalysts,* 3**,** 189.

JAMES R. BOLTON, KEITH G. BIRCHER, WILLIAM TUMAS, AND CHADWICK A. TOLMAN 2001. Figures-of-merit for the technical development and application of advanced oxidation technologies for both electric- and solar-driven systems. *Pure and Applied Chemistry* 73**,** 627-637.

KLAVARIOTI, M., MANTZAVINOS, D. & KASSINOS, D. 2009. Removal of residual pharmaceuticals from aqueous systems by advanced oxidation processes. *Environment International,* 35**,** 402-417.

LEBLEBICI, M. E., RONGÉ, J., MARTENS, J. A., STEFANIDIS, G. D. & VAN GERVEN, T. 2015. Computational modelling of a photocatalytic UV-LED reactor with internal mass and photon transfer consideration. *Chemical Engineering Journal,* 264**,** 962-970.

LIU, Z.-H., KANJO, Y. & MIZUTANI, S. 2009. Removal mechanisms for endocrine disrupting compounds (EDCs) in wastewater treatment — physical means, biodegradation, and chemical advanced oxidation: A review. *Science of The Total Environment,* 407**,** 731-748.

MALATO, S., FERNÁNDEZ-IBÁÑEZ, P., MALDONADO, M. I., BLANCO, J. & GERNJAK, W. 2009. Decontamination and disinfection of water by solar photocatalysis: Recent overview and trends. *Catalysis Today,* 147**,** 1-59.

SANG, Z., JIANG, Y., TSOI, Y.-K. & LEUNG, K. S.-Y. 2014. Evaluating the environmental impact of artificial sweeteners: A study of their distributions, photodegradation and toxicities. *Water Research,* 52**,** 260-274.

SHARMA, J., MISHRA, I. M. & KUMAR, V. 2015. Degradation and mineralization of Bisphenol A (BPA) in aqueous solution using advanced oxidation processes: UV/H2O2 and oxidation systems. *Journal of Environmental Management,* 156**,** 266-275.

SIN, J.-C., LAM, S.-M., MOHAMED, A. R. & LEE, K.-T. 2012. Degrading Endocrine Disrupting Chemicals from Wastewater by TiO2 Photocatalysis: A Review. *International Journal of Photoenergy,* 2012.

TIJANI, J., FATOBA, O. & PETRIK, L. F. 2013. A Review of Pharmaceuticals and Endocrine-Disrupting Compounds: Sources, Effects, Removal, and Detections. *Water, Air, & Soil Pollution,* 224**,** 1-29.

TORRES, R. A., PÉTRIER, C., COMBET, E., MOULET, F. & PULGARIN, C. 2007. Bisphenol A Mineralization by Integrated Ultrasound-UV-Iron (II) Treatment. *Environmental Science & Technology,* 41**,** 297-302.

TSAI, W.-T., LEE, M.-K., SU, T.-Y. & CHANG, Y.-M. 2009. Photodegradation of bisphenol-A in a batch TiO2 suspension reactor. *Journal of Hazardous Materials,* 168**,** 269-275.

XU, H., OUYANG, S., LIU, L., REUNCHAN, P., UMEZAWA, N. & YE, J. 2014. Recent advances in TiO2-based photocatalysis. *Journal of Materials Chemistry A,* 2**,** 12642-12661.

ZHANG, Y. & ZHOU, J. L. 2008. Occurrence and removal of endocrine disrupting chemicals in wastewater. *Chemosphere,* 73**,** 848-853.

Infrastructure and Environment Scotland 3rd Postgraduate Conference
9th December 2015
Heriot-Watt University, Edinburgh

Novel Finite Elements for initial value problems of light waves in the time domain

M. Drolia*, M. S. Mohamed*, O. Laghrouche*, M. Seaid**, and J. Trevelyan**,
*Institute for Infrastructure and Environment,
Heriot Watt University
**School of Engineering and Computing Sciences,
Durham University, Durham DH1 3LE, UK
(e-mail: md272@hw.ac.uk)

ABSTRACT

This paper proposes a novel scheme for the solution of Maxwell equations in the time domain. A discretization scheme in time is developed to render implicit solution of system of equations possible.
The scheme allows for calculation of the field values at different time slices in an iterative fashion. This facilitates us to tackle problems whose solutions have harmonic or even more general dependency on time. The spatial grid is partitioned into finite number of elements with intrinsic shape functions to form the bases of solution. Furthermore, the finite elements are enriched with plane wave functions. This significantly reduces the number of nodes required to discretize the geometry, without compromising on the accuracy or allowed tolerance in the errors, as compared to that of classical FEM. Also, this considerably reduces the computational costs, viz. memory and processing time. Parametric studies, presented herewith, confirm the robustness and efficiency of the proposed method. The numerical scheme can thus be further developed for solution of problems where analytical solutions cannot be developed, or even when the solution cannot be categorized as time-harmonic in nature.

1. INTRODUCTION

The Maxwell equations for electromagnetism provide a solid structure for analysis of light waves in various applications. These are routinely simulated in industry to aid in the design and optimisation of a wide spectrum of devices/systems e.g. high speed electronic circuits, radar, medical imaging etc.
The standard software today are based on the finite differences (FDM) or finite element (FEM) methods for discretization of the grid (space/time) for digital computation. The proposed research aims at reducing the cost (processing time, memory requirements etc.) of such computation extensive processes. Further, the FEM for electromagnetism deals generally with time-harmonic problems. This paper aims to obtain a numerical model for more general and non-time-harmonic solutions of the wave equation in the time domain.

2. Transverse Electric Mode of propagation

Let Ω be a unit square defined on a 2D Euclidean space, with its four edges as the boundary Γ. The boundary value problem be defined as follows

$$\frac{\partial^2 E}{\partial t^2} - c^2\nabla^2 E = f(t,x,y) \text{ on } \Omega \qquad (1a)$$

$$\frac{\partial E}{\partial v} + hE = g(t,x,y) \qquad \text{on } \Gamma \qquad (1b)$$

$$E^0 = U_0 \qquad (1c)$$

$$\frac{\partial E^0}{\partial t} = V_0 \qquad (1d)$$

where E is the magnitude of the transverse electric field in the z direction perpendicular to the Euclidean plane. The above equation can be approximated using finite element and finite difference schemes for numerical solution. Let's discretize the time derivative in the following way (in order to facilitate the development of time-dependent formulations (Mohamed M.S et.al. 2014) as seen in analyses for transient response (Mohamed M.S et.al. 2014) or diffusion problems (Mohamed M.S et.al. 2013)

$$\frac{\partial^2 E^n}{\partial t^2} = \frac{E^n - 2E^{n-1} + E^{n-2}}{\Delta t^2} \qquad (2)$$

Where the superscript n stands for the value of the field at the time instance t = nΔt. Substituting in (1a) gives

$$E^n - (c^2\Delta t^2)\nabla^2 E^n = 2E^{n-1} - E^{n-2} + (\Delta t\text{^}2) f(t,x,y) \qquad (3)$$

The equation (3) can be used to obtain a weak form which can be further solved over a finite number of elements in space as a linear system of equations. Let u be a test function multiplied to (3)

$$u(E^n - (c^2\Delta t^2)\nabla^2 E^n) = u(2E^{n-1} - E^{n-2} + (\Delta t\hat{}2)f(t,x,y)) \quad (4)$$

Integrating the left and right hand sides, over the domain Ω with boundary Γ, and applying the divergence theorem we get

$$\int_\Omega uE^n d\Omega + (c^2\Delta t^2)\{\int_\Omega \nabla u \cdot \nabla E^n d\Omega - \int_\Gamma u\hat{v} \cdot \nabla E^n d\Gamma\} = \int_\Omega u\big(2E^{n-1} - E^{n-2} + (\Delta t^2)f(t,x,y)\big)d\Omega \quad (5)$$

Where **v** is the normal unit vector to Γ. From (1b) and (5) we get the solvable weak form

$$\int_\Omega uE^n d\Omega + (c^2\Delta t^2)\int_\Omega \nabla u \cdot \nabla E^n d\Omega + (c^2\Delta t^2)\int_\Gamma u(hE^n)d\Gamma = \int_\Omega u\big(2E^{n-1} - E^{n-2} + (\Delta t^2)f(t,x,y)\big)d\Omega + (c^2\Delta t^2)\int_\Omega u\, g(t,x,y)d\Gamma \quad (6)$$

This equation (6) can be used to solve for E^n for the given set of boundary and initial conditions. The equation can then be iterated over n to obtain subsequent values of the fields for consecutive time steps. This paper validates the proposed method against a problem where the solution is a cylindrical wave such that

$$E = e^{i(kr - wt + \varphi)} \quad (7)$$

where k is the wave number, ω angular frequency, φ phase shift, r length of the position vector, e the natural exponent and i the imaginary number. Then the above constant c becomes the phase velocity defined such as $c = \omega/k$ and f (t,x,y) = 0 while the function g(t,x,y) is defined on each domain edge according to the relevant normal direction.

The initial conditions are defined by

$$U_0 = e^{i(kr+\varphi)} \quad (8a)$$
$$V_0 = e^{i(kr+\varphi)}(-i\omega) \quad (8b)$$

To solve the weak form (6) using the finite element method we mesh the domain into a set of elements where the field E over each element is approximated in terms of a set of nodal values E_i and nodal shape functions N_i such as

$$E = \sum_{i=1}^{n} E_i N_i \quad (9)$$

Using the partition of unity (Melenk JM, Babuska 1996) property one may further express the nodal values of the potential Ei as a combination of Q plane waves (Laghrouche and Bettess 2002) such that

$$E = \sum_{i=1}^{n}\sum_{q=1}^{Q} A_i^q\, N_i e^{i(kx\cos\alpha_q + ky\sin\alpha_q + \varphi_q)} \quad (10)$$

where φ_q and α_q are the phase and the angle of the q[th] plane wave respectively. Now by solving the linear system resulting from the above discrete representation we get the amplitudes A_i^q of the plane waves which is the q[th] plane wave contribution at the node i.

3. Error analysis

In this paper we present results from 2 sets of studies, with the aim to check the behaviour of the proposed PUFEM for different analysis parameters, and to compare the method with FEM in the time domain for a given wave problem. The angular frequency ω of the progressive wave (being captured) was fixed (at 1). The data represented herein are solely numeric in nature, which have been used for qualitative analysis. The domain considered for analyses was (as discussed in the previous section) a unit square, with its vertices at points (1,1), (2,1), (2,2), (1,2). Linear (square) elements were used to mesh the geometry. However, the number of nodes in each direction (m), and hence the number of elements, varied for the two sets of experiments studied.

For investigation of the role of problem parameters (like step size in time) on the numerical error for the field-enriched FEM in the time domain, 4×4 elements were used, i.e. we had 5 nodes in either of the two directions (fig 1(bottom)). Three different values for the step-size in time were used, viz. Δt = 0.001, 0.005, and 0.009. The values of λ (wavelength) studied were 1/4, 1/6 and 1/9. Thus we had 3×3 = 9 cases in total. The degrees of freedom per wavelength (τ), the number of plane waves used (Q) for a given wavelength(λ) and the number of nodes in each direction (m), were related by the equation (11), however for the purpose of this study Q was also forced to be an even integer with 2 as its minimum value.

$$\tau = \lambda m\sqrt{Q} \rightarrow Q = \left(\frac{\tau}{\lambda m}\right)^2 \quad (11)$$

Thus, the values of λ,τ,Q corresponding to the three wavelengths studied were computed to be (1/4, 4.3, 12), (1/6, 4.08, 24), and (1/9, 3.04, 30) respectively. The 9 cases were run on a computer (each for a total time = 1) and figure(1) below shows a snapshot.

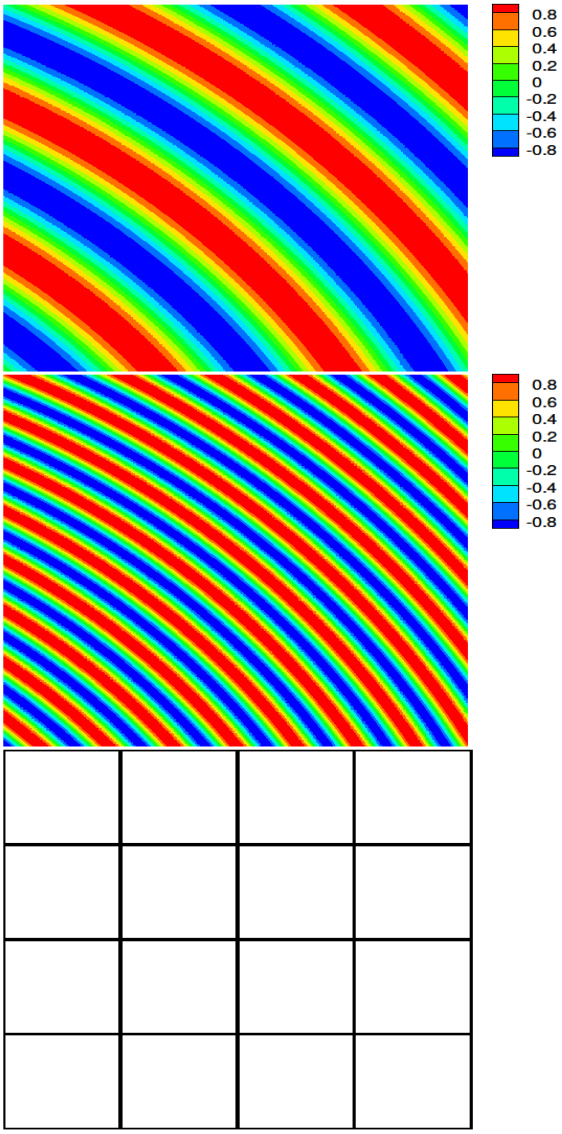

Figure 1. Real part of the numerical solution for E, for largest (top) and smallest (mid) wavelengths considered, recovered on the coarse mesh (bottom picture).

The relative errors (i.e. L^2 error percentage) obtained were plotted on a semi log graph as shown in figure 2(a). It can be observed that the error in all cases is below 2%. Also, for a given λ, a decrease in time step Δt recorded a lower error. The largest λ (blue lines) had the least number of plane waves for enrichment, and resulted in maximum error recorded (for any Δt category) as compared to that for smaller wavelengths. For any given Δt the smaller wavelengths (red and black lines) showed higher rate of increase in error for initial iterations as compared to that observed for the largest λ. For later iterations in time, the rates for all wavelengths behaved very similarly. It can be inferred that the error contributed by the step size Δt in time dominated the spatial error in the cases studied.

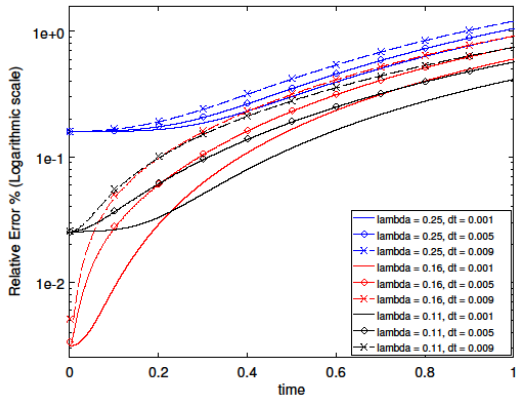

(a) Graph for parametric studies using PUFEM.

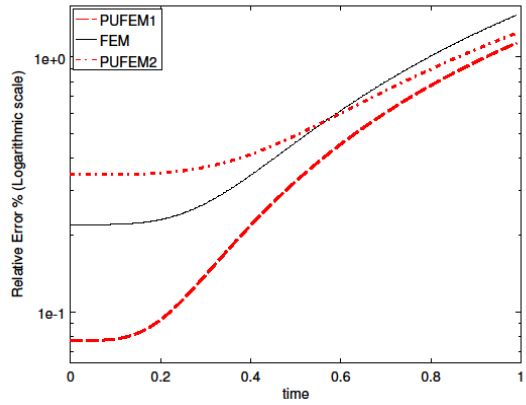

(b) PUFEM vs. FEM

Figure 2. Plots of relative errors observed in analysis.

For comparision of the suggested PUFEM with classical FEM for the given problem, a further parametric study was conducted.

Table 1. Parameters for PUFEM vs. FEM

Type	time step	λ	m	Q	T
PUFEM1	10^{-4}	$1/3$	5	10	5.27
PUFEM2	10^{-4}	$1/3$	5	8	4.71
FEM	10^{-4}	$1/3$	31	n/a	10.33

Table 1 shows the values of the parameters studied for each method. The τ for FEM was calculated as $\tau = \lambda m$. The parameters were so chosen in order to get the range of errors in both methods comparable to each other in the first few iterations, to have a fair ground for comparison. The errors were computed for 10,000 iterations in time for each method (resulting in a total time = 1). The results obtained were plotted on a semilog graph as shown in figure 2(b). In all the three cases, the error was always below 2%. For FEM (black line), the initial iterations (≈ till 4000) show rate of increase of error comparable to that of the

other two cases. However, we see a considerable hike in the later iterations. Similar hike is observed in case of PUFEM1 and PUFEM2, however, the errors are lower than that observed in FEM.

4. Conclusions

The parametric studies on the suggested PUFEM (fig. 2(a)) clearly show that for a given wavelength under test, the error in analysis increases with increasing discrete step size. This is expected as the coarser time step worsens the linear approximation of the (second order accurate) time derivative. Further, for a fixed time step (Δt), a reduction in the wavelength under study (with other parameters being constant) should have led to higher errors. However, the number of plane waves used for enrichment was increased with decreasing wavelength, in an attempt to minimize the change in τ. This led to a considerable reduction in errors due to higher enrichment. Hence, it would be fair to conclude that the error due to discretization in time contributed as the dominant part of error in the analyses with higher plane waves for enrichment. Comparison of the errors observed for PUFEM with that for FEM (fig. 2(b)), suggest that the relative errors are smaller as compared to that observed in the latter for large iterations in time. However, there is scope for further study to investigate this behaviour.

REFERENCES

Mohamed M.S., Seaid M., Trevelyan J. and Laghrouche O. (2014), An enriched finite element model with q-refinement for radiative boundary layers in glass cooling. Journal of Computational Physics, doi: http://dx.doi.org/10.1016/j.jcp.2013.11.005

Mohamed M.S., Seaid M., Trevelyan J. and Laghrouche O. (2014), Time-independent hybrid enrichment for finite element solution of transient conduction-radiation in di_usive grey media. Journal of Computational Physics, doi: http://dx.doi.org/10.1016/j.jcp.2013.05.030

Mohamed M.S., Seaid M., Trevelyan J. and Laghrouche O. (2013), A partition of unity FEM for time-dependent di_usion problems using multiple enrichment functions. International Journal for Numerical Methods in Engineering, 93: 245265. doi: 10.1002/nme.4383

Melenk JM, Babu˘ska I. The partition of unity finite element method: basic theory and applications. Computer Methods in Applied Mechanics and Engineering 1996; 139:289314.

Laghrouche O., Bettess P. and Astley R. J. (2002), Modelling of short wave di_raction problems using approximating systems of plane waves. International Journal for Numerical Methods in Engineering, 54: 15011533. doi: 10.1002/nme.478

Infrastructure and Environment Scotland 3rd Postgraduate Conference
9th December 2015
Heriot-Watt University, Edinburgh

'Modular composite beams utilizing precast slabs and a steel yielding mechanism: numerical pilot study'

Eliza Feidaki, George Vasdravellis
Institute for Infrastructure and Environment,
Heriot –Watt University
ef4@hw.ac.uk

ABSTRACT

The proposed steel composite connection utilizes precast hollow core slabs and a steel yielding mechanism to provide composite action. Apart from the standard advantages derived from the use of the hollow core units, the proposed system offers straightforward deconstruction by separating the slabs from the steel beams, easy and fast assembly on-site without the use of weld and off-site quality-controlled production of all the components. The proposed shear connection mechanism is first designed using fundamental mechanics so that it provides a predictable strength and stiffness under shear loading. A nonlinear finite element model was also constructed in Abaqus, simulating a pushout test. Comparison of the numerical solution with the simplified equations showed that the strength and stiffness of the proposed steel yielding mechanism are reasonably predicted and that the proposed shear connection has a ductile failure mode. Parametric analyses showed that increased shear resistance can be achieved by altering two geometrical characteristics of the steel yielding mechanism.

1. INTRODUCTION

1.1 Background

There is an urgent demand for sustainable development in modern societies. The UK government has set as target an 80% reduction of carbon emissions by 2050, relative to the 1990 baseline [1]. The construction sector plays an important role towards this target, since it is responsible for the 53% of the total emissions, according to the Green Construction Board [2]. The increasing need for sustainable infrastructure is backed up by major industry leaders, who recently aligned with the UK government towards that direction and signed an endorsement that the infrastructure sector should pursue lower carbon solutions [3]. In a European level, the European Union has set a number of challenging sustainability targets, starting with drastically reducing carbon emissions and resources consumption. The CEN committee CEN/TC250 "Structural Eurocodes" has already recognised that the next generation of Eurocodes need to incorporate the additional demands of modern societies, such as life extension and sustainability, as portrayed in the requirement for "*sustainable use of natural resources*" of the future European regulation for construction products [4]. Communities cannot meet these targets without reducing the life-cycle environmental cost of their building infrastructure. High sustainability standards in construction can be achieved by demountable structural systems offering the advantages of adaptability (change of building geometry) and reuse of materials and structural members at the end of the building life. In that way, construction will use less energy, produce less pollution and less waste and generally realise a responsible management of resources. This paper presents a numerical study on a proposed demountable shear connection for use in steel-concrete composite floor systems in conjunction with precast slab units.

1.2 Conventional composite floor systems

In the UK, steel-concrete composite construction has achieved an over 70% market share in the non-residential multi-storey building sector in the last twenty years, where the advantages of long spans, steel weight savings, speed of construction, increased space, service integration, improved quality and reduced environmental impact offered by this type of construction are widely recognised [5]. The composite action between the slab and the steel beam is achieved by the use of mechanical shear connectors. Current practice requires the use of headed shear studs welded to the steel beam's top flange and embedded into the concrete slab. Composite beams can be constructed with either cast-on-site or precast concrete slabs. However, in both cases the monolithic nature of current shear connection practice renders the deconstruction of a composite structure problematic, since, in practice, in order to

dismantle the composite floor system, the concrete slab has to be demolished at least around the studs. In addition, the demolition of the slab may result in damage of the welded shear connectors, further complicating the reuse of the steel beams.
An efficient composite floor system can be achieved using precast concrete hollow core slab units (HCU) acting compositely with the steel beams. HCU are precast slabs that have open cores (circular or elongated) in one direction, as the one shown in **Fig. 1**, resulting in greater depths than solid slabs and, thus, greater spans without secondary beams can be achieved.

Fig. 1 Section of a hollow core unit with elongated holes

In particular, composite beams with HCU have additional advantages over traditional composite beams: a) off site and controlled quality fabrication of all structural components; b) HCU have spans that require few or no secondary beams, therefore faster erection of the steel frame; c) a wide range of sizes of precast units is available, and custom 'tailored made' geometries can be easily fabricated; d) HCU are more durable; e) HCU may have a pre-camper to satisfy more economically the deflection checks; and f) the optimum number of shear connectors may be pre-installed on the steel beam (fewer operations on site). Furthermore, the experimental works by Lam [6, 7] showed that composite beams with HCU (see **Fig.2**) are twice as strong and three times stiffer than non-composite beams with HCU; therefore, significant weight savings can be achieved if composite action is provided. A recent case study has shown that providing composite action between the HCU and the steel frame results in 17% reduction of the total weight of the steelwork of a building and 55% reduction in the internal beam weight (more details on: *http://impact.ref.ac.uk/CaseStudies/CaseStudy.aspx?Id=31022*).

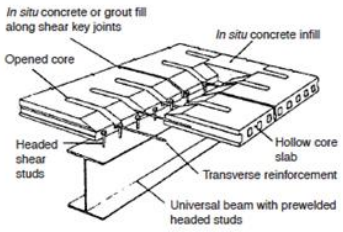

Fig. 2 Composite beam with HCU, tested in [3]

Composite beams using HCU are currently designed according to the Steel Construction Institute P401 document [9] which provides specific design guidance for this type of composite floors based on the research results and recommendations presented in [6-9]. The research findings of those works show that the transverse reinforcement size and the strength of the in situ concrete are the most critical parameters that affect the force-slip behaviour of welded studs. However, the issue of 'deconstructability' is still relevant, since the shear studs are embedded in the *in situ* concrete.

1.3 Composite beams with demountable shear connectors

The issue of 'deconstructability' of composite floors has recently emerged as a critical factor towards a more sustainable construction; however, the existing body of research is still in a developing stage. Very few works proposed alternatives to welded shear studs to achieve demountable shear connection. The research so far is limited to pushout tests using either threaded headed studs embedded into *in situ* concrete [10], or friction grip bolts in conjunction with solid precast slabs [11], relying on friction forces to resist the longitudinal shear. Only three experiments were conducted on composite beams with demountable shear connection [12]; those tests included threaded studs embedded into *in situ* composite slabs formed in a profile steel decking. Blind bolts embedded in concrete were proposed in [13]. There is no research work in the existing literature that deals with the deconstruction procedure of composite beams using HCU.

2. MODULAR COMPOSITE BEAMS WITH HCU

2.1 Description of the proposed system

The proposed steel concrete composite connection uses HCU and a steel yielding mechanism, denoted as yielding pocket (**YP**), to provide composite action. **Fig. 3** shows a plan view of a steel beam with two precast HCU. The HCU include opened cores to place transverse reinforcement for the effective connection between adjacent units. An additional edge cut out is required through the depth of the HCU and it is formed in the middle position of the unit's width and in the longitudinal direction of the steel beam, as indicated in **Fig. 3.** The purpose of this additional cut-out is the accommodation of the YP. The YP is a steel hollow section having an additional plate welded at the bottom and total length equal to the slab's depth. Additional vertical slits are opened on the sides of the YP parallel to the steel beam, i.e. in the direction of the longitudinal shear force, as shown in **Fig. 4**. The steel strips which are formed between the vertical slits resist the longitudinal shear force, as will be described later in more detail. Additional aligned slotted holes are opened on the sides of the YP parallel to the steel beam axis. A rebar passes through the aligned holes and placed in the middle open core of the HCU. This rebar serves to prevent

the slab from uplifting and the holes are slotted in order to ensure that this rebar is not involved in the shear resisting mechanism. After the placement of the HCU and the YPs, blind bolts are used to fix the YP on the steel beam. As a last step, *in situ* concrete is poured to cover the opened cores and the gaps between the YPs and the HCU. Before pouring the concrete, polythene foam is used to create a 'tooth' in the HCU, and so, to reduce the contact area between the concrete and the YP, as shown in **Fig. 4**. In this way, a ductile yielding failure of the YP is promoted instead of a brittle shear failure of the bolts that would occur if the concrete was in full-depth contact with the YP. Thus, the shear resistance is provided by bending of the YP's steel strips and vertical walls that are perpendicular to the direction of the steel beam.

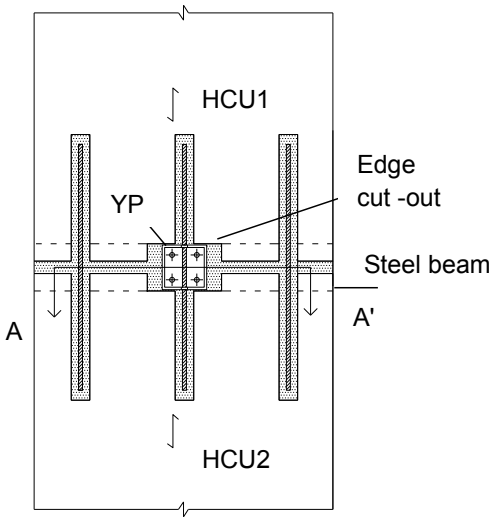

Fig.3 Plan view of the proposed connection

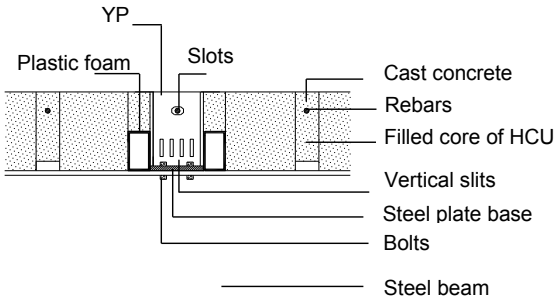

Fig.4 Section AA' of the proposed connection

The construction procedure consists of the following steps: a) The HCU are positioned on the steel beams; b) the YPs are placed on the appropriate positions; c) blind bolts are used to fix the YPs on the flanges of the steel beams with a single sided operation; and d) *in situ* concrete is poured to fill the open cores with the rebars and the gaps around the YPs. The deconstruction procedure consists of the following steps: a) The bolts are removed with a single sided operation b) the concrete around the pocket is removed and the rebars passing through the YPs are cut; c) the YPs are pulled out; and d) the HCU are removed and all components are ready to be reused.

2.2 Mechanics of the proposed system

The strength of the YP is the result of two mechanisms: a) the in-plane bending of the steel strips; and b) the bending of the YP's walls transverse to the beam direction.

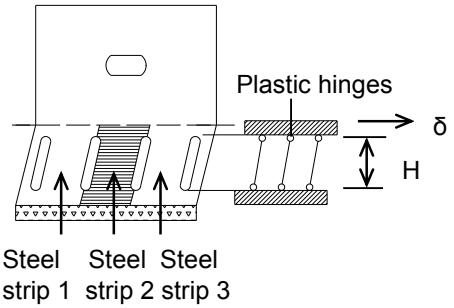

Fig.5 Deformed shape of the YP

The deformed shape of the YP is shown in **Fig. 5**. The YP is deformed under displacement imposed by the concrete 'tooth'. The dashed line in **Fig. 5** represents the bottom fibre of the concrete 'tooth'. Simple hand calculations derived from plastic beam analysis are used to predict the structural behaviour of the YP. Fully fixed boundary conditions are assumed for the end supports of the steel strips and the vertical walls as indicated in **Fig.5**. **Fig. 6** shows the geometrical characteristics of the YP.

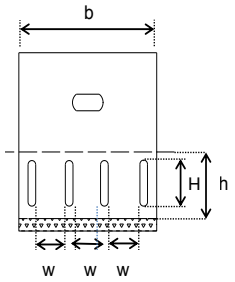

Fig. 6 Geometrical characteristics of the YP

Plastic hinges are expected to develop at the ends of the steel strips and at the ends of the vertical walls. The plastic moment resistance of a rectangular cross section is calculated using the equation:

$$M_{p,strip} = f_y \frac{t\, w^2}{4} \qquad \textbf{(1)}$$

where f_y is the yield strength of the YP's material, t and w are the thickness and the width of the steel strip respectively. Based on plastic analysis principles, the shear strength provided by the steel strips is given by:

$$F_{p,strips} = \frac{2\, M_{p,strip}}{H}\, n \qquad \textbf{(2)}$$

where H is the assumed height of the steel strips and n is the total number of the YP's steel strips. Accordingly, the plastic moment resistance of the vertical walls of the YP is given by:

$$M_{p,wall} = \frac{f_y t^2 b}{4} \quad \textbf{(3)}$$

where b is the transverse width of the YP. The strength provided by the walls is given by:

$$F_{p,walls} = \frac{2M_{p,wall}}{h} * 2 \quad \textbf{(4)}$$

where h is the height of the vertical walls. Thus, the total shear resistance provided by the YP is given by:

$$F_P = F_{p,strips} + F_{p,walls} \quad \textbf{(5)}$$

The stiffness of the YP is the sum of the stiffness of the steel strips and the YP's vertical walls:

$$k = \frac{12\,E\,I_{strips}}{H^3} n + \frac{12\,E\,I_{walls}}{h^3} * 2 \quad \textbf{(6)}$$

where I_{strips} and I_{walls} are the second moments of areas for the steel strips and the walls respectively. Since the stiffness of the vertical walls is different from the stiffness of the steel strips the final load-slip curve is a tri-linear curve. Capacity design rules are applied in order to ensure that the bolts and the steel plate base of the YP remain elastic. The concrete slab is checked in compression. The shear strength of the bolts and the bearing resistance of the connected plates at the bolt holes are also checked.

3. PILOT FINITE ELEMENT ANALYSIS

Pilot numerical analysis based on the finite element method (**FEM**) was conducted to prove the conceptual basis of the proposed shear connection mechanism. The strength and the stiffness of the YP are predicted by creating a numerical model for push out test using the Abaqus software [16].

3.1 Materials, geometry, boundary conditions and loading

The numerical model for the push out test is shown in **Fig.7**. One half of the steel beam is modelled. The 'tooth' is formed in the middle of the slab's depth. Concrete slab of 40Mpa strength and 200mm depth is used taking into account bilinear compressive strain-stress behaviour. Concrete damage plasticity parameters are considered. A steel hollow section of SHS180x8 series is used for the YP.

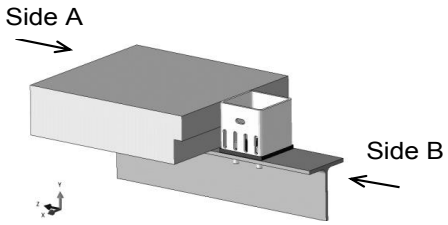

Fig. 7 Numerical model of push out test

Each YP includes three vertical slits on each side parallel to the axis of the steel beam. The thickness of the steel plate welded at the bottom of the YP is 15mm. A steel beam of IPE450 series is utilized for the pilot study. Four bolts of 20mm diameter and grade 8.8 are used to model the blind bolts. The steel grade is S355 for all the steel parts of the connection apart from the bolts. The hardening part of the steel material is taken into account according to the prediction proposed by Gattesco [15]. Fully fixed boundary conditions are assigned to the right end of the steel beam at the 'Side B', as shown in **Fig. 8**. Symmetry boundary conditions are assigned to the web of the half steel beam. The uplifting of the concrete slab is restricted along the axis Y'Y. The slab is also restrained along the X'X axis. Five contact pairs are defined: 1) concrete slab and steel beam; 2) concrete slab and YP; 3) steel beam and YP's steel plate base; 4) bolts and steel plate base; and 5) bolts and steel beam. Hard contact and penalty friction formulation are used to describe the normal and the tangential behaviour of each contact pair. The friction coefficient is assumed 0.45 for all the contact pairs. The finite sliding formulation with surface to surface discretization is applied for all the contact pairs apart from the contact surface between the concrete slab and the steel section, where the node-to-surface discretization is employed. The surface smoothing technique is used for the circular contact surface between the bolts, the YP and the steel beam to ensure analysis convergence. Tie constrains are enforced between the bottom base of the YP and the steel plate base, simulating the welding. Three dimensional 8-node linear brick elements with reduced integration (C3D8R) are used for all the component parts of the connection. A coarse mesh of 35mm is adopted for the concrete slab and the steel beam. A refined mesh of 7mm is adopted for the region of the steel beam near the drilled holes. A refined mesh of 5-10mm is utilized for the YP and the steel plate base. Uniform distributed displacement is applied at the 'Side A' of the concrete slab, as shown in **Fig. 7**. Two steps of analysis are created. The first step includes only the contact interaction to avoid numerical problems. The displacement is applied during the second step of the analysis. The general static procedure is used.

3.2 Results

The load-slip curve of the push out specimen denoted as M1 is extracted from the Abaqus software and comparisons are drawn between the model and the analytical predictions using **Eq. (1)-(6).** The load-slip curve of a 19mm diameter headed stud obtained from previously conducted push out tests [14] is superimposed to the previously obtained load-slip curves. **Table 1** shows the geometrical characteristics of the YP modelled. **Fig. 8** and **Fig. 9** show the contour plot of the equivalent plastic strain and the load-slip curves for the model M1 respectively. Plastic strains concentration occurs at the ends of the steel strips and at the ends of the YP's walls transverse to the beam direction as shown in **Fig. 8** and confirms the assumption of fixed ends in the steel strips. The steel plate base and the bolts remain elastic. The results show that the strength and the stiffness of the YP can be reasonably predicted by the simplified equations and that the load-slip curve has comparable stiffness to that of a welded headed stud as shown in **Fig.9**.

Table 1 Geometrical characteristics of the YP modelled

Strip height H [mm]	Strip width w [mm]	YP's width b [mm]	Wall height h [mm]	YP's thickness t [mm]
75	36	180	85	8

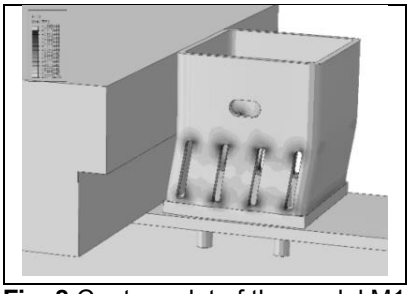

Fig. 8 Contour plot of the model M1

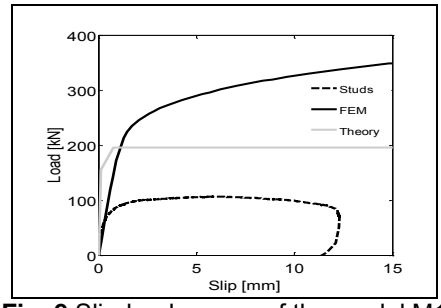

Fig. 9 Slip-load curves of the model M1

4. PARAMETRIC STUDIES

Parametric studies are carried out using the numerical model. The parameters varied are the width and the height of the YP's steel strips. The geometrical characteristics of the YP varied in each numerical model are arranged in two groups denoted as G1 and G2 in **Table 2**. The load-slip curves for the push out specimens are shown in **Fig. 10** and **Fig. 11** for the group G1 and G2 respectively. The yielding strength of the YP derived from **Eq. (5)** and the one obtained from the FEM analysis are given in **Table 3**. The ratio $F_{p,theory}/F_{p,FEM}$ is provided. The parametric curves show that increased shear resistance is achieved by altering the width and the height of the YP's steel strips. The maximum value for the shear resistance can be realized provided that the bolts and the steel plate base remain elastic.

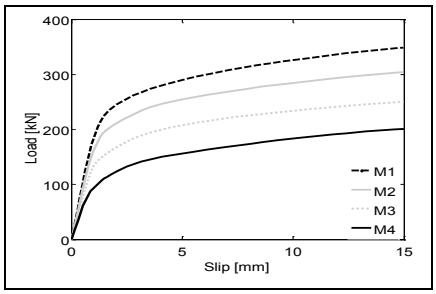

Fig. 10 Slip-load curves of group G1

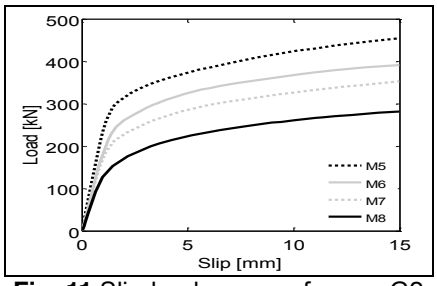

Fig. 11 Slip-load curves of group G2

Table 2 Geometrical characteristics of the YP for parametric studies

Group	Model	Strip height H [mm]	Strip width w [mm]
G1	M1	75	36
	M2	75	31
	M3	75	25
	M4	75	17.3
G2	M5	55	36
	M6	55	31
	M7	55	25
	M8	55	17.3

A more careful assumption of the strips' height should probably be considered to account for the low ratios shown in **Table 3**. Another probable explanation for the divergence between theoretical and FEM solutions is the contribution of the YP's curved corners to the strength mechanism. The simplified equations neglect the corners of the YP resulting in a decrease of the plastic force compared to the one obtained from the FEM analysis.

Table 3 Comparisons of YP's strength between FEM and simplified equations

Model	$F_{p,theory}$ [kN]	$F_{p,FEM}$ [kN]	$F_{p,theory}/F_{p,FEM}$
M1	195.35	250	0.78
M2	157.30	235	0.67
M3	119.10	190	0.63
M4	82.24	130	0.63
M5	263.70	325	0.81
M6	211.80	300	0.71
M7	159.75	250	0.64
M8	109.50	195	0.56

5. CONCLUSIONS AND FUTURE WORK

A novel demountable shear connection is proposed for composite floor systems utilising precast hollow-core slab units. The structural behaviour of the proposed mechanism is predicted by simple mechanics equations and a pilot numerical study is conducted based on a nonlinear finite element model. The following conclusions are drawn:

- The finite element model constructed to simulate a pushout test using the proposed structural typology has shown that the intended ductile behaviour of the yielding pocket can be achieved.
- Capacity design rules ensure that the yielding pocket is the only damaged component, while the rest of the parts involved in the shear resisting mechanism remain elastic.
- The numerical pilot study has shown that the load-slip behaviour of the novel demountable shear connection mechanism is conservatively predicted using the simplified equations derived from fundamental mechanics principles.
- The numerical pilot study has shown that the proposed shear connection satisfies the requirements of Eurocode 4 in terms of strength and ductility.

Future work includes pushout experimental tests to study the physical behaviour of the proposed shear connection mechanism, full-scale beam tests on composite beams using the proposed typology, and life cycle analysis of buildings employing a 'design for deconstruction' concept.

REFERENCES

1.Infrastructure Carbon Review. Available from: <https://www.gov.uk/government/publications/infrastructure-carbon-review>. (15 Oct.2015)

2. The Green Construction Board. Available from: <http://www.greenconstructionboard.org/>. (15 Oct.2015)

3.Infrastructure Cost Review: main report.Available from:<https://www.gov.uk/government/publications/infrastructure-cost-review>. (15 Oct.2015)

4. Establishing Enviromental Sudtainability Thresholds and Indicators. Available from:<http://ec.europa.eu/environment/enveco/waste/>. (15 Oct.2015)

5.Multi-storey office buildings. Available from:<http://www.steelconstruction.info/Multi-storey_office_buildings>. (25 Oct.2015)

6. Lam D., Elliott K.S., Nethercot D.A.(2000). Experiments on composite steel beams with precast concrete hollow core floor slabs. Proc. Inst. Civ. Eng., Structures and Buildings,140:127–38.

7. Lam, D. (2007). Capacities of headed stud shear connectors in composite steel beams with precast hollowcore slabs. J. Const. Steel Res., 63(9):1160–1174.

8. Lam D., Elliott K.S., Nethercot D.A. (2000). Designing composite steel beams with precast concrete hollow core slabs. Proc. Inst. Civ. Eng., Structures and Buildings,140:139–49.

9. G.H. Couchman (2014). Design of composite beams using precast concrete slabs in accordance with Eurocode 4 . SCI Publication P401.

10. Dai X.D.,Lam D.,Saveri E.(2015).Effect of concrete strength and stud collar size to shear capacity of demountabe shear connectors. , J. Struct. Eng.141(11):04015025-1-04015025-10

11. Liu, X., Bradford, M.A., Lee, S.S.M.(2014). Behaviour of high strength friction grip bolted shear connectors in sustainable composite beams. J. Struct.Eng.,141(6):04014149-1-04014149-12

12. Moynihan, M., Allwood, J.M. (2014). Viability and performance of demountable composite connectors. J. Constr. Steel Res., 99:47-56

13. Pathirana, I.S.W., Mirza, O., Uy, B., Zhu, X.Q. (2012). Experimental study on the behaviour of steel concrete composite beams utilizing innovative blind bolts. Proc.of the 10thInt. Conf. on Advances in Steel Concrete Composite and Hybrid Structures, Singapore.

14. Vasdravellis,G., Uy, B.,Tan,E.I., Kirkland, B.(2015).Behaviour and design of composite beam subjected to sagging bending and axial compression. J. Constr. Res.110:29-39

15. Gattesco, N. (1999). Analytical modelling of nonlinear behavior of composite beams with deformable connection. J. Constr. Steel Res., 52(2): 195-218.

16. ABAQUS 6.14(2014).Analysis User's guide. DS SIMULIA Corp. Velizy Villacoublay. France

Infrastructure and Environment Scotland 3rd Postgraduate Conference
9th December 2015
Heriot-Watt University, Edinburgh

An investigation of the accuracy of the partition of unity method for time dependent heat transfer problems

M. Iqbal[1,*], H. Gimperlein[2,3], M. S. Mohamed[1], O. Laghrouche[1]
[1]Institute for Infrastructure and Environment, Heriot Watt University
[2]Maxwell Institute for Mathematical Sciences and Department of Mathematics, Heriot Watt University
[3]Institute for Mathematics, University of Paderborn, Warburger Str. 100, 33098 Paderborn, Germany
[*](Email: mi130@hw.ac.uk)

ABSTRACT

This paper investigates the accuracy of the partition of unity method (PUM) for the solution of time dependent heat transfer problems. We propose a mathematically rigorous, computable error estimate and test the accuracy of PUM against this error estimate. It is shown that the proposed error estimate provides reliable and practically useful upper bounds for the numerical errors, independent of the heuristically chosen enrichment functions. We considered two model problems to test the method. First we considered a problem for which we know the exact mathematical solution. For the second case a problem is considered for which the exact solution is not known. We use different number of time steps to capture the results, and it is confirmed that at every time step the actual error in the solution is bounded by the error estimates.

1. INTRODUCTION

In recent years various generalized and meshless numerical methods have been introduced to solve complex engineering problems with ease and suffcient accuracy. One of the important subclass of these methods is the Partition of Unity Method PUM. This method was introduced by Melenk and Babuska [1], who developed the mathematical background of this method. They showed how the partition of unity finite element method can be used to employ the structure of the differential equation under consideration to construct effective and robust methods.

PUM used coarse meshes and incorporates special functions into the finite element space to approximate the solution. These special functions are called enrichment functions and are chosen based on an approximate analytical solution of the problem. To a great extent the effectiveness of the PUM depends on the proper selection of enrichment functions. Strouboulis *et al.* [2] showed that the choice of enrichment function affects the solution of the problem. The fact that PUM uses coarse meshes to approximate the finite element solution of complex problems, it is necessary to address the accuracy and reliability of this method.

PUM has found applications in wide variety of applications. This method is effectively used to solve engineering problems both in solid and fluid mechanics. Munts *et al.* [5] investigated the effectiveness of PUM for convection-diffusion problems. O'Hara *et al.* [3] used it for transient analysis of sharp thermal gradients. They used global-local enrichment functions to problems of transient heat transfer involving localized features. Laghrouche and Mohamed [4] used it for solving the Helmholtz equation in two dimensions. They constructed oscillatory shape functions as the product of polynomial shape functions and either Bessel functions or planer waves. In their work they dealt with the diffraction of an incident plane wave by a rigid circular cylinder. Duarte and Kim [6] used PUM for accurately modeling a crack using enrichment functions from the asymptotic expansion of the elasticity in the neighborhood of the crack. Mohamed *et al.* [7] used PUM for the solution of time dependent diffusion problems. They used multiple enrichment function to obtain the results. In their work they compared the results of both finite element method and PUM and concluded that in general the PUM shows higher accuracy than the conventional FEM for a fixed number of degrees of freedom. They showed that PUM requires less computational resources for the time-dependent diffusion problems than the standard FEM. A full description of previous work can be found in their work.

In our present work we define mathematically rigorous, computable error estimates. We use PUM to solve time-dependent diffusion problem and compare the actual errors in the solution the error estimates. For an acceptable numerical solution, the actual errors in the solution should be less than the error estimates. We define the governing PDE for transient diffusion problem with appropriate initial and boundary conditions and its transformation to weak form in the next section. In

Section 3, we define the error estimates followed by results of numerical analyses in Section 4. Some concluding remarks are presented in Section 5.

2. PROBLEM FORMULATION AND NUMERICAL APPROXIMATION

Given an open domain $\Omega \subset \mathbb{R}^2$ with boundary Γ and given time interval]0,T], we consider the following transient diffusion equation

$$\frac{\partial u}{\partial t} - \lambda \Delta u = f(t, \boldsymbol{x}), \quad (t, \boldsymbol{x}) \in]0, T] \, x \, \Omega \tag{1}$$

Where $\boldsymbol{x} = (x, y)^T$ are the spatial coordinates, u is the temperature, t is the time variable, $\lambda > 0$ is the diffusion coefficient and the right hand side $f(t, \boldsymbol{x})$ represents the effect of internal sources/sinks. We consider an initial condition

$$u(t = 0, \boldsymbol{x}) = u_0(\boldsymbol{x}), \quad (\boldsymbol{x} \in \Omega) \tag{2}$$

where $u_0(\boldsymbol{x})$ is a prescribed initial field. We impose Robin type boundary condition

$$\frac{\partial u}{\partial \boldsymbol{n}} + hu = g(t, \boldsymbol{x}), \quad (t, \boldsymbol{x}) \in]0, T] \, x \, \Gamma \tag{3}$$

here $\boldsymbol{n}$ denotes the outward normal on the boundary Γ, $h \geq 0$ is the convection heat transfer coefficient and g represents a given boundary function.

To solve equation (1)-(3) numerically, we divide the time interval into N_t subintervals $[t_n, t_{n+1}]$ with duration $\Delta t = t_{n+1} - t_n$ for $n = 0, 1, 2, \ldots N_t$. We discretize equation (1) in time using an implicit scheme.

$$\frac{u^{n+1} - u^n}{\delta t} - \lambda \Delta u^{n+1} = f(t_{n+1}, \boldsymbol{x}) \tag{4}$$

rearranging gives

$$-\Delta u^{n+1} + k u^{n+1} = F \tag{5}$$

where

$$F = k(\delta f(t_{n+1}, \boldsymbol{x}) + u^n), \quad k = \frac{1}{\lambda \delta t}$$

To solve equation (5) with the finite element method we first multiply the equation with a smooth test function, W, and then integrate over Ω

$$-\int_\Omega W \, \Delta u^{n+1} d\Omega + \int_\Omega W \, k u^{n+1} d\Omega = \int_\Omega W \, F d\Omega \tag{6}$$

Now suppose we have a function, S, such that

$$S = W \nabla u^{n+1} = \begin{pmatrix} W \frac{\partial u^{n+1}}{\partial x} \\ W \frac{\partial u^{n+1}}{\partial y} \end{pmatrix} \tag{7}$$

Taking divergence of the function S and applying the divergence theorem, we get

$$\int_\Omega (\nabla W . \nabla u^{n+1} + \mathrm{W} k u^{n+1}) d\Omega - \int_\Gamma W \nabla u^{n+1} . n \, d\Gamma = \int_\Omega W F \, d\Omega \tag{8}$$

Substituting the boundary conditions and rearranging, we get

$$\int_\Omega (\nabla W . \nabla u^{n+1} + W k u^{n+1}) d\Omega + \int_\Gamma W (k u^{n+1} - g) \, d\Gamma = \int_\Omega W F \, d\Omega \tag{9}$$

Our aim is to find an approximate solution of the weak form (9) using PUM. To do so, the temperature u over each element is approximated as

$$\mathrm{u} = \sum_{j=1}^{M} \sum_{\mathrm{q}=1}^{Q} A_j^q \, N_j(\boldsymbol{x}) \, G_q(\boldsymbol{x}) \tag{10}$$

Here $A_j^q \in \mathbb{R}$, and N_j are the piecewise polynomial shape functions. As in [7], we use the following global enrichment functions

$$G_q(\boldsymbol{x}) = \frac{e^{-\left(\frac{R_0}{C}\right)^q} - e^{-\left(\frac{R_c}{C}\right)^q}}{1 - e^{-\left(\frac{R_c}{C}\right)^q}}, \quad q = 1, 2, 3, \ldots . Q \tag{11}$$

with $R_0 := |\boldsymbol{x} - \boldsymbol{x_c}|$ being the distance from the function control point $\boldsymbol{x_c}$= (1,1) to the point $\boldsymbol{x}$. The constants $R_c = \sqrt{\frac{14}{1.195}}$ and $C = \sqrt{\frac{1}{1.195}}$ control the shape of the exponential function, G_q. Alturi and Zhu [8] also used an enrichment function similar to (12) with $q = 2$ as a weight function in the context of meshless methods for solving the linear Poisson equation. Similar functions are used when $q = 1$ in [5, 9] and $q = 2$ in [3, 10].

For simplicity we write the product of the enrichment function G_q with the polynomial shape function N_j as

$$P_{(j-1)q+Q} = N_j G_q \tag{12}$$

The derivatives of the new shape function are given as

$$\frac{\partial P_{(j-1)q+Q}}{\partial x} = G_q \frac{\partial N_j}{\partial x} - N_j(x - x_c)\frac{q}{C^q}\frac{e^{-\left(\frac{R_0}{C}\right)^q}}{1 - e^{-\left(\frac{R_c}{C}\right)^q}} R_0^{(q-2)}$$

and

$$\frac{\partial P_{(j-1)q+Q}}{\partial y} = G_q \frac{\partial N_j}{\partial y} - N_j(y - y_c)\frac{q}{C^q}\frac{e^{-(\frac{R_0}{C})^q}}{1 - e^{-(\frac{R_c}{C})^q}} R_0^{(q-2)}$$

The second derivatives of the new shape function are given as

$$\frac{\partial^2 P_{(j-1)q+Q}}{\partial x^2} = [-2\frac{\partial N_j}{\partial x}(x - x_c)\frac{q}{C^q}\frac{e^{-\left(\frac{R_0}{C}\right)^q}}{1 - e^{-\left(\frac{R_c}{C}\right)^q}} R_0^{(q-2)}$$
$$+N_j \frac{q}{C^q}\frac{e^{-\left(\frac{R_0}{C}\right)^q}}{1 - e^{-\left(\frac{R_c}{C}\right)^q}}(1 - \frac{q}{C^q}R_0^{(q-2)}(x - x_c)^2$$
$$+\frac{q-2}{R_0^2}(x - x_c)^2]$$

and

$$\frac{\partial^2 P_{(j-1)q+Q}}{\partial y^2} = [-2\frac{\partial N_j}{\partial y}(y - y_c)\frac{q}{C^q}\frac{e^{-\left(\frac{R_0}{C}\right)^q}}{1 - e^{-\left(\frac{R_c}{C}\right)^q}} R_0^{(q-2)}$$
$$+N_j \frac{q}{C^q}\frac{e^{-\left(\frac{R_0}{C}\right)^q}}{1 - e^{-\left(\frac{R_c}{C}\right)^q}}(1 - \frac{q}{C^q}R_0^{(q-2)}(y - y_c)^2$$
$$+\frac{q-2}{R_0^2}(y - y_c)^2]$$

3. DEFINITION OF ERROR ESTIMATES

In this section we define the error estimate for the method. We will then compare the results obtained by the PUM to the error estimate.

Let us define

$$u(\boldsymbol{x}, t) = \frac{t - t_n}{t_{n+1} - t_n} u^{n+1}(\boldsymbol{x}) + \frac{t_{n+1} - t}{t_{n+1} - t_n} u^n(\boldsymbol{x})$$

and

$$\hat{u}(\boldsymbol{x}, t) = u(\boldsymbol{x}, t_{n+1}), \dot{\hat{I}}(\boldsymbol{x}, t) = f(\boldsymbol{x}, t_{n+1}), t \in [t_n, t_{n+1}]$$

Let u and U be the numerical and exact solution respectively of the equation (1), with

$$U(0, \boldsymbol{x}) = U_0(\boldsymbol{x}) \text{ and } U|_\Omega = 0$$

then

$$\int_\Omega |U(t_{(n+1)}, \boldsymbol{x}) - u(t_{(n+1)}, \boldsymbol{x})|^2 dx +$$
$$\lambda \int_{t_n}^{t_{n+1}} \int_\Omega |\nabla(U - u)|^2 d\boldsymbol{x}\, dt \le \eta_2^2 + \eta_4^2 + \eta_5^2 \qquad (13)$$

where

$$\eta_2^2 = \int_{t_n}^{t_{n+1}} ||f - \partial_t u - \Delta u||^2_{H^{-1}(\Omega)}$$
$$\le \int_{t_n}^{t_{n+1}} dt \int_\Delta (f - \partial_t u - \Delta u)^2 \, d\Omega$$
$$\cong \int_\Delta (f^{n+1} - \frac{u^{n+1} - u^n}{\delta t} - (\frac{\partial^2 u^{n+1}}{\partial x^2} + \frac{\partial^2 u^{n+1}}{\partial y^2}))^2 \frac{\delta t}{2} d\Omega$$
$$+ \int_\Delta (f^n - \frac{u^{n+1} - u^n}{\delta t} - (\frac{\partial^2 u^n}{\partial x^2} + \frac{\partial^2 u^n}{\partial y^2}))^2 \frac{\delta t}{2} d\Omega \qquad (14)$$

and

$$\eta_4^2 = \int_{t_n}^{t_{n+1}} ||\nabla(u - \hat{u}||^2_{L^2(\Omega)}$$
$$= \int_{t_n}^{t_{n+1}} \left(\frac{t_{n+1} - t}{t_{n+1} - t_n}\right)^2 dt \int_\Delta [\,(\frac{\partial u^{n+1}}{\partial x} - \frac{\partial u^n}{\partial x})^2 +$$
$$(\frac{\partial u^{n+1}}{\partial y} - \frac{\partial u^n}{\partial y})^2 \, d\Omega$$

Simplifying

$$= \frac{(t_{n+1} - t_n)}{3} \int_\Delta [\,(\frac{\partial u^{n+1}}{\partial x} - \frac{\partial u^n}{\partial x})^2 +$$
$$(\frac{\partial u^{n+1}}{\partial x} - \frac{\partial u^n}{\partial x})^2] \, d\Omega \qquad (15)$$

$$\eta_5^2 = \sum_{\text{edges}} \int_{t_n}^{t_{n+1}} ||\frac{\partial \hat{u}}{\partial \boldsymbol{n}}||^2_{L^2(E)}$$
$$= \sum_{\text{edges}} \int_{t_n}^{t_{n+1}} ||\nabla u^{n+1}.\boldsymbol{n}\,||^2_{L^2(E)}$$
$$= \sum_{\text{edges}} \int_{t_n}^{t_{n+1}} dt \int_E [\left(\frac{\partial u^{n+1}}{\partial x}\, n1_x + \frac{\partial u^{n+1}}{\partial y}\, n1_y\right)_{E_1}$$
$$-\left(\frac{\partial u^n}{\partial x}\, n1_x \frac{\partial u^n}{\partial y}\, n1_y\right)_{E_2}] \, dE \qquad (16)$$

We will calculate the quantities defined in (13), and will then compare it with the error terms η_2^2 , η_4^2 and η_5^2. The left hand side of (13) quantifies the actual error in the numerical solution compared to the exact solution and the right hand side calculates the error indicator consisting of three terms $\eta_{2,}^2$ η_4^2 and η_5^2. As defined by (13), the actual error in the solution should be less than or equal to the error indicator.

4. NUMERICAL ANALYSIS

Numerical results of the PUM for the proposed problem are presented here. We consider a square domain $\Omega = [0,2]\,\mathrm{x}\,[0,2]$ with heat diffusion coefficient $\lambda = 0.1\ kg\ m/C^0 s^2$ and convection heat transfer coefficient $h = 1\ kg/C^0 s^2$. We find numerical solution to heat transfer problem (1) - (3) with reaction term $f(t, \boldsymbol{x})$, the boundary function g.

For numerical analyses we choose square mesh with all integrals over Ω evaluated using Gauss-Legendre quadrature with 22 integration points.

To quantify the error for different model problems, we compute the relative error between the exact solution U and its PUM approximation u, defined as the square root of

$$\frac{\int_\Omega |U-u|^2 d\Omega + \lambda \int_{t_n}^{t_{n+1}} \int_\Omega |\nabla(U-u)|^2 d\Omega\, dt}{\int_\Omega |U|^2 d\Omega + \lambda \int_{t_n}^{t_{n+1}} \int_\Omega |\nabla U|^2 d\Omega\, dt} \qquad (17)$$

And the corresponding relative error indicator is defined as the square root of

$$\frac{\eta_2^2 + \eta_4^2 + \eta_5^2}{\int_\Omega |U|^2 d\Omega + \lambda \int_{t_n}^{t_{n+1}} \int_\Omega |\nabla U|^2 d\Omega\, dt} \qquad (18)$$

For the case where the exact solution U is not known, we use a reference FEM solution with very fine mesh instead.

4.1 Model Problem 1

For model problem 1 we select a problem for which the exact solution U is known. We solve the heat transfer problem (1) - (3) with reaction term $f(t, \boldsymbol{x})$, the boundary function g and the initial condition $u_0(\boldsymbol{x})$ chosen such that the exact solution is given by

$$U = x^{20} y^{20} (2-x)^{20} (2-y)^{20} (1 - e^{-\lambda t}) \qquad (19)$$

We use a coarse spatial mesh of 25 elements and vary the number of enrichment functions $Q = 2,3,,,6$. To quantify the error in the solution, we compute the actual error of the PUM solution and the error indicator as defined by (17) and (18) respectively. Figures 1(a)-1(c) show the comparison of these quantities for different number of enrichment functions Q and time steps δt at times $t = 0.1$ and $1\ s$. The number of enrichment functions Q are plotted on abscissa and the relative error, relative error indicator on the ordinate, both on logarithmic scale.

In all the cases the actual error of PUM solution is less than the error indicators. The error in solution decreases as we increase the number of enrichment functions. The error indicators also show similar decreasing pattern with the increase of enrichment functions and effectively capture the behaviour of numerical error in the solution.

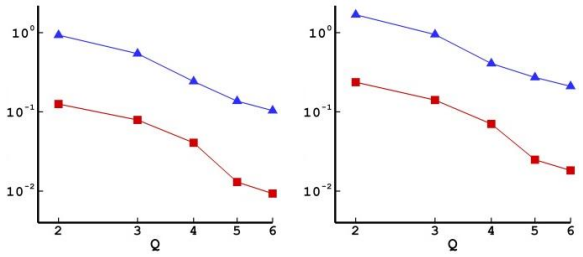

(a) (b)

Figure 1(a). Comparison of relative error (red line) and relative error estimate (blue line) at (a) 10th time step, (b) 100th time step for $\delta t = 0.0001\ s$

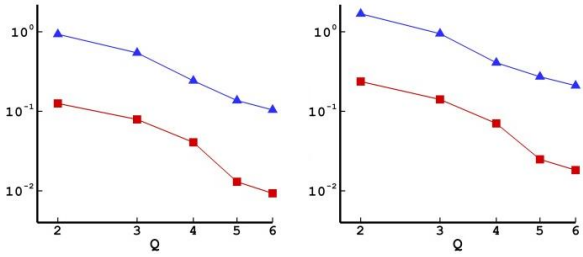

Figure 1(b). Comparison of relative error (red line) and relative error estimate (blue line) at (a) 10th time step, (b) 100th time step for $\delta t = 0.001\ s$

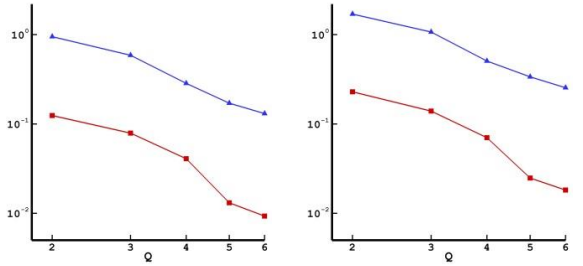

Figure 1(c). Comparison of relative error (red line) and relative error estimate (blue line) at (a) 10th time step, (b) 100th time step for $\delta t = 0.01\ s$

4.2 Model Problem 2

The model problem 2 considers a square domain with a heat source in the centre of domain as shown in figure 2. The source dissipates heat at two different rates. The centre part $x, y \in [0.8, 1.2]$ dissipates at constant rate $f = 200\ C^0/s$ and outside it f decreases linearly from $200\ C^0/s$ to 0 where either x, y is one of $\in [0.4, 1.6]$.

As the exact solution is not known in model problem 2, we only calculate the relative error indicator. As defined by (18), the exact solution U is replaced with a reference FEM solution on a very fine mesh of 12800 triangular elements. Both the PUM and FEM meshes are shown in figure 3.

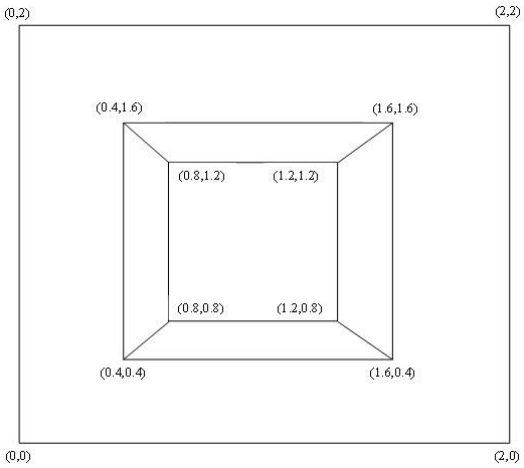

Figure 2. Domain configuration for model problem 2 with heat source in the centre.

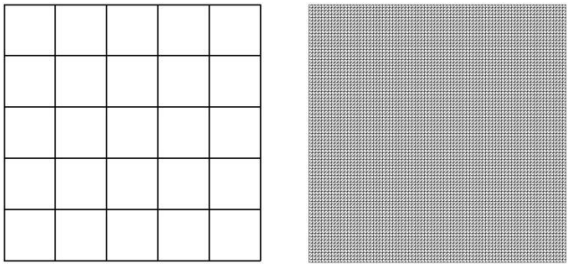

(a) PUM mesh (b) FEM mesh

Figure 3. Meshes used for the computations

Figures 4 (a) – (c) show the relative error indicator as a function of number of enrichment functions Q. Results are shown at $t = 0.01, 0.05$ and $0.1\ s$ using different values of time steps $\delta t = 0.001, 0.0001$ and $0.00001\ s$. The results show a decrease in the values of error indicator as we increase the number of enrichment functions. At early times results show similar trends for values of all values of δt (Figure 4(a)). At later time steps values decrease when we increase the number of Q from 2 to 4 but then increase when we further increase Q to 5 and 6. This can be clearly seen in Figure 4(c) specially for the smallest value of $\delta t = 0.00001\ s$. This is because the conditioning number of the system matrix deteriorates as we increase the number of enrichment functions. For $\delta t = 0.00001\ s$, the conditioning number increases from 1.5E+5 for $Q = 2$ to 2.0E+13 for $Q = 6$.

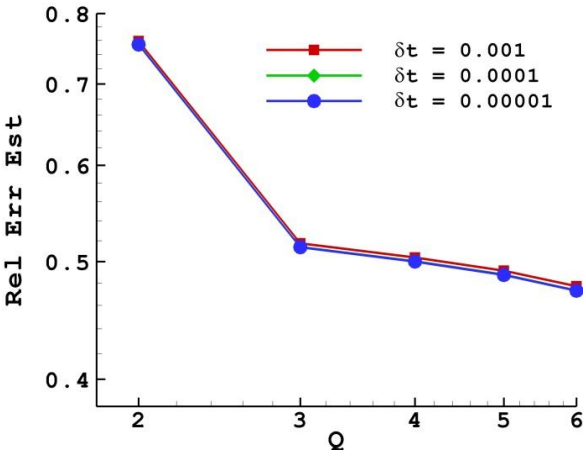

Figure 4(a). Relative error indicator at $t = 0.01\ s$

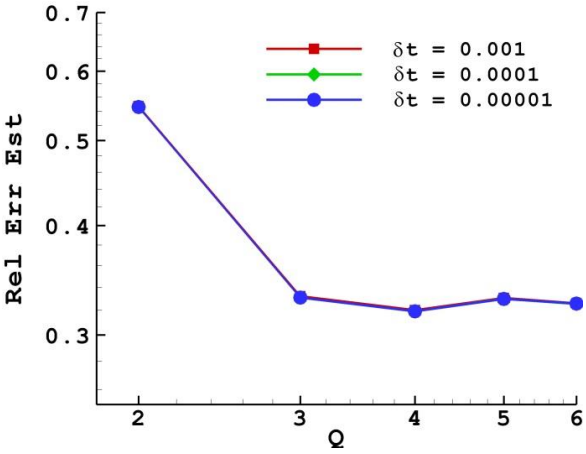

Figure 4(b). Relative error indicator at $t = 0.05\ s$

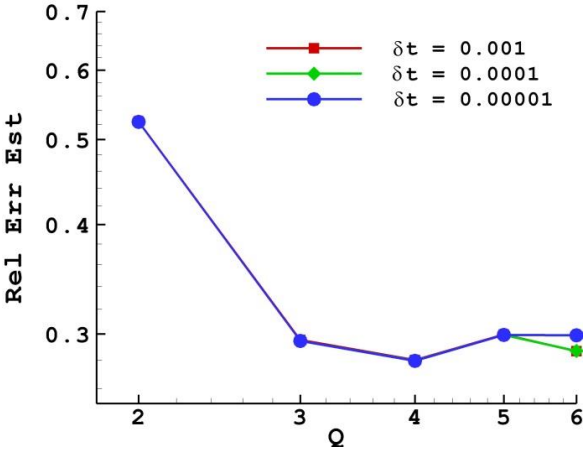

Figure 4(c). Relative error indicator at $t = 0.1\ s$

5. CONCLUSIONS

In this paper, we used the PUM to solve the time dependent heat diffusion equation. We calculated

the errors in the solution and its derivatives for the PUFEM. We defined an error estimate and compared the actual error in the method with the defined error estimate. We used different number of enrichment functions and showed their effect on the solution. Based on the analysis, we can draw the following conclusions:

- Results of the actual error are well below the defined error estimate and both show similar decrease with increasing number of enrichment functions.
- The proposed error estimates do not depend on the choice of enrichment function. These estimates are easy to implement and effectively reflect the behaviour of numerical error.
- The error indicators also reflect the errors incurred in the poorly conditioned systems.
- Increasing the number of enrichment functions produce better results but the enrichment functions can be increase only up to certain limit after which the system becomes ill-conditioned.

6. REFERENCES

[1] Melenk, J. M. & Babuška, I. (1996). The partition of unity finite element method: basic theory and applications. *Computer methods in applied mechanics and engineering*, *139*(1): 289-314.

[2] Strouboulis, T., Copps, K. & Babuska, I. (2000). The generalized finite element method: an example of its implementation and illustration of its performance. *International Journal for Numerical Methods in Engineering*, *47*(8): 1401-1417.

[3] O'Hara, P., Duarte, C. A. & Eason, T. (2011). Transient analysis of sharp thermal gradients using coarse finite element meshes. *Computer Methods in Applied Mechanics and Engineering*, *200*(5): 812-829.

[4] Laghrouche, O. & Mohamed, M. S. (2010). Locally enriched finite elements for the Helmholtz equation in two dimensions. *Computers & structures*, *88*(23): 1469-1473.

[5] Munts, E. A., Hulshoff, S. J. & Des Borst, R. (2003). The partition-of-unity method for linear diffusion and convection problems: accuracy, stabilization and multiscale interpretation. *International journal for numerical methods in fluids*, *43*(2): 199-213.

[6] Duarte, C. A. & Kim, D. J. (2008). Analysis and applications of a generalized finite element method with global–local enrichment functions. Computer Methods in Applied Mechanics and Engineering, 197(6): 487-504.

[7] S. Mohamed, M., Seaid, M., Trevelyan, J. & Laghrouche, O. (2013). A partition of unity FEM for time dependent diffusion problems using multiple enrichment functions. International Journal for Numerical Methods in Engineering, 93(3): 245-265.

[8] Atluri, S. N. & Zhu, T. (1998). A new meshless local Petrov-Galerkin (MLPG) approach in computational mechanics. Computational mechanics, 22(2): 117-127.

[9] Van der Meer, F. P., Al-Khoury, R. & Sluys, L. J. (2009). Time-dependent shape functions for modeling highly transient geothermal systems. International journal for numerical methods in engineering, 77(2): 240-260.

[10] O'Hara, P., Duarte, C. A. & Eason, T. (2009). Generalized finite element analysis of three-dimensional heat transfer problems exhibiting sharp thermal gradients. Computer Methods in Applied Mechanics and Engineering, 198(21): 1857-1871.

Infrastructure and Environment Scotland 3rd Postgraduate Conference
9th December 2015
Heriot-Watt University, Edinburgh

An Ecosystem Services approach: how does rainfall variation influence habitat provision in ponds?

J.A Jarvie, Dr S Arthur, Dr L.C. Beevers.
Institute for Infrastructure and Environment,
Heriot Watt University
(e-mail: jaj31@hw.ac.uk)

ABSTRACT

Sustainable Urban Drainage Systems (SUDS) are soft engineering solutions for urban pollution, flood risk management with the intention to mimic natural systems while maintaining hydraulic features (such as flow control). Their design is based on the SUDS triangle which incorporates water quality, water quantity, and amenity and biodiversity components. Until recently, the main focus was on diffuse pollution and how SUDS offered a unique, and feasible, solution from urban and peri-urban water courses. However, with the looming threat of climate change, the research goal has widened to include the influence of flooding and how these solutions exist to minimise the associated impacts from localised floods. In terms of amenity, and biodiversity, little research has been completed to quantify the wider benefits with respect to three main pillars of sustainability: economic, social and environmental factors. Ecosystem Services refer to the end user benefits which may be derived from the natural environment. Few studies to date assess the links between Ecosystem Services and SUDS- although conceptual studies (Jose et al., 2015; Scholz et al., 2013; Lundy and Wade, 2011) exist, none have assigned a monetary value to these services.

It is therefore the intention of this paper to make the connection between aquatic habitats (ponds) and suggest feasible methods to quantify the wider Ecosystem benefits and services. Habitat provision is of strong importance for environmental benefits. It is therefore the focus of this paper to make the connection between aquatic habitats (ponds) and the amenity and biodiversity functions offered. This will be achieved by investigating whether there is a statistically significant association between two variables (pond area, total rainfall) and ASPT (average score per taxon).

1. INTRODUCTION

Ponds refer to the features on the landscape which have been naturally formed due to glaciation or existing hollows in forest environments (Pond Action, 1998). With the number of ponds rapidly decreasing, more effort and care has been taken to establish new ponds within the urban and rural settings of the UK. The initiative refers to changes in urban planning- where size of development and pollution risk is taken into account; as well as the relative risk of flooding (SPP7; Scottish Government, 2014).

1.1 SUDS

Sustainable urban drainage systems (SUDS) build on existing drainage systems and their design incorporates flood risk management, water quality, and amenity and biodiversity. Their systems mimic natural systems and reduce pressure on drainage by providing attenuation (swales and wetlands) and retention systems (ponds). The latter is the focus of the research- which assesses the importance of ponds in urban settings; as well as the intrinsic appeal.

1.2 Multiple benefits & ES

Ecosystem Services refers to the wider benefits derived from the natural environment (Costanza et al., 1997), and to date there are multiple interpretations on Ecosystem Service frameworks. Dailly et al., (1997) discusses the importance of environmental benefits in relation to society, and the drive to restore the systems with changes in environmental management is fundamental to this balance. Costanza *et al.,* (1997) focuses on the importance of environment at a global scale and the question whether nature should have a price. These papers were central to the development of Ecosystem Services theory (MA, 2005), but it was not until recently that the focus was on applying these policies at a national scale (NEA, 2011).

Ponds have multiple benefits, and these incorporate the three pillars of sustainability: social, economic and environmental ideals. Previous

studies look at the importance of ponds in the urban landscape (Hassall, 2014); as well as the links with amenity (Bastien *et al.,* 2012), but very few have assessed the benefits in an ecosystem services context (Scholz and Uzomah, 2013; Jose *et al.,* 2015). None have quantified the benefits relating to habitat provision, although Briers (2014) undertook a field investigation in the East of Scotland in relation to SUDS ponds.

1.3 Habitat provision (supporting ES)

The focus of the paper is: how does rainfall variation influence habitat provision in ponds? Coupled with this is one of the hypotheses for habitat provision which suggests: periods of high rainfall will reduce the number of pollution sensitive organisms in each pond. This may be tested with respect to the pond area to see whether pond size influences the water quality of the pond. Biggs *et al.,* (2005) discussed the importance of preserving ponds; as the presence of wildfowl (ducks, swans, moorhens etc) or pollution results in degradation. This is partially in relation to ponds having a smaller volume than rivers (Biggs et al., 2005). However, in the case of the smallest, and perhaps isolated, ponds- the water quality is protected due to the size of catchment, so it is less likely to become degraded due to pollution (Biggs et al., 2005). So the underlying question is: how does rainfall variation affect the pond ecosystem and how can these differences be accounted for?

In the context of this paper, ponds with a natural origin, and man-made, will be compared with SUDS ponds (engineered after 1994).

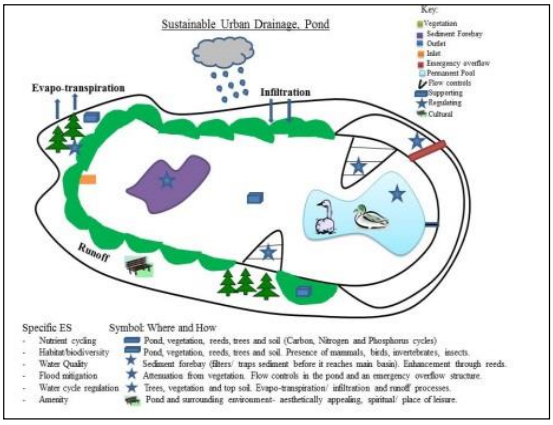

Figure 1. Ecosystem Services of ponds (SUDS as illustration, Jarvie *et al.,* 2015)

2. FIELD SITES AND METHODS

This section will outline the main study sites and the respective methods.

2.1 Field sites

For the purpose of this paper, six field sites in Edinburgh were visited at monthly intervals to assess suitability for habitat with respect to ponds with a natural origin, manmade, and SUDS (Figure 2). Natural origin implies that once the pond was natural, and has been modified by humans. Man-made refers to a pond which was built for a purpose- for example; Inverleith pond was designed as a boating pond in the 19th Century, and was not intended to host wildlife. SUDS ponds refer to those established after 1994 and with specific engineering functions for stormwater management, and diffuse pollution, as well as the amenity and biodiversity they provide.

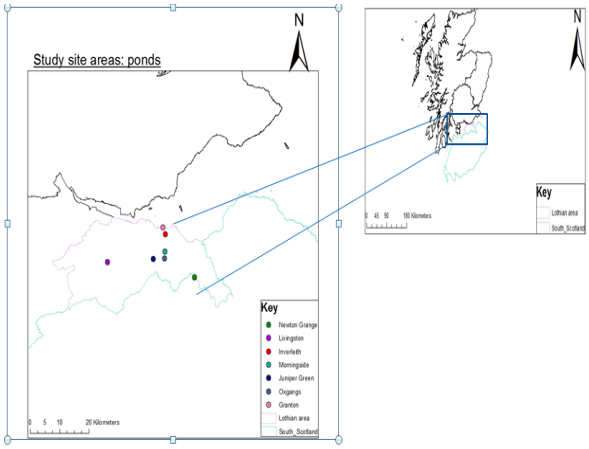

Figure 2. Map showing each study-site

2.2. Methods

The methods outlined are in accordance with the British Standards for still water; as well as the recommended guidance from NPS (Pond Action, 1998). Further details, including the framework for the methods, are documented in Jarvie *et al.,* (2015).

2.2.1 Sweep sampling

The standard approach was BS EN 10870:2012 and this refers to sweep sampling methods and other freshwater methods for still water. The method was as follows:

- Check that the net was free from debris or sediment
- Substrate was gently agitated for one minute
- The net was swept through the surface of the water column to capture surface dwellers, and this process lasts three minutes, and benthic invertebrates.
- The net was removed and emptied into a white tray.
- Invertebrate samples are stored in a bottle and preserved with alcohol.

2.2.2 Analysis of macro-invertebrates

Macro-invertebrate samples were analysed in the laboratory using a compound microscope, provided by the School of Life Sciences. Initially, samples are sieved and flushed to remove excess sediment or debris- as smaller invertebrates may be hiding. The next step was to place the macro-invertebrates in their family groups in the white tray. Counting was repeated to make the results

reliable, and if possible this was verified by an independent witness. Macro-invertebrates were placed under the microscope and identified to family level with the assistance of keys (Croft, 1986).

Out with the laboratory, data were computed using NPS BMWP (Biological Monitoring Working Party) Scores for ponds. Spreadsheets were created in Microsoft Excel and then the ASPT was calculated by dividing the BMWP score by the number of families present. ASPT is a proxy indicator for water quality and thus habitat provision.

2.2.3 Mapping vegetation and monitoring abundance

Figure 5 summarised the approach taken to record vegetation in still water environments in relation to the standard method BS EN 15460:2007. The steps are summarised below:

- Vegetation was recorded along transects
- Vegetation was categorised as: floating, submerged, and emergent
- Field results were compared with DAFOR (BS EN 15460-2007)
- Further analysis was carried out using Shannon-Index for biodiversity

2.2.4 Secondary data and analysis

Rainfall data were provided by the Met Office data service; as well as additional data on the Royal Botanic Gardens, Edinburgh, server. For the purpose of this paper, six ponds in Edinburgh were compared with six months of rainfall data to see whether patterns existed with respect to changes in ASPT. Pond area is tested in relation to the water quality proxy ASPT, because previous studies suggested that smaller ponds (areas) will be protected from degradation due to the catchment size (Biggs *et al.,* 2005). This may not be as applicable to SUDS ponds, for example, (Briers, 2014) which degrade over short timescales.

Furthermore, pond area was calculated using Edina-Digimap measurement tools and validated with field measurements collected in summer 2015.

Data were processed using tools within Microsoft EXCEL and SPSS. Preliminary tests, using Shapiro-Wilk, confirmed that the data followed a normal distribution of values ($p>0.05$). Tests were performed to see whether there were relationships between rainfall and ASPT, and ASPT and pond area using Pearson's Product Moment.

3. RESULTS

Results will be presented for six ponds in Edinburgh (Figure 3, 4) with respect to the influence of rainfall data on the provision of habitat at the inlet and outlet of each pond. Pond area and habitat provision- floating vegetation, and wildfowl (ducks, swans, moorhens, and coots) will also be considered.

3.1 ASPT

ASPT refers to the average score per taxon which as aforementioned is the BMWP score divided by the number of families in a given sample.

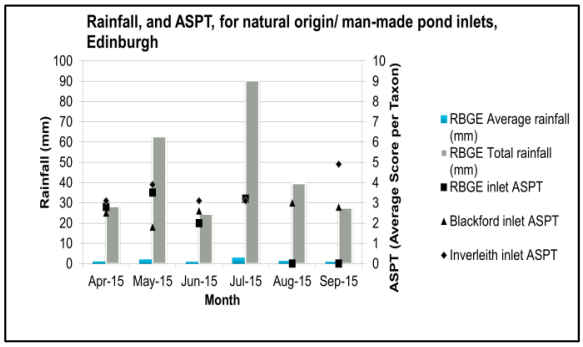

Figure 3. Comparing average monthly, and total, rainfall with ASPT for natural origin pond inlets, Edinburgh

Figure 3 reveals that September has the highest observed ASPT for the inlet during the start of the autumn season (September) which corresponds with the second lowest total rainfall with less than 30mm. 5 is fair in terms of habitat provision. In July, each pond has the same ASPT of 3.2 which is poor in terms of habitat provision for summer season. The lowest observed ASPT is 0 in August and September for the Royal Botanic Gardens- due to temporary draining.

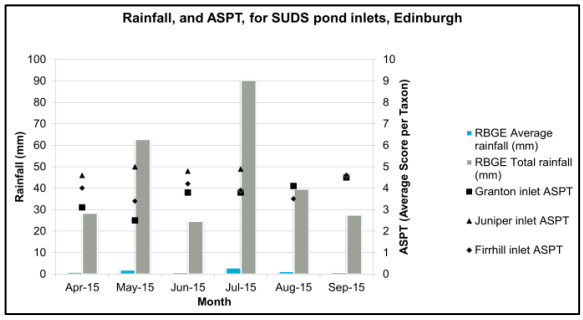

Figure 4. Comparing average monthly, and total, rainfall data with ASPT for SUDS pond inlets, Edinburgh

Juniper Green has the highest observed ASPT in May with 5 which corresponds with the second highest total rainfall (Figure 4). Juniper Green has a constant supply of water available from the grey water and rainfall harvested from the roof- which feeds into the inlet of the pond. This may explain why the ASPT is higher than other ponds at their inlets.

Granton pond has the highest ASPT in September where the second lowest rainfall is observed. Within the area sampled, there is a spawning ground for fish nearby- however the invertebrates

found tolerate pollution: such as lesser water boatman (corixidae), water hog-louse (asselidae) and non-biting midges (chironomidae). The midge population is fed on by invertebrates and Stickleback within the pond (Candolin *et al.,* 2015).

Equally, damselfly (Zygoptera) larvae are discovered near the inlet of Firrhill pond in September- where there are an abundance of small fish present (minnows). However, there were none present in previous months- which may suggest that during wetter months (July), the invertebrates seek refuge in the benthic sediment of the pond (Vadher, 2014). Furthermore, Juniper Green and Firrhill have floating vegetation present (pond weed, frog-bit and water lilies) which may factor into the differences observed through field studies.

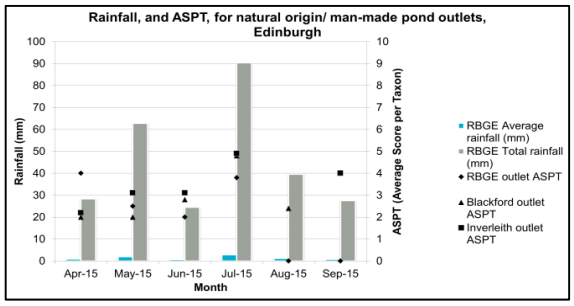

Figure 5. Comparing average monthly, and total, rainfall with ASPT for natural origin pond outlets, Edinburgh

Figure 5 highlights that outlet ASPT is highest for Inverleith in July (5) and this is fair in terms of water quality. The outlet ASPT is higher than the observed inlet, and for the case of July greater than 20 caddisflies (Trichoptera) are discovered in the field sample. Caddisflies are sensitive to organic pollution and score highly in terms of BMWP (see Jarvie *et al.,* 2015), so their presence suggests that the pond conditions are favourable for habitat. Caddisflies adapt to their surroundings, and in the case of Inverleith the substrate is wood and plant material casing. Trichoptera are important for ecosystem health as they filter organic debris and materials in the water (Wiggins, 1998; Johansen, 2015)

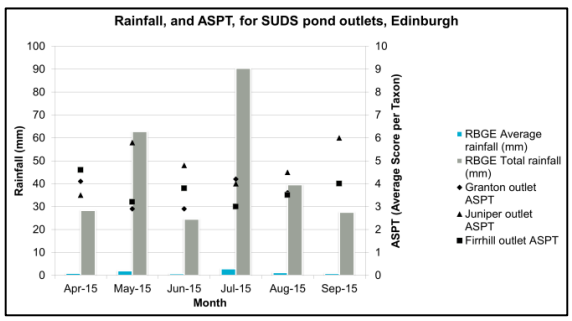

Figure 6. . Comparing average monthly, and total, rainfall data with ASPT for SUDS pond outlets, Edinburgh

Juniper Green has the highest ASPT for the SUDS ponds with a range of 2 (4 to 6). In September, with lower rainfall, the ASPT is 6.
Pollution sensitive organisms are found in two of the three SUDS ponds- with a variety of families (shrimp, caseless caddis, and damselfly larvae) found at Juniper Green pond. Granton has no sensitive organisms, to date, in the main pond- although earlier studies indicate that shrimp exist in the wetland (Jarvie *et al.,* 2015). Furthermore, presence of shrimp at Firrhill outlet suggests that there is some improvement in habitat throughout the pond.

3.2 Pond area and habitat provision.

Ponds with larger pond areas do not have floating vegetation present (as indicated from previous mapping). Floating vegetation such as water lilies and frog-bit are fundamental to habitat provision in ponds (Pond Action, 1998; Grutters et al., 2015), and it is interesting to note that this is absent from ponds with the larger surface area. Inverleith pond has the largest pond area with a wetland pond. The main "boating" pond has no vegetation cover present- but hosts over 200 birds: ducks, swans, moorhens, and kittiwakes. ASPT (figure 4 and 6) is better in ponds with limited or no wild-fowl present: Firrhill and Juniper Green, respectively.

Table 1. Pond area, vegetation and wildfowl.

Pond name	Pond area (m^2)	Floating vegetation (present)	Wild fowl
RBGE	1956	outlet	yes
Inverleith	9371	none	yes
Blackford	7803	none	yes
Firrhill	1688	outlet	limited
Granton	3137	none	yes
Juniper Green	192	Middle and outlet	no

3.4 Statistical Analysis

The analysis methods were chosen to investigate whether there were relationships between the water quality proxy, ASPT, and pond area; as well as any statistical difference between ASPT and rainfall data. The reason for this is to determine whether there is a clear statistical difference between stormwater retention (SUDS) ponds and pond with natural origins, and their associated habitats at the inlet and outlet. Pearson's Product Moment was chosen as the data conformed to the normal distribution of values.

Results of the statistical tests using Pearson's Product Moment will be displayed. One objective objective is to see whether a relationship exists between rainfall data from the Royal Botanic Garden weather station and habitat provision using the water quality proxy ASPT. The associated hypotheses are:

H_1: There is an association between total rainfall (RBGE) and observed ASPT

H_0: There is not an association between total rainfall (RBGE) and observed ASPT

An additional objective is to see whether pond area influences habitat provision at the inlet and outlet- as characterised by ASPT. The hypotheses are:

H_1: There is an association between pond area and observed ASPT

H_0: There is no association between pond area and observed ASPT

3.4.1 Pearson's Product Moment

A moderate correlation exists between rainfall data and observed ASPT (0.557) for the inlet of Juniper Green with poorer correlations for Inverleith (0.491) and Firrhill (0.139). Weak negative correlations exist for RBGE (-2.35) and Blackford (-2.64); suggesting that there a weak association between rainfall and observed ASPT at the pond inlet. None of the pond inlets have significant results observed; thus, the working hypothesis is rejected and the null hypothesis (there is not an association between rainfall and observed ASPT) is accepted.

Pearson's Product results indicate that a strong association exists between ASPT and pond area for RBGE (.856) and Blackford (.797) inlet for spring and summer seasons. The correlation is not significant at the 0.05 benchmark. However, a strong negative association exists between pond area and ASPT for Juniper Green (-.895) which is significant (.016). While, the larger ponds have a strong positive association, and no significance, the smallest pond has a strong negative association suggesting there is little or no association between the observed inlet ASPT and pond area.

Some association exists between the pond area and observed ASPT at the inlet of each pond. Larger ponds have strong positive correlations with the exception of Inverleith with a strong negative correlation. However, only one of six ponds had a significant result; therefore the null hypothesis is accepted for five ponds, there is no association between pond area and observed ASPT at the inlet.

A moderate-strong positive correlation exists between rainfall data and observed ASPT (0.655) for the outlet of RBGE. Weaker correlations exist for Juniper Green (.488), Firrhill (.469) and Blackford (.178). Granton has a strong negative correlation (-.815) suggesting there is no association between rainfall and observed ASPT at the outlet.

Weaker correlations exist between pond area and outlet ASPT. Juniper Green has a strong negative correlation (-.884) which is significant (.020) suggesting there is a very weak association between pond area and ASPT for the outlet. Overall, there is no association between pond area and observed ASPT.

4. CONCLUSIONS AND RECOMMENDATIONS

4.1 Conclusions

Habitat provision has some association with rainfall availability. Ponds with natural origins have better habitat provision in terms of presence of wild fowl and fish- which adds to local biodiversity. Juniper Green pond has consistently good ASPT at its inlet- which may be due to the absence of wildfowl, or the delivery of nutrients through the system by rainfall. ASPT is a useful proxy for water quality and to indicate whether a pond provides suitable habitat for macro-invertebrates, birds and fish. The latter is of key importance for demonstrating water quality- as fish cannot survive in oxygen deficient or impacted water.

Pearson's Product results indicate that there is not an association, of statistical significance, between total rainfall and observed ASPT; and, similarly for pond area and observed ASPT. However, there is some association between the pond area and ASPT at each pond inlet.

4.2 Recommendations

- Comparison of seasons when 1 year of continuous data is available- from spring 2015- spring 2016.
- Further investigation is needed with respect to the interaction of chemical parameters for habitat provision (DO, EC, pH, and Water temperature); as well as the influence of turbidity. This will be completed after spring 2016.
- Future studies may incorporate less urban areas- as all of the Edinburgh ponds are in urban settings.

REFERENCES

Bastien, N.R.P., Arthur, S., and McLoughlin, M.J., (2012) Valuing amenity: public perceptions of sustainable drainage systems ponds, *Water and Environment Journal,* **26**, p19-29

Briers, R.A., (2014) Invertebrate Communities and Environmental Conditions in a Series of Urban Drainage Ponds in Eastern Scotland: Implications for Biodiversity and Conservation Value of SUDS, *CLEAN – Soil, Air, Water Special Issue: Surface Water Management Using Sustainable Drainage – SUDS,* **42**(2), p193–200

British Standards Online, Water quality — Guidelines for the selection of sampling methods and devices for benthic macro invertebrates in fresh waters (ISO 10870:2012), accessed [online] at: www.bsigroup.com/standards, on 05/08/2014

British Standards Online, Water quality - Guidance standard for the surveying of
macrophytes in lakes (EN 15460:2007), accessed [online] at: www.bsigroup.com/standards, on 12/08/2014

Candolin, U., Johanson, A., and Budria, A., (2015) The Influence of Stickleback on the Accumulation of Primary Production: a Comparison of Field and Experimental Data, *Estuaries and Coasts*, p1-10

Costanza, R., *et al.,* (1997) The value of the world's ecosystem services and natural capital. *NATURE*, **387**, p253-260

Croft, P.S., (1986) A key to the major groups of British freshwater invertebrates, *Field Studies Council Aid Gap Guides,* UK.

Daily, G.C., Chapter 1, Introduction: What are Ecosystem Services? In (Ed) Dailly, G.C., *Nature's Services: Societal Dependence on Natural Ecosystems*, Island Press, Washington D.C.

Grutters, B.M.C et al., (2015) Native and Non-Native Plants Provide Similar Refuge to Invertebrate Prey, but Less than Artificial Plants. *PLoS ONE* **10**(4), p1-18

Hassall, C., (2014) The ecology and biodiversity of urban ponds, *WIREs Water,* **1:** 187–206.

Jarvie, J., Arthur, S., and Beevers, L.C., (2015) A field approach for comparing the Ecosystem Services from SUDS and non-SUDS ponds, *E-proceedings of the 36th IAHR World Congress 28 June – 3 July, 2015*, The Hague, the Netherlands

Johanson, K.A., (2015) Trichoptera (Caddisflies) in Eds Bocher, J., *et al., Greenland Entomofauna: An identification guide of spiders, insects and their allies,* Brille, Leiden, The Netherlands

Jose, R., Wade, R., and Jefferies, C., (2015) Smart SUDS: recognising the multiple-benefit potential of sustainable surface water management systems, *Water Science and Technology*

MA (2005) Ecosystems and human wellbeing: synthesis, accessed [online] at: http://www.millenniumassessment.org/documents/document.356.aspx.pdf, on: 05/03/2015

UK National Ecosystem Assessment Follow-on (2014) The UK National Ecosystem Assessment Follow-on: Synthesis of the Key Findings. UNEP-WCMC, LWEC, UK.

Pond Action (1998) A guide to methods of the National Pond Survey, accessed [online] at: http://www.freshwaterhabitats.org.uk/wordpress/wp-content/uploads/2013/09/National-Pond-Survey-Methods.pdf, on: 01/03/2014

Scholz, M., and Uzomah, V.C., (2013) Rapid decision support tool based on novel ecosystem service variables for retrofitting of permeable pavement systems in the presence of trees. *Science of the Total Environment* **458-460**, p486-498

Scottish Government (2015) Scottish Planning Policy (SPP) 7 Planning and Flooding, accessed [online]
at:http://www.gov.scot/Publications/2004/02/18880/32954, on 27/10/2015

Vadher, A.N., et al., (2015) Fine sediment reduces vertical migrations of Gammurus Pulex (Crustacea: Amphipoda) in response to surface water loss, *Hydrobiologia,* **753** (1), p66-71

Wiggins, G.B., (1998) *The Caddisfly Family Phryganeidae (Trichoptera)*, University of Toronto Press

Infrastructure and Environment Scotland 3rd Postgraduate Conference
9th December 2015
Heriot-Watt University, Edinburgh

1D modelling of non-uniform sediment transport in compound open channels

Ji Li
Institute for Infrastructure and Environment
Heriot-Watt University, Edinburgh, U.K.
(email: jl362@hw.ac.uk)

ABSTRACT

The last few decades have witnessed extensive improvement in the understanding of uniform and non-uniform sediment transport in compound open channels. However, most commercial computer models are still limited by; capacity-based sediment transport or steady or subcritical flow assumptions. To overcome these limitations the 1D model presented here is a fully coupled non-capacity model, capable of simulating flows and non-uniform sediment transport in compound open channels. The model is tested against a range of cases that represent complex hydraulic and sediment conditions that occur in compound channels. The satisfactory agreement between the computed results and measured data demonstrates that the model is, not only capable of predicting sediment transport, morphological evolution, bed-material sorting; but also of resolving the discontinuity of overall roughness and the momentum flux across the bankfull/overbank level.

Keywords: 1D modelling, sediment transport, finite volume scheme

1. INTRODUCTION

Recent research studies (e.g. Lane et al., 2007; Raven et al., 2009) and flood events of Cockermouth (2009), Carlisle (2009) and the Somerset Levels (2013/14) have indicated that, in-channel morphological changes can lead to a serious increase in flood risk by reducing the conveyance capacity of the channel. With the Pitt Review highlighting that river morphology and sediment supply may become the most influential drivers of flood risk in the 2050s, it is necessary to develop an appropriate numerical applicable for assessing these implications. Many commercially available mathematical models (e.g. ISIS and HEC-RAS) are based on simplified, un-coupled, descriptions of the hydrodynamics (steady-state flow in HEC-RAS) and capacity sediment transport Thus, the overall aim of this paper is to present a 1D fully coupled non-capacity model for non-uniform sediment transport in natural channels.

In natural channels the flow regime regularly undergoes rapid changes. Therefore, to solve the governing equations, the finite volume SLIC (Slope Limiter Centred) scheme is employed. This will provide a robust model suitable for sediment transport and morphological modelling in alluvial rivers.

To assess the models applicability, it is tested against observed and numerical results from experiments designed to reproduce flow and sediment transport in compound channels, including (i) the routing of a flood wave in a compound channel; and (ii) non-uniform sediment transport under an unsteady hydrograph. Successful development and testing of such a model will allow for it to be incorporated into applied modelling frameworks, allowing for more informed decisions to be made in the future.

2. NUMERICAL MODEL

2.1 Governing equations

Consider 1D flows in a compound open channel with a mobile bed composed of N size classes. Let d_k denote the diameter of the *k*th size of sediment, where k = 1, 2, ... N. The governing equations for non-uniform sediment transport are derived from the conservation laws under the framework of shallow water hydrodynamics, including the complete mass and momentum conservation

equations for the water-sediment mixture; the size-specific mass conservation equation for the sediments carried by the flow; the total mass conservation equation for the sediments in the bed; and the size-specific mass conservation equation for the sediments in the active layer of the bed surface.

$$\frac{\partial \mathbf{U}}{\partial t}+\frac{\partial \mathbf{F}}{\partial x}=\mathbf{S} \tag{1}$$

$$\mathbf{U}=\begin{bmatrix} A \\ Q \\ Ac_k \end{bmatrix},\quad \mathbf{F}=\begin{bmatrix} Q \\ \beta Q^2/A+gA^2/2B_w \\ Qc_k\lambda_k \end{bmatrix} \tag{2a, b}$$

$$\mathbf{S}=\begin{bmatrix} \int \frac{E_T-D_T}{1-p}dy \\ N \\ \int_{B_w}(E_k-D_k)dy \end{bmatrix} \tag{2c}$$

$$N=gA(S_b-S_f)-\frac{Q}{A}\frac{\rho_s-\rho_w}{\rho}(1-\frac{C_T}{1-p})\int_{B_w}(E_T-D_T)dy$$
$$-\frac{(\rho_s-\rho_w)gAh_c}{\rho}\frac{\partial C_T}{\partial x}-\frac{(\rho_s-\rho_w)(\beta-1)Q^2}{A\rho}\frac{\partial C_T}{\partial x}$$
$$+\frac{Q(\rho_s-\rho_w)}{A\rho}\frac{\partial Q\sum c_i(\alpha_i-1)}{\partial x}-\frac{1}{2}\frac{A^2}{B_w^2}\frac{\partial B_w}{\partial x} \tag{2d}$$

$$\frac{\partial A_b}{\partial t}=-\int_{B_w}\frac{E_T-D_T}{1-p}dy \tag{3}$$

$$\frac{\partial \delta f_{ak}}{\partial t}+f_{Ik}\frac{\partial \xi}{\partial t}=\frac{D_k-E_k}{1-p} \tag{4}$$

where $t=$ time; $x=$ streamwise coordinate; $g=$ gravitational acceleration; $A=$ cross-sectional area; $A_b=$ cross-sectional area of erosion and deposition bed; $Q=$ discharge; $\beta=$ momentum correction coefficient; $p=$ bed sediment porosity; $B_w=$ whole width of water surface; $z_b=$ bed elevation at any node; $c_k=$ size-specific sediment concentration and $C_T=\Sigma c_k=$ total sediment concentration; $S_f=$ friction slope; $S_b=$ bed slope; $\rho=\rho_w(1-C_T)+\rho_s C_T=$ density of the water-sediment mixture; $h_c=$ height of the centroid of cross-section; ρ_s and $\rho_w=$ densities of water and sediment respectively; $\rho=\rho_w p+\rho_s(1-p)=$ density of the saturated bed; $\lambda_k=$ an empirical coefficient representing the velocity differences between sediment phase and water-sediment mixture flow; $E_T=\Sigma E_k$; and $D_T=\Sigma D_k$ are the total sediment entrainment and deposition fluxes, E_k and $D_k=$ size-specific sediment entrainment and deposition fluxes. The widely used active layer formulation proposed by Hirano (1997) (i.e., Eq.4), is adopted to resolve the change in bed composition. In Eq.(4), δ is the thickness of the active layer, f_{ak} is the fraction of the *k*th size sediment in the active layer; $\xi=z_b-\delta$ is the elevation of the bottom surface of the active layer; and f_{Ik} is the fraction of the k th size sediment in the interface between the active layer and substrate layer.

2.2 Model closure

To close the governing equations, auxiliary relationships have to be introduced. In this case the flow resistance is represented using Manning's formula

$$S_f=Q^2/K^2,\quad K=AR_h^{2/3}/n_0 \tag{5a, b}$$

where $K=$ conveyance; $R_h=$ hydraulic radius; and $n_0=$ overall roughness.

Cao et al. (2006) define the momentum correction coefficient in Eq. (2b) as

$$\beta=I_1 I_{2R1}/I_{R1}^2 \tag{6}$$

where $I_1=\int_{B_w}(h/h_m)dy$,

$I_{R1}=\int_{B_w}(h/h_m)^{R+1}(n_m/n)^{3R/2}dy$,

$I_{2R1}=\int_{B_w}(h/h_m)^{2R+1}(n_m/n)^{3R}dy$

and the overall roughness is

$$n_0=\frac{I_{2R13}^{1/2}I_1^{7/6}}{I_{R1}P^{2/3}} \tag{7}$$

where

$I_{2R13}=\int_{B_w}n^2(h/h_m)^{2R-1/3}(n_m/n)^{3R}\sqrt{1+(\partial z_b/\partial y)^2}dy$,

$P=\int_{B_w}\sqrt{1+(\partial z_b/\partial y)^2}dy$, and *R* = parameter to be determined by Cao et al. (2006); and u_m, h_m, n_m = velocity, flow depth and roughness at a reference location. Generally, h_m can be defined as the maximum flow depth in a cross section, where the bed elevation is z, u, h, n velocity, flow depth and roughness at any location respectively. The velocity discrepancy coefficient λ_k is estimated by the relationship of Greimann et al. (2008). Bedload sediment is usually transported at an appreciably lower

velocity than the flow; so $\lambda_k < 1$ is common.

Two distinct mechanisms are involved in the exchange of sediment between the water column and bed (i.e. sediment entrainment due to turbulence and sediment deposition due to gravitational settling). They are estimated empirically by

$$E_k = \alpha_k \omega_k c_{ek}, \quad D_k = \alpha_k \omega_k c_k \qquad (8)$$

where ω_k is the size-specific settling velocity calculated by the formula of Zhang and Xie (1993); $\alpha_k = c_{bk}/c_k$ is an empirical parameter representing the difference between the near-bed sediment concentration c_{bk} and the depth-averaged sediment concentration c_k. The size-specific sediment concentration at capacity c_{ek} is computed as $c_{ek} = F_k q_k/(hu)$, q_k is the unit-width size-specific sediment transport rate at capacity regime, F_k is the areal exposure fraction of the k th sediment on the bed surface, given by Parker (1991a, b).

The systematic assessment of twelve empirical formulations for q_k conducted by Van der Scheer (2002), identified the formula of Wu et al. (2000) as the most appropriate for alluvial channels. Thus this formula is used here, as described below

$$\frac{q_k}{\sqrt{(\rho_s/\rho_w - 1) g d_k^3}} = 0.0053 \left[\left(\frac{n'}{n_b}\right)^{1.5} \frac{\tau_b}{\tau_{ck}} - 1 \right]^{2.2} + 0.0000262 \left[\left(\frac{\tau}{\tau_{ck}} - 1\right) \frac{u}{\omega_k} \right]^{1.74} \qquad (9)$$

where $n' = d_{50}^{1/6}/20$ is the Manning roughness corresponding to grain resistance; n_b is the Manning roughness for channel bed; τ_b is the bed shear stress; τ is the shear stress at channel cross-section; τ_{ck} is the critical shear stress for incipient motion of bed material, approximated by $\tau_{ck} = 0.03 \gamma_k (\rho_s - \rho) g d_k$ where γ_k represents the correction factor accounting for the hiding and exposure mechanisms in non-uniform sediment (Wu et al., 2000). The following relation is employed to evaluate f_{Ik} (Hoey and Ferguson, 1994; Toro-Escobar et al., 1996)

$$f_{Ik} = \begin{cases} f_{sk} & \partial\xi/\partial t \le 0 \\ \phi c_k / C_T + (1-\phi) f_{ak} & \partial\xi/\partial t > 0 \end{cases} \qquad (10)$$

where f_{sk} is the fraction of the k th size sediment in the substrate layer; ϕ is the empirical weighting parameter.

2.3 *Numerical algorithm*

To solve the ensemble of governing equations described in the previous section, a standard finite volume method (FVM) splitting discretization (Toro 2001) is applied to the advection of Eq. (1), with a third-order Runge-Kutta method used for the source terms

$$\mathbf{U}_i^* = \mathbf{U}_i^m - \frac{\Delta t}{\Delta x}\left[\mathbf{F}_{i+1/2} - \mathbf{F}_{i-1/2}\right] \qquad (11a)$$

$$\mathbf{U}_i^{m+1} = \mathbf{U}_i^* + \frac{\Delta t}{6}[\mathbf{S}(\mathbf{U}_i^{*1}) + 4\mathbf{S}(\mathbf{U}_i^{*2}) + \mathbf{S}(\mathbf{U}_i^{*3})] \qquad (11b)$$

with $\mathbf{U}_i^{*1} = \mathbf{U}_i^*$, $\mathbf{U}_i^{*2} = \mathbf{U}_i^{*1} + \frac{\Delta t}{2}\mathbf{S}(\mathbf{U}_i^{*1})$, $\mathbf{U}_i^{*3} = 2[\mathbf{U}_i^{*1} + \Delta t \mathbf{S}(\mathbf{U}_i^{*2})] - [\mathbf{U}_i^{*1} + \Delta t \mathbf{S}(\mathbf{U}_i^{*1})]$

where Δt is the time step; Δx is the spatial step; the subscript i denotes the spatial node index; the superscript m denotes the time step index; $\mathbf{F}_{i+1/2}$ and $\mathbf{F}_{i-1/2}$ represent the inter-cell numerical fluxes.

Due to the presence of momentum correction coefficient β, the SLIC solver, which is of the slope-limiter type, non-upwind and results from replacing the Godunov flux by the FORCE flux in the MUSCL-Hancock scheme, is employed to computed the numerical fluxes involved in Eq. (11a). For numerical stability, the time step is specified according to the Courant-Friedrichs-Lewy (CFL) condition $\Delta t = C_r \Delta x/\lambda_{\max}$, where C_r is the Courant number and $C_r < 1$ and $\lambda_{\max}$ is the maximum celerity computed from the Jacobian matrix $\partial\mathbf{F}/\partial\mathbf{U}$.

The bed deformation and bed surface material composition are updated by the discretisations of Eq.(3) and Eq.(4) respectively

$$A_{bi}^{m+1} = A_{bi}^m + \Delta t \int \frac{(D_T - E_T)_i^{RK} dy}{1-p} \qquad (12)$$

$$\frac{(\delta f_{ak})_i^{m+1} - (\delta f_{ak})_i^m}{\Delta t} + (f_{Ik})_i^m \frac{\xi_i^{m+1} - \xi_i^m}{\Delta t} = \left(\frac{D_k - E_k}{1-p}\right)_i^{RK} \qquad (13)$$

In Eqs. (12) and (13) the superscript *RK* indicates that the sediment exchange is estimated by the third-order Runge-Kutta method for the source terms.

3. MODEL TESTING

3.1 *Unsteady Flood Routing in a Compound Channel*

To test the hydrodynamic component of the model, the routing of a flood wave along a compound channel was tested. This test was developed conceptually by Cao et al. (2006) and as such there are no experimental results for comparison. As such the model results were compared to those presented by Cao et al. (2006), whose model was shown to well replicate the discontinuity of overall roughness and the momentum flux across the bankfull/overbank level. Notably the model of Cao et al. (2006) only concerns clear-water flow and is numerical solved by the conventional method of characteristics, while the present model incorporates sediment transport and employ the state-of-art FVM method.

The channel cross-section is defined as a prismatic compound open channel (Fig. 1) and extended for a length of 100 km. Specific geometrical parameters are: complete width $B = 400$ m, channel bottom width $b = 20$ m, side slope $s = 3.0$, and bankfull depth $h_{bf} = 5$ m, floodplain roughness n_{fp} and main channel roughness n_{mc} are both 0.03.

The flood wave was defined as a log-Pearson Type III hydrograph with an initial base flow of 120 m^3/s, a peak discharge of 1200 m^3/s at $t = 15$ hours, and total duration of 150 hours (Fig. 2a). At the downstream boundary, a stage-discharge relationship was specified. The initial steady state corresponds to an entirely in-bank flow, with flow depth ranging approximately from 3.7 m at the upstream end to 4.5 m at the downstream boundary. The Courant number $C_r = 0.5$ and the spatial step $\Delta x = 25$ m.

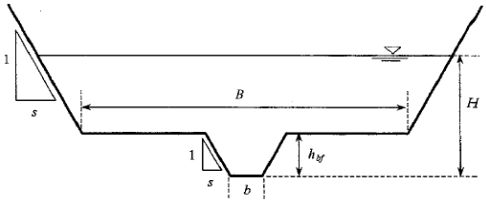

Figure 1. Configuration of compound channel cross-section

Fig. 2a illustrates the outflow discharge hydrographs (*x*=100 km) produced by the present model and that of Cao et al. (2006), and the inflow discharge hydrograph is also included. The temporal stage hydrographs at specific locations throughout the domain are shown in Fig. 2b. It can be seen from Figs. 2a and b that the flow returns to the initial state after 105 hours, according to the both numerical results.

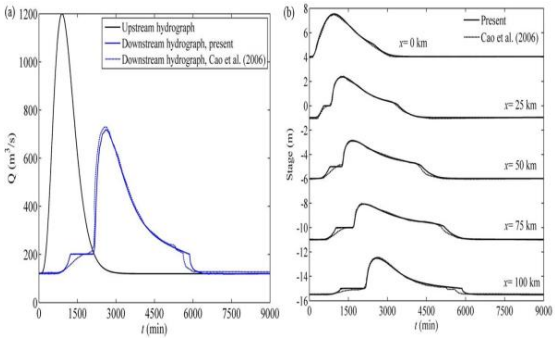

Figure 2. (a) discharge hydrographs at upstream and downstream boundaries; and (b) stage hydrographs along the channel

This test demonstrates the proposed model's capability of capturing the transition from in-bank to overbank flow, and vice versa. Additionally, it confirms its ability to simulate the long-standing computational challenge in unsteady flood routing of, small flow depths across wide, flat, flood plains.

3.2 Non-uniform Bedload Sediment Transport with Unsteady Flow

The second comparison was designed to test the models ability to replicate sediment transport and morphological change under an unsteady flood hydrograph (Wang et al., 2014). The experimental flume was 21 m long and 0.75 m wide with a slope of 0.002. A symmetrical unsteady hydrograph was specified at the inlet, with the downstream boundary being defined as a measured stage level (Fig. 3a). The bed was composed of graded sediments with six size fractions, ranging from 1.95 mm to 11.6 mm. The detailed bed material composition is given in Table 1. The Courant number $C_r = 0.5$ and the spatial step $\Delta x =$ 0.025 m. The porosity of the deposited sediment is also estimated by $p = 0.13 + 0.21/(d_{50} + 0.002)^{0.2}$ and the roughness $n =$ 0.01. The active layer thickness $\delta = 2d_{84}$ and the weighted factor $\phi = 0.7$ is used.

Fig. 3a shows the inflow discharge as well as the measured and computed upstream hydrographs, demonstration the model set up is well calibrated to the experimental conditions. The variation tendency of stage hydrograph is consistent with that of inflow

discharge. Fig.(3b) illustrates the computed and measured size-specific sediment transport rate at downstream. From Fig. (3b), the size-specific sediment transport rate always peaks when the inflow discharge reaches maximum value. The overall magnitude and variation trend for the computed and measured sediment transport rates compare well, although appreciable quantitative differences are observed, especially for the finer sediment during the peak flow. Fig. (3c) presents the final computed water surface and a comparison with the final bed levels along the channel. From this it can be seen that the computed bed agrees well with the measured bed by replicating the general downstream decreasing trend in the bed scour depth.

Table 1 Bed material composition of the non-uniform sediment transport experiment

d_k (mm)	1.95	3.4	5.15	7.15	9.0	11.6
(%)	44.19	23.83	14.36	9.10	6.24	2.27

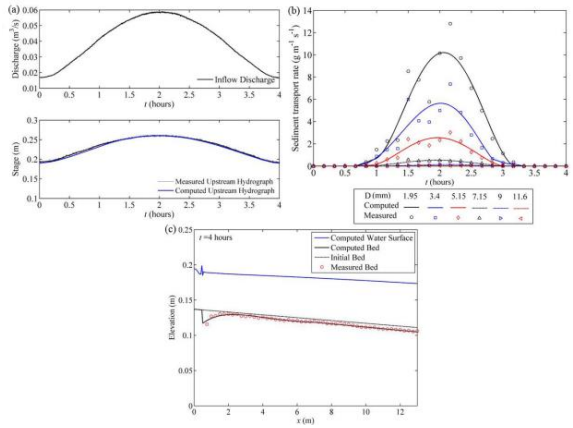

Figure 3: (a) inflow discharge and measured and computed upstream hydrographs; (b) computed and measured size-specific sediment transport rate at downstream; and (c) water surface and bed

4. CONCLUSIONS

This paper has presented a state-of-the-art 1D numerical model for the non-uniform sediment transport and morphological change in alluvial rivers. The model is based on a shock-capturing finite volume numerical scheme, meaning it can simulate the complete range of flow conditions that may occur in natural river channels. The agreement between computational results and experimental data is encouraging, featuring that the model can satisfactorily reproduce both the hydrodynamics and morphodynamics in alluvial rivers, especially in river reaches where the floodplains provide temporary storage of flood hydrographs. It should find further applications in applied projects that involve the modelling and understanding of alluvial sediment transport after some further development and testing.

REFERENCES

Cao, Z., Meng, J., Pender, G., Wallis, S. (2006). Flow resistance and momentum flux in compound open channels. *J. Hydraul. Eng.*, 132(12), 1272-1282.

Greimann, B., Lai, Y., Huang, J. (2008) Two-Dimensional Total Sediment Load Model Equations. *J. Hydraul. Eng.*, 134, 1142–1146.

Hirano, M. (1971). River bed degradation with armouring. *Trans. Jpn. Soc. Civ. Eng*, 3(2), 194-195.

Hoey, T. B., Ferguson, R. (1994). Numerical simulation of downstream fining by selective transport in gravel bed rivers: Model development and illustration. *Water Resour. Res.*, 30, 2251–2260.

Lane, S. N., Tayefi, V., Reid, S. C., Yu, D., and Hardy, R. J. (2007). Interactions between sediment delivery, channel change, climate change and flood risk in a temperate upland environment. *Earth Surf Process Landforms*, 32(3), 429-446.

Parker, G. (1991a). Selective Sorting and Abrasion of River Gravel. I: Theory. *J. Hydraul. Eng.*, 117, 131-147.

Parker, G. (1991b). Selective Sorting and Abrasion of River Gravel. II: Applications. *J. Hydraul. Eng.*, 117, 150–171.

Raven, E. K., Lane, S. N., Ferguson, R. I., Bracken, L. J. (2009). The spatial and temporal patterns of aggradation in a temperate, upland, gravel-bed river. *Earth Surf Process Landforms*, 34(9), 1181-1197.

Toro-Escobar, C. M., Paola, C., Parker, G. (1996). Transfer function for the deposition of poorly sorted gravel in response to streambed aggradation. *J. Hydraul. Res.*, 34, 35–53.

Toro, E. F. (2001). Shock-capturing methods for free-surface shallow flows. Wiley, Chichester, UK

Van der Scheer, P., Ribberink, J. S., Blom, A. (2002). Transport formulas for graded sediment - Behaviour of transport formulas and verification with experimental data.

Wang, L., Cuthbertson, A., Pender, G., Cao, Z. (2014). The response of bed-load sediment transport and bed evolution under unsteady hydrograph flows. Proc. 7th IAHR River Flow Conf.

Wu, W., Wang, S. S. Y., Jia, Y. (2000). Nonuniform sediment transport in alluvial rivers. *J. Hydraul. Res.*, 38, 427–434.

Zhang, R.J., Xie, J. H. (1993) Sedimentation research in China-systematic selections. China Water and Power Press, Beijing, China

Infrastructure and Environment Scotland 3rd Postgraduate Conference
9th December 2015
Heriot-Watt University, Edinburgh

Laboratory experiment to select variables for predicting foaming in anaerobic digester

Ifeyinwa Rita Kanu, Thomas J. Aspray, Scott Arthur, Adebayo J. Adeloye
Institute for Infrastructure and Environment,
Heriot Watt University
(e-mail: irk1@hw.ac.uk)

ABSTRACT

Foaming has been a persistent problem for the operators of anaerobic digesters. Efforts from various researchers have been channeled towards understanding the mechanism of foaming in anaerobic digester however; there has not been an explicit explanation for this phenomenon due to insufficient data on anaerobic digester foaming episodes. In this study, extensive literature review was followed by laboratory set up to monitor foaming in anaerobic digester. Secondary data collected from full scale wastewater treatment plant in combination with preliminary data obtained during the experiment were helpful in widening understanding on the mechanism of foaming in anaerobic digester. This informed the basis for variable selection to be used in developing a predictive model of anaerobic digester foaming. Using a semi-batch laboratory anaerobic digester, organic loading rate, surfactant concentration and biogas production rate were selected as the most sensitive variables as they correlate with anaerobic digester foaming

1. INTRODUCTION

Energy in sewage sludge (thermal, chemical and mechanical) has been estimated to about 2-4 times the amount of energy employed in wastewater treatment (Banfield & Littlejohn, 2013). Sludge production during wastewater treatment process occurs mainly in the course of primary treatment and secondary treatment thus they are usually known as primary sludge (PS) and secondary sludge (SS). An activated sludge (AS) wastewater treatment plant in Scotland with a population equivalent of 806,883 and inflow rate of 335,226m3/d generates sludge in the range of 640m3/d and 360m3/d of 5% thickened PS and SS respectively (Sourced data_Seafield performance log). In United Kingdom, 1.1 Million tonnes of sludge is generated per annum with possible production of up to 110MW of electricity per annum through anaerobic digestion (WRAP & NNFCC, 2015).

Though anaerobic digestion has been a well-established technology that has gone through a lot of development, nevertheless, foaming continues to pose a significant challenge to its operation. AD foaming is highly unpleasant with potential loss of active digester volume, structural damage, spillage, damage to the gas-handling system and subsequent reduction in biogas production (Kanu et al., 2015). When foaming occurs in an anaerobic digester (AD), it tends to reduce the production of gas by up to 40% (Moeller, et al., 2010). Issues relating to AD foaming date as far back as 1985 when a survey by the American Society of Civil Engineers reported half of the AD to have experienced foaming once during their operating lives (Filbert, 1985). Attempts have been made by several researchers to resolve AD foaming without success as most remedies proposed are either site specific or not impracticable at a full scale AD (Niekerk et al., 1987; Barjebruch et al., 2000; Barber, 2005; Dalmau, et al., 2009; Ganidi et al., (2009); Moeller, et al., 2010; Subramanian, et al., 2012; Rodríguez-Roda et al., 2013; etc.). The complications encountered in solving the problem of foaming in AD stems from the fact that it is occurring in an environment of microbiological complexity requiring adherence to some specific operating conditions such as temperature, pH, organic loading rate, volatile fatty acid (VFA) to alkalinity ratio, etc to function optimally. However, in practice, it is difficult to consistently maintain such operating conditions and in some instances, it is not easy to ascertain deviations from the optimal operating conditions until the system has gone bad such as the occurrence of AD foaming. Thus, major deficiencies exist in the present knowledge of efficient remedial actions for mitigating foaming in anaerobic digesters (Subramanian et al, 2012). On this premise, modelling becomes a useful tool for monitoring treatment plants and is technically the most feasible and probably the least costly way of attaining a sustainable improvement in performance (Dalmau, et al., 2009; Rustum & Adeloye, 2012).

Modelling AD foaming has faced its own challenges over time. With regards to mechanistic model, there has been lack of basic knowledge on the mechanism of foaming in AD. Thus it is hard developing a kinetic relationship to explain foaming occurrence. On the other hand, modelling AD foaming using knowledge based techniques has faced the challenge of non-existing record of

foaming which was observed during the process of collecting data from AD operators. When foaming occurs, it cause so much nuisance that the operators are keen to resolve the foaming issue rather to measure and record the extent of foaming. Consequently, the only available AD foaming model faced this challenge. Dalmau et al., (2010) tried developing a knowledge based model of foaming in AD based on heuristic knowledge which on validation exhibited discrepancies such that the model showed relatively high foaming risk compared to the real data. To avert such circumstance in this study, an experiment was set up to monitor anaerobic digester foaming based on knowledge derived from existing literature on possible causes of foaming in anaerobic digester.

The aim of this initial phase of the experiment was to develop a better understanding of the mechanism of anaerobic digester foam and the link between the feed sludge characteristics and the operating conditions. This result will be crucial in selecting variables needed to develop a model to predict foaming in anaerobic digester. These variables will be used to calibrate and test the predictive model which will then form the basis of operating anaerobic digesters in a mode that reduces foaming.

2. Existing knowledge in the literature

There has been conflicting ideas on the factors that cause foaming in anaerobic digester with the deduction that some of these factors are site specific. Ganidi et al., (2009) noted that filamentous microorganisms were present in sludge and foam samples during bench scale batch digestion but their contribution to foaming was considered insignificant. Heard et al., (2007) suggested that the filamentous microorganism cells themselves do not cause foaming but they do produce biosurfactant that aids foam formation while they stabilise the foam by reducing the rate of drainage from the foam lamellae. Based on a survey carried out by Subramanian, et al., (2012) and Rodríguez-Roda et al. (2013) in U.S.A and Spain respectively, they concluded that the presence of foam causing filaments is the most common cause of foaming. In a survey and laboratory study carried out by van Niekerk et al. (1987), high ratio of waste activated sludge (WAS) to primary sludge (PS) was identified as one of the causes of foaming in AD. On the contrary a laboratory scale investigation of foaming in AD conducted by Ross and Ellis (1992) reported thickest foam in digesters receiving a low WAS to PS ration. They related foaming to high organic loading ratio (ORL), hydraulic retention time (HRT), high total volatile acid: total alkalinity ratios (TVA: TA), low volatile solids reductions and low pH.

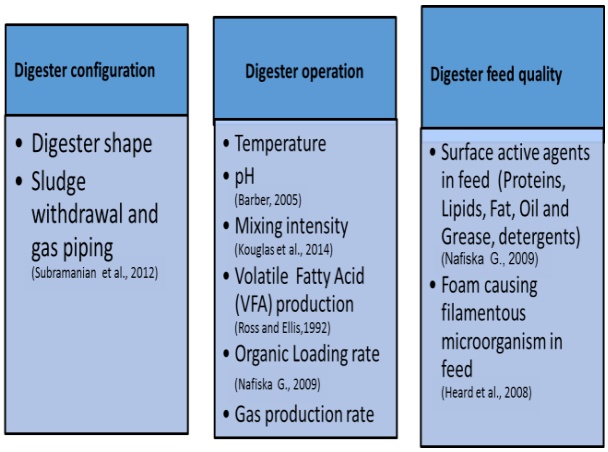

Figure 1: Factors contributing to foaming in anaerobic digester

Notwithstanding the contradictions existing in the literature as regards the factors causing AD foaming, some of these factors were consistently present such as surface active agents, organic loading rate (OLR), VFA concentration, rate of biogas production, temperature, pH and mixing. Based on these consistent factors, an experiment was set up to monitor their influence in anaerobic digester foaming.

3.0 Methodology

3.1 Description of the full scale sewage treatment works and sample collection

Sludge samples used for the experiment were collected from a wastewater treatment plants (WWTP) in Scotland with features as shown in table 1. The WWTP had experienced series of foaming in the past. The level of foam is visually checked sporadically through a sight glass on top of digesters and monitoring the pressure relief valve. Since there is no means of measuring foam, continuous dosing of Antifoam(BURST) in the heating recirculation circuit has been the practice as it is deemed expedient for the efficient running of the digester. Nevertheless, the operators were not certain that the antifoam dose was the major reason for not witnessing foaming over the time as some other operational conditions such as reduction in organic loading rate had been adjusted within the time to curb the foaming incidence.
A plastic container was used to collect sludge samples daily from the digester feed tank and store them in a cold room at 4 ^{0}C until when needed.

Table 1 : Features of field scale wastewater treatment plant

Inflow to WWTP	
PE	806883
Flow rate to the works (m^3/d)	335226
Chemical oxygen demand (mg/l)	297
Total suspended solid (mg/l)	168
Ammonia-nitrogen (mg/l)	17
Biological oxygen demand (mg/l)	116
Digester configuration	
No of cylinders	6
Diameter (m)	15
Height (m)	13.84
Volume (m^3)	2446
Digester feeding	
Proportion of feed to Digester	36% thickened at 5.72% DS secondary sludge + import (Gravity belt thickener) and 64% thickened at 4.28% DS primary sludge (Picked fence thickener)
Frequency of feeding	20 min / 2 hours
Organic loading rate	2.8 kgVS/m3.d
Digester operation	
Temperature	35
pH	7.2, (5.7 feed)
VFA/Alkalinity	0.1 to 0.3
Organic loading rate	2.8 kgVS/m3.d
Mixing	Sludge recycling
Biogas (m^3/d)	23255
Biogas (methane)%	63

3.2 Laboratory semi-batch anaerobic digester

Three semi batch reactors run in duplicate duplicates were fed with glucose and sludge sample using seed sludge from a non-foaming AD (Figure 2). One digester fed with glucose functioned as the control which is essential to ensure that the inoculum contain sufficient biomass to carry on the digestion process as well as an evidence to prove that the setup and procedure is suitable for anaerobic digestion and production of biogas.

Based on available literature for the onset of AD foaming, and the operating condition of the field scale AD, the organic loading rate (OLR) for the digesters were varied from an initial start-up of 0.16kgVS/m^3d to 2.8kgVS/m^3d provided that the digester process-control parameters (pH, tVFA and Alkalinity) are within the desired limits. The temperature of the digester was maintained at 35^{o}C using a thermostatically set water bath. A thermometer was placed in the water bath to monitor and ensure that the set temperature was maintained during the period of the experiment. Sample withdrawal will be followed by digester feed and manual mixing to be done once in a day.

Figure 2: Semi-batch anaerobic digester set up

3.3 Data collection

3.3.1 Surfactants

Anionic, cationic and non-ionic surfactant were determined using Hach cuvettes; LCK 433_Anionic Surfactants, 0.05-2.0 mg/l, LCK331_Cationic surfactants, 0.2-2.0 mg/l and LCK 332_Non-ionic surfactants, 0.2-6.0 mg/l. Total surfactant concentration was determined as the sum of the three. The procedure as applied in this experiment was carried out as per manufacturer's instructions after centrifugation of samples at 6000 rpm for 10 minutes.

3.3.2 Organic loading rate

This was determined based on the volatile solid concentration of the feed sludge. Volatile solids and total solids were determined as stipulated in (APHA, 2012)

3.3.3 Volatile fatty acid (VFA)

Montgomery et al., (1962) proposed an empirical method of determining organic acids based on colorimetric ferric hydroxamate. The method was carried out as per procedure stated in Montgomery et al., (1962) after centrifugation of the samples at 6000 rpm for 10 minutes.

3.3.4 Biogas production rate

Biogas was collected in a cylindrical glass as shown in figure 3. The difference in height is recorded on daily basis as well as the daily room temperature and atmospheric pressure. The volume of biogas taking measures to offset the effect of atmospheric pressure.

3.3.5 pH

Anaerobic digester can operate within pH range of 6.0 to 8.0. However, the ideal range should be within 6.8 to 7.2 for maximum biogas production. Unionised volatile acid at pH below 6.0 or unionised aqueous ammonia at pH above 8.0 becomes toxic to methane forming bacteria (WEF, 2007). The pH reading was taken immediately the samples were collected from the digester using a pH probe.

3.3.6 Foaming

The highest volume of foam observed in the digester was recorded. On collecting the feed sludge sample from WWTP, Alka-Seltzer © foaming potential test (Fryer, et al., 2011) was carried out to estimate the foaming propensity. This was recorded as the highest volume of foam observed.

4.0 Statistical analysis

Calculation of mean values, standard deviations and standard errors were carried out for all data obtained during the experiment.

5.0 Results and discussions

The experiment was scheduled to be repeated three times, however, as at the time of this report it was only the first set of the experiment that has been carried out for the period of 25/11/2015 to 03/11/2015.

During the period of the experiment, the digester was monitored and VFA to alkalinity ratio was in the range of 0.1 and 0.2. The pH range varied between 6.0 and 8.0. Thus based on these conditions, the digesters are considered to be operating at optimal conditions (Metcalf and Eddy, 2012).

It was observed that foaming occur within 1 hour of introducing the feed sample. This has been considered to be as a result of the increase in surfactant concentration in the digester from the feed sludge. The increase in biogas production due to methanogenesis taking place at the same time as increment in surfactant concentration results in emulsification of the gas bubbles by the surfactants thereby producing lots of foam. The observed foam lasted for some time and then starts to collapse.

As already illustrated by Ganidi et al (2011), it was observed in this experiment that organic loading rates below 2.5kgVS/m^3 did not result in foaming, while an initial increase in OLR results in a significant increase in foaming but not subsequently. This could be attributed to the fact that microorganisms have the ability to adjust easily to their environment. Thus an initial increase affects the foaming potential but when maintained does not have much influence.

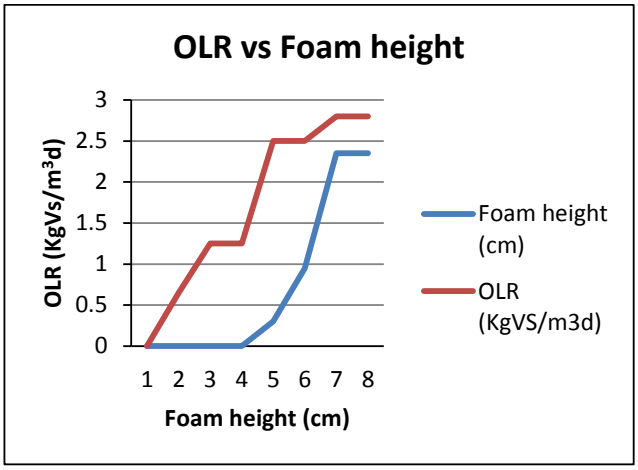

Figure 3: OLR Foam height

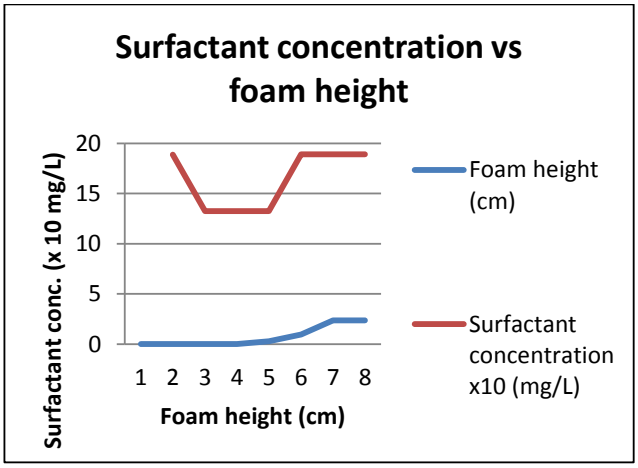

Figure 4: Surfactant concentration versus foam height

The surfactant concentration of the feed sludge was taken when collected from the WWTP. It was observed that an increase in surfactant concentration result to an increase in the foaming potential. Another observation was an increase in surfactant and soluble protein concentration with storage time. It is thought that as the sludge is kept for a longer time, digestion progresses thus the increase in protein and surfactant concentration which is supposedly a result hydrolysis.

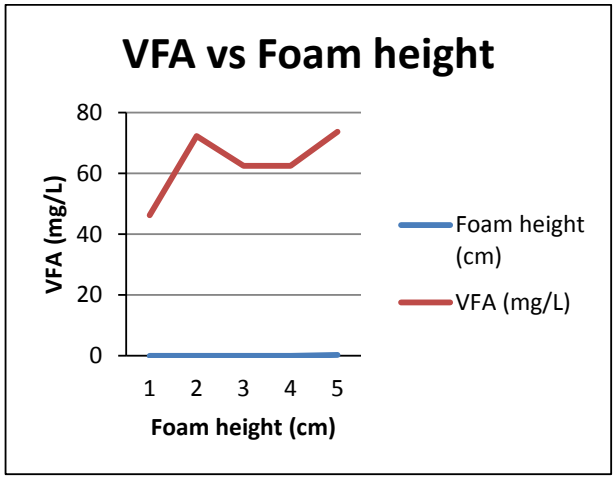

Figure 5: VFA versus foam height

VFA concentration did not seem to have any significant influence on foaming as variations in the volatile acid concentration did not concur with variations in foaming as shown in figure.
Digester fed with glucose did not foam even when fed with a higher organic loading rate this is supposedly attributed to the absence of surfactant in the fed glucose. In addition, glucose is not a complex particle that needs to undergo hydrolysis thus there is no secretion of extracellular substance necessary for hydrolysis (Metcalf and Eddy, 2010).

8.0 Conclusion

In conclusion, the experiment was useful in developing a better understanding of foaming in anaerobic digester. Based on the preliminary data collected, surfactant concentration, percentage variation in organic loading rate, rate of biogas production and percentage of digester volume covered with foam were viewed as the significant variables necessary for a proper modelling of anaerobic digester foaming.

9.0 Future work

The next step will be to select a suitable model and carry on with laboratory experiment as to generate sufficient data to fit into the model. The model when developed will be useful in predicting anaerobic digester foaming such that dosing of antifoam will only be done when necessary

Acknowledgement
I sincerely appreciate all the assistance from Veolia Water Uk for all their contribution in terms of providing sludge samples and historical data.

REFERENCES

[1] APHA, 2012. Standard Methods for the Examination of water and Wastewater. 22 ed. Washinghton: American Public Health Association.

[2] Banfield, P. & Littlejohn, J., 2013. Waste 2 Energy_Seafield Case Study. (Online) Available at: http://www.ice.org.uk/ice_web_portal/media/scotland/gwos-waste2energy-seafield-100113.pdf (Accessed 24 February 2014).

[3] Barber, W., 2014. Influence of wastewater treatment on sludge production and processing. Water and Environment Journal, 28(1), pp. 1-10.

[4] Barjenbruch, M., H., H., O., K. & J., T., 2000. Minimising of foaming in digesters by pretreatment of the surplus sludge. Water Science and technology, 42(9), pp. 235-241.

[5] Batstone, D. et al., 2002. Anaerobic Digestion Model No. 1, London: IWA publishing.

[6] Dalmau, J., Cosmas, J., Rodriguez-Roda, I., Latrille, E., Steyer, J., 2010. Validation of a knowledge-based risk model for biological foaming in an anerobic digestion simulation. Environmental Engineering and management Journal, Volume 9, 2, pp. 223-229.

[7] Dalmau, J., Cosmas, J., Rodriguez-Roda, I., Pagilla, K., Steyer, J., 2009. Model development for predicting risk of foaming in anaerobic digester. Bioresource Technology, Volume 101, pp. 4306-4314

[8] Fryer, M., O'Flaherty, E. & Gray, N., 2011. Evaluating the Measurement of Activated Sludge Foam Potential. Water, pp. 424-444.

[9] Kanu, I., Aspray, T. & Adeloye, A., 2015. Understanding and Predicting Foam in Anaerobic Digester. International Journal of Biological, Biomolecular, Agricultural, Food and Biotechnological Engineering, 9(10).

[10] Filbert, J. W., 1985. A survey of anaerobic digester operations, Boston: Specialty conference, Environmental Engineering, American Society of Civil Engineers.

[11] Ganidi, N., Tyrel, S. & Cartmell, E., 2009. Anaerobic digestion foaming causes - A review. Bioresource Technology, Volume 100, pp. 5546 - 5554.

[12] Ganidi, N., Tyrrel, S. & Cartmell, E., 2011. The effect of organic loading rate on foam initiation during mesophilic anaerobic digestion of municipal wastewater sludge. Bioresource Technology , Volume 102, pp. 6637-6643.

[13] Guitian, J. & Joseph, D., 1998. How bubbly mixtures foam and foam control using a fluidized bed. International Journal of Multiphase Flow, pp. 1-16.

[14] Metcalf and Eddy 2014. Wastewater Engineering - Treatment and Resource recovery. Fifth Ed. New York: McGraw-Hill International

[15] McGinnis, D. et al., 2006. Fate of rising methane bubbles in stratified waters: How much methane reaches the atmosphere? Journal of Geophysical Research, 111(C9).

[16] Moeller, L., Herbes, C., Müller, R. A. & Zehnsdorf, A., 2010. Formation and removal of foam in the process of Anaerobic Digester. Landtechnik 65, 3(Energy production), pp. 207-207.

[17] Moeller, L. et al., 2012. Comparative review of foam formation in biogas plants and ruminant bloat. Energy, Sustainability and Society, 2(12).

[18] Montgomery, H. A., Dymock, J. F., & Thom, N. S. (1962). The rapid colorimetric determination of organic acids and their salts in sewage-sludge liquor. Water Pollution Research Laboratory.

[19] Niekerk, A. et al., 1987. Foaming in anaerobic digesters- a survey and laboratory investigation. Journal of Water Pollution Control Federation, 59(5), pp. 249-253

[20] Oerther, D., De Los Reyes, F., De Los Reyes, M. & Raskin, L., 2001. Quantifying filamentous microorganisms in activated sludge before, during and after an incident of foaming by oligonucleotide probe hybridizations and antibody staining. s.l.: Water Research 35, 14, 3325-3336.

[21] Rodriguez-Roda, I. et al., 2013. Anaerobic Digester Foaming: occurrence and control in Spain, s.l.: IWA; accessed on February, 10, 2014. URL: http://www.redbiogas.cl/wordpress/wp-content/uploads/2013/07/IWA-11509.pdf.

[22] Rustum, R. & Adeloye, A., 2011. *Artificial Intelligence Modeling of Wastewater Treatment plants:Theory, applications and limitations..* 1 ed. s.l.:VDM

[23] Subramanian, B. et al., 2012. Survey of causes and prevention/control of anaerobic digester foaming- A WERF study, s.l.: WERF.

[24] Subramanian, B. & Pagilla, K., 2015. Mechanisms of foam formation in anaerobic digesters. Colloids and Surfaces B: Biointerfaces, Volume 126, pp. 621-630.

[25] WEFTEC, 2007. Anaerobic Digestion. In: Operation of Municipal Wastewater Treatment Plants. s.l.:WWW. WEFNET.org, pp. 30-3 to 30-58.

[26] Westlund, A., Hagland, E. & M., R., 1998. Operational aspects on foaming in digesters caused by Microthrix parvecilla. Water science and technology, 38(8-9), pp. 29-34.

[27] Williams, T. O. & Tim, S., 2012. Mixing Anaerobic Digester with high strenght waste addition. Amherst, Massachusetts, North East Residuals & Biosolids Conference.
[28] WRAP & NNFCC, 2015. *The Official Information Portal on Anaerobic Digestion.* [Online] Available at: http://www.biogas-info.co.uk/index.php/ad-map.html [Accessed 28 January 2015]

Infrastructure and Environment Scotland 3rd Postgraduate Conference
9th December 2015
Heriot-Watt University, Edinburgh

Analysis of breakage of sand under triaxial compression

Z. Karatza[a], E. Andò[b,c], S.-A. Papanicolopulos[a], J. Y. Ooi[a], G. Viggiani[b,c]
[a]Institute for Infrastructure and Environment, University of Edinburgh, U.K.
[b]Université Grenoble Alpes, 3SR, France
[c]CNRS, France
(e-mail: z.karatza@ed.ac.uk)

ABSTRACT

Breakage of grains is encountered in many engineering practices; some examples are pile driving and cone penetration testing, milling of industrial products and sanding oil wells. Therefore, among several fields including geomechanics, geoscience, particle technology, minerals and mining engineering, geology and geophysics, the mechanisms leading to breakage pose a challenge, since changes in the microstructure can lead to significant changes in the macroscopic bulk behaviour of a material. The main goal of this research is to develop a new understanding of the particle breakage mechanisms in a granular material under triaxial loading at high confinement. This is achieved by observing and measuring the microscopic changes that an assembly of grains undergoes while being loaded/deformed. The possibility to study and visualise the 3D volume of a specimen during loading is given by x-ray computed tomography. In the present work, image processing tools have been developed in the prospect of quantifying breakage and linking it to the macroscopic response of a sand. This is done by Digital Image Correlation where conclusions have been drawn about the maximum shear stress and the volumetric response of the specimen. The evolution of the grain size distribution is presented, along with an analysis of the size of the grains that tend to break; both of which have never been presented before to knowledge of the authors. This information is linked to the kinematic shear band as it has been defined by a Digital Image Correlation.

1. INTRODUCTION

Be it a specimen in a laboratory or a whole soil formation in nature (natural or man-made e.g. dam, mountain, tunnel, embankment) or in industry (e.g. silo, material transported on a conveyor belt) particle breakage is important because it can cause significant changes in the microstructure of a material, that will greatly affect its macroscopic behaviour. The most important michromechanical changes would be in the particle size distribution and the contact network, since particles that break into smaller particles will start filling the pore space, creating more contacts per particle at the location where breakage takes place. This will possibly reduce the permeability and the overall strength of the material, will make it volumetrically respond differently under shear loading (*e.g.* start compacting with an increasing rate) and the concentration of breakage could cause discontinuities and/or localised deformation. The aforementioned are an undeniable reason as to why grain breakage has been extensively studied experimentally, theoretically and numerically. However, even though it has been a common research topic among several fields (*e.g.* geomechanics, particle technology, material processing, mining engineering, geophysics, civil engineering), there are still key aspects that ought to be studied in order to fully understand and describe this phenomenon.

There are many examples in the literature (*e.g.* Roscoe et al., 1958, Colliat-Dangus et a., 1988 Nakata et al., 2001) that present a detailed analysis of experiments performed on sands regarding its bulk behaviour under triaxial loading. A specimen can dilate and/or compact depending on its relative density, the lubrication of the end surfaces, the initial grading and shape of the particles and the mean stress among other factors. When a loose sand is sheared it contracts and the grains start to slide and roll relative to each other; when it can't contract any longer and a stress threshold has been surpassed it starts to dilate. This dilatancy will produce additional compaction potential to the material and should the imposed stress be high, then particles will start to break. The breakage will cause a continuous evolution in the grain size distribution, essentially creating a new material, with higher compressibility, different grading and fabric. Therefore the critical state will not be as predicted from the intact material.

These studies, contribute greatly to the understanding of how dry granular materials will behave in the macro scale under various loading schemes. However, making a link between the microscopic changes caused by breakage and the bulk response of a material is quite challenging.

Continuum constitutive models can predict the evolution of breakage, contact network or strain localisation, taking into account experimental observations and measurements about the bulk response and the post-testing state of the specimen.. So, being able to quantitatively describe breakage at all loading stages is necessary in order to gain a better understanding.

In this work, x-ray computed micro-tomography (hereinafter XCT) has been employed. XCT has enabled the observation in 3D of the deformation of the materials under load. Even though XCT has been used extensively as a medical diagnostic tool since the 1970s, it has only recently been used as a research tool in geomechanics (*e.g.* Desrues et al., 1996, Alshibli and Hasan, 2008, Hall et al., 2010, Andò et al., 2011, Saadatfar et al., 2012, Wildenschild and Sheppard, 2013, Nguyen et al., 2015). The breakthrough with it is that 3D images are acquired as a function of the density of the specimen and apart from mere observation, discrete measurements can be made from processing the images, provided that the resolution (magnification) is such that enough pixels comprise each grain. The high resolution of the images of this study (down to 8.2μm) enabled the clear observation and precise measurement of the deformation and kinematics of each grain (*e.g.* size, shape, position, translation, rotation). This valuable information not only helps understand in depth the mechanisms that govern breakage, but can also be used as an improved benchmark test for the calibration and comparison of DEM particle scale simulations (*e.g.* Cil and Alshibli, 2015).

2. EXPERIMENTAL CAMPAIGN

2.1 Tested material

The material used for this study is Caicos ooids (CO); a sand with very rounded particles that grow from fragments of corals (concretions of calcium carbonate and aragonite crystals), coming from the Ambergris Shoal in the Caicos platform, in the British West Indies (Lloyd et al., 1987). The material was chosen because it is small enough to create a specimen rather than an assembly of grains, due to the limitation of the size of the apparatus, dictated by the image acquisition. Also it is big enough for the resolution of the tomograph and so reasonable information can be gathered.

The material provided by Exxon Mobile has a D_{50} of 320μm and it is well graded (COW) with a coefficient of uniformity equal to 1.33 ($Cu=D_{60}/D_{10}$). The e_{min} and e_{max} have been experimentally determined (using a vibratory table [ASTM D4253]) and are 0.34 and 0.71 respectively. Since uniformly graded (almost mono-disperse) specimens will have larger voids among grains, helping develop more plastic deformation and breakage, the material was sieved (opening of 315μm), in order to create specimens with a more uniform (COU) grain size distribution, resulting to a slight increase of the D_{50}, which has now gone up to 380μm. The e_{min} and e_{max} are for this case 0.63 and 0.92 respectively and the coefficient of uniformity 1.19.

2.2 X-ray computed tomography

As shown on Figure 1, an x-ray source emits a polychromatic beam of photons which interacts with the material that is being scanned. The number of photons that cross the material (ergo not attenuated by the material) are recorded by a detector (opposite to the source) as a projection of the density of the whole scanned object at a certain orientation. To get a 3D image of the specimen, it is necessary to acquire multiple projections at different orientations, therefore the specimen is being rotated. The number of times the specimen is rotated will define the number of acquisitions, that will be later on reconstructed into a 32-bit grey scale stack of images (3D volume – Figure 2). With XCT it is possible therefore to extract incremental 4D (4th dimension being time) information about the deformation of a material, in a non destructive way.

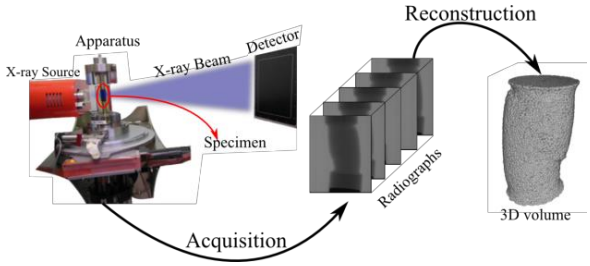

Figure 1. X-ray scanner in Laboratoire 3SR, Grenoble, France and a schematic of the image acquisition process.

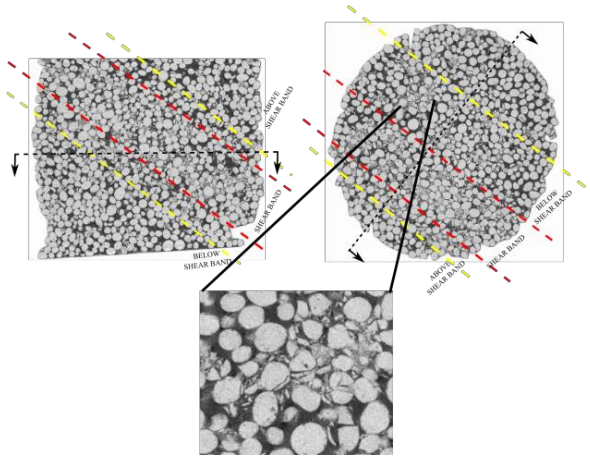

Figure 2. Vertical (half) and horizontal sections of TrCOU03, with detail of breakage.

2.3 Testing program & macroscopic response

Table 1 summarizes some basic information about the performed triaxial tests and together with the stress-strain response (Figure 3), it can be concluded that the tests are fairly repeatable.

Table 1. Details on performed tests

Test	H [mm]	D [mm]	D_{50} [mm]	Resolution [mm]	Scans
TrCOW01	22.3	10.1	0.32	N/A	N/A
TrCOU01	23.5	9.4	0.38	0.016	12
TrCOU02	24.5	9.4	0.28	0.016	7
TrCOU03	20.5	10.5	0.38	0.008	2
TrCOU04	22.0	10.0	0.38	0.015	6

The triaxial cell and the specimen preparation method are described in detail in Alikarami et al., 2015. During XCT, the specimen must not be straining or changing in any way, and therefore the loading was paused for the duration of the image acquisition (indicated by the stress relaxations that can be observed in Figure 3). These increments will be referred to as loading stages (LS). The loading direction at all tests was ascending with a displacement rate of 21μm/min (ε_a=0.001%) and the confining pressure was always 7MPa.

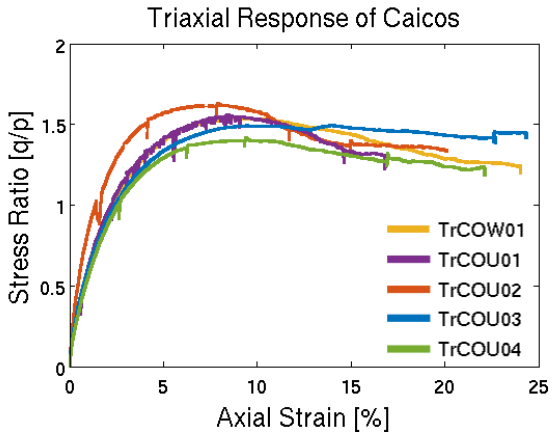

Figure 3. Macroscopic response of triaxial tests performed on Caicos ooids.

The response of the triaxial tests largely depends on the grain size and the initial relative density of the specimens. The response indicates that TrCOU02 is the strongest among the specimens and TrCOU04 the least, which is consistent with their initial relative density. It is also clear that all specimens yield at a similar stress value (plateau) apart from TrCOU03, for which it should be mentioned that this increase of q/p is likely due to a drop in the mean pressure form a sudden increase in confinement during the test. TrCOU02 has a much smaller D_{50} and the response is stiffer compared to the rest of the specimens. It should be mentioned that the contribution of the membrane to the lateral stress has been accounted for (Bishop and Henkel, 1957).

3. IMAGE PROCESSING

Since this work focuses on studying the microscopic changes that an assembly of grains undergoes *during* loading, it is only appropriate to say that the need to investigate the deformation other than the bulk stress-strain response is vast. Even if local changes in the specimen are obvious to the naked eye, they can not always be scientifically described by conventional experimental means. It is impossible for any information to be gained between measurement points (loading stages), unless the deformation process is perfectly homogeneous in which case the material itself would have to be perfectly homogeneous. The breakthrough with XCT is that 3D images of the whole specimen are acquired and along with the high resolution of the images, a clear observation and precise measurements of the deformation and kinematics of each grain are enabled. The algorithms that are employed in order to pre-process the images (not described in this paper) and then measure the desired parameters, are what is called *image processing*. Such measurements can be described as *full-field measurements*, which are non-contact measurements of a field of data (e.g. kinematics) over the entirety of a specimen, that help characterise local variations of a property in the response of a specimen (Viggiani and Hall, 2008).

The measurements that are performed taking into consideration the grey scale variations can be described as continuous measurements. These are measurements where the grains are not identified as single entities and the results are displayed as maps of the variable property. The main benefits of grey scale image processing is that there is no need to distinguish between different phases (elimination of thresholding errors) and also it can provide good information about localisation. It is not possible to gain information regarding the fabric of the specimen and to identify individual grains and track their deformation. To do so, the image has to be binarised, in which case a thresholding algorithm has to be developed to segment the image into two phases (most commonly into solid and void). Although with such discrete measurements many limitations of the continuous approach are overcome, the decision of the thresholding algorithm is not always straight-

forward and most algorithms are sensitive to slight variations of the threshold and do not work well at contacts and when there is some texture inside a grain (*e.g.* pores, denser matter).

3.1 Digital image correlation

Digital Image Correlation (Hall, 2006; Viggiani and Hall, 2008) which will be referred to as DIC from now on, is a method of non-contact full-field kinematics measurements of planar or non-planar surfaces undergoing deformation. In this paper a 3D volumetric version of the DIC has been employed. It is a mathematical tool for assessing the spacial transformation (warping) between 2 digital images, so it is a way to monitor deformation. DIC is performed incrementally between sequential loading stages. The reference image is segmented into smaller cubic regions (REV) and each of them will be correlated with cubic regions of the same size within a predefined region in the deformed image. The REV with the highest normalised cross correlation of the grey intensity will represent the deformed state of the cube under investigation and based on their spacial coordinates the displacement vectors will be defined. A great advantage of this method is that processes can be identified while a specimen is loaded, that are not visible at the beginning or the end of a test. Making a continuum hypothesis, with a shape function of a hexahedron with 8 nodes, from the 3D displacement vectors the strain tensor can be computed based on the large strain theory.

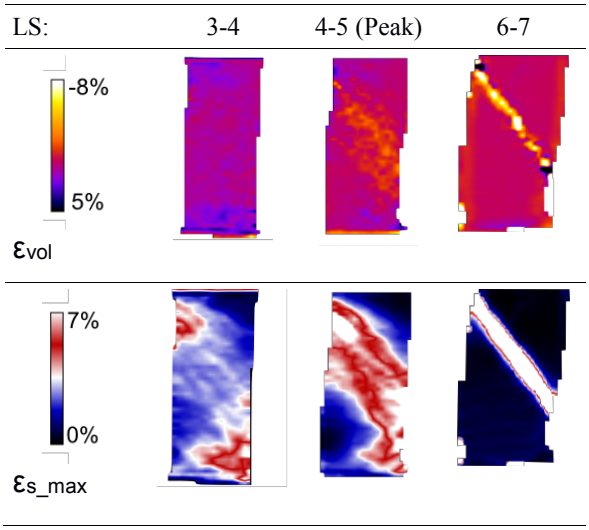

Figure 4. DIC results on selected increments of TrCOU01.

Only a few interesting increments of the DIC analysis are presented in this paper, the whole study will be presented in a future paper. Between LS3-LS4 (both pre-peak) there is a high compaction (Figure 4 top left) where high shear stresses are present (Figure 4 bottom left) and slight compaction throughout the rest of the specimen; no dilation is present yet. Between LS4-LS5 (pre-peak & peak) regarding the volumetric strains we only observe a slight dilation (1-2%) around where later on the strain will localise, the rest of the specimen will compact a bit. However, there is an intense increase of the maximum shear strain during this increment, from which it is concluded that the shear band will not form from one distinct point, but rather from the accumulation of shear strains on the top and bottom that eventually meet. At its residual strength (LS6-LS7) a shear band can be identified and will have a thickness of 4-5 particles (Figure 5) and hardly any strain is present to the rest of the specimen. Finally, from the last increment at the volumetric strain, it appears that where the shear band will form there is a dilatant (6-8%) band of 2-3 particles thick, whereas the rest of the specimen seems to not undergo any serious volumetric changes. To conclude, only from the DIC analysis, it is clear that even before peak stress the specimen will only produce a dilative response, especially along where intense shearing has been calculated. However, conclusions on whether the specimen dilates because it starts to break when it has been sheared or the other way around can not be drawn from a DIC analysis.

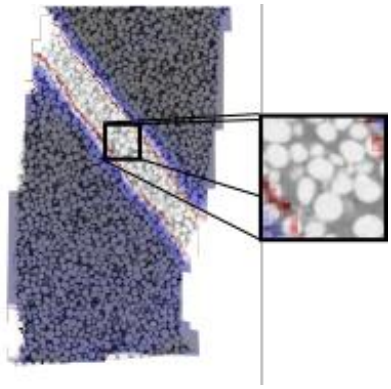

Figure 5. Thickness of shear band.

3.2 Evolution of grading

The most common particle size measurement, especially in geotechnical engineering and in industrial applications is sieving. It has been proven (*e.g.* Syvitski, 1991) that sieves sort particles according to size and shape, unless the size of the particles is defined in terms of the nominal diameter (based on the equivalent volume of a sphere), in which case the sieving process does not sort according to size. However, recent studies insist on using the nominal diameter as an equivalence to the particle size, whether this comes from a sieving process, a screening process (*e.g.* Mastersizer) or from 3D image-based measurements of particle volume (*e.g.* Coop et al., 2004, Cavarreta et al., 2009, Fonseca et al., 2014, Alshibli et al., 2014, Sun et al., 2015). In this work an effort has been made to correlate 3D image

based measurements of both the intact and post-test deformed specimens with various 2D size measurement techniques. From the XCT images, each individual grain was identified and labelled and different shape and size properties were measured. Considering an infinite number of sieves, the grading curves (based on a corrected nominal diameter) were plotted next to the grading curves from a sieve process in order to be compared (Figure 6). The correction seems to have been shifting the curve measured from the images towards the direction of the sieve, which will allow a direct comparison to previous studies where image processing was not possible.

A grading analysis provides information about the degree of breakage and many authors have used the shape of the grading curve to create Continuum Breakage Mechanics (CBM) models (*e.g.* Hardin, 1985, Einav, 2007a, Einav, 2007b, Sun et al., 2015, Tengattini et al., 2015) to investigate the compressibility and degree of breakage of the specimen. However, most of these studies rely on the difference of the shape of the grading curve before and after performing a compression test. The contribution of the XCT images and the image analysis has lead the authors to investigate the evolution of the grading at different loading stages during an experiment (Figure 7); and to the knowledge of the authors this has not been presented before. From the histogram of the grain sizes, it is obvious that the majority of grain sizes range between 0.30 and 0.45mm. While loading progresses, it is clear that grains above 0.45mm will not break (but they only comprise a small amount of the grains in the specimen), grains close to the D_{50} will clearly start to break, whereas the production of fines is also clear but does not allow the observation of the number of small particles that have also broken. This can be achieved only by tracking each individual grain, which will be presented in the future by the authors.

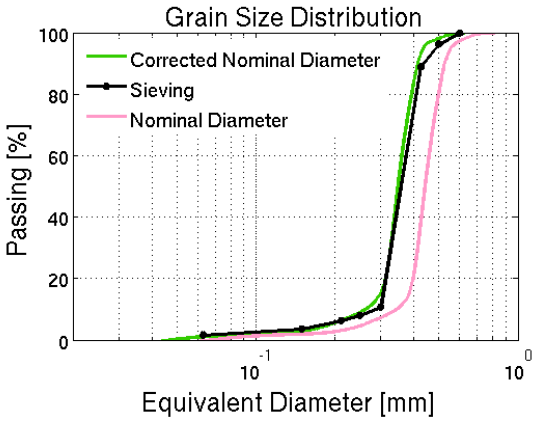

Figure 6. Comparison between sieve curve (black) and image processing curve based on nominal diameter (pink) and corrected curve based on shape parameters (green).

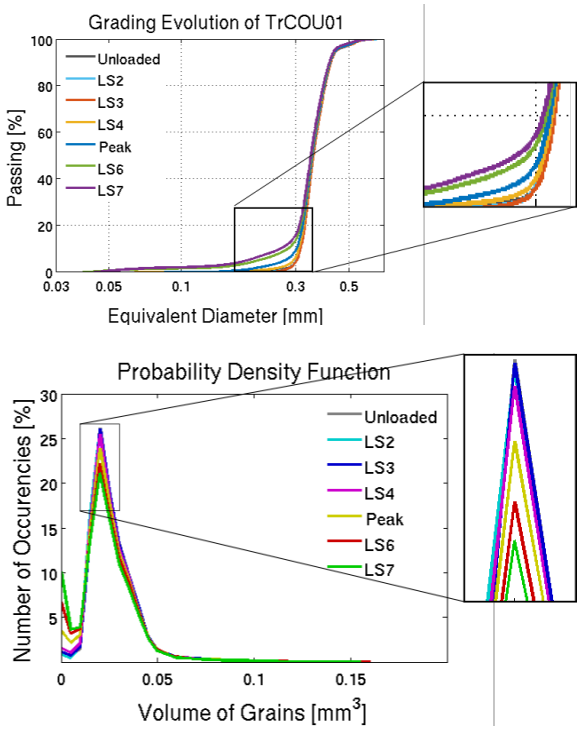

Figure 7. Evolution of GSD and PDF for TrCOU01.

4. CONCLUSIONS

In this paper, part of the quantitative analysis regarding breakage of a sand under triaxial loading is presented. X-ray computed micro-tomography (XCT) has been employed in order to enable the observation in 3D of the deformation and kinematics (the full response) of the sand under load. The XCT images have been processed and *full-field measurements*, such as Digital Image Correlation (DIC), were performed in order to characterise local variations of the density, from which displacement (and strain) fields were calculated. It was concluded that during breakage only dilation occurred, a shear band of 4-5 particles was formed, where the inner part of a couple of particles was described by a high dilation surrounded by a region of hardly any volumetric strain. From discrete image processing the evolution of the particle grading during loading was also presented here. It is evident that the first change in grading, which indicates breakage, happens at LS4, before peak stress is reached. However the first important change in grading occurred during peak, even though from the DIC analysis even before peak there is a lot of shearing happening throughout the specimen. Finally, from the probability density function a reduction of the number of grains right below the D_{50} proves that those will be the main grains affected by breakage. However, to measure how many smaller grains will

break and correlate the breakage of the shear band, as described by the DIC, further analysis needs to take place. Such research helps understand more about the mechanisms that govern breakage, but can also be used as an improved benchmark test for the calibration and comparison of DEM particle scale simulations.

REFERENCES

Alikarami, R., Andò, E., Gkiousas-Kapnisis, M., Torabi, A., Viggiani, G. (2015). Strain localisation and grain breakage in sand under shearing at high mean stress: insights from in situ x-ray tomography. *Acta Geotechnica,* 10:15-30.

Alshibli, K.A., Druckrey, A.M., Al-Raoush, R.I., Weiskittel, T., Lavrik, N.V. (2014). Quantifying morphology of sands using 3D imaging. *Journal of Mat. In Civ. Eng.,* 27(10):1-10.

Alshibli, K.A., Hasan, A. (2008). Spatial variation of void ratio and shear band thickness in sand using X-ray computed tomography. *Géotechnique,* 58(4):249-257.

Andò, E., Hall, S.A., Viggiani, G., Desrues, J., Bésuelle, P. (2011). Grain-scale experimental investigation of localised deformation in sand: a discrete particle tracking approach. *Acta geotech.*

Bishop, A.W., Henkel, D.J. (1957). The measurement of soil properties in the triaxial test.

Cavarretta, I., O'Sullivan, C., Coop, M.R. (2009). Applying 2D shape analysis techniques to granular materials with 3D particle geometries. *Proc. of 6th International Conference on the Micromechanics of Granular Media.*

Cil, M.B, Alshibli, A. (2015). Modeling the influence of particle morphology on the fracture behaviour of silica sand using a 3D discrete element method. *Comptes Rendus Mechanique,* 343:133-142.

Colliat-Dangus, J.L., Desrue, J., Foray, P. (1988). Triaxial testing of granular soil under elevated cell pressure. *Proc. of conference on advanced triaxial testing for soil and rocks, Philadelphia: American Society for Testing and Materials.,* STP977:290-310.

Coop, M.R., Sorensen, K.K., Bodas Freitas, T., Georgoutsos, G. (2004). Particle breakage during shearing of a carbonate sand. *Géotechnique,* 54(3):157-163.

Desrues, J., Chambon, R., Mokni, M., Mazerolle, F. (1996). Void ratio evolution inside shear bands in triaxial sand specimens studied by computed tomography. *Géotechnique,* 46(3):529-546.

Einav, I. (2007a). Breakage mechanics part I: theory. *Journal of Mech and Phys of Solids* 55(6):1274-1297.

Einav, I. (2007b). Breakage mechanics part II: modelling granular materials. *Journal of Mech. and Phys. of Solids* 55(6):1298-1320.

Fonseca, J., Sim, W.W., Shire, T., O'Sullivan, C. (2014). Microstructural analysis of sands with varying degrees of internal stability. *Géotechnique* 64(5):405-411.

Hall, S.A. (2006). A methodology for 7D warping and deformation monitoring using time-lapse seismic data. *Geophysics,* 71(4):21-31.

Hall, S.A., Bornert, M., Desrues, J., Pannier, Y., Lenoir, N., Viggiani, G., Bésuelle, P. (2010). Discrete and continuum analysis of localised deformation in sand using X-ray μCT and volumetric digital image correlation. *Géotechnique,* 60(5):315-322.

Lloyd, R.M., Perkins, R.D., Kerr, S.D. (1987). Beach and shoreface ooid deposition on shallow interior banks, Turks and Caicos islands, British West Indies. *Journal of Sedimentary Petrology,* 57(6):976-982.

Nakata, Y., Hyodo, M., Hyde, A.F.L., Kato, Y., Murata, H. (2001). Microscopic particle crushing of sand subjected to high pressure one-dimensional compression. *Soils and Found.*, 41(1):69-82.

Nguyen, T.T., Yvonnet, J., Zhu, Q.-Z., Bornert, M., Chateau, C. (2015). Crack nucleation and propagation in highly heterogeneous microstructures models based on X-ray CT images of real materials. *Proc. of 12e Colloque National en Calcul des Structures*, *Presqu'île de Giens, France.*

Roscoe, K., Schofield, A.N., Wroth, C.P. (1958). On the yielding of soils. *Soils and Found.*, 54(3):451-461.

Saadatfar, M., Sheppard, A.P., Senden, T.J., Kabla, A.J. (2012). Mapping forces in a 3D elastic assembly of grains. *Journal of Mech. And Phys. of Solids,* 60:55-66.

Sun, Y.F., Xiao, Y., Hanif, K.F. (2015). Compressibility dependence on grain size distribution and relative density in sands. *Technological Sciences,* 58(3):443-448.

Syvitski, J.P.M. (1991). Principles, methods and application of particle size analysis. *Cambridge University Press.*

Tengattini, A., Das, A., Einav, I. (2015). A theory predicting breakage dependence of critical state in sand. *Geomechanics from Micro to Macro, CRC Press,* 695-698.

Viggiani, G., Hall, S.A. (2012). Full-field measurements, a new tool for laboratory experimental geomechanics. *ALERT Doctoral school.*

Wildenschild, D., Sheppard, A.P. (2013). X-ray imaging and analysis techniques for quantifying pore-scale structure and processes in subsurface porous medium systems. *Advances in Water Resources,* 51:217-246.

Infrastructure and Environment Scotland 3rd Postgraduate Conference
9th December 2015
Heriot-Watt University, Edinburgh

Near-Bed Turbulence Characteristics in Unsteady Hydrograph Flows over Mobile and Immobile Gravel Beds

Jonathan Kean, Alan Cuthbertson & Lindsay Beevers
Institute for Infrastructure and Environment,
Heriot-Watt University
(e-mail: jk103@hw.ac.uk)

ABSTRACT

Improvements to sediment transport prediction requires enhanced understanding of the turbulent flow conditions present within the wall region. However, current knowledge of changes to near-bed turbulent flow structure under unsteady hydrograph flows and mobile sediment conditions is lacking. This paper looks specifically at the effects of differences between mobile and immobile beds on the near-bed turbulent burst and sweep events generated, as well as considering the influence of unsteady flow on these phenomena over both mobile and immobile gravel beds. Quadrant analysis has been used to estimate the number and strength of turbulent burst and sweep events over both types of bed. Initial results indicate that the mobile bed experiences less burst and sweep events in the wall region compared to the immobile bed. However, those that do occur are stronger than those detected over the immobile bed. Further study to examine how the results of a hole-size analysis of quadrant plots may be correlated with observed sediment transport in unsteady hydrograph flows can now be carried out following these results, which have demonstrated that higher strength rather than higher volume of turbulent burst/sweep events are found where conditions are favourable for sediment transport.

1. INTRODUCTION

Existing methods of sediment transport prediction, based on excess shear stress (e.g. Shields) tend to yield poor and/or unreliable results, particularly under unsteady flow conditions. New approaches that consider turbulent flow-sediment particle interactions in greater detail are therefore needed to improve predictive capabilities for sediment transport.

In particular, the lack of research investigating the temporal variation in near-bed turbulence structure in open-channel flows over the duration of smooth, natural-shaped flood hydrographs has been recently highlighted (e.g. Jain et al. 2015; Taberestani and Zarrati 2015). Some previous studies have been conducted on the effects of flow unsteadiness on the near-bed turbulent structure. One key study by Nezu et al (1997) produced the finding that turbulence is stronger in the rising stage than in the falling stage of the hydrograph. This has also been observed by Bares, Jirak and Pollert (2008) who commented on the 'strong' hysteresis effect, this time in a closed channel. These findings introduce the idea of loop properties in turbulence under unsteady flow conditions showing a major difference between turbulence under unsteady hydrographs in comparison with the equivalent values under steady flow conditions.

Existing methods of sediment transport which are based on shear stress originate from a calculation based on the streamwise and vertical velocity fluctuations from the mean. These velocity components have been identified by a number of authors (Einstein, 1950; Gordon, 1975; Pedlosky, 1987; Kundu 1990) as having high influence over sediment transport. Several authors (e.g. Boyer, Roy and Best, 2006) extended this idea to examine the RMS value of velocity fluctuations to obtain the turbulence intensity. This has led to further research, such as that by Paiment-Paradis, Marquis and Roy (2011) looking at turbulence and its effect on drag and lift forces on individual sediment grains, and thus also sediment transport.

One aspect of turbulence which has been examined in conjunction with sediment transport is the quadrant technique, outlined by Lu and Willmarth (1973). According to Paiment-Paradis, Marquis & Roy (2011), this method can be used to examine the original instantaneous velocity time series output and then detect specific turbulent structures (Inward interactions, Bursts, Outward Interactions and Sweeps). There are two specific outputs from the quadrant technique which have attracted more attention in the literature than any other, these are the burst (Q2) and sweep (Q4) events. One of the earliest findings in this area was by Drake et al. (1988) who studied instantaneous velocities in alluvial streams and concluded that 'the majority' of transport which occurred was

associated with the occurrence of sweep events. Hofland et al. (2005) found that sweep events in particular were of interest as they had the energy to penetrate deeper within the gravel bed compared to other coherent flow structures which had previously been looked into. This opens up the possibility of having one dominant turbulent event that has significantly higher influence over the transport rate than others.

While Drake et al. (1988) looked at transport as a whole, Paiment-Paradis, Marquis & Roy (2011) examined individual grains being transported in rolling motion. They found, to the contrary, that burst events were those which were dominant at the same time as transport of an individual grain occurred. There are mixed views on which, if either burst (Q2) or sweep (Q4) are more responsible for bedload transport events. Dey, Sarkar and Solari (2011), for example, began a study focusing specifically on burst events; but stated in their conclusion that they believed sweep events were more responsible for entrainment of particles at the beginning of transport. They did, however, not reach a firm conclusion on the link between burst/sweep occurrence and the overall transport of bedload. Sechet and Le Guennec (1999) also agree with the opinion that burst and sweep events, in particular, exert a strong influence on the bed surface and thus result directly in the transport of individual sediment grains – however they did suggest a more probabilistic approach following statistical analysis of their data having identified that burst and sweep events could each potentially be two separate modes of transport.

Specific details of the fluid-sediment interactions generated, and how these vary between (i) steady and unsteady flow conditions and (ii) static and mobile bed conditions remains relatively poorly understood. This is because previous studies have not focused specifically on the interactions with an erodible sediment bed. Therefore, a missing element from previous studies is a comparison between near-bed turbulent structure over an erodible bed and an immobile bed, which would improve understanding of the turbulence conditions under which sediment transport occurs in unsteady flow.

The natural progression, given the proposed link between burst/sweep events and the transport of individual sediment particles, is therefore to study the influence of flow unsteadiness on the near-bed turbulent structure over both mobile and immobile sediment beds. As such, this will provide new understanding of the reciprocal near-bed, fluid-sediment interactions that would be expected to have a primary role in determining sediment transport rates.

This paper aims to improve understanding of the near-bed turbulent conditions which exist during sediment transport across unsteady flow by use of the quadrant technique to draw comparisons between burst/sweep events observed over immobile and transportable gravel beds. This will provide insight into the quantity and strength of burst/sweep events required for the transport of sediment. The experimental technique employed will first be explained, followed by a discussion of the results obtained.

2. METHODOLOGY

Laboratory experiments have been conducted to measure the temporal evolution of near-bed turbulent structure (in particular, the strength and frequency of burst/sweep motions in the wall region) within a tilting, recirculating (Armfield) flume with dimensions 8 m-long x 0.3 m-wide x 0.3 m-deep. The flume bed was filled with a fine, graded gravel layer (D_{50} = 3.4 mm; D_{84} = 9.0 mm) to a depth of 50 mm. For the immobile bed runs, the bed slope was fixed at 1:300 (i.e. below the threshold slope for bedload transport), while for the mobile bed runs the slope was increased to 1:150. Flow discharge is provided by a pump which is controlled by computer input to a frequency inverter to produce the desired flow hydrograph. A smooth, symmetrical, bell-shaped hydrograph of 2 hours total duration, and with base and peak flows equal to 8.3 $l.s^{-1}$ and 17.3 $l.s^{-1}$, respectively, was used in each test (i.e. the same hydrograph was used for both the mobile and immobile bed runs). Each run (mobile and immobile) were conducted twice to show repeatability of results.

To ensure repeatability, a consistent flume set-up has been carried out prior to each run. The bed is first mixed randomly and then scraped to a constant depth of 50mm using a screed board. This depth is equal to the top level of the sediment trap at the downstream end of the flume. During initial filling of the flume, water is filled slowly such as not to result in transport of any grains on the bed, and the use of a tailgate is employed to ensure that the initial antecedent flow is provided under steady, uniform condition as a consistent starting condition for each run. Antecedent conditions can result in re-arrangement of bed grains; particularly under laboratory conditions such as is the case here. Ockelford (2011) has carried out work which has shown that the volume of transported sediment subject to flow above the threshold for transport following antecedent flow conditions decreases exponentially to a constant value with an increase in initial antecedent flow time. Based on these findings a consistent initial antecedent flow condition of 3 hours to account for bedding-in is applied.

Measurements of instantaneous velocity fluctuations were made throughout the hydrograph using an acoustic doppler velocimeter (ADV) probe positioned on the channel centerline. In order to capture the point at which turbulence is most likely to influence the sediment grains, the ADV sample volume must record data where turbulence is at its greatest. According to Nezu and Nakagawa (1993), turbulent energy is extracted from the mean flow in the wall region (*y/h* 0.0 – 0.15, where *h* is the total flow depth at peak flow) and bursting phenomena in this region occur 'violently'. One feature of this region, outlined by Grass (1971) and Song et al. (1994) is that there is a vertical point of maximum turbulence intensity which decreases slowly moving above the maximum point, however decreases rapidly moving below the maximum point. A result of this is that care must be taken for the ADV sample volume not to fall within the region of rapidly decreasing turbulence intensity. In order to estimate the point of maximum turbulence intensity, vertical profiles have been taken as shown in Figure 1 with a maximum turbulence intensity value noted at *y/h* = 0.05. As the water level fluctuates between approximately 63mm and 100mm, the ADV is positioned with the centre of the sample volume set to be 8mm from the bed. This ensures that the sample volume is positioned entirely at a normalised elevation of *y/h* = 0.06 at the peak flow with no risk of any record being taken in the zone of rapid turbulence intensity reduction.

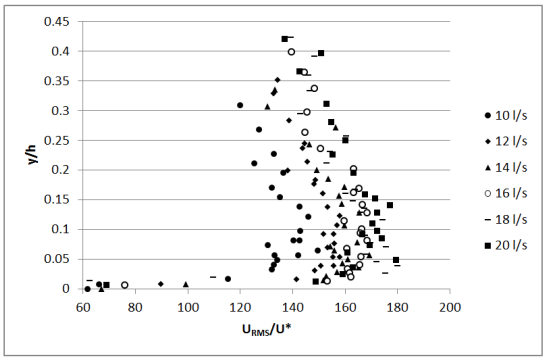

Figure 1. Vertical profiles of nondimensional turbulence intensity in the streamwise direction for flows of 10,12,14,16,18 and 20l/s.

Working close to the bed presents unique challenges when relying on the use of ADV for instantaneous velocity data collection. One particular issue is that of reflections from the surface that can significantly contribute to background noise in the return signal. Two considerations are made in order eliminate this potential source of error: (i) The ADV is run on low power output to reduce the overall background noise produced by reflections; and (ii) Adequate provision of seeding is needed to increase correlation (an indicator of the amount of noise and the quality of the return signal) to a level greater than 70%, as recommended by the instrument manufacturer (Nortek). Probe check charts were consulted in order to confirm that this approach was successful, and Figure 2 shows an annotated comparison between a poor and good return ADV signal.

3. RESULTS

3.1 Velocity and Turbulence over Unsteady Flow

It is seen that the turbulence intensity (RMS value of the fluctuations from the mean velocity) follows a similar pattern over the erodible and immobile beds where the value of turbulence intensity increases with increasing flow, and then decreases with decreasing flow. An example of this is shown in Figure 3. The overall value of turbulence intensity is greater with a greater bed slope; however there is less consistency between the two sets of results over the erodible bed in comparison with the two sets of results over an immobile bed. Further investigation of these results are planned over different hydrograph shapes, however as the results for a single hydrograph shape do not provide detailed insight into the differences between turbulence over erodible and immobile gravel beds, further investigation via quadrant analysis is needed.

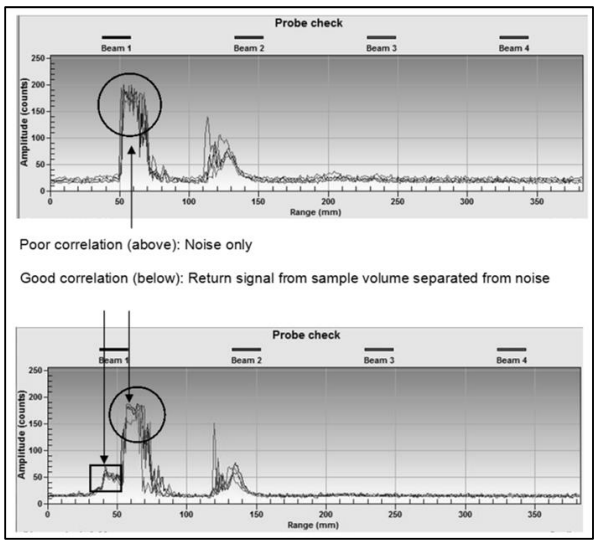

Figure 2. Probe check charts with annotations showing noise (circle) and clean return signal from sample volume (rectangle, bottom chart only)

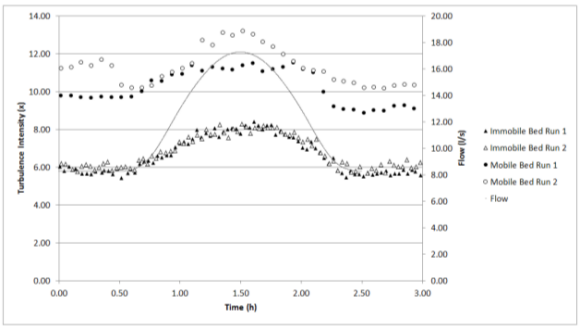

Figure 3. Streamwise turbulence intensity for both an immobile and erodible bed over the symmetrical hydrograph tested

3.2 Quadrant Analysis

Instantaneous velocity data were processed and analysed using the Quadrant Technique, outlined by Lu and Willmarth (1973), to determine the number and strength of the Q2 (burst) and Q4 (sweep) events occurring during each five-minute measurement interval over the duration of the hydrograph. This further detail is an improvement over simply examining turbulence intensity data, as the quadrant technique combines vertical and streamwise turbulent fluctuations to show where the associated effects of extreme fluctuations may have influence on sediment transport.

Quadrant analysis of the near-bed turbulent flow indicates that the total number of overall Q2+Q4 (burst/sweep) events detected above the immobile sediment bed is significantly greater than those detected above the mobile sediment bed. This is somewhat unexpected given previous studies (e.g. Sechet & Le Guennec 1999) suggested that a correlation exists between bedload transport and the prevalence of burst/sweep events. Lu and Willmarth (1973) also introduced the idea of a 'hole' in the quadrant plot to exclude low strength events. This analysis technique has been used in the past by a number of authors (e.g. Sarkar and Dey, 2010) with previous authors either selecting hole size values to compare with previous work, or until a particular effect is observed. In this case, hole-size analysis of specific quadrant plots for individual sample times throughout the hydrographs provides a possible explanation for the apparent discrepancy between results over erodible bed compared to an immobile bed. Figure 5 (a) shows the distribution of the u′ and v′ velocity fluctuations over the immobile (red) and mobile (green) sediment beds. While the turbulent flow over the immobile bed appears to show a greater prevalence of Q2+Q4 events, there is less indication of this in the mobile bed data. However, when a hole-size *H*′ = 3 is applied to both data sets (Figure 5(b)), the number of higher magnitude Q2+Q4 (i.e. burst/sweep) events is greater in the mobile bed, compared to the immobile bed.

In addition, when looking at the occurrence of Q1+Q3 events, along with Q2+Q4 events over the hydrograph with H' = 3 applied is that rather than observing an increase in Q2+Q4 events, we observe a decrease in Q1+Q3 events. Further investigation is needed to conclude upon the causes and effects of the suppression of these events.

A further finding from the analysis is that the proportion of detected near-bed Q2+Q4 events increased by up to 10% between the base and peak flow on the hydrograph rising limb, before reducing back to pre-hydrograph levels again during the falling limb. The next steps will be to conduct a statistical analysis with a view to determining how significant a correlation there is between this increase and the occurrence of bedload transport.

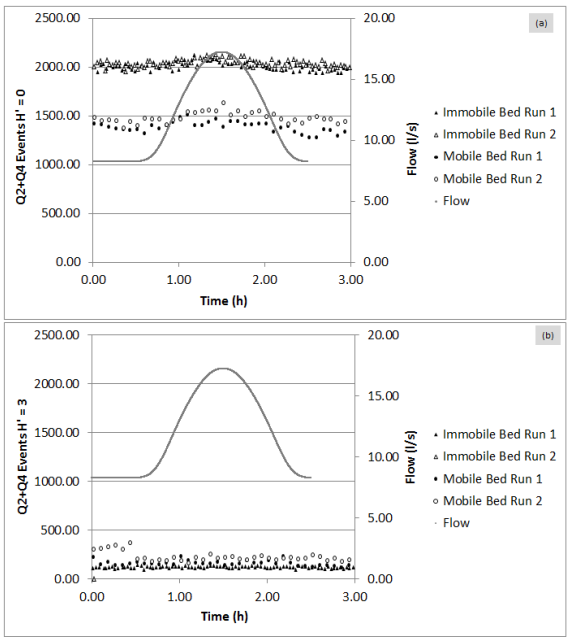

Figure 4. Number of burst and sweep events detected across the hydrograph (a) H' = 0 and (b) H' = 3 for the immobile and erodible bed runs.

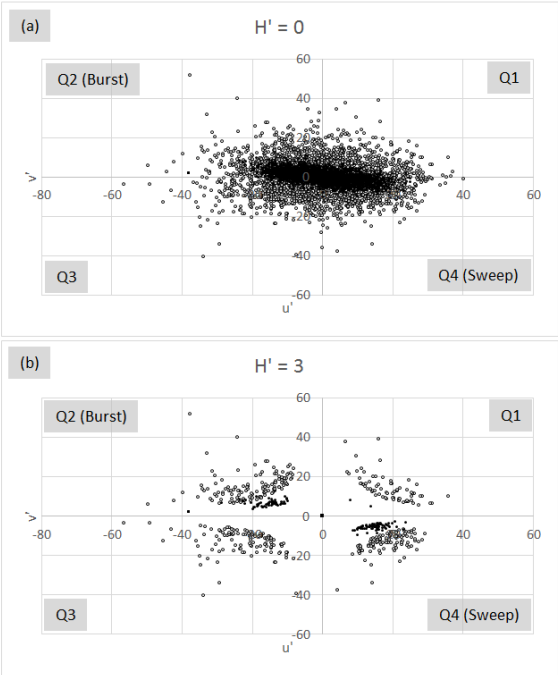

Figure 5. Quadrant Plots at (a) H' = 0 and (b) H' = 3 at t = 0.5h from start of hydrograph rising limb. Darker solid points are from the immobile bed results, and lighter hollow points are from the erodible bed results.

4. CONCLUSIONS AND FUTURE WORK

Overall, fewer, but stronger, burst and sweep motions have been found to occur over a mobile sediment bed compared to an equivalent immobile bed. This finding, along with the increase in the overall percentage of burst/sweep motions occurring during the rising limb of the hydrograph, provides an initial indication of the potential influence that near-bed turbulence may have on the transport of bedload sediment over the duration of an unsteady flow hydrograph. Further analysis will consider the above findings in relation to the temporal variations in measured bedload sediment transport rates during the mobile bed runs. Thus, by considering the near-bed turbulence characteristics, and corresponding interactions with static and mobile beds in greater detail, it is hoped that existing prediction methods for sediment transport that are based on average flow characteristics (e.g. boundary shear stress) may be improved upon.

REFERENCES

Bores, V.; Jirak, J.; and Pollert, J. (2008) 'Spatial and temporal variation of turbulence characteristics in combined sewer flow', *Flow Measurement and Instrumentation*, 19(3), pp145-154.

Boyer, C., A. G. Roy, and J. L. Best (2006) "Dynamics of a river channel confluence with discordant beds: Flow turbulence, bed load sediment transport, and bed morphology" *Journal of Geophysical Research,* 111

Dey, S., Sarkar, S., and Solari, L. (2011). "Near-Bed Turbulence Characteristics at the Entrainment Threshold of Sediment Beds." *Journal of Hydraulic Engineering,* 137(9) pp.945–958

Drake, T. G., R. L. Shreve, W. E. Dietrich, P. J. Whiting, and L. B. Leopold (1988), "Bedload transport of fine gravel observed by motion-picture photography" *Journal of Fluid Mechanics,* 192 pp193– 217

Einstein, H. A. (1950) "The bedload function for sediment transport in open channel flow" Technical Bulletin 1026, 71 pp.,U.S. Department of Agriculture, Washington, D.C.

Gordon, C. M. (1975) "Sediment entrainment and suspension in a turbulent tidal flow" *Marine Geology*, 18 pp57–64.

Grass, A. J. 1971, "Structural features of turbulent flow over smooth and rough
Boundaries" *Journal of Fluid Mechanics*, Vol. 50, Part 2, pp. 233-255.

Hofland, B.; Battjes, J; and Booij, R. (2005) "Measurement of fluctuating pressures on coarse bed material" *Journal of Fluid Mechanics,* 131(9) pp.770-781.

Jain, R.K., Kumar, A., and Kothyari, U.C. (2015) "Turbulence statistics of flow through degraded Channel bed of sand-gravel mixture" *Journal of Hydro-Environment Research* [In Press]

Kundu, D. H. (1990), Fluid Dynamics, pp638, Elsevier, New York Lu, J.J. and Willmarth W.W. (1973) "Measurement of the structure of the Reynolds stress in a turbulent boundary layer" *Journal of Fluid Mechanics,* 60(3): 481-511

Marquis, G.; and Roy, A. (2011) "Bridging the gap between turbulence and larger scales of flow motions in rivers" *Earth Surface Processes and Landforms,* 36(4) pp.563-568.

Nezu, I., Kadota, A. and Nakagawa, H. (1997) "Turbulent structure in unsteady depth-varying open-channel flows" *Journal of Hydraulic Engineering,* 123(9) pp.752-763

Ockelford, A-M. (2011) "The impact of stress history on non-cohesive sediment bed stability and structure" PhD Thesis, University of Glasgow.

Paiement-Paradis, G.; Marquis, G.; and Roy, A. (2011) "Effects of turbulence on the transport of

individual particles as bedload in a gravel bed river" *Earth Surface Processes and Landforms,* 36(1) pp.107-116

Pedlosky, J. (1987), Geophysical Fluid Dynamics, 2nd edition, pp710, Springer, New York

Sarkar and Dey (2010) "Double Averaging Turbulence Characteristics in Flows over a Gravel Bed" *Journal of Hydraulic Research* 48(6) pp.801 809.

Sechet, P. and Le Guennec, B. (1999) "Bursting Phenomenon and incipient motion of solid particles In bed-load transport" *Journal of Hydraulic Research*, 37(5):683-696

Song, T., Graf, W. H., Lemmin, U. 1994, "Uniform flow in open channels with moveable bed", *Journal of Hydraulic Research,* 32(6) pp. 861-876.

Taberestani, M.K. and Zarrati, A.R. (2015) "Sediment transport during flood event: A review" *International Journal of Environment, Science and Technology,* 12 pp.775-788

Infrastructure and Environment Scotland 3rd Postgraduate Conference
9th December 2015
Heriot-Watt University, Edinburgh

Assessing the Load-Bearing Capacity of RC Beams under Impact Loading

N. Madjlessi, D.M.Cotsovos
Institute for Infrastructure and Environment,
Heriot-Watt University
(e-mail: nm387@hw.ac.uk)

ABSTRACT

Data obtained from drop-weight tests reveals that the response exhibited by RC beams under impact loading differs significantly from that established during equivalent static testing. This shift predominantly takes the form of: (i) an increase in the maximum sustained load and (ii) a reduction in the portion of the beam span reacting to the imposed load. However, measurements concerning certain aspects of RC structural response often correspond to a specimen physical-state characterised by high concrete disintegration as well as low residual strength and stiffness. This stage of structural response has little practical significance as it depends heavily on post-failure mechanisms for transferring the applied loads to the supports. In view of the above, the available test data cannot provide insight into the mechanisms underlying RC structural response up to failure. To study these mechanisms in more detail a dynamic nonlinear finite element analysis (NLFEA) package is presently employed which is capable of realistically accounting for: (i) the brittle nature and triaxiality characterising concrete material behaviour as well as (ii) the characteristics of the problem at hand (a wave propagation problem within a highly nonlinear medium). After validating the numerical predictions against available test data a parametric study is carried out to identify the true load bearing capacity of the RC beams for specific rates of impact loading. The latter investigation reveals that the load bearing capacity associated with high-loading rates is significantly lower than the values of the maximum sustained load established experimentally.

Keywords: Reinforced concrete, beams, dynamic loading, nonlinear finite element analysis, loading rate, impact, drop-weight testing.

1. INTRODUCTION

It has been established, experimentally (Hughes & Speirs 1982, May & Chen 2006, Saatci & Vecchio 2009, Fujikake & Soeun 2009, Abbas et al. 2010) and numerically (Miyamoto, et al. 1989, Cotsovos et al. 2009, Cotsovos & Pavlović 2012), that the dynamic response of reinforced concrete (RC) beams under impact loading exhibits significant departures from that recorded during static testing as certain thresholds of the applied loading rates are surpassed. The analysis of the available published experimental and numerical data reveals that the observed shift in structural response is owed to the combined effect of the inertia forces developing along the element span and the localized response exhibited by the RC member. (Cotsovos & Pavlovic 2012, Cotsovos et al. 2009, Cotsovos 2010). More specifically, it has been established that the length of the element span (L_{eff}) reacting to the applied load reduces with increasing loading rates. This can be explained when viewing the problem at hand as a wave propagation problem within a highly nonlinear medium. In such cases the deformation of the beam during loading is dependent on: (i) the intensity and speed of the stress waves generated during the application of the impact load which travel away from the location at which the load is exerted and (ii) the level of damage (cracking) sustained by the RC beam which will locally reduce the stiffness of the element (Cotsovos et al. 2009, Cotsovos 2010). Under high loading rates, structural failure is exhibited prior to the stress waves reaching the supports of the beam resulting in localized response. The higher the loading-rate the more localized the response becomes as the distance that the stress-waves travel prior to failure reduces (Cotsovos & Pavlovic 2012). This reduction of the element span reacting to the imposed load can be used to explain the observed increase in the stiffness and the load-carrying capacity of the beam with increasing loading rates.

Present work forms an extension to already published studies investigating numerically (Cotsovos & Pavlovic 2012, Cotsovos et al. 2009) the effect of loading rate on the response of RC beams under concentrated loads applied '*monotonically*' until failure. The aim of the investigation is to determine the true load-bearing of RC beams when subjected to specific rates of impact loading applied in a form of a '*pulse*'. To achieve this pulses characterised by specific loading rates but different intensities are considered

(see Fig.1). A three-dimensional (3D) dynamic nonlinear finite element analysis (NLFEA) package is employed (ADINA) which is capable of realistically accounting for the brittle nature and triaxiality characterising concrete material behaviour as well as the characteristics of the problem at hand: a wave propagation problem with a highly nonlinear medium. Emphasis is focused on studying certain important aspects of structural response such as the mode of failure, the time history of the reaction forces as well as the deformation and cracking profiles exhibited at various levels of loading.

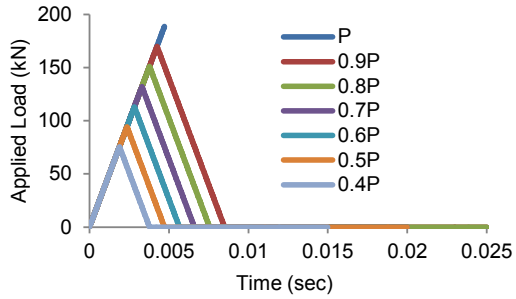

Figure 1. Pulse time function

2. EXPERIMENTAL BACKGROUND

A large number of drop weight tests have been conducted to date on RC beams (Hughes & Speirs 1982, Chen & May 2006, Saatci & Vecchio 2009, Fujikake & Soeun 2009, Abbas et al. 2010). During such tests the load is applied though a steel striker which is allowed to fall freely from a predefined height (depending on the desired rate of loading) onto the mid-span region of the specimen. The drop-weight test setup currently employed at Heriot Watt University is shown Fig.2. Different pads (e.g. steel, rubber and ply) are used to moderate the level of damage sustained at the impact surface and avoid the development of high stress concentrations that can result in localized cracking.

Attention is usually focused on recording the deformation profile and cracking process of the specimens up to failure, as this information is essential for accurately determining the internal stress-state developing within the specimen. The information published concerning crack patterns and deformation profiles is often recorded after (and not throughout) the application of the impact load. Therefore, it usually relates to a specimen physical-state characterised by high concrete disintegration and low residual strength and stiffness. Measurements concerning certain aspects of the specimen response during impact (e.g. the variation of strain, displacement and acceleration at specific points of the specimen as well as the applied load and reaction forces throughout testing) is obtained through the combined use of a high-speed, high-resolution video camera and conventional instrumentation (strain gauges, LVDTs, accelerometers and dynamic load-cells).

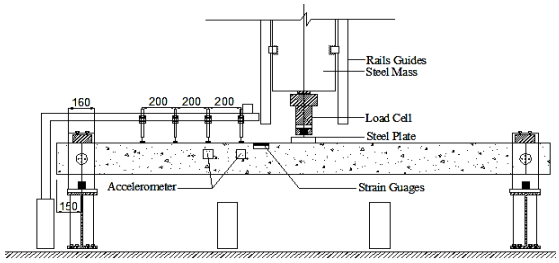

Figure 2. Drop-weight test setup employed at HWU

Typical load-deflection curves describing the behaviour of RC beams under impact and equivalent static loading applied at mid-span are shown in Fig.3 obtained from tests recently conducted using the setup shown in Fig.2. The curves reveal that as the rate of loading increases, the beams sustain higher values of applied load. In addition, the exhibited crack patterns (see Fig.4) suggest that with increasing loading rates the span of the beam mostly affected by the impact load tends to shorten and concentrate at the mid-span region where the load is applied.

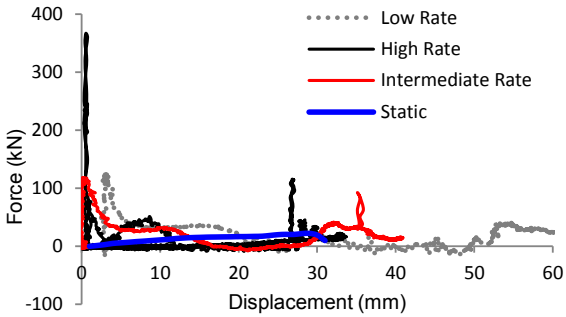

Figure 3. Typical load-deflection curves recorded during static and drop-weight testing of RC beams.

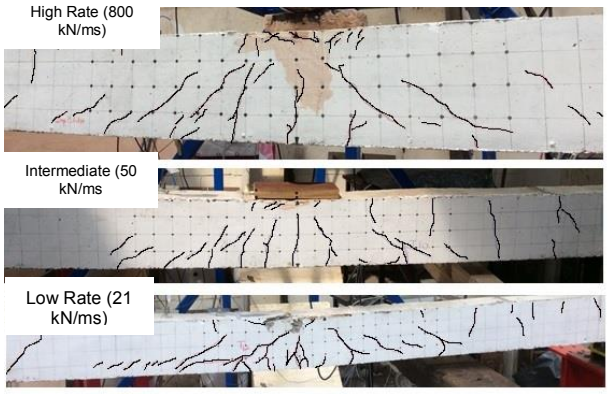

Figure 4. Crack patterns developing on RC beams under different rates of impact loading

It should be noted, that drop-weight tests are difficult to conduct as the intensity of the loads generated increases rapidly (in a few msec) from zero to a maximum value often leading to explosive (brittle) forms of failure which can in turn damage the instruments employed. Data obtained from such tests is characterised by large scatter (see Fig.5) partly due to a wide range of parameters (associated with the different experimental

techniques used, the variation of the size and shape of the impactor and the design details of the RC specimens.) which differ from test to test (Cotsovos, 2010, Abbas et al. 2010). This scatter also reflects the difficulty in correlating the measured response to the actual physical state of the specimens; in fact, the measured maximum value of imposed load frequently corresponds to a specimen physical-state characterised by high concrete disintegration as well as low residual strength and stiffness. This stage of structural response has little practical significance as it depends heavily on post-failure mechanisms for transferring the applied loads to the specimen supports. In view of the above, the available test data cannot provide detailed insight into the mechanisms underlying RC structural response; it can, however, provide a qualitative description of the effect of loading-rate on specimen behaviour.

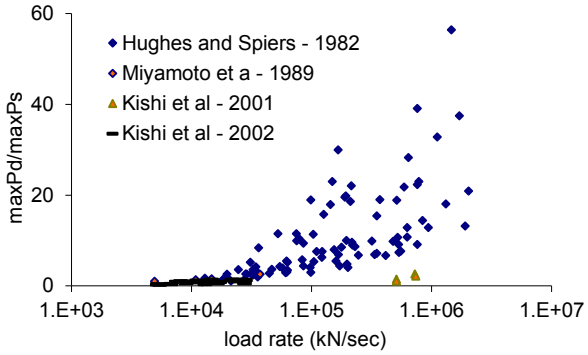

Figure 5. Test data expressing the variation of maximum sustained load during impact ($maxP_d$) in relation to the static load-carrying capacity ($maxP_s$) with increasing values of loading rate

3. LIMITATIONS OF EXISTING NLFEA

NLFEA can be used as a safer and more cost-efficient method (compared to drop-weight testing) for investigating RC structural response under impact loading. To date a range of NLFEA packages have been employed to study the behavior of RC beams under impact (Saatci & Vecchio, 2009, Thabet & Haldane 2000, Izatt et al. 2009). The use of NLFEA allows the study of more complex structural forms (compared to the simple structural configurations studied experimentally) while providing (i) a more detailed description of the exhibited response (i.e. stress and strain distribution, deformation profiles, failure modes and crack patterns) as well as (ii) insight into the underlying mechanics.

The majority of the available NLFEA packages incorporate models of concrete behaviour, the derivation of which has been based on the regression analysis of test data obtained from static uniaxial compression and tension tests on plain concrete specimens. Furthermore, they assume than the material of concrete are strain-rate sensitive and emply laws (in the form of dynamic increase factors) describing the variation of key material properties with strain-rate. The analytical formulations of these material models include a number of parameters which are mainly linked to post-peak concrete characteristics such as strain softening, tension stiffening, and shear-retention ability. Such parameters are defined at the structural, rather than at the material level and attribute ductile characteristics to concrete behaviour not compatible with its brittle nature and not justified by the available test data (Kotsovos & Pavlović, 1995). As a result, the use of such parameters can affect the objectivity of the numerical predictions obtained since they require recalibration depending on the type of problem investigated.

4. GENERAL ASPECTS OF THE FE MODEL PRESENTLY ADOPTED

The NLFEA package (ADINA) employed herein shares a number of characteristics with RCFINEL which has been found capable of realistically predicting the response of a wide range of RC structural configurations under static and dynamic loading (Kotsovos, 2015). The equation of motion – which governs structural response – is solved numerically through the use of an implicit Newmark integration scheme. The choice of 3D-NLFEA is dictated by (a) the nonlinear behaviour of concrete under triaxial stress conditions, which invariably develop prior to local failure (i.e. cracking), and (b) the introduction of non-homogeneity and stress redistribution after the occurrence of cracking.

3.1 Material Modelling

The concrete material model employed stems from experimental data obtained from tests conducted on concrete cylinders under triaxial loading conditions (Kotsovos, 2015). It realistically accounts for the brittle nature and the triaxiallity which characterises concrete material behavior. Its formulation is characterised by both simplicity (fully brittle, with neither strain-rate nor load-path dependency, fully defined by a single material parameter - the uniaxial cylinder compressive strength f_c) and attention to the actual physical behaviour of concrete in a structure. The subject model has been successfully used to predict behavior of plain concrete prisms subjected to high rate uniaxial compressive and tensile loading (Cotsovos & Pavlović, 2008a,b). The predictions obtained from the latter studies suggest that the observed shifts in plain concrete specimen behaviour under high rates of compressive and tensile loading is mainly attributed to parameters associated with structural response (i.e. inertia, boundary conditions imposed, geometry) and the characteristics of the problem at hand (a wave propagation problem within a highly nonlinear medium) rather than to strain-rate sensitivity of material properties of concrete.

In order to describe the behavior of steel a simple bilinear hardening model (see Fig.6) is presently employed. Both models describing the behaviour of

concrete and steel assume that the mechanical properties are independent of the loading-rate. In addition, full bond is assumed between the steel and the concrete.

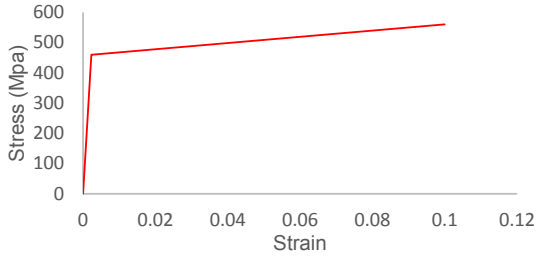

Figure 6. Stress-strain relations for steel bars

3.2 Nonlinear Strategy Adopted

During each time step the equation of motion governing the nonlinear dynamic problem considered is solved as a sequence of equivalent static problems through the use of the Newmark family of approximation methods. At the beginning of each iteration and based on the values of displacement, velocity and acceleration obtained from the previous iteration, the effective stiffness and load matrix are calculated and an equivalent static problem is formulated (Kotsovos, 2015). The equivalent static problem is solved through an iterative procedure based on a modified Newton-Raphson method (Kotsovos & Pavlović 1995). During the solution process of the equivalent static problem every Gauss point is checked to determine whether loading or unloading takes place and to establish whether any cracks close or form. Depending on the results of the previous checks, changes are introduced to the stress-strain matrices of the individual FE's and, to the stiffness matrix of the structure. Convergence is checked locally at each Gauss point; this involves the use of the constitutive relations for the calculation of the stresses increments which correspond to the estimated values of the strain increments. Once the values of the strain and the corresponding stress increments become less than a small predefined value then convergence is accomplished. When this is not achieved, the residual forces are calculated and are then re-imposed onto the FE model the RC form investigated until convergence is finally achieved.

3.3 Modelling of Cracking

Crack formation is modelled by using the smeared-crack approach. A crack forms when the stress developing in a given part of the structure (calculated at the integration point of the FE model employed) corresponds to a point in the principal stress space that lies outside the predefined failure surface of concrete material, thus resulting in localised material failure. This failure takes the form of a crack and is followed by immediate loss of load-carrying capacity in the direction normal to the plane of the crack. At the same time, the shear stiffness is also reduced drastically to a small percentage (about 10%) of its previous value (before the occurrence of the crack). However, it is not set to zero in order to minimize the risk of numerical instabilities during the execution of the solution procedure, as explained elsewhere (Kotsovos & Pavlović 1995). It should be noted that each integration point can develop up to three cracks. To compensate for the brittle nature of the concrete material model employed and to safeguard the numerical stability of the solution procedure a small value of 'fracture energy' is employed in order to control the rate at which the crack propagates. The value of fracture energy was such that the brittle nature of the concrete material model is not jeopardized.

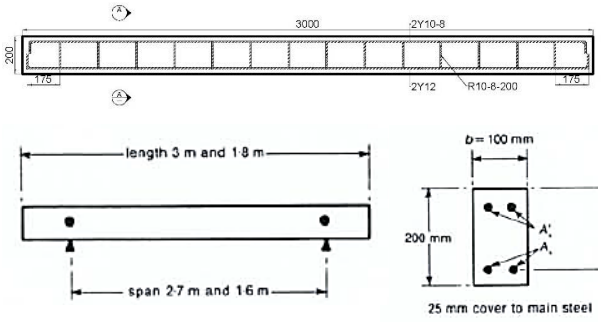

Figure 7. RC beam investigated

5. STRUCTURAL FORM INVESTIGATED

The behaviour of the RC beam specimen considered herein has been experimentally investigated in the past (Hughes & Speirs, 1982). During the latter experimental study a range of RC beams with different reinforcement details were tested under static and impact loading. The specimen investigated numerically in this study is presented in Fig.7.The longitudinal reinforcement consists of four bars: two 6 mm and two 12 mm diameter bars in the compression and tension respectively. In addition 6 mm diameter stirrups spaced at 180 mm were also used (see Fig.7).The elasticity modulus (E_S), the yield stress (f_y), and the ultimate strength (f_u) of both the longitudinal and transverse reinforcement bars are 206 GPa, 460 MPa and 560 MPa, respectively. The uniaxial compressive strength (f_c) of concrete is 45 MPa. The subject beam was subjected to drop weight testing at its mid-span. Mild steel, rubber or ply pads were placed on the top face of the specimen in order to prevent or moderate local damage in the impact area.

6. FE MODELLING OF THE PROBLEM AT HAND

The concrete medium is modelled by using an mesh of 27-noded brick elements with an edge size of approximately 40 mm. Due to the double symmetry of the problem at hand, only a quarter of the RC beam is modelled with suitable boundary conditions, see Fig.8. The load is applied onto the

mid-span of the beam through a steel plate. The load is initially imposed monotonically at a constant rate until failure. Then it was applied in the form of the pulse (see Fig.1). Different magnitudes of pulse load are considered for specific rates of loading rates (as shown in Fig.1) aiming to identify the magnitude for which the specimen did not fail.

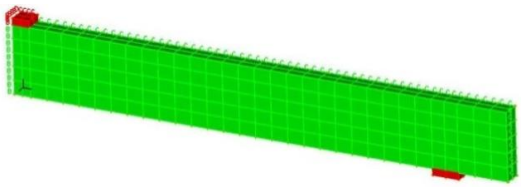

Figure 8. FE mesh adopted

7. NUMERICAL PREDICTIONS

The predictions obtained are presented in the form of a dynamic increase factor (DIF) which is the ratio between maximum sustained dynamic load and the static load bearing capacity of the specimen ($maxP_d/maxP_s$) (see Fig 9). As it can be seen, the values of DIF, (for the case of monotonic loading) associated with different loading rates are in good agreement with their experimentally established counterparts. However, it is interesting to note that when comparing the values of DIF under monotonic loading with their counterparts obtained from the case of pulse loading, the latter were considerably lower.

The true load carrying capacity of the RC beams is considered to correspond to a physical state in which the specimen is still capable of undertaking the imposed loads without relying on post-failure mechanisms (e.g. catenary action) and is therefore are capable of being re-loaded without exhibiting a significant loss of stiffness and strength. Based on the above the maximum sustained load ($maxP_d$) imposed on the RC beams in the case of monotonic loading should not be considered as the 'load carrying capacity'. The $maxP_d$ in this case results in the collapse of the RC structural element as the latter is no longer capable of behaving as an RC member as its response heavily relies on post-failure mechanism and its residual strength and stiffness is essentially diminished (compared to that exhibited prior to the load being applied).

In the case of pulse loads (characterised by the same loading rates but different intensities) in order to determine whether the $maxP_d$ corresponds to the actual load-bearing capacity resort is made to the curves describing the variation of the mid-span deflection with time (see Fig.11) and the imposed load (see Fig.10). From these curves it is observed that when $maxP_d$ of the pulse is equal to 25% of the $maxP_d$ obtained for the case of monotonic loading characterised by the same loading rates, the RC beam does not fail and continues to oscillate after unloading takes place. However, when the $maxP_d$ of the pulse becomes higher than 30% of the $maxP_d$ predicted for the case of monotonic loading the beam fails during unloading. The above results suggest that the data obtained for drop-weight tests on RC beam are often associated with the post-failure behaviour of the specimens and as a result do not provide the true load-bearing capacity of the specimen considered.

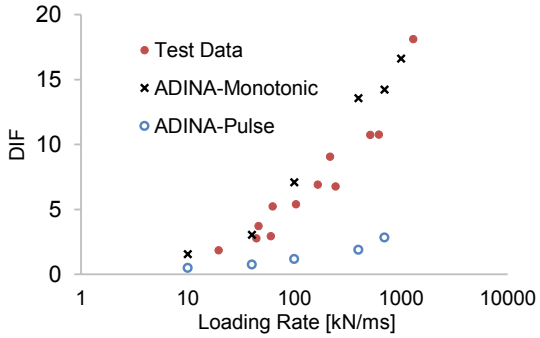

Figure 9. Comparison between experimental and numerical predictions

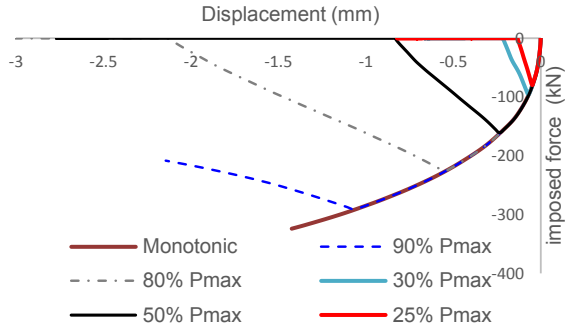

Figure 10. Predicted load-deflection curves obtained for pulse loads with $\dot{P}$ = 100 kN/ms

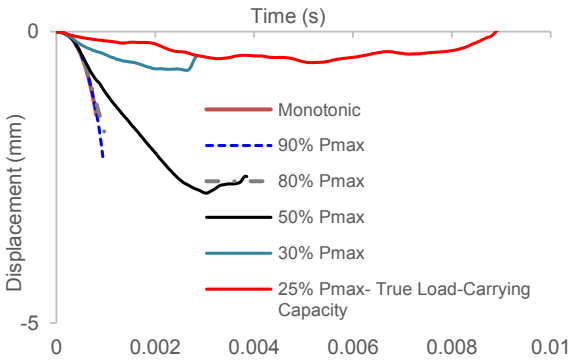

Figure 11. Predicted mid-span displacement time history obtained for pulse loads with $\dot{P}$= 100 kN/ms

The deformation profile of the beam in combination with predicted crack patterns exhibited when the peak load is attained is presented in Fig.12 for the case of pulse loads characterised by the same loading rate but different intensities. Based on the deformation profile and the crack patterns it is also possible to determine the effective length (L_{eff}) of the RC beam which essentially responding to the applied load. It is observed that for a specific loading rate (100kN/msec) as the peak value of the imposed pulse load reduces (form 100% to 25% of $maxP_d$ obtained under monotonic loading) a larger portion

of the span reacts to the applied load. This suggests that the mechanics underlying RC structural response will be affected not only by the rate of applied loading but also by its intensity. Furthermore, the predicted crack patterns suggest that for the case of a pulse load with a magnitude of 25% of the maximum sustained load for the case of monotonic loading, the beam suffers little damage and therefore its post-impact strength and stiffness will not be considerably affected.

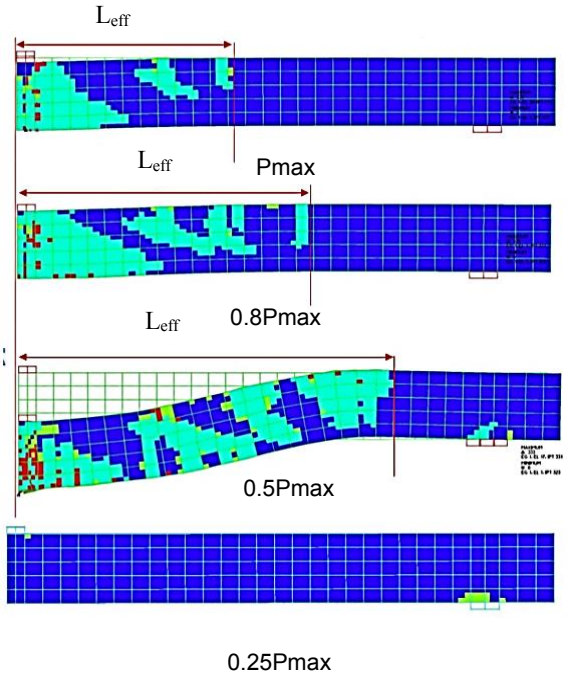

Figure 12. Development of crack pattern and deformation profile predicted by ADINA

8. CONCLUDING REMARKS

The present NLEFEA package is proved capable of successfully predicting the response of a RC beams under impact loading using a material model capable of realistically accounting for the brittle nature and the triaxiality characterizing concrete material behavior. The predictions obtained provide evidence that the available test data is often associated with the post-failure behaviour and cannot provide the true load-bearing capacity of the specimen considered. Both the intensity and the rate of the applied impact load affect the mechanics underlying RC structural response under impact loading. More detailed experimental and numerical studies are currently being conducted investigating the effect of a range of parameters on RC structural response under impact loading. This study will be also extended in order to include other RC structural configurations such as columns and frames.

REFERENCES

Hughes. G., Spiers. D. M. (1982), “An investigation on the beam impact problem.” Cement and Concrete Association, Technical Report 546.

Saatci. S., Vecchio F. J. (2009), “Effects of shear mechanisms on impact behaviour of reinforced concrete beams.” ACI Structural Journal 106 (1), PP. 78-86.

May. I. M, Chen. Y, Roger. D, Owen. J, Feng. Y. T, and Thiele. P. J. (2006), “Reinforced concrete beams under drop-weight impact loads.” Computers and Concrete 3, (2-3), pp. 79-90.

Fujikake. K, Li. B, Soeun. S. (2009), “Impact response of reinforced concrete beam and its analytical evaluation.” ASCE Journal of Structural Engineering; 135(8), PP. 938-50.

Miyamoto. A, King. M. W, Fujii. M. (1989) “Non-linear dynamic analysis and design concepts for RC beams under impulsive loads.” Bulletin of the New Zealand National Society for Earthquake Engineering, (22), pp. 98-111.

Cotsovos. DM, Stathopoulos. ND, and Zeris. Ch. (2008), “Behaviour of RC beams subjected to high rates of concentrated loading.” Journal of Structural Engineering ASCE 134(12), pp. 1839-1851.

Cotsovos. D.M., Pavlović. M.N. (2008a), “Numerical investigation of concrete subjected to compressive impact loading. Part 1: A fundamental explanation for the apparent strength gain at high loading rates”, Comp. & Struct., 86(1-2), 145-163.

Cotsovos. D.M., Pavlović. M.N. (2008b) “Numerical investigation of concrete subjected to compressive impact loading. Part 2: Parametric investigation of factors affecting behaviour at high loading rates”, Comp. & Struct, 86(1-2), pp. 164-180.

Cotsovos. D.M. Pavlović. M.N. (2008c) “Numerical investigation of concrete subjected to high rates of uniaxial tensile loading”. International Journal of Impact Engineering, 35(5), pp. 319-335.

Cotsovos. D.M. (2010), “A simplified approach for assessing the load-carrying capacity of reinforced concrete beams under concentrated load applied at high rates.” International Journal of Impact Engineering 37, pp. 907-917.

Abbas, A.A., Pullen, A.D., Cotsovos,D.M. (2010).“Structural response of RC wide beams under low-rate and impact loading.’’ Magazine of Concrete Research 62(10), PP. 723-740.

Izatt. C., May, I.M., Chen, Y.,Algaard,W. et al., (2009). “Perforation owing to impacts on reinforced concrete slabs.” Proceedings of the ICE-Structures and Buildings 162(1), PP. 37-44.

Thabet. A, Haldane. D. (2000), “Three-Dimensional Simulation of Nonlinear Response of Reinforced Concrete Members Subjected to Impact Loading.” ACI Structural Journal 97(5), PP. 689-702.

Saatci. S, Vecchio F. J. (2009), “Nonlinear Finite Element Modelling of Reinforced Concrete Structures under Impact Loads.” ACI structural Journal 106 (5), PP. 717-725.

Kotsovos. M. D., Pavlović. M. N. (1995), “Structural Concrete: Finite-element analysis and design”, London, Thomas Telford.

Kotsovos M.D. (2015) “Finite-Element Modelling of Structural Concrete: Short-Term Static and Dynamic”,Boca Raton,CRC Press.

Infrastructure and Environment Scotland 3rd Postgraduate Conference
9th December 2015
Heriot-Watt University, Edinburgh

Validation of Three-dimensional Finite Element Model for Critical Velocity

S. Mezher, P. Woodward, O. Laghrouche, D. Connolly,
Institute for Infrastructure and Environment,
Heriot-Watt University
(e-mail: sbm30@hw.ac.uk)

ABSTRACT

This paper studies the response of soft soils to high-speed trains, using finite element methods. Critical velocity effects occur once the train speed approaches a certain limit and large deflections are observed in the track. Several phenomena are associated with critical velocities, including the generation of ground surface waves and vibrations in the underlying soil layers beneath the track. These effects increase track damage, thus causing safety considerations and increasing maintenance costs. The main concern is soft soils, due to their low stiffness, which results in larger ground amplification response. Being able to predict the critical velocity effects is useful for designers, because it allows them to define strategies to mitigate the damage caused by the amplified response, and, therefore, increase the safety and comfort of passengers. A three-dimensional model of the Alfa-Pendular train track in Portugal is developed and validated. Another model, based upon a site in Ledsgard, Sweden, is also used for validation. The Ledsgard site is characterised by weak soft soils. The simulations are run in the time domain and the results of the ground response are presented in terms of vertical deflections and velocities. The outcomes of the simulations are compared against actual field results.

Keywords: high-speed, railway tracks, numerical modelling, finite element analysis, ground vibration.

1. INTRODUCTION

The problems arising as a result of increasing train speeds in sites that are characterised by weak soft soils have been a major concern in the past few years. Many researchers started investigating critical velocities after the occurrence of high dynamic ground responses in some European sites when a certain speed limit was exceeded. A well-known example occurred with the X2000 train in Sweden, when surface waves started developing on the ground during the inspection stage due to the large stresses induced by the train into the ground layers (Hall, 2000). It is believed that the critical velocity effects occur once the train speed and surface wave velocity coincide. The effects include extreme vibrations of the ground, resulting in surface waves' transmission, track uplift and underground resonance (Banimahd *et al*, 2012). The structural response of the track is different for each case, as it depends on the axle load, wheel axle spacing and train speed (Krylov, 2000). The critical velocity effects can cause great damage to the track, and, therefore, increase the risk to passenger safety, as well as an increase in noise and maintenance costs. In order to minimise these effects, it is important to predict the behaviour of the ground prior to the construction stages. Many have successfully followed numerical modelling using different software to obtain a similar response to actual field results (Madshus and Kaynia, 2000). Due to the high complexity of track geometry and non-linearity of the soil, the time it takes to develop these models and run the simulations is extensive. Therefore, a simplified model is required to reduce the computational time of the analysis and produce accurate ground response, which is the main focus of this paper.

The three-dimensional model was developed on Abaqus software, which is a commercial finite element software that allows the implementation of user-defined subroutines in the analyses. The trains that are used for the model validation are Alfa-Pendular in Portugal and the X2000 in Sweden. The Alfa-Pendular train operates at a speed of 220 km/h, while the X2000 operates at 200 km/h. The latter crosses organic clay and weak marine clay layers that are approximately 50 m in depth, which caused the high response experience in the site (Hall, 2012, Madshus and Kaynia, 2000, Costa *et al*, 2012). Previous research was carried out using Abaqus for the X2000 train track by Hall (2000) to confirm the critical velocity effects. His model is 50 m deep and the track is 65 m long, and the analysis was performed using the implicit time integration with a fixed time step of 0.001 s. Others have used

different approaches, such as Madshus and Kaynia (2000), who used the VibTrain computer program to model the Swedish track, where the rail and track systems were represented as beams with finite elements and the ground was modelled using Green's functions. For the Portuguese track, Costa (2011 and 2012) carried out experimental field tests in Portugal and compared the results effectively with his 2.5D model, using a combination of finite element method and boundary element method for the irregular domain and ground, respectively. The 2.5D model uses domain Fourier transformations for the coordinates along the track, allowing less computational effort. They were all able to model the tracks realistically and managed to produce accurate results of the ground response. This paper proposes a simple three-dimensional model that is capable of producing accurate results efficiently and in a short period of simulation time. The modelling aspects and finite element approach are described briefly and the track deflections and velocities are presented in comparison with field test results for both trains.

2. FINITE ELEMENT ANALYSIS

Abaqus software is widely used in industry and institutions for its ability to provide wide material modelling and coupling of different systems in finite element analysis. The software allows viewing various outcomes, such as deflections, stresses, energy and many others. User-defined subroutines can be used for customised definitions. VDLOAD and VUFIELD are examples of the subroutines used previously by Connolly (2013) and which are also used in this paper. The VDLOAD allows the variation of magnitudes of forces applied on nodes, while the VUFIELD allows defining field variables at the nodes, and these variables are passed and used in the VDLOAD. Abaqus also allows the use of infinite elements, which are used in this model, for the sides of the ground section in order to prevent waves being reflected. The parameters and modelling aspects of the train and track on Abaqus are explained in this section.

2.1 Track Model

The rail is modelled as a 50 m beam element, a three-dimensional Euler-Bernoulli beam with a total of 500 elements. The track and ground are modelled using 8-noded brick elements 100 m long with 25 m on each side for the definition of infinite elements. The soil is 8 m deep and 12 m wide (4 m of the width is also defined as infinite elements). The infinite elements prevent the reflection of waves. Previously, Hall (2000) used dashpots on the sides and springs for the sleepers to keep them in place; however, with infinite elements, it is not necessary to build a very deep and wide soil model. Only half of the model is considered, with symmetry boundary conditions applied. The model is fixed from the bottom. The track is modelled with the embedded sleepers as one part, which avoids surface contact problems between different layers. This also results in more efficient analysis and less computational effort. The spacing between sleepers is taken as 0.6 m. The meshing sizes of the rail, track and soil are 0.1, 0.2 and 0.6, respectively. Figures 1 and 2 show the meshed three-dimensional model.

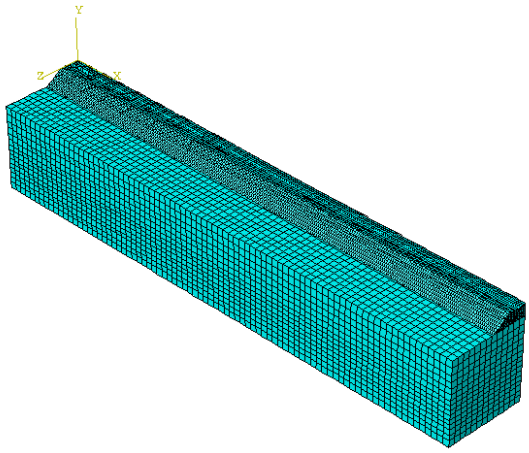

Figure 1. 3D mesh of the model on Abaqus.

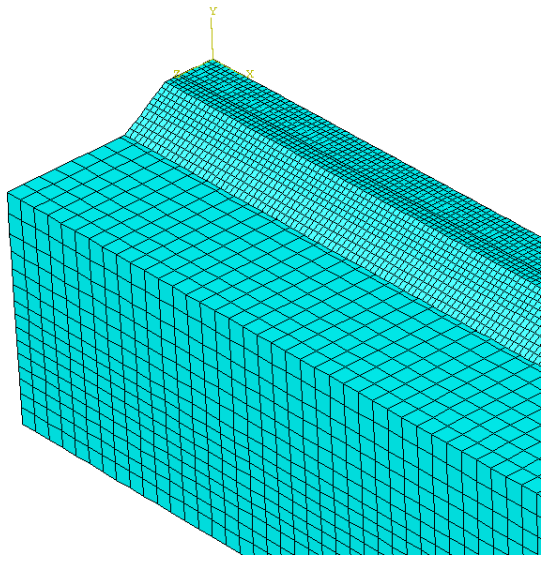

Figure 2. Close up view of the 3D model meshing.

Both train tracks, the Swedish and Portuguese, are modelled similarly, with different parameters and depths of the track and soil layers. The tables show the approximated parameters used for the track and ground (Hall, 2012, Costa *et al*, 2012, and Paolucci *et al*, 2003). The parameters of the soil layers of the Portuguese track are obtained from field tests (Costa *et al*, 2012, and Costa, 2011), up to 8 m depth; however, only the top layer

is provided in table 1. Each layer is assumed to be homogeneous. Rayleigh damping is defined for soil layers, which is defined by a linear combination of mass $\mathbb{M}$ and stiffness $\mathbb{K}$ matrices using parameters that are frequency dependant, as shown in equation (1). The parameters α and β are assumed as 0 and 0.0004, respectively.

$$\mathbb{C} = \alpha\mathbb{M} + \beta\mathbb{K} \quad (1)$$

Table 1. Track parameters of the Swedish and Portuguese tracks (Hall, 2012, Madshus and Kaynia, 2000, Costa *et al*, 2012, Paolucci *et al*, 2003, Takemiya, 2003, and Sheng *et al*, 2003)

Layer	D (m)	E (MPa)	γ	ρ (kg/m^3)
X2000 track				
Top Ballast	0.5	124	0.4	1800
Embankment	0.5	430	0.3	1900
Crust	1	20	0.491	1500
Organic Clay	3	6	0.498	1250
Marine Clay	4	24.5	0.498	1470
Alfa-Pendular track				
Top Ballast	0.57	97	0.12	1590
Subballast	0.55	212	0.2	1910
Soil	1.4	93	0.49	2000

2.2 Train Model

The X2000 train has five carriages and 20 axle loads, while the Alfa-Pendular train has six vehicles and 24 axle loads. Figures 3 and 4 show the geometry and axle spacing. The axle loads of the X2000 train are shown in table 2 (Paolucci *et al*, 2003, and Sheng *et al*, 2003). The load of the Alfa-Pendular is calculated from the average car, bogie and wheel masses, as shown in table 3 (Costa *et al*, 2012).

Explicit time integration is carried out with a total time of 4 s. The time steps are calculated automatically using Abaqus and are equal to 4.37×10^{-6} s and 8.38×10^{-6} for the Swedish and Portuguese tracks, respectively. The time steps are small which ensures accuracy.

Table 2. Axle loads of the X2000 train (Sheng *et al*, 2003)

No. of wheels	**1**	**2**	**3,4**	**5,6,7,8, 13,14,15, 16**
Axle load (kN)	188.5	183	185.7	122
No. of wheels	**9,10, 11,12**	**17,18**	**19**	**20**
Axle load (kN)	125	143.2	119	167.5

Table 3. Train properties of the Alfa-Pendular train (Costa *et al*, 2012)

Component	Mass (kg)
Car body	32900 - 35710
Bogies	4712 - 4932
Axles	1538 - 1884

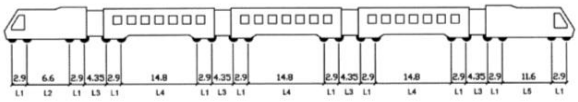

Figure 3. The geometry of the X2000 train (Paolucci *et al*, 2003).

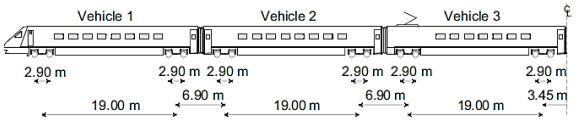

Figure 4. The geometry of the Alfa-Pendular train (Costa *et al*, 2012).

3. SIMULATIONS AND COMPARISON

The simulations were run for linear analysis of the two models, the Swedish and Portuguese tracks. The duration of the runs took approximately six hours each for selected points on the rail, track and soil layers. As stated, the focus of the paper is validation of the models' ability to produce accurate ground response results. Figures 5 and 6 show the vertical displacement and velocity responses of the rail, respectively, for the Portuguese track. The simulation outcomes are compared against field results obtained from experimental tests (Costa *et al*, 2012, and Costa, 2011). Referring to figure 5, the deflections are in good agreement with the measured results. The vibrations before and after the passage of the train are not clearly identified since only a linear analysis was carried out. The pattern of the velocity response, as shown in figure 6, is almost identical in both results, but the amplitudes are slightly lower for the computed model. The track uplift is indicated by the positive values in the displacement plot. Vibrations are also detected, which confirm the effects of increasing train speeds.

The field tests of the Ledsgard site, for the X2000 train, are provided by the Swedish National Rail Administration (Banverket) (Hall, 2012, Madshus and Kaynia, 2000, and Paolucci et al, 2003). Figure 7 shows the measured vertical deflection response of the Ledsgard site compared to the Abaqus model results.

The simulations were run for a lower speed of 19 m/s and not for the maximum speed of the train, due to validation purposes, and higher speeds will be considered in future runs. The deflections are in good agreement with the field results. The site is known for high dynamic amplifications and soil layers that are very low in stiffness; thus, a linear model is not sufficient, which explains the slight difference between results.

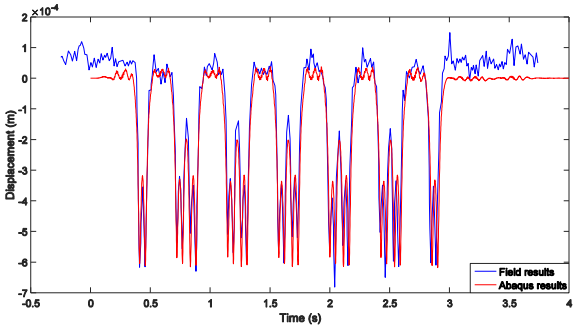

Figure 5. Vertical displacement response (Portuguese track).

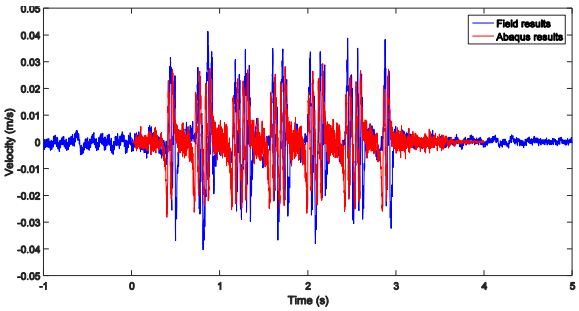

Figure 6. Vertical velocity response (Portuguese track)

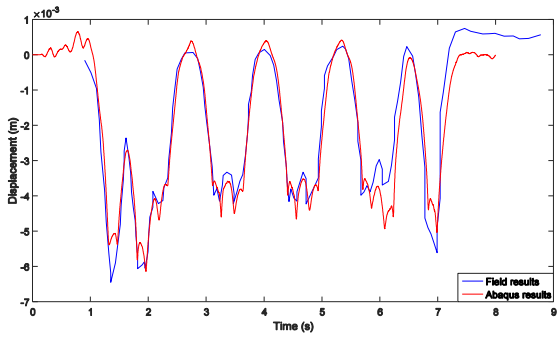

Figure 7. Vertical displacement response (Swedish track)

Estimated deflections are calculated using equations (2), (3) and (4) for extra validation purposes, where s is the track support stiffness calculated using stiffness values of the track layers, and $\mathrm{EI_r}$ is the bending stiffness of the rail (Thompson, 2009).

$$s = \left(\frac{1}{K_{ballast}} + \frac{1}{K_{subballast}} + \frac{1}{K_{top\ soil\ layer}}\right)^{-1} \quad (2)$$

$$\text{Total track stiffness} = 2\sqrt{2}(\mathrm{EI_r})^{1/4}s^{3/4} \quad (3)$$

$$\text{Rail deflection} = \frac{\text{Axle force}}{\text{Total track stiffness}} \quad (4)$$

The deflection for the Portuguese track is calculated as 10.8×10^{-4} m, while the deflection for the Swedish track is 3.9×10^{-3} m. these values are within the range of computed deflections.

4. CONCLUSION

The ground responses of the X2000 and Alfa-Pendular trains are confirmed using Abaqus three-dimensional finite element models. Implementing user-defined subroutines made the definition of moving forces more efficient. Considering only a linear analysis was carried out, the results are in good agreement with actual field tests. The model proved to be quick and capable of predicting ground behaviour, especially for deflection responses in the time domain. This is an ongoing work.

REFERENCES

Krylov, V. V., Dawson, A. R., Heelis, M. E., & Collop, A. C. (2000). Rail movement and ground waves caused by high-speed trains approaching track-soil critical velocities. Proceedings of the Institution of Mechanical Engineers, Part F: Journal of Rail and Rapid Transit, 214(2), 107-116.

Hall. L. (2000). Simulations and analyses of train-induced ground vibrations, a comparative study of two and three-dimensional calculations with actual measurements. PhD thesis, Royal Institute of Technology, Sweden.

Banimahd, M., Woodward, P., Kennedy, J., & Medero, G. (2012). Three-dimensional modelling of high speed ballasted railway tracks. Proceedings of the ICE-Transport, 166(2), 113-123. http://dx.doi.org/10.1680/tran.9.00048

Madshus, C., & Kaynia, A. M. (2000). High-speed railway lines on soft ground: dynamic behaviour at critical train speed. Journal of Sound and Vibration, 231(3), 689-701. doi:10.1006/jsvi.1999.2647

Costa, P., Calçada, R., & Cardoso, A. (2012). Track–ground vibrations induced by railway traffic: In-situ measurements and validation of a 2.5 D FEM-BEM model. Soil Dynamics and Earthquake Engineering, 32.1: 111-128. doi:10.1016/j.soildyn.2011.09.002

Costa, P. A. (2011). Vibrações do sistema via-maciço induzidas por tráfego ferroviário-

Modelação númerica e validação experimental. Tese de Doutoramento, Departamento de Engenharia Civil da Faculdade de Engenharia da Universidade do Porto: Porto.
Costa, P. A., Calcada, R., Cardoso, A. S., & Bodare, A. (2010). Influence of soil non-linearity on the dynamic response of high-speed railway tracks. Soil Dynamics and Earthquake Engineering, 30, 221–235. doi:10.1016/j.soildyn.2009.11.002
Connolly, D., Giannopoulos, A., & Forde, M. C. (2013). Numerical modelling of ground borne vibrations from high speed rail lines on embankments. Soil Dynamics and Earthquake Engineering, 46, 13–19. doi:10.1016/j.soildyn.2012.12.003
Connolly, D. P., Kouroussis, G., Woodward, P. K., Verlinden, O., Alves Costa, P., & Forde, M. C. (2014). Field testing and analysis of high speed rail vibrations. Soil Dynamics and Earthquake Engineering, 67, 102–118. doi:10.1016/j.soildyn.2014.08.013
Shih, J.-J., Thompson, D., & Zervos, A. (2014). Assessment of track-ground coupled vibration induced by high speed trains. In 21st International Congress on Sound and Vibration, 13–17.
Paolucci, R., Maffeis, A., Scandella, L., Stupazzini, M., and Vanini, M. (2003). Numerical prediction of low-frequency ground vibrations induced by high-speed trains at Ledsgard, Sweden. Soil Dynamics and Earthquake Engineering 23, 425-433. doi:10.1016/S0267-7261(03)00061-7
Takemiya, H. (2003). Simulation of track-ground vibrations due to high-speed train: the case of X-2000 at Ledsgard. Journal of Sound and Vibration 261, 503-526.
Chopra, A.K. (2001). Dynamics of structures: theory and applications to earthquake engineering. New Jersey: Prentice Hall.
Adolfsson, K., Andreasson, B., Benktsson, P. E., & Zakrisson, P. (1999). High speed train X2000 on soft organic clay-measurements in Sweden. Geotechnical Engineering for Transportation Infrastructure: Theory and Practice, Planning and Design, Construction and Maintenance: Proceedings of the Twelfth European Conference on Soil Mechanics and Geotechnical Engineering, Amsterdam, Netherlands, Vol. 3.
Caughey, T. K. (1960). Classical normal modes in damped linear dynamic systems. Journal of Applied Mechanics, 27(2), 269-271.
Hung, H.H., and Yang, B.Y. (2001). A review of researches in ground-borne vibrations with emphasis on those induced by trains. Proceedings of National Research Council, part A: Phys. Sci. & Eng., 25(1), 1-16.
Sheng, X., Jones, C. J. C., & Thompson, D. J. (2003). A comparison of a theoretical model for quasi-statically and dynamically induced environmental vibration from trains with measurements. Journal of Sound and Vibration, 267, 621–635. doi:10.1016/S0022-460X(03)00728-4
Thompson, D. (2009). Railway Noise and Vibration: Mechanisms. Modelling and Means of Control: Elsevier.

Infrastructure and Environment Scotland 3rd Postgraduate Conference
9th December 2015
Heriot-Watt University, Edinburgh

The flow behaviour of granular suspensions

Christopher Ness
Institute for Infrastructure and Environment
University of Edinburgh
(chris.ness@ed.ac.uk)

ABSTRACT

Granular suspensions, assemblies of discrete particles surrounded by an interstitial liquid, are ubiquitous in everyday life: the coffee grounds suspended in our cafetiere, the toothpaste we brush our teeth with and the cement in the structures around us being just a few examples. From managing the silt deposits of the Nile, to designing particulate filling agents to optimise speciality plastics, the engineering challenges associated with suspension processing have challenged generations of thinkers. Today, suspensions exist as intermediates and products in agriculture, mining, pharmaceuticals and manufacturing, representing tens of billions of pounds of revenue worldwide annually. A thorough understanding of the flow behaviour of suspensions is therefore imperative, facilitating prediction, description and control of these interesting materials. In this paper, we review some popular descriptions of granular suspensions and their properties, and highlight recent developments in the field of *shear-thickening* suspensions.

1. INTRODUCTION

Experience tells us that suspensions can be observed to behave in either a solid-like or fluid-like way. For example, clay may sit at rest on a surface and appear to be solid, yet under the application of a large force it will deform like a highly viscous liquid. As such, the analyses of these systems have historically evolved from those of static and flowing systems. From a solid-like point of view, the most simple description of static behaviour is that proposed by Coulomb, who described a yield criterion for granular materials in terms of a linear relationship between shear and normal stresses on a yield plane. Fluid-like descriptions ultimately began with the work of Newton and later Navier and Stokes, who described liquids as a continuum, giving them a constant resistance to flow called a viscosity, later complemented by Einstein's proposal for the increase of this viscosity upon addition of suspended solids. While there has been sustained progress over the past century in extending these early descriptions, and much effort in bridging the gaps between models for solid- and fluid-like behaviour, a unified, comprehensive description of granular suspension flow behaviour remains elusive.

2. DESCRIBING A GRANULAR SUSPENSION

We begin by outlining the main properties of suspensions that determine their bulk behaviour under flow. We consider assemblies of a large number of finite sized, spherical (radius *r*), solid particles, fully immersed in an interstitial liquid. For simplicity, neutral buoyancy is assumed throughout, meaning gravitational effects can be omitted.

2.1 Particle Size

The flow properties of suspensions are governed by details of particle level physics. Potentially significant effects include hydrodynamics (i.e. fluid mediated forces on the particles), Brownian motion, electrostatic or steric repulsion, and transient or sustained particle-particle contact and friction forces. Particle size is perhaps the most important factor in determining which of these factors is most relevant.

Peclet number - Suspensions can be catagorised as Brownian or non-Brownian depending on a dimensionless parameter called the Peclet number, Pe [1]. In this context, the Peclet number is the ratio of the time required for a particle to translate by its own radius under Brownian motion and the time required for a particle to move the same distance due to a driving shear flow. For Pe<1, Brownian motion is rapid compared to the driving flow rate, allowing continual rehomogenisation of the suspension inspite of an imposed flow or shear. For Pe>1, Brownian motion is too slow to maintain equilibrium, so particle motion is governed by the driving flow, and the suspension may adopt a non-equilibrium inhomogeneous microstructure. Since the Peclet number has r^3 dependence, it is typically found that small particles (say, r<1μm) are Brownian, whereas large particles are non-Brownian.

Particle Stokes number - A further shear flow property that largely depends on particle size is the viscous-inertial distinction, delineated by the particle Stokes number, St, which loosely compares the viscous dissipation, governed by the fluid viscosity, with the collisional dissipation,

governed by particle contacts [2]. For St<1, viscous dissipation dominates, leading to shear stresses that scale linearly with shear rates, reminiscient of Newtonian liquids. For St>1, inertial particle collisions dominate, so the stress scales quadratically with the shear rate, consistent with dry granular rheology. Since St has r^2 dependence, it is typically found that large particle (say, r>100μm) suspensions are inertial while small particle suspensions are viscous.

Onset stress - Suspended particles may be stabilised against agglomeration by electrostatics or sterics. A widespread model system is polymer coated PMMA (polymethylmethacrylyte) spheres suspended in decalin. The stabilising polymer coating leads to a normal repulsive force between neighbouring particles that prevents surface contacts [3]. When a sufficiently large stress is applied to the system, the normal repulsion may be overcome, so particle surfaces touch, giving tangential friction forces (dependent on surface roughness) in addition to normal repulsion. Recent experiments demonstrate that the onset stress σ^* is proportional to $1/r^2$, meaning large particles (say, r>10μm) usually exhibit frictional and normal contact forces, while small particles usually exhibit normal forces only.

In Figure 1, we illustrate how a suspension may be characterized according to the above criteria under a typical processing shear rate.

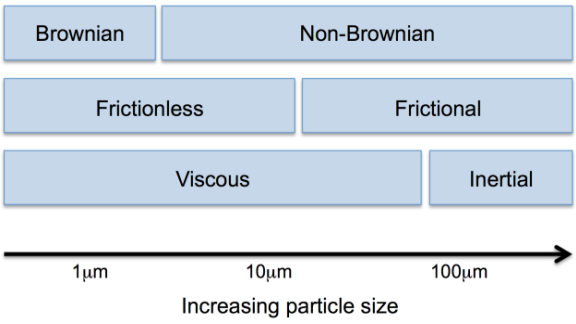

Figure 1. Suspension flow regimes (in terms of Peclet, onset stress and Stokes number) as a function of particle size, at a typical processing shear rate.

2.2 Particle Hardness

The suspended particles may generally be described as either hard or soft. Alumina pastes are a typical example of a hard particle suspension; suspended biological cells may be more accurately described as soft. Hard particles are not able to deform and have zero interaction potential with one another, except when surfaces contact, when they exhibit extremely strong repulsion. Soft particles are able to deform upon contact, and exhibit repulsive forces that are proportional to the extent of deformation. Hard particles remain rigid under all flow conditions and therefore may lead to suspensions being prone to "arrest" or "jamming" when particle contacts restrict flow. By contrast, soft particles are compliant and able to change their shape to remain "flowable" under similar conditions.

2.3 Solid volume fraction

The relative volume of solid present in the system is quantified by the volume fraction ϕ, defined as the total volume of the solid particles relative to the total suspension volume. The volume fraction can vary from 0 (i.e. pure liquid with no solids present) to an upper limit, the maximum packing fraction, which is intimately linked to particle shape, size distribution and surface details. For low volume fractions (ϕ<0.1) the behaviour of the system is dominated by particle-fluid interactions and the particles are assumed not to "see" or interact with each other, while for intermediate volume fractions transient particle-particle interactions will be more common and will have a significant contribution to the properties of the system. For high volume fractions (ϕ>0.55), sustained particle-particle contacts will be prevalent and will govern the material properties of the system.

As mentioned above, a granular suspension can be observed to flow like a liquid or to behave as a solid. At the interface between these regimes is the jamming transition [4], a critical point at which the rheological properties of the material change dramatically. In the jammed state the particles are tightly packed and in persistent contact with one another meaning they cannot move around and explore alternative configurations. Under zero applied stress, the system is jammed at volume fractions above approximately 0.64 [5] (for smooth particles - for rough particles this value is reduced [6]). A system that is in the jammed state under zero applied stress will then "unjam" if a stress is applied that exceeds the yield stress.

3. SUSPENSION RHEOLOGY

3.1 Background

Suspensions are studied in terms of their response to an applied stress or rate of strain, i.e. their *rheology*. Characterising suspension rheology under highly controlled, idealised conditions enables both a deeper understanding of flowability and processability of suspensions, and the development of constitutive models. A typical rheological experiment involves applying a shear deformation to the suspension of interest, and extracting the stress-strainrate relationship, which can be used to obtain the suspension *viscosity*.

When solid particles are suspended in a liquid, the viscosity increases [7]. Einstein derived analytically the increase in viscosity with volume fraction to a first order approximation, for ϕ<0.02. Batchelor [8] extended this analysis and took particle-particle interactions into account, arriving at a second order approximation valid for ϕ<0.1. The relationships between suspension viscosity and volume fraction

above were further extended by Krieger and Dougherty [9], to predict the viscosity of suspensions with volume fractions up to the maximum packing fraction, ϕ_c. As ϕ approaches ϕ_c, the viscosity of the suspension diverges, at which point the material enters the "solid" regime.

So far we have assumed that suspensions behave as Newtonian fluids, with a constant viscosity that depends on ϕ. This is not the case for most suspensions, which can exhibit complex *shear rate* dependence [10]. Shear thinning (viscosity decreases with increasing shear rate) has been observed and thoroughly studied theoretically and experimentally [11], and is typically associated with the Brownian-to-non-Brownian transition. Shear thickening (viscosity increases with increasing shear rate, most notably demonstrated in cornstarch suspensions) may also be observed [12], and is attributed to both the viscous-inertial and the frictionless-frictional transitions, as will be discussed later. Predictive models for suspension rheology must therefore account for shear rate (in addition to volume fraction) dependence of viscosity.

3.2 Experiments

Seminal work by Boyer et al [13] elegantly demonstrated that shear flows of suspensions of hard particles may be described in precisely the same framework as their dry granular counterparts. A suspension of large (r=0.5mm) particles was sheared at fixed normal stress and fixed shear stress using a novel rheometer. Under normal shearing conditions, the suspension can be uniquely characterized based on its volume fraction ϕ and the ratio of shear to normal stresses $\mu = \sigma/P$. In addition, these properties vary monotonically with a parameter called the *viscous number*, defined as $J = \eta\gamma/P$. This has proved to be a popular and effective framework for suspension rheology. This framework is not suitable for suspensions of soft particles, though a number of useful parallels may be drawn [14].

Other flow geometries have also shed light on suspension rheology. In Poiseuille flow, partial plug flow is observed [15], with apparent wall slip due to hydrodynamic forces resulting in a reduced particle concentration and apparent reduced viscosity at the walls. In Couette flows, the fluid is observed to have a stagnant region adjacent to the stationary boundary and a flowing region at the moving boundary [16], with the interface location being dependent on the velocity of the upper plate. This has been described as yield stress behaviour [17], with the yield stress not being dependent on the interstitial fluid viscosity, but on the physical details of the particles.

Experimental micromechanical work by Behringer and co-workers at Duke University has looked at force distributions in granular media, and how frictional forces between particles in contact influence these distributions [18]. Photoelastic disks, two dimensional plastic disks whose light transmission properties are dependent on the compressive force applied to them, are poured into piles, and the resulting distribution of force chains is observed visually. In this instance it is found that the force chains are predominately aligned in the vertical axis, as expected, and they distribute in weight of the pile in such a way that it is spread across the ground surface area rather than localised below the centre of mass. Analyses such as these contribute to our understanding of dense suspensions, as for high volume fractions the flow behaviour is dominated by persistent particle-particle contacts, meaning force chains will be established. Later work by this group found that when these disks are sheared, long-range uni-directional force chains are established that are not present in isotropically compressed systems [19] Furthermore, it was found that at a critical volume fraction (thought to correspond to the jamming point), there was a non-linear and rapid increase in the coordination number of the system (the average number of particle contacts, per particle), suggesting that at this point the force transmission through sustained particle-particle contacts becomes significantly more important. Though these works pertain specifically to dry granular materials, the close parallels suggested by [13] provide evidence that it also applies to suspensions.

Individual particle data such as location and velocity components have traditionally been very difficult to extract from experiments of granular media. The recent development of confocal rheometry [20] has allowed a 3D particle scale imaging technique, confocal microscopy, to be coupled with real time rheological measurements. This procedure can be implemented in some of the traditional rheological geometries, including Couette flow, Poiseuille flow and cone and plate rheometry. Algorithms have been developed that are able to determine the location, velocity and size of every particle in a suspension under shear, at frame rates of 5-100 Hz. These data now offer unparalleled levels of simulation validation.

3.3 Simulations

Computational work in the field of suspension rheology can be broadly split into two categories: particle based and continuum based simulations.

Particle based simulations involve the explicit calculation of particle properties such as position, velocity and contact force, for a particle assembly or suspension. A classical particle simulation technique is Stokesian Dynamics (SD) [21], in which long- and short-range hydrodynamics are solved numerically for the motion of solid particles in a continuous interestitial fluid. This technique is able to capture suspension flow behaviour well for

non-equilibrium flows at relatively low ϕ. The long range hydrodynamic forces are extremely expensive to solve, meaning SD simulations are limited to systems of size O(1000) particles, even with modern computers.

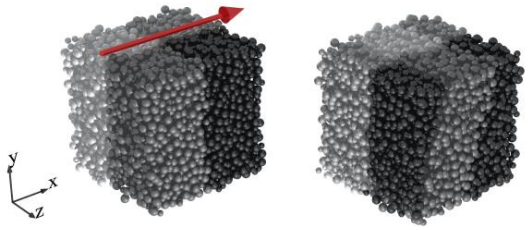

Figure 2. A 3-dimensional simulation of shear flow in a high volume fraction suspension, using the discrete element method.

An alternative particle simulation method more recently adopted for suspension rheology is the Discrete Element Method (DEM) [22]. DEM is very closely related to traditional molecular dynamics simulations, in which the motion and interactions of individual particles are solved explicitly. While still rather computationally expensive, DEM simulations are cheaper than SD because they typically limit calculation to short-range hydrodynamic and contact forces.

Particle simulations provide a level of solution detail that cannot be paralleled by continuum methods. For example, at any point in time during a DEM simulation, the precise coordinates, velocity components and force components of every particle being simulated can be obtained, visualised and used for calculations. Furthermore, the particle interaction forces can be refined to accurately model additional forces such as particle cohesion and friction. The processing power required by DEM is related to the number of particles being simulated, and the length of the simulation. Computational advances in the past 20 years have led to a surge in the application of DEM simulations to granular problems. DEM has been used extensively to study the behaviour of dense granular materials under shear, in periodic domains [23]. In these simulations, a domain is constructed with particles at a desired volume fraction. Lees-Edwards boundary conditions [24] are then applied to simulate simple shear (see Figure 2), and the resulting stress response is analysed.

Using this approach, Campbell [25] successfully predicted ϕ_c (approximately 0.62) above which the material is in the jammed regime, and below which it is in a flowing regime. Latterly, such simulations have successfully captured transitions between viscous and inertial rheology and hard and soft rheology [2,6,26].

The evolution of suspension microstructure during shearing is critical to the rheological behaviour. Anisotropies that form during shearing simulations have been quantified through the fabric tensor, which has been incorporated into constitutive models for granular materials [27], guided by DEM results.

4. SHEAR THICKENING

Non-Newtonian rheology [28] has been observed and studied for centuries in numerous materials, flow regimes and applications. In this section we consider suspensions of non-Brownian spheres, and the phenomenon of shear thickening [29]. This flow behaviour, in which the shear stress increases faster than linearly with the shear rate, is observed in systems such as dry granular materials at constant volume [6, 17] industrial pastes [30] and well characterised model systems. Recent work demonstrates one manifestation of shear thickening in granular suspensions, due to a viscous-to-inertial transition during flow [2, 26, 31], as the Stokes number exceeds 1. Cornstarch suspensions, for example, have been observed [32] to shear thicken far more strongly than can be accounted for by the onset of inertia, and at Stokes numbers significantly less than 1. This behaviour has variously become known as ``shear jamming", ``dynamic jamming" and ``discontinuous shear thickening" (DST). A number of competing mechanisms for DST have been proposed, in what is an exciting and rapidly advancing area of the suspension literature.

One explanation of DST is based on the shear-induced formation of ``hydroclusters" [33], mesoscale particle agglomerates stabilised by hydrodynamic interactions that result in massive dissipation under shear. For sufficiently high particle volume fractions, the hydrodynamics of the suspension can be considered to be dominated by what happens in the gaps between very close neighbouring particles [34]. The force required to bring smooth neighbouring particles into contact is given by classical lubrication theory, and diverges with the inverse of the interparticle gap. Near-touching particles are therefore subject to massive lubrication forces, which resist particle separation and result in the evolution of dynamically correlated clusters, which have been observed using confocal-rheometry [35].

Another proposed origin of DST is dilatancy, the tendency of the suspension to increase in volume upon shearing [32]. Under imposed stress and constant volume conditions, dilatant behaviour can result in complete arrest of flow. Closely related with this notion is the idea that macroscopic volume fraction inhomogeneities can emerge in a dilatant suspension, with a low volume fraction flowing (but not shear-thickening) region co-existing with high volume fraction arrested region, as has been demonstrated for cornstarch suspensions [36].

Competing with these explanations of DST is an emerging body of theoretical [37], experimental [3, 38] and computational [39] work that attributes shear thickening to a microscale change in the observed particle interaction potential under stress (namely a proliferation of frictional contacts), meaning thickening can be observed as a completely local phenomenon under homogeneous shear flow, in stark contrast with the macroscopic ``hydroclustering'' and volume fraction bifurcation discussed above. This hypothesis allows homogeneous flow with finite viscosity in the shear thickened state, consistent with the notion of hydroclusters, but in contrast to the dilatancy argument, which requires bifurcation of the volume fraction for flow above shear thickening. The origin of this shear thickening behaviour can be addressed by considering the relative properties of suspensions of small versus large particles.

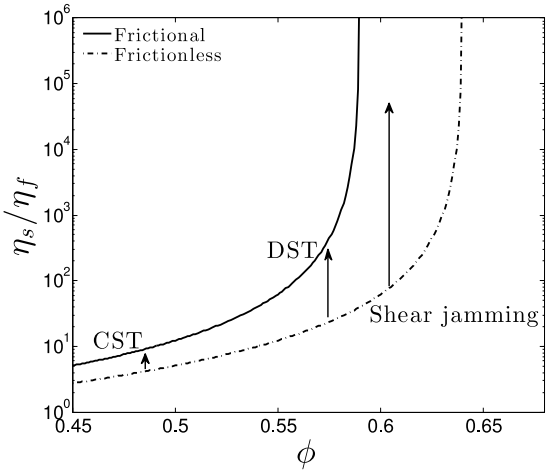

Figure 3. Suspension viscosity (scaled by interstitial fluid viscosity) for suspensions of frictionless and frictional particles, as a function of volume fraction

Very small particles (r< 10μm) in suspension can behave like frictionless hard spheres under shear. Repulsive normal forces such as electrostatics keep particles separated, while their viscosity increases with volume fraction, diverging at the random closed packing (RCP) limit (ϕ_{RCP}=0.64). Suspensions of larger particles can exhibit frictional interactions between contacting surfaces reducing the number of available degrees of freedom and resulting in a viscosity that diverges with volume fraction at an interparticle friction dependent point, ϕ_J=0.58 [6]. Particles of intermediate size in suspension may exhibit repulsive normal forces like colloids, for example due to electrostatic or polymer hair stabilisation, and yet may also exhibit frictional behaviour if their surfaces are forced into contact. Experiments in well characterised systems of polymer coated PMMA particles [3] demonstrate a co-existence of frictionless and frictional rheology within a single material as a function of shear rate, arising due to the nature of the particle-particle interaction. For particles colliding with weak contact forces, the response is mediated through the polymer hairs, generating only a normal repulsion and maintaining a lubrication film, consistent with colloid rheology. For larger contact forces, particle surfaces come into closer proximity, breaking the lubrication layer, leading to interdigitation of the polymer hairs and resulting in an increased resistance to sliding motion and a frictional surface interaction, consistent with granular suspension rheology. The result is that when the particle system undergoes a critical or ``onset'' bulk stress σ^*, the quasi-Newtonian rheology at St<1 can switch from being frictionless to frictional. For particles of radius r, σ^* scales with $1/r^2$, meaning that in the range of experimentally accessible shear rates, small particles are always in the frictionless state, while large particles are always frictional. Particles of intermediate size can be experimentally observed to switch between regimes as a function of the applied stress or shear rate.

The effect of such transitions on the rheology is most conveniently explained (as has been done by others) by considering the viscosity divergence of suspensions of frictional and frictionless particles, as in Figure 3. For low volume fractions, a transition from frictionless to frictional rheology upon exceeding the bulk onset stress results in a slight increase in the quasi-Newtonian viscosity of the suspension, a phenomenon we describe as continuous shear thickening (CST). As ϕ increases, the frictional viscosity diverges considerably faster than the frictionless one, so the separation between the flow curves becomes large. A transition from frictionless to frictional rheology close to (but less than) ϕ_J therefore results in a massive jump in the quasi-Newtonian viscosity, which we describe as discontinuous shear thickening (DST). For $\phi_J<\phi<\phi_{RCP}$, quasi-Newtonian flow is possible on the frictionless branch, but upon exceeding the onset stress at which the particle-particle contacts become frictional, the material becomes shear jammed and is either arrested (hard particles) or quasistatic (soft particles). No quasi-Newtonian flow is possible in either regime for $\phi>\phi_{RCP}$.

Recent simulations and experiments [40] used the elegant technique of shear reversal to demonstrate conclusively that this picture of shear thickening is prevalent in model PMMA systems as well as silica pastes, and may well be a general feature of all shear thickening systems.

5. OUTLOOK

Understanding suspension rheology remains an ongoing challenge within the physics and engineering community. In future, it is hoped that a deep fundamental and predictive understanding of the intimate links between microscale physics and

macroscale suspension properties will be exploited to “tailor-make” materials with desired properties. This would prove highly advantageous to many areas of engineering, for example paste extrusion, where poorly understood rheology and reliance on “rules-of-thumb” have hindered development for years.

ACKNOWLEDGEMENT
The author thanks J. Sun, B.M. Guy, M. Hermes, N.Y.C. Lin, W.C.K. Poon, M.E. Cates, M. Marigo, P. McGuire, H. Stitt, H. Xu and J. Ooi for helpful discussions. The work is funded by a CASE Studentship with EPSRC and Johnson Matthey.

REFERENCES
[1] Russel, W.B. (1981). Brownian motion of small particles suspended in liquids. *Annual Review of Fluid Mechanics*, 13:425:455
[2] Ness, C., Sun, J (2015). Flow regime transitions in dense suspensions. *Physical Review E*, 91(1)
[3] Guy, B.M. et al. (2015). Towards a unified description of the rheology of hard-particle suspensions. *Physical Review Letters*, 115(8)
[4] Liu, A.J. and Nagel, S.R. (1998). Jamming is just not cool anymore. *Nature*, 396
[5] Song, C. et al (2008). A phase diagram for jammed matter. *Nature*, 453(7195):629-632
[6] Chialvo, S. et al (2012). Bridging the rheology of granular flows in three regimes. *Physical Review E*, 85(2)
[7] Mewis, J. and Spaull, A.J.B. (1976). Rheology of concentrated dispersions. *Advances in Colloids and Interface Science*, 6:173-200
[8] Batchelor, G.K. (1977). The effect of Brownian motion on the bulk stress in a suspension of spherical particles. *Journal of Fluid Mechanics*, 83(1):97-117
[9] Krieger, M. and Dougherty, T.J. (1959). A mechanism for non-Newtonian flow in suspensions of rigid spheres. *Journal of Rheology*, 3:137-152
[10] Stickel, J.J. and Powell, R.L. (2005). Fluid mechanics and rheology of dense suspensions. *Annual Review of Fluid Mechanics*, 37(1):129-149
[11] Roberts, G.P. et al (2001). Modelling the flow behaviour of very shear-thinning liquids. *Chemical Engineering Science*, 56(19):5617-5623
[12] Barnes, H.A. (1989). Shear-thickening in suspensions of nonaggregating solid particles. *Journal of Rheology*, 33:329
[13] Boyer, F. et al (2011). Unifying suspension and granular rheology. *Physical Review Letters*, 107
[14] Nordstrom, K.N. et al (2010). Microfluidic rheology of soft colloids above and below jamming. *Physical Review Letters*, 105(17):175701
[15] Isa, L. et al (2007). Shear zones and wall slip in the capillary flow of concentrated colloidal dispersions. *Physical Review Letters,* 98(19):4
[16] Bocquent, L. et al (2001). Granular shear flow dynamics and forces. *Physical Review E*, 65
[17] Jop, P. et al (2006). A constitutive law for dense granular flows. *Nature*, 441(7094):727-730
[18] Behringer, R.P. (1999). Predictability and granular materials. *Physics D*, 133:1-17
[19] Majmudar, T.S. and Behringer, R.P. (2005). Contact force measurements and stress-induced anisotropy in granular materials. *Nature*, 435(7045):1079-1082
[20] Besseling, R. et al (2009). Shear banding and flow-concentration coupling in colloidal glasses. *Physical Review Letters*, 105(26):4
[21] Brady, J.F. and Bossis, G. (1988) Stokesian Dynamics. *Annual Review of Fluid Mechanics*, 20(1):111-157
[22] Cundall, P.A. and Strack, O.D.L. (1979). A discrete numerical model for granular assemblies. *Geotechnique*, 29(1):47-65
[23] Olsson, P. and Teitel, S. (2007). Critical scaling of shear viscosity at the jamming transition. *Physical Review Letters*, 98(17)
[24] Lees, A.W. and Edward, S.F. (1972). The computer study of transport processes under extreme conditions. *Journal of Physics C*, 5(15):1921-1928
[25] Campbell, C. (2002). Granular shear flows at the elastic limit. *Journal of Fluid Mechanics*, 465
[26] Trulsson, M. et al (2012). Transition from the viscous to inertial regime in dense suspensions. *Physical Review Letters*, 109(11)
[27] Sun, J. and Sundaresan, S. (2011). A constitutive model with microstructure evolution for flow of rate-independent granular materials. *Journal of Fluid Mechanics*, 682:590-616
[28] Denn, M.M. (2004). Fifty years of non-Newtonian fluid dynamics.
[29] Brown, E. (2013). Friction’s role in shear thickening. *Physics*, 6:125
[30] Benbow, J. and Bridgwater, J. (1993). Paste Flow and Extrusion. Clarendon Press
[31] Fall, A. et al (2010). Shear thickening and migration in granular suspensions. *Physical Review Letters,* 105
[32] Fall, A. et al. (2008). Shear thickening of cornstarch suspensions as a reentrant jamming transition. *Physical Review Letters*, 100
[33] Wagner, N.J. and Brady, J.F. (2009). Shear thickening in colloidal dispersions. *Physics Today*, 62:27-32
[34] Ball, R.C. and Melrose, J.R. (1997). A simulation technique for many spheres in quasi-static motion under frame-invariant pair drag and Brownian forces. *Physica A*, 247(1-4):444-472
[35] Cheng, X. et al (2011). Imaging the microscopic structure of shear thinning and thickening colloidal suspensions. *Science*, September:1276-1280
[36] Fall, A. et al (2015). Shear thickening versus local shear jamming in cornstarch. *Physical Review Letters*, 114(9)
[37] Wyart, M. and Cates, M.E. (2014). Discontinuous shear thickening without inertia in dense non-Brownian suspensions. *Physical Review Letters*, 112
[38] Pan, Z. et al (2015). S-shaped flow curves of shear thickening suspensions. *Physical Review E*, 92(3)
[39] Seto, R. et al (2013). Discontinuous shear thickening of frictional hard-sphere suspensions. *Physical Review Letters*, 111
[40] Lin, N. et al (2015). Hydrodynamic and contact contributions to shear thickening in colloidal suspensions. *arXiv*, 1509.02750

Infrastructure and Environment Scotland 3rd Postgraduate Conference
9th December 2015
Heriot-Watt University, Edinburgh

MODELLING OF MASONRY WALL RETROFITTED WITH ENGINEERED CEMENTITIOUS COMPOSITES

S. Pourfalah, B. Suryanto & D. M. Cotsovos
Institute for Infrastructure and Environment,
Heriot Watt University
(sp315@hw.ac.uk)

ABSTRACT

Nonlinear finite element analyses is currently employed to assess the potential benefits stemming from the use of engineered cementitious composites (ECC) in order to enhance the out-of-plane performance of masonry infill walls. Attention is focused on the response of beam-like masonry specimens which were strengthened with a thin layer of ECC and subjected to four-point bending test. Three nonlinear material models are employed for describing the behavior of masonry, ECC and mortar in combination with two cohesive interface models representing the brick/mortar and brick/ECC interfaces. The primary objective of the present investigation is to calibrate these models on the basis of the available experimental data, in order to develop a representative numerical model of the retrofitted masonry specimens. The numerical predictions obtained reveal that the use of a thin ECC layer enhances the out-of-plane load-carrying capacity and ductility of the beam-like masonry specimens. It is shown that the failure mode of the specimens and the crack patterns in the ECC layer are affected by the bond between the masonry and the ECC layer.

1. INTRODUCTION

The contribution of masonry infill walls to the overall behaviour of frame structures has been acknowledged through numerous experimental and numerical investigations (Kyriakides et al., 2012, Pourfalah et al.) and the need to consider their effects on the overall structural response has been recognized in the latest generation of structural design codes. However, masonry walls are characterized by poor out-of-plane performance (Davidson et al., 2005) which often results in these elements sustaining damage or even collapsing when subjected to actions such as earthquakes, extreme wind loads and blast waves. Damages sustained by masonry infill walls during earthquakes have been identified as the primary cause of injuries and fatalities (Tiedeman, 1980). In addition, it is estimated that the repair costs related to damages sustained by the non-structural elements (including the infill walls) represent approximately 80% of the total repair costs of frame structures

A series of retrofitting methods have been developed for improving the out-of-plane performance of infill masonry walls. These methods involve the use of: (i) external reinforcement meshes embedded cement render (Abrams and Lynch, 2001, ElGawady et al., 2004) and (ii) metal or fibre reinforced polymer straps bonded to the wall surface (Taghdi, 1998, Carney and Myers, 2003). Although these methods have been proven effective in enhancing the out-of-plane behaviour of masonry walls, their implementation is characterized by several problems such as: (i) a notable increase in the self-weight of the buildings; (ii) the risk of de-bonding from the surface of the masonry walls and (iii) their inability to prevent the generation of fragments when subjected to impact or blast loads.

A new method for enhancing the out-of-plane behaviour of infill masonry walls was recently developed, using a thin layer of ductile cementitious composite known as an Engineered Cementitious Composite (ECC) (Kyriakides et al., 2012, Pourfalah et al. 2015). An ECC is a fibre-reinforced mortar which exhibits a tensile strain capacity of 3–5% and forms multiple fine cracks, typically with widths of less than 100 micron (Li, 2003). It has been demonstrated that the application of a thin layer of ECC to one side of a masonry wall can enhance lateral resistance, stiffness, ductility, load carrying capacity and energy dissipation (Dehghani et al., 2015, Billington et al., 2009). It is also expected that this layer could reduce the generation of fragments as it will be able to act as a net.

Present work sets out to develop a finite element model capable of realistically predicting and quantifying the benefits stemming from the use of a thin ECC layer on the out-of-plain behavior of masonry infill walls. For this purpose, beam-like masonry specimens (consisting of a stack of 10 bricks) are subjected to four-point static bending tests. The latter beams are retrofitted with a thin ECC layer (see Fig.1). The test data obtained are employed for the development of a finite element

(FE) model capable of realistically predicting the behavior of the subject specimen. The latter FE model employs a number of constitutive models capable of describing the nonlinear behavior of the materials involved (masonry, ECC and mortar) and their interaction (achieved through the use of a brick-mortar and brick-ECC interface model). The models are calibrated based on relevant data obtained from a series of laboratory tests conducted prior to this study. The numerical predictions obtained are validated against data obtained from the four point bending tests (Pourfalah et al. 2015). It is shown that the use of a thin ECC layer can significantly improve the out-of-plane load-bearing capacity and ductility of masonry infill walls.

2. EXPERIMENTAL BACKGROUND

In order to develop suitable FE models, two groups of experiments were considered: (i) the first group aims at calibrating the individual parameters of the various material and interface models presently employed and (ii) the second is employed for validating the predictions of the FE model representing the retrofitted masonry beam-like specimens subjected to four-point static bending tests (Pourfalah et al. 2015) (see Fig. 1).

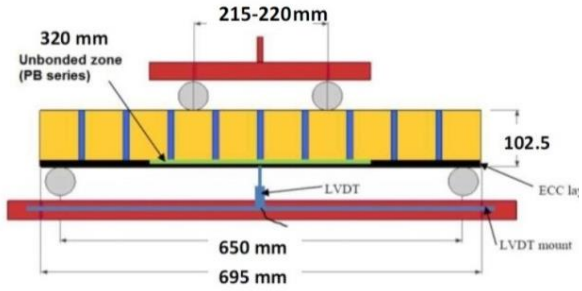

Fig. 1. Masonry specimen test configuration.

3. MODELLING OF THE MASONRY SPECIMENS

Several FE models have been developed to date aiming to predict the in-plane and out-of-plane behaviour of masonry walls (Hashemi, 2007, Drysdale and Essawy, 1988). Such models can be categorised in three groups (Asteris et al., 2013): (1) one-phase models, in which the brick, mortar and interface are modelled as an isotropic continuum material; (2) two-phase models, in which the mortar and brick-mortar interface is considered as one layer; and (3) three-phase model, in which masonry unit, mortar and interface are modelled separately. The latter group of models is considered more representative of the problem at hand, but requires significant computational power (Kyriakides et al., 2012)

In this study, commercial nonlinear finite element analysis (NLFEA) software (ADINA, 2014) is used. Figure 2 shows the 2-dimensional (2D) FE model developed representing the retrofitted beam-like specimen shown in Fig.1. The package incorporates a number of constitutive models capable of realistically describing the behaviour of the relevant materials and interfaces. It also employs an iterative solution procedure based on the Newton-Raphson method to account for the stress redistributions due to the exhibited cracking. 4-node solid elements are employed to model the bricks, the mortar and the ECC layer. The material properties of the masonry unit and the mortar are described using the concrete material model. The ECC is modelled as a multi-linear plastic material. Elastic steel elements are used to represent the plates located at the supports and at the point where the load is exerted. These elements are used to avoid the development of high stress concentrations that can result in the formation of localised cracking.

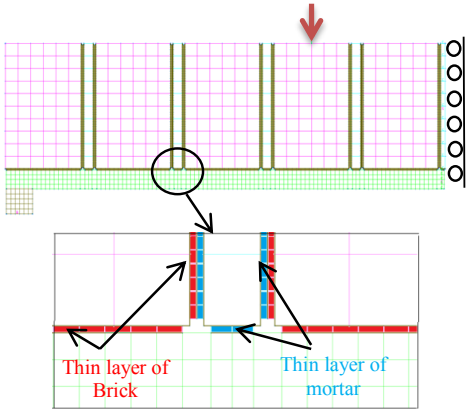

Fig.2. FE model of the masonry specimen in Fig.1

4. CALIBRATION PROCESS

Table 1 presents relevant material properties that were obtained experimentally. These values are used for calibrating the parameters of the various constitutive models employed. An overview of the calibration process is provided in the following sections.

Table 1. Parameters of the various material and interface models employed.

Property	Symbol	Value
Brick		
Elastic modulus	E_{brick}	40Gpa
Compression strength	fc_{brick}	60MPa
Tensile strength	ft_{brick}	6 MPa
Mortar		
Elastic modulus	E_{mortar}	20GPa
Compression strength	Fc_{mortar}	20MPa
Tensile strength	Ft_{mortar}	6 MPa
ECC		
Elastic modulus	E_{ECC}	20GPa
Compression strength	fc_{ECC}	30MPa
First crack stress	$\sigma_{First\ crack}$	2.8MPa

First crack strain	$E_{first\ crakc}$	0.00016
Maximum stress	σ_{max}	3.75
Maximum strain	ε_{max}	0.035
Failure strain	$\varepsilon_{failure}$	0.04
Brick-mortar interface		
Shear strength	V_{BM}	0.8Mpa
Shear modulus	G_{BM}	16GPa
Tensile strength	T_{BM}	0.5Mpa
Brick-mortar interface		
Shear strength	V_{BM}	1.5MPa
Shear modulus	G_{BM}	50GPa

4.1. Tensile test on ECC dog-bone sample

To determine the tensile properties of the ECC, five dog-bone specimens similar to that shown in Fig. 4 were tested under uniaxial tensile. On the basis of the test data obtained ECC is modelled as a multi-linear plastic material and its behaviour in tension and is described by a simple tri-linear stress-strain curve presented in Fig. 3. The numerical predictions obtained from the FE model representing the dog-bone specimen in Fig.4a are in good agreement with their experimental counterparts (see Fig. 5). Figure 6 shows the comparison of the predicted and observed tensile strain fields at failure.

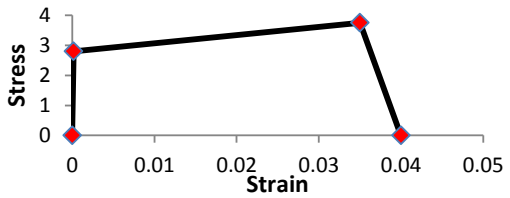

Figure3. Stress-strain curve describing the behaviour of ECC dog-bone specimen in tension.

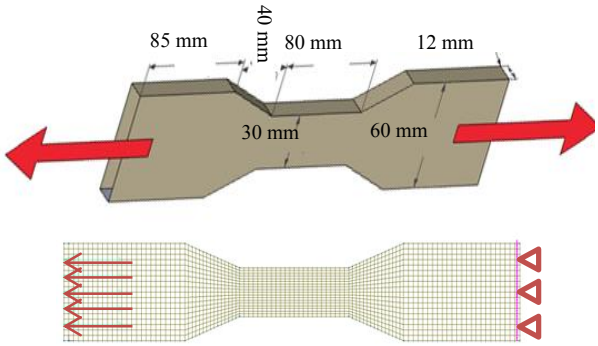

Figure.4. Dog-bone ECC specimens and its FE model.

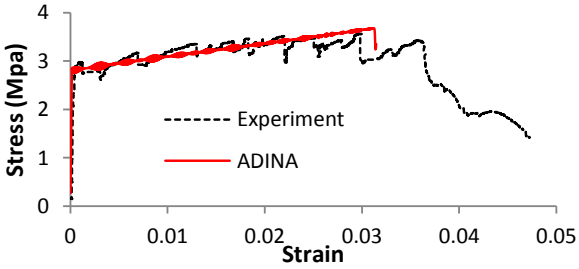

Figure.5. Comparison between the numerically predicted and experimentally established behaviour of the ECC dog-bone specimen under uniaxial tension.

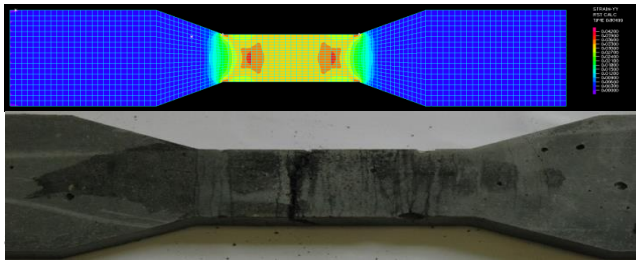

4.2.4 Tensile test of brick-mortar interface

The experimental setup employed in order to study the behaviour of the brick-mortar interface in tension accompanied by its 2D FE model are presented in Fig.7. A cohesive interface element (representing the bond between brick-mortar-) is employed in combination with the mixed mode interaction criterion (ADINA MANUAL). The parameters of this model are defined based on the experimentally established values of tensile strength of the subject interface (Table 1). The bottom face of the FE mesh representing the specimen is assumed fixed and the load is applied onto the upper face in the form of displacement increments. A total vertical displacement of 0.05mm applied in 1000 step. The predicted tensile strength of the subject interface is in agreement to its experimentally established value (see Table 2). It should be noted that failure occurred at the interface in both the experimental and numerical study.

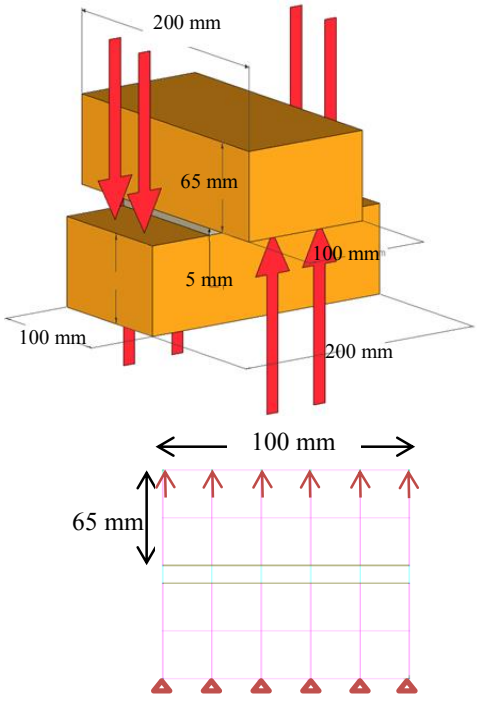

Figure7. Specimen used for defining the tensile strength of the brick-mortar interface accompanied by its FE model.

Table 2. Experimentally and numerically established values of the brick-mortar interface tensile test

Test	Results
Experiment	0.5 MPa
Model	0.5 MPa

4.2.5 Shear test of brick-mortar interface

The experimental setup employed in order to study the behaviour of the brick-mortar interface in shear accompanied by its 2D numerical model are presented in Fig.6. The specimen used comprises three bricks connected via mortar layers (Fig.8). To define properties of the cohesive element between brick and mortar 3 different set of parameters were employed (see Table 3). The same cohesive element used for representing the brick-mortar bond in the preceding section is employed herein and developed in combination with the mixed mode interaction criterion (ADINA MANUAL). The boundary conditions imposed onto the specimen are shown in Fig. 8. The load is applied onto middle brick in the form of displacement increments. A total vertical displacement of 0.1 mm is imposed in 1000 load-step.

A comparison of the predictions obtained from the 3 set of parameters (see Fig.9) with the experimentally established values of shear strength of the interface presented in table (see Table 1) reveals generally good agreement for the 2nd and 3rd case study.

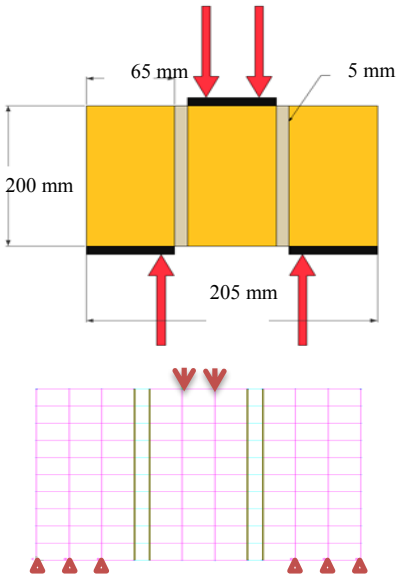

Figure 8. Specimens used for defining the shear strength of the brick-mortar interface and its FE model.

Table 3. Brick-mortar cohesive bond properties

Interface name	Shear strength	Toughness	Penalty stiffness
ADINA1	1.8 MPa	19.4 N.m	10^{11}
ADINA2	2 MPa	2.4 N.m	10^{12}
ADINA3	1.8 MPa	0.194 N.m	10^{13}

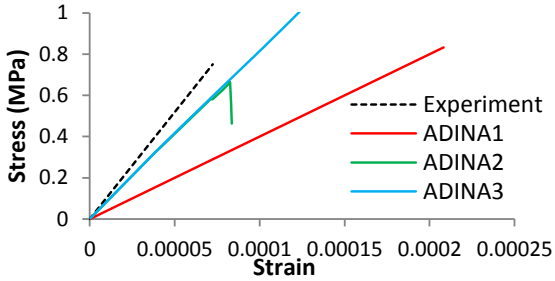

Figure9. Brick-mortar shear test results.

4.2.6 Shear test of brick-ECC interface

The same modelling process described in section 4.6 is adopted calibrating the ECC-brick interface element. Three sets of parameters are employed for defining for defining cohesive bond presented in Table 4. The predictions obtained from the model are presented in Figure 10 where it can be seen that the predictions obtained form case study ADINA2 provides the closest fit to the experimental data.

Table 4. Brick-ECC cohesive bond properties

Interface name	Shear strength	Toughness	Penalty stiffness
ADINA1	10 MPa	600	10^{11}
ADINA2	10 MPa	60	10^{12}
ADINA3	15 MPa	13.5	10^{13}

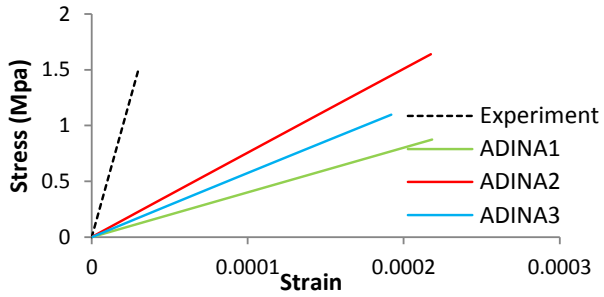

Figure10. Brick-ECC shear test results.

5. Modelling of masonry beam-like specimen

The experimental setup used to study the behaviour of the masonry beam-like specimens under 4-pont bending tests is shown in Fig.1 and the relevant experimental investigation is presented in details elsewhere (Pourfalah et al. 2015).

5.1 Plain masonry bending test

The FE model representing the plain masonry specimen is presented in Fig.10. Due to the symmetry characterising the problem at hand only half of the specimen was simulated. The FE model comprises five brick units and a five mortar layers between the bricks. The size of the bricks was 100 x 65 mm. Each brick unit was modelled by a 6x10 FE mesh. The thickness of mortar layer

(joint) was 10mm except in the case of the layer at the mid-span of the specimen which had a thickness of 5mm. All mortar layers were modelled by a FE mesh of 1x10. Cohesive elements were defined at the interface between the brick and the mortar layer based on the study presented in section 4.2.5. A 20x20 mm steel element is used for supporting the masonry specimen in the vertical direction Also for one end of specimen that have been cut due to symmetry, whole nodes were fixed in Y direction. The total displacement of 1 mm assigned to forces in 1000 step. The resulting model was used to investigate the mechanics underlying the behaviour of the masonry specimen up to failure.

The predictions obtained from the FE model concerning the mode of failure (see Fig.10) as well as the load–defection curves associated with the mid-span (see Fig.11) exhibit similar trends with their experimentally established counterparts. However, the numerically predicted load-bearing capacity is higher than that established experimentally. This difference can be attributed to range of reasons such as the variation of the material properties that often characterise masonry or to the effect of imperfections associated with the manufacturing process of the subject specimen. During NLFEA failure occurred due to failure in the cohesive interface which was confirmed form the experiment (Fig. 10).

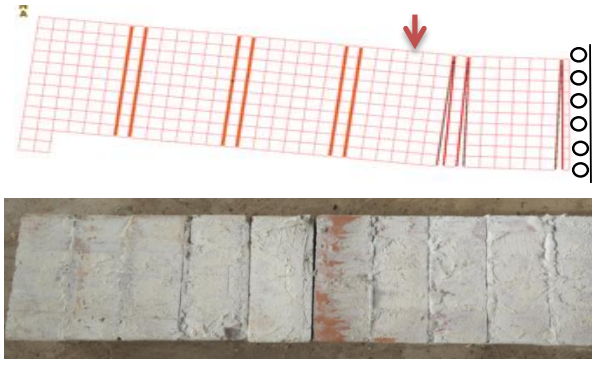

Figure 10. Comparison of the plain masonry model with the specimen investigated experimentally.

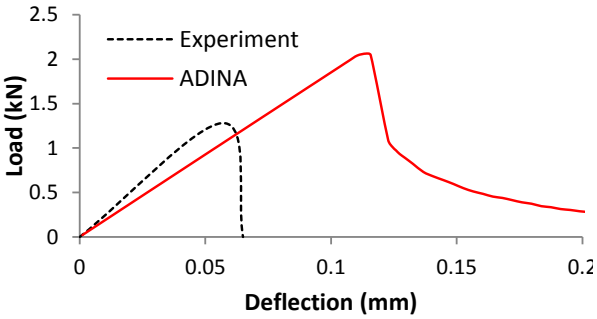

Figure 11. Comparison of the experimentally and numerically established behaviour of the plain masonry specimen presented in Figure 10.

5.2 Full bond ECC bending test

The same model was essentially adopted when investigating the behaviour of the ECC retrofitted specimen. A 15mm thick layer of ECC was added at the lower face of the masonry beam and was modelled by a 4x100 FE mesh. The ECC layer was considered fully bonded to the lower face of masonry specimen. The properties of interface forming between ECC and masonry beam were defined according section 4.2.6. The support and fixity conditions imposed onto the retrofitted specimen were the same as those used in the case of the plain masonry beam. A total displacement of 10 mm was imposed in a total of 1000 step. The load also was applied monotonically until failure in displacement increments.

The results obtained from the FE model are presented in Figure 14 in the form of curves expressing the variation of the applied load with the defection exhibited at mid-span. The predicted response is in generally good agreement with that established experimentally. The load bearing capacity established experimentally is higher than that the predicted numerically. This can be attributed to the thickness of the ECC layer in the region of the mortar joints which is about 1-2 mm thicker in real test and also to the fact that the ECC layer used in the specimen is possible stronger and stiffer due to the absorption (immediately after casting) by the bricks.

It can be observed that the numerical predictions tend underestimate the ductility. This can be attributed to the fact that during the test de-bonding occured locally between only one brick and the ECC layer in the area between two points which the loads are applied (approximately the middle third of the span). This localised de-bonding can cause uniform cracking in the ECC layer ultimately resulting in local failure in this region (see Fig 15). However this mechanism is not adequately simulated in model.

Failure in the model occurred in the cohesive interface between the brick and mortar which is in agreement with the failure mode observed during testing. This is followed by tensile failure in the ECC layer. The distribution of strain within the FE model is presented in Figure 15. This strain distribution is related with crack pattern in actual specimens. It can be observed that the strain distribution is compatible with crack pattern exhibited in during testing.

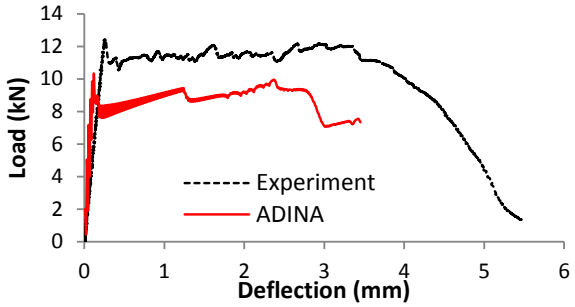

Figure 14. Full bond beam bending test results.

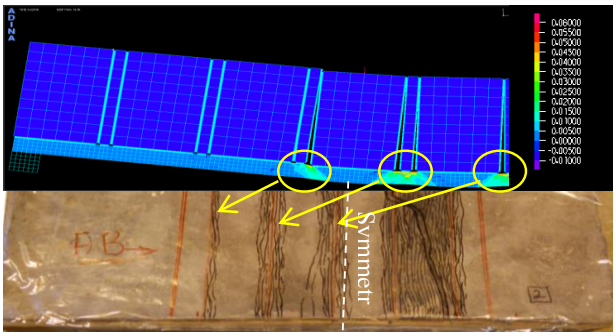

Figure15. Comparison of the numerically established strain distribution in combination with the crack patterns exhibited during testing.

5.3 Partial bond ECC bending test

To simulate the partial bond specimen the same model which was used in the previous section is employed. However, in the experimental investigation an unbonded zone between ECC layer and masonry beam is formed in middle third span of the specimen (green line, Fig. 1). This unbonded zone is also accounted in the FE model by introducing a contact surface between ECC layer and masonry.

The results of the FE model are shown in Figure 16, in the form of load-defection curves at mid-span. The numerical predictions are in good agreement with their experimentally established counterparts. For the same reasons disused in the preceding section the numerical analysis tends to underestimate the load bearing capacity. However, in terms of ductility the experimental and numerical predictions are in agreement.

Failure in the model happens in the cohesive interface between the brick and mortar, followed by tensile failure in the ECC layer. The same procedure has been observed during experiment test .The distribution of strain within the FE model is presented in figure 17. This strain distribution is related with crack pattern in real specimens. It can be observed that the uniform strain distribution in middle third span is compatible with crack pattern exhibited in experimental test.

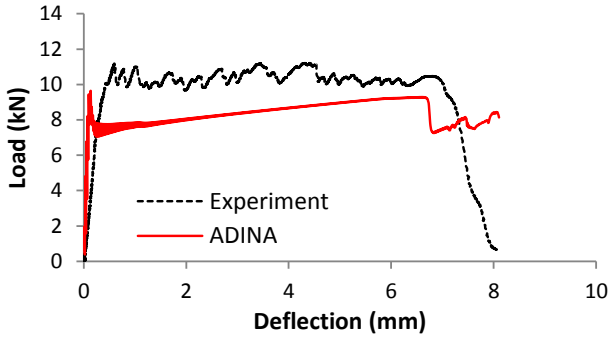

Figure 16. Partial bond beam bending test results.

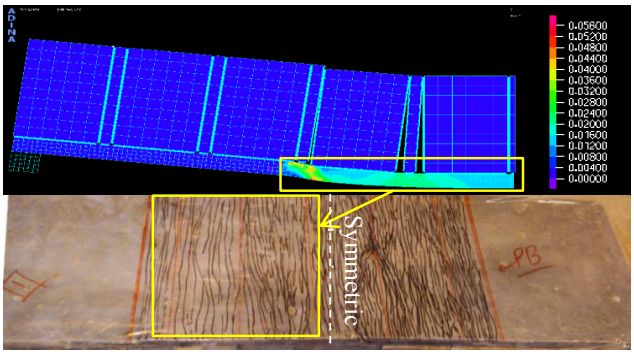

Figure17. Comparison of the numerically established strain distribution in combination with the crack patterns exhibited during testing.

6. CONCLUSIONS

FE models for predicting the response of ECC-retrofitted masonry beams subjected to four-point bending load have been developed in this study. It is shown that the models could replicate the behaviour observed from the experiments with sufficient accuracy. It is also presented that the modelling has been particularly useful for explaining the different crack patterns when the bond between the masonry and the ECC is altered. In the full bond case, it is confirmed that this occurs due to stress concentration occurring near the middle third span joints, leading to the formation of a radial crack pattern. In the partial bond case, the lack of the bond between ECC layer and masonry beam in middle third span is found to lead to the formation of uniform distribution of multiple-crack in the middle third span. The same crack pattern was observed experimentally.

REFERENCES

Abrams, D. & Lynch, J. (2001) Flexural behavior of retrofitted masonry piers. KEERC-MAE Joint. *Seminar on risk mitigation for regions of moderate seismicity*.

Asteris, P., Cotsovos, D., Chrysostomou, C., Mohebkhah, A. & Al-Chaar, G. (2013) Mathematical micromodeling of infilled frames: state of the art. *Engineering Structures,* 56(1):1905-1921.

Billington, S. L., Kyriakides, M. A., Blackard, B., Willam, K., Stavridis, A. & Shing, P. B. (2009). Evaluation of a sprayable, ductile cement-based composite for the seismic retrofit of unreinforced masonry infills. *AIC & SEI Conference on Improving the Seismic Performance of Existing Buildings and Other Structures, California.*

Carney, P. & Myers, J. J. (2003). Shear and flexural strengthening of masonry infill walls with FRP for extreme out-of-plane loading. *Proceedings of the Architectural Engineering Institute 2003 Annual Meetin,*. 246-250.

Davidson, J. S., Fisher, J. W., Hammons, M. I., Porter, J. R. & Dinan, R. J. (2005). Failure mechanisms of polymer-reinforced concrete masonry walls subjected to blast. *Journal of Structural Engineering* 24(1):935-941.

Dehghani, A., Fischer, G. & Alahi, F. N. (2015). Strengthening masonry infill panels using engineered cementitious composites. *Materials and Structures,* 48(1):185-204.

Drysdale, R. G. & Essawy, A. S. (1988). Out-of-plane bending of concrete block walls. *Journal of Structural Engineering,* 114(2):121-133.

Elgawady, M., Lestuzzi, P. & Badoux, M. A. (2004). Review of conventional seismic retrofitting techniques for URM. *13th international brick and block masonry conference,. Citeseer*, 1-10.

Hashemi, S. A. (2007). Seismic evaluation of reinforced concrete buildings including effects of masonry infill walls, *University of California, Berkeley*.

Kyriakides, M., Hendriks, M. & Billington, S. (2012). Simulation of unreinforced masonry beams retrofitted with engineered cementitious composites in flexure. *Journal of Materials in Civil Engineering,* 24(2):506-515.

LI, V. C. 2003. On engineered cementitious composites (ECC). *Journal of advanced concrete technology,* 1 (1):215-230.

Pourfalah, S., Suryanto, B. & Cotsovos, D.(2015). Enhancing the out-of-plane behaviour of masonry infill walls using engineered cementitious composites. *CONFAB, Glasgow*.

Taghdi, M. 1998. Seismic retrofit of low-rise masonry and concrete walls by steel strips, *University of Ottawa (Canada)*.

Tiedeman, H. A statistical evaluation of the importance of non-structural damage to buildings. *Proc., 7th World Conf. on Earthquake Engrg*, 1980. 617-624.

Infrastructure and Environment Scotland 3rd Postgraduate Conference
9th December 2015
Heriot-Watt University, Edinburgh

Analysis of Emotional Attributes that Predicts Gap Acceptance Riding Behaviour among Motorcyclists

O.O. Samuel,
Institute for Infrastructure and Environment,
Heriot Watt University, Edinburgh Campus
(oos30@hw.ac.uk)

G.H. Walker,
Institute for Infrastructure and Environment,
Heriot Watt University, Edinburgh Campus
(GH.Walker@hw.ac.uk)

ABSTRACT

Motorcycle riding is a vulnerable road activity, and one of the commonly engaged riding behaviour is gap acceptance, which relates to how riders enters or merge into traffic flow. Conflict and crashes are common during this process, and researchers have previously explained this through post-crash studies. A new approach to further research other human factor reasons is the study of the emotional attributes of the rider. These are internal changes in the rider that impact how and when they accept gaps in traffic. The study therefore is an empirical assessment of the psychological and affective attributes that predicts gap acceptance. The data for the study is from an on-road semi-naturalistic study into motorcycle riders' situational awareness. The regression model indicates the elements of anticipation, compliance, fear and being upset predicts gap acceptance at r^2=81%. The study was found to be statistically significant with an F-ratio of 0.034 and reliable at a p-value of <0.05. Recommendations on improving gap acceptance process include use of visual timers attached to lights at intersection to reduce the pressure of anticipation, developing training interventions that addresses the psycho-emotional issues of fear and distress.

1. INTRODUCTION

This study is focused on establishing the affective dimension to gap acceptance riding behaviour by motorcyclists. Motorcycle accident was reported to be the leading cause of death on roads globally in the WHO 2013 Road Safety Report. One way this occurs is when and how riders accept gaps in traffic, a type speed/distance judgment error (Pai, 2011). Motorcycle riders' engage in specific decision making process on when, how and where to enter, access, cross or merge with a traffic stream. This is what gap acceptance is all about. Where this in not properly executed, conflicts and crashes is the result. The virtual space available for joining the traffic flow is usually a mental conception. This mental state can be emotionally laden and therefore shape the execution of the gap acceptance (Megías et al., 2011). Riders have specific goals they seek to achieve in every segment of the road while riding, and all of these within the constraint of the interactive riding environment. How riders perceive their personal abilities within the system is a factor that dominates their riding pattern (Nja and Nesvag, 2007). Their understanding and dependence on their behavioural ability and emotional stability is the basis for the kind of riding task they will execute. Invariably traffic study and research on emotions of road user is still very limited (Mesken, 2003).

2. COGNITIVE-AFFECTIVE FRAMEWORK - A THEORETICAL BACKGROUND

Human emotions have been linked to motivations that influence behaviour (Tompkins, 1995). What people perceive in their environment influences their emotion, and their emotion also affects how they perceive and respond to environment stimuli (Mischel and Shoda, 1995; Mesken, 2003; Diefenbach et al., 2008). This position is borne out in the wider literature, for example, Oliver, (2002), writing on the affective appraisal of the scenic environment, reported the finding of Mehrabian and Russell (1974) where they found a direct significant relationship between levels of arousal and environmental knowledge. Russell and Lanius (1984) further reported another dimension to this affective response to places, where they stated that an environment can evoke pleasant or unpleasant feelings in the observer. Other studies that have shown similar affects-environment relationship include Russell and Snodgrass (1987)

who found that emotion is the key to understanding the human relationship to landscape. Zimring et al., (2004), reported that how hospital environments are perceived affects the emotion and reported a link between depressed emotion and the hospital environment.

In transport psychology, the road environment which includes its elements and events like seeing an accident scene, roadside advert or viewing warning alert systems have been reported to induce emotional responses in the driver (Megías et al., 2011, Serrano et al., 2013 and Tay et al., 2011). There is no conceptual reason why the constraints and conflicts within the road environment cannot also trigger different emotional states in motorcycle riders (Norman & Ortony, 2003; Van der Meer et al., 2007).

The cognitive-affective framework is rooted in the cognitive-affective theory (Bargh, 1994; Mischel and Shoda, 1995). The theory is premised on the knowledge that actors engage multiple levels of awareness and automaticity in dealing with cognitive and emotional encoding of information in their environment (Bargh, 1994; Kihlstrom, 1990). The theory incorporates and explains the process of transforming cognitions and affects into 'stable, meaningful patterns of social action in relationship to situations' (Mischel and Shoda, 1995). Cognition in this context also encompasses visual perception, while affect is more of feeling emanating from the human cognitive domain (Oliver, 1997). Mischel and Shoda (1995) explained that events and happening in the external environment activates 'a set of internal reactions' in people and these are not just cognitive but also affective in nature.

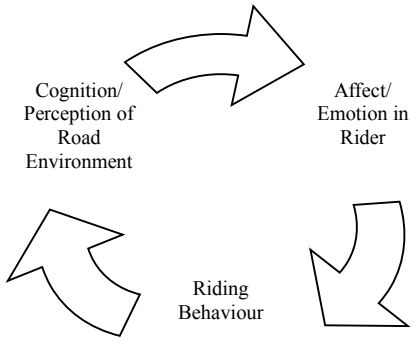

Figure 1: The Motorcycle cognitive–affective model

The cognitive–affective model has used been be various researchers recently to study user satisfaction (Coursaris & Van Osch (2015), responses to natural scenes (Valtchanov & Ellard (2015), and determinants of satisfaction (López-Mosquera & Sánchez (2014). The link between human emotions and their ability to influence behaviour has also been well established in literature (e.g. Tompkins, 1995; Cosmides & Tooby, 2000; Urda & Loch, 2013; Serrano et al., 2014; Megías et al., 2011). It has further been shown that emotions can be independent of each other in the way they become manifest either behaviourally, psychologically or physiologically (Posner et al. 2005). This theory however, have not been well researched to recognize how cognitively motivated emotions influences various behavioural tendencies among road users (Lajunen et al., 1998; Underwood et al., 1999; Gatersleben and Uzzell, 2007). Mischel and Shoda, (1995) have argued that cognition determines affective interpretation and reactions to events or situations in the environment. The theory which also argued that the feelings are the result of cognitive evaluation process was adapted as the risk-as-feelings hypothesis proposed by Loewenstein et al., (2001). The theoretical position for this study also support that emotions are a post-cognitive phenomenon in the context of the cognitive-affective theory (Damasio, 1994; Mischel and Shoda, (1995); Diefenbach et al., 2008).

2.1. Cognitive and Affective Dimension to Motorcycle riding

Motorcycle riding is a physically and cognitively challenging road activity (Reagan et al., 2015), and could be emotionally involving as it is for driving (Megías et al., 2011, Serrano et al., 2013 and Tay et al., 2011). While much has been written on perceptible riding behaviours like filtering, speeding, gap acceptance, and so on, very few studies have recognized that affective attributes influence how a selected riding behaviour is executed. The rider like every other road users', is always concerned with 'what is going on' around them (Salmon et al., 2013; Walker et al., 2011), and this shapes their riding attitudes in many ways. What they 'see' and the cognitive interpretation given to it is assumed to shape their riding behaviour. Research has also shown that riders' perception, reaction and comprehension are connected to riding errors (Watson et al., 2007). However the place of emotion in the actual playout of these errors is neglected.

Motorcycling interactive system which is focused on the systemic interaction between the rider, the motorcycle and the road environment (Steadmon, 2015, Mcnally, 2003) influences how the riders' emotion is shaped by the happenings, constraints and challenges that they are cognitively aware of while interacting with the various elements in the system (Walker et al., 2007; Walker et al., 2011). The actual execution of a riding activity cannot be fully separated from the rider's affective state. In a dynamic road system, riders try to concentrate their cognitive resources on constraints as they present themselves, and this at times can cause their emotion to vacillate from one state to the other (Harworth et al., 2000; Ekman, 1992). It seems obvious that riders could at different points

feel happy or sad, confident or nervous, moreover, they will enact certain types of riding behaviour to move themselves from one state to another. As posited by Hu et al., (2013), how people view situations, happenings and events in the environment is dependent on their emotional state and the view could be positive or negative, thus colouring the event as positive or negative. It has further been shown that emotions can be independent of each other in the way they become manifest either behaviourally, psychologically or physiologically (Posner et al., 2005). So the actual execution of a riding task cannot be fully separated from the rider's affective state.

While human emotions can be clearly independent in their manifestation, they are often interrelated in the way they transit from one state to another (Russell, 1980). Emotions change from one state to the other due to their transient nature, and they could be that of anger, disgust, fear, happiness, sadness and surprise (Ekman, 1992). Indeed, by knowing the affective state of the rider we should be able to predict their behaviour. More than that, it could be possible to design road environments to influence emotion in order to indirectly influence behaviour.

3. GAP ACCEPTANCE – A brief review

A gap is a time based occurrence which reflect the difference in time between the rear bumper of a front vehicle and front bumper of a following vehicle both moving in the same trajectory. Many researches have been done on gap acceptance as it relates to motor vehicles, with few on motorcycles (Hawkes, 1968; Mori et al., 1996; Sangole et al., 2011). It is a common pattern exhibited by all road users in traffic, whether they are motor vehicles, motorcycles, bicycles, pedestrian, etc. Road user engage in specific decision making process on when, how and where to enter, access, cross or merge with a traffic stream. They must decide when a gap is acceptable or crossable and also time when to take it with minimal disruption to the flow traffic. The virtual space available for joining the traffic flow is usually a mental conception.

Kearney et al., (2006), explained that "road crossing is a complex perceptual-motor task that requires accurate perception of the gap sizes in a dynamic stream of traffic and fine coordination to synchronize the onset of movement with the approaching gap".

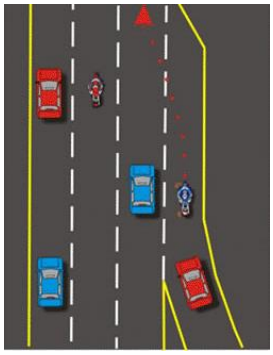

Figure 2: Motorcycle Gap Acceptance

Gap acceptance is an essential skill for safe motorcycle riding, and it requires careful human-bike coordination. Gap acceptance is strongly influence by certain contextual factors which from a social psychological perspective are behavioural in origin. It involves the interaction of the human mind with his immediate environment. Gap acceptance behaviour generally is influenced by factors such as age, gender, vehicle type, gap size and waiting time. (Sangole et al., 2011). Gap acceptance by motorcyclist though similar to that of motorist, differ when the factors of size, width and manoeuvrability interplays. A gap in traffic rejected by a driver may be accepted by a rider who enjoys burst of start-up acceleration and relative small size. Research shows that more careful drivers tend to reject small gaps than less cautious ones (Kearney et al., 2006).

Although motorcycle accident is one of the leading causes of death in road accident, it is still less researched when compared to other road users like drivers, cyclists and pedestrians. This study of the emotional dimension in gap acceptance by riders will contribute to the needed research support towards achieving sustainable safety among motorcyclists.

4. DESIGN AND METHODOLOGY

4.1 Research Design

This research utilized secondary data, obtained for the author's PhD study through collaborations between the Heriot Watt University, Edinburgh and two Australian Universities, Monash University in Melbourne, and the University of the Sunshine Coast in Queensland respectively. It is part of an investigative research into "Distributed situation awareness and road safety: Development of theory, measures, guidelines and interventions".

Secondary research data generally include survey results, interview recordings or various experimental outcomes collected by the data owners. The data output for this study covers tens of hours of information on motorcyclist on-road information, riders' concurrent verbal protocols,

video recording (frontal and rear view of rider), verbal protocol transcripts and demographic information and information on past riding behaviour. This paper is part of a detail research output covering riding behaviour which safe and risky riding, filtering, lane changing and gap acceptance. The focus of the paper is therefore to explore whether a significant relationship exists between gap acceptance riding behaviour and riders' emotional attributes, and if yes, describe how they occur.

4.1.1 Adopting the Mixed Method Research Approach

Every researcher adopts appropriate method to answer their research questions. This could be qualitative or quantitative methods depending on the nature of research. This study has however adopted the new paradigm in research methodology known as the mixed method approach. This was adopted to explore and describe how riders' affective patterns shape and influence their riding behaviour.

Mixed method approach refers to the design strategy which advocates that both qualitative and quantitative data can be collected and analysed in a single study has become popular among social scientists (Driscoll et al., 2007; Tashakkorri and Teddlie, 2003; Martens, 2005; Creswell, 2003). While some researchers have argued for and against it due to it's perceived 'philosophical difficulties' (Srnka and Koeszegi, 2007); it has gained prominence among pragmatist who sought to apply qualitative data in theory building and development by the combined strength of both qualitative and quantitative research design approaches to reveal knowledge that either may not accomplish alone (Rossman and Wilson, 1991; Davis, 2003; Creswell and Plano Clark, 2003; Driscoll et al., 2007).

The mixed method research design has been given various classifications based on the pattern and way in which the qualitative and quantitative data are collected and analysed. This study adopted the integrated design strategy (Srnka and Koeszegi, 2007), also known as generalisation model (Mayring, 2001), Combination design (Davis, 2003), transformative design (Creswell and Plano Clark, 2003; Driscoll et al., 2007 or Completeness approach (Bryman, 2012). It is a mixed method process whereby qualitative data is collected and transformed into categorical data to be used in quantitative analysis. And the aim is to derive both theory and arrive at a generalizable result (Srnka and Koeszegi, 2007). The following integrated blueprint suggested by Srnka and Koeszegi, (2007) was adapted for this research.

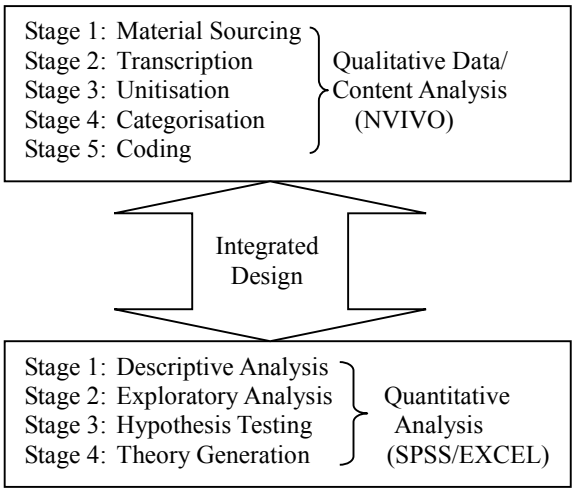

Figure 3: Integrated (Mixed method) Research Design

4.2. Research Method

The integrated design adopted in this study is premised on the ground that it allows the researcher to carry out both qualitative and quantitative analysis using the same single research process. That means the same data can be 'treated both hermeneutically and statistically' (Bryman, 2012). The researcher transformed the qualitative data collected into codes and quantitative units to be used in qualitative and quantitative analysis (Bryman, 2012). This is also referred to as 'quantitizing' (Driscoll, et al., 2007).

4.2.1 Participants

15 riders made of 14 males and 1 female rider made took part in the study. The age range was 21-64 years (Mean=45.5years, SD=12.87). They all had valid license, thus the research excludes all inexperienced riders. The riders were all expected to own their own motorcycles and have the required safety clothing.

4.2.2 Material

Riders rode on their own motorcycle which was fitted with an Oregon Scientific ATC9K portable camera, which depending on their model was fixed to either the handle bar or the front head lamp assembly. The visual scene, speed and distance travelled (via GPS) were recorded by the ATC9K camera. Also to record the riders' verbal protocol, a microphone was fitted inside each rider's helmet. The route is a 15 km urban route, located in the south-eastern suburbs of Melbourne, was used for the on-road study component. The route comprised a mix of arterial roads (50, 60 and 80 km/h speed limits), residential roads (50 km/h speed limit) and university campus private roads (40 km/h speed limit).

4.2.3 Procedure

Riders provided concurrent verbal protocols as they rode along the pre-defined route. They were requested to 'think aloud' what they were doing and seeing, without rationalising or explaining their behaviour, this way the impact of the verbalization will be less on their riding.

In order to control for traffic conditions, all trials took place at the same pre-defined times on weekdays (10 am or 2 pm Monday to Friday). These times were subject to pilot testing prior to the study in order to confirm the presence of similar traffic conditions. Upon completion of an informed consent form and demographic questionnaire, participants were briefed on the research and its aims.

Following this, they were given a verbal protocol training session in which they received a description of the method and instructions on how to provide concurrent verbal protocols. The use of verbal protocol or 'think aloud' protocol to elicit cognitive patterns is rich method of ethnographic study (Mulvihill et al., 2013). Brainbridge (1979) was among early researcher to recommend it as a tool to elicit knowledge of the thinking process. Klein et al. (1989) used it to study the role cognition plays in complex systems decision making process, Walker et al. (2011) used it in the study of behavioural and cognitive awareness of road users. (Mulvihill et al., (2013) studied riders filtering behaviour through their verbal protocol.

Upon completing the verbal protocol training, participants were shown the study route and were given time to memorise it. Whilst participants were practicing the VPA method and familiarising themselves with the route, a technician fitted the ATC9K camera to their motorcycle or cycling helmet. When comfortable with the VPA procedure and route, participants were taken to their vehicle and asked to prepare themselves for the test. They were then given a demonstration of the video and audio recording equipment, which was also set to record at this point. Following this, the experimenter instructed the participant to begin negotiating the study route. Each motorcyclist is followed by an experimenter behind in a car ready to intervene if the participants strayed off route (Salmon et al., 2014).

4.2.4 Content analysis

Riders' verbal protocols were transcribed verbatim using Microsoft Word for content analysis. Content analysis has been used in various studies of motorcycle riders' behaviours (Tunnicliff et al., 2007; Walker et al., 2012; Salmon et al., 2013). Emotional/psychological state of a person can be established through the analysis of their verbal behaviour (Gottschalk, 1995).

In other to elicit the behaviours common to riders as they engaged in different riding tasks, a coding unitisation and categorisation was develop and applied to the transcripts. The transcripts captures the verbal description of what riders think about as they ride and the emotional attributes linked to it. The coding categories were constantly restructured as the coding process progressed, merging related categories into one, and deleting ambiguous ones so as to achieve reliability. For the purpose of this analysis, textual coding was used instead of word or concept coding. A good reliability percentage agreement (92%) was obtained for the data when done by two independent coders.

Exploring the psychological and emotional attributes associated with riding behaviour involves the use of NVIVO to code the categories and obtain their distribution. It was also used to explore the coding distribution of riders' references to gap acceptance in relation to various affective elements. The software also allows the researchers to classify, sort and arrange information; examine qualitative relationships in the data. The distribution of the variables as referenced by each rider in their verbal protocol is presented in the table below.

Table 1. Riders' gap acceptance and emotional attributes as referenced in verbal protocol

Rider	Gap Acceptance	Anticipation	Fear /Anxiety	Cautious	Excited /Happy	Compliance	Confused	Upset/Distress
Rider1	2	6	3	5	7	1	0	0
Rider 2	15	63	21	53	29	57	22	2
Rider 3	16	31	6	21	6	7	13	0
Rider 4	17	7	2	9	0	22	1	0
Rider 5	4	9	11	9	5	2	9	0
Rider 6	7	31	14	6	11	22	11	1
Rider 7	4	16	3	12	2	4	2	15
Rider 8	5	2	3	30	3	14	3	1
Rider 9	1	7	11	13	7	3	29	9
Rider 10	5	8	2	1	16	8	5	3
Rider 11	4	6	3	38	9	7	8	0
Rider 12	9	19	8	5	15	4	15	2
Rider 13	1	4	1	27	8	0	8	3
Rider 14	8	38	12	18	9	11	24	4
Rider 15	6	1	3	6	3	1	0	0

4.2.5 Quantitative Analysis

To generate the quantitative data for this stage of analysis, all references made by individual riders against the corresponding coding categories are recorded and tabulated as shown below. In establishing the significance of this relationship, a regression analysis was conducted using gap

acceptance as the dependent variable and the elements of assumption/anticipation, fear/anxiety, cautious, excited/happy, compliance, confused, and upset/distressed as the independent variables.

5. RESULT AND DISCUSSION

This paper studies the emotional factor that predicts gap acceptance behaviour among motorcycle riders. Human emotions have been linked to motivations. The study found that there is indeed a relationship between gap acceptance and the emotional attributes of the riders (Figure 4).

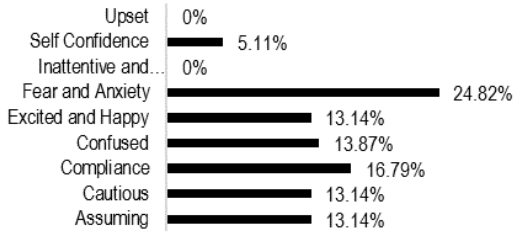

Figure 4. Gap acceptance and rider's emotion.

Gap acceptance was linked to the emotional attributes of fear and anxiety (24.82%). Gap acceptance is also done as an act of compliance to traffic rules (16.79%). Other psychological and emotional attributes like being cautious, anticipation and assumption, excitement and being confused is reported to relate to gap acceptance. The factor of inattentiveness and being upset do not contribute to gap acceptance behaviours.

5.1 Regression Analysis

Table 2. Multiple regression output

Regression Statistics	
Multiple R	0.902695468
R Square	0.814859108
Adjusted R Squar	0.629718215
Standard Error	3.18246578
Observations	15

ANOVA

	df	*SS*	*MS*	*F*	*gnificance F*
Regression	7	312.0367	44.57667	4.401292	0.034575
Residual	7	70.89662	10.12809		
Total	14	382.9333			

	Coefficients	*Standard Error*	*t Stat*	*P-value*	*Lower 95%*	*Upper 95%*
Intercept	8.89442866	1.758093	5.059133	0.001465	4.737198	13.05166
Assumption/ Anticipation	0.297955739	0.10494	2.839295	0.02507	0.049812	0.5461
Fear/Anxiety	-0.884999963	0.360489	-2.455	0.043785	-1.73742	-0.03258
Cautious	-0.138068265	0.079981	-1.72627	0.127944	-0.32719	0.051056
Excited/Happy	-0.376858399	0.180268	-2.09055	0.074909	-0.80312	0.049407
Compliance	0.324156129	0.123193	2.631278	0.03385	0.03285	0.615462
Confused	0.259108392	0.176166	1.470819	0.184808	-0.15746	0.675675
Upset	-0.498382548	0.221501	-2.25002	0.059196	-1.02215	0.025384

The regression analysis was carried out using Microsoft Excel at $p<0.05$ and results obtained. The analysis indicated that a good relationship exists between the riding behaviour of gap acceptance and riders' emotion with an R^2 of 0.81. This means 81% of the independent variables predicted or explained the dependent variable of gap acceptance. The analysis was also found to be statistically significant with an ANOVA value of $F=0.00345$ which is less than $p<0.05$.

The regression analysis is expected to produce an equation that will predict the dependent variable of gap acceptance using the independent variables of Anticipation, fear, caution, excitement, compliance, confused and upset. This model equation for this analysis is giving below.

$$Y = a + b1X1 + b2X2 + ... + bnXn$$

GAP_ACCP = 8.894 + 0.298(assume) – 0.885(fear) + 0.324(comply) – 0.498(upset)

In any multiple linear regression, the size of the coefficient for each independent variable shows the size of the effect that variable is having on the dependent variable, and the sign on the coefficient (positive or negative) gives the direction of the effect. In the multiple regression model above, the coefficients values explained that the probability of riders engaging in gap acceptance increases by 0.298 when the independent variable assumption/anticipation increases by one unit, holding all the other independent variables constant. It decreases by 0.885 when the independent variable fear/anxiety increases by one, and increases by 0.324 when the independent variable of compliance increases by one unit. Lastly, the model predict gap acceptance decreases by 0.498 when the independent variable of upset increases by one unit. Other variables of caution, excited and confused emotions were left out of the model due to their high p-value. Research has shown that more cautious drivers are less like likely to accept small gaps (Kearney et al., 2006), but is not significant in this model involving riders, as the increase to gap acceptance is very minimal (0.14) even though the p-value is slightly above 0.05, hence another reason why it was not included in the model.

6. DISCUSSION

The result above shows that there is a good and significant relationship between the riding behaviour of gap acceptance and selected riders emotions. The strongest emotional effect is fear and anxiety which decreases the willingness of riders to engage in gap acceptance. This implies that riders' who referenced fear and anxiety in their verbal protocol are 88% less likely to engage in gap acceptance. The reason could be they feel unsure whether to accept the gap or it is considered too small for them to accept (Horswill and Helman, 2003). A good intervention towards this is to ensure riders complete and successfully

qualify for their licence before they ride, this is because fear in making riding decision has been linked to inexperience, which can lead to failure in observing surrounding traffic conditions, or in this case 'over-observation' thereby delaying their choice of which gap to accept (Bellaby and Lawrenson, 2001) .

The emotion of disgust or being upset was next found to explain gap acceptance choice by riders', where decreases it by about 50%. This implies that when riders feel upset or disgusted about a traffic scenario at the point of accepting gap, they are half a chance less likely to accept it. Being upset could lead to anger (Underwood et al, 1999). Reasons for these could be road condition, external elements affecting their visibility, or the behaviour of other road user at the point of accepting gap. Research has shown that emotion affects motivation to act (Lang, et al., 1998).

The emotional element of compliance to road rules and etiquette increases the rider's chances of accepting gaps in traffic (32%). So an increase in the feeling to do what is 'right' as a road user will make them accept gaps when needed. A challenge to this is the pressure to comply and accept gap even when it is perceived as risky, but because others around them are accepting the gap, they tend to join in. Riders should be trained to reject gaps they perceive risky, even if others around them are accepting it, and this is only possible at uncontrolled road sections.

Lastly, the affective attribute of anticipation or assumption where riders makes presumed judgement about a road situation, predicts gap acceptance by increasing it by about 30% with every unit increase in anticipation. The implication of this is that riders pre-judged how a traffic situation will play out as they merge into or leave traffic. This could be at signalled intersection, where their anticipation of a change in lights shapes their gap acceptance decision.

Conclusion and Further Reading

Motorcycle riding is a series of trajectory activities that requires focus and involving emotional changes that determines behaviour. The study has shown that there is a significant relationship between gap acceptance and riders' emotion, and how these emotional attributes can either increase or decrease their willingness to accept gaps in traffic. The regression model predicts the gap acceptance based on variables like fear, anticipation, willingness to comply with rules and emotion of disgust or upset. The study is limited in the number of participants, thus studies involving more riders may yield more understanding on the role emotions play in motorcycle riding. Other studies being explored by the researcher is the role of emotion on other riding behaviours such as filtering, lane changing and risky riding.

Acknowledgement

The data for this work is part of an investigative research entitled "Distributed situation awareness and road safety: Development of theory, measures, guidelines and interventions", led by Prof. Paul Salmon. It was a large scale on-road semi-naturalistic study into road users' situational awareness funded by the Australian National Health and Medical Research Council post-Doctoral Training Fellowship, in conjunction with the Monash University Research Accelerator Program. It was obtained through collaboration with the data owner for the authors' PhD research. The author therefore appreciates the owner's permission to use the data for this paper.

REFERENCES

Bainbridge, L. (1979). Verbal reports as evidence of the process operator's knowledge. *International Journal of Man-Machine Studies*, *11*(4), 411-436.

Bellaby, P., and Lawrenson, D. (2001). Approaches to the risk of riding motorcycles: Reflections on the problem of reconciling statistical risk assessment and motorcyclists' own reasons for riding. *The Sociological Review*, *49*(3), pp. 368-388.

Bryman, A. (2012). *Social research methods*. Oxford university press. 4th edition. Oxford. Pp.637

Creswell, J. W. (2013). *Research design: Qualitative, quantitative, and mixed methods approaches*. 2nd Edition, Thousand Oaks, London, and New Delhi: Sage

Davies, B. (2003). The role of quantitative and qualitative research in industrial studies of tourism. *International Journal of Tourism Research*, *5*(2), 97-111.

Ekman, P. (1992). An argument for basic emotions. *Cognition & Emotion*, 6(3), pp.169-200.

Engelmann, J. and Pogosyan, M. (2013). Emotion perception across cultures: the role of cognitive mechanisms. *Frontiers in Psychology*, 4.

Gottschalk, L. A. (1995). *Content analysis of verbal behaviour: New findings and clinical applications*. Hillsdale, Lawrence Erlbaum Associates, New Jersey, pp.4-17.

Hawkes, A. (1968). Gap-Acceptance in Road Traffic. *Journal of Applied Probability*, 5(1), p.84.

Haworth, N., Kowadlo, N. and Smith, R. (2000). *Evaluation of rider training curriculum in Victoria*. Monash University Accident Research Centre.

Horswill, M. and Helman, S. (2003). A behavioural comparison between motorcyclists and a matched group of non-motorcycling car drivers: factors influencing accident risk. *Accident Analysis and Prevention*, 35(4), pp-589-597.

Kearney, J., Grechkin, T., Cremer, J., and Plumert, J. (2006). Traffic generation for studies of gap acceptance. In *Proc. DSC,* pp. 177-186.

Lang, P., Bradley, M., and Cuthbert, B. (1998). Emotion, motivation, and anxiety: brain mechanisms and psychophysiology. *Biological psychiatry*, 44(12), pp. 1248-1263.

Levenson, J., Brannon, Y., Fortney, T., and Baker, J. (2007). Public perceptions about sex offenders and community protection policies. *Analyses of Social Issues and Public Policy*, *7*(1), pp.137-161.

Mertens, D. M. (2014). *Research and evaluation in education and psychology: Integrating diversity with quantitative, qualitative, and mixed methods*. Thousand Oaks, London, New Delhi: Sage.

Mori, K., Honma, M. and Saito, T. (1996). Modeling Of Gap Acceptance Characteristics of Right-Turning Vehicles at Signalized Intersections. *Infrastructure Planning Review*, 13, pp.901-906.

Mulvihill, C., Salmon, P., Filtness, A., Lenné, M., Walker, G., Cornelissen, M., and Young, K. (2013). Lane filtering and situation awareness in motorcyclists: An on-road proof of concept study. In *Proceedings of the 2013 Australasian Road Safety Research, Policing & Education Conference*.

Nja, O. and S. M. Nesvag (2007). Traffic behavior among adolescents using mopeds and light motorcycles. *Journal of Safety Research.* 38, pp. 481-492

Pai, C. (2011). Motorcycle right-of-way accidents—a literature review. *Accident Analysis & Prevention*, 43(3), pp.971-982.

Posner, J., Russell, J., & Peterson, B. (2005). The circumplex model of affect: An integrative approach to affective neuroscience, cognitive development, and psychopathology. *Development and psychopathology*, 17(3), pp. 715-734.

Rossman, G. B., & Wilson, B. L. (1985). Numbers and words combining quantitative and qualitative methods in a single large-scale evaluation study. *Evaluation review*, *9*(5), 627-643.

Russell, J. (1980). A circumplex model of affect. *Journal of Personality and Social Psychology*, 39(6), pp.1161-1178.

Salmon, P. M., Lenné, M. G., Walker, G. H., & Filtness, A. (2013). Awesome foursome? The compatibility of driver, cyclist, motorcyclist, and pedestrian situation awareness at intersections. In *Engineering Psychology and Cognitive Ergonomics. Applications and Services*. Springer Berlin Heidelberg, pp. 53-62.

Sangole, J., Patil, G. and Patare, P. (2011). Modelling Gap Acceptance Behavior of Two-Wheelers at Uncontrolled Intersection Using Neuro-Fuzzy. *Procedia - Social and Behavioral Sciences*, 20, pp.927-941.

Srnka, K. J., & Koeszegi, S. T. (2007). From words to numbers: how to transform qualitative data into meaningful quantitative results. *Schmalenbach Business Review*, 59(1), pp.29-57.

Stein, N., Leventhal, B., and Trabasso, T. (Eds.). (1990). *Psychological and biological approaches to emotion*. Lawrence Earburn Associate, New Jersey, Psychology Press.

Tashakkori, A., & Teddlie, C. (1998). *Mixed methodology: Combining qualitative and quantitative approaches* (Vol. 46). Sage.

Tompkins, R. (1995). Parenting plans. *Family Court Review*, 33(3), pp. 286-297.

Tunnicliff, D., Watson, B., White, K., Hyde, M., Schonfeld, C. and Wishart, D. (2012). Understanding the factors influencing safe and unsafe motorcycle rider intentions. *Accident Analysis & Prevention*, 49, pp.133-141.

Underwood, G., Chapman, P., Wright, S., and Crundall, D. (1999). Anger while driving. *Transportation Research Part F: Traffic Psychology and Behaviour*, 2(1), pp. 55-68.

Walker, G., Stanton, N., and Salmon, P. (2011). Cognitive compatibility of motorcyclists and car drivers. *Accident Analysis & Prevention*, *43*(3), pp. 878-888.

World Health Organization. (2013). *WHO global status report on road safety 2013: supporting a decade of action*. Geneva, Switzerland: World Health Organisation (WHO). pp. vii, 1–8, 53ff, 244–251, pp.296–303.

Infrastructure and Environment Scotland 3rdPostgraduateConference
9th December 2015
Heriot-Watt University, Edinburgh

A Partition of Unity Boundary Element Method for Transient Wave Propagation

David Stark[1], Heiko Gimperlein[2]
Maxwell Institute for Mathematical Sciences and Department of Mathematics
Heriot-Watt University, Edinburgh[1,2]
Institute for Mathematics, University of Paderborn, Warburger, Str. 100, 33098 Paderborn, Germany[2]
(e-mail: ds221@hw.ac.uk)[1]

ABSTRACT

We propose a time-domain partition of unity boundary element method for wave propagation problems at high frequency. Travelling waves are included as enrichment functions into a time-domain boundary element solver. A major problem is the numerically-accurate set-up of the Galerkin matrix. We present preliminary numerical results of this method, discuss algorithmic aspects involved, and comment on relevant engineering applications.

1. INTRODUCTION

Boundary element methods (BEM) provide an efficient and extensively analyzed numerical scheme for time-independent or time-harmonic scattering and emission problems. In recent years, they have been explored for the simulation of transient phenomena, such as modeling of environmental noise [1] or electromagnetic scattering [2,3]. Further classical applications arise in computational and fluid mechanics. In terms of numerical methods, time-dependant boundary element methods were introduced by Bamberger and Ha-Duong [9]. The numerical implementation of the resulting marching-on-in-time schemes have since been extensively investigated especially in the French numerical community [2], with fast collocation methods developed for applications [3]. Adaptive mesh refinement methods have been explored recently [4]. See also [3,4] for some mathematical background.

Unlike finite element discretisations, BEM has the advantage of reducing the computation from the three dimensional domain to its two-dimensional boundary. Solving an integral equation on this boundary, the entire sound pressure field can be evaluated at any point in space even for the unbounded domains of scattering problems. With the FEM, one necessarily needs to mesh and possibly truncate the whole computational domain.

On the other hand, for time-harmonic wave propagation partition-of-unity finite and boundary element methods (PUFEM / PUBEM) have emerged as a practically efficient solution to deal with the rapid oscillations and numerical pollution at high wave numbers [5,6,7]. Enriched with local solutions to the Helmholtz equation, such discretisations considerably reduce the number of degrees of freedom to achieve engineering accuracy, as compared to standard FEM and BEM: The nature of the exact solution is encoded in the ansatz functions of the numerical method. In special situations, a careful choice of the enrichment functions leads to numerical methods whose performance is independent of the frequency.

In this work we introduce a time-domain partition-of-unity boundary element method. It extends the above works for time-harmonic wave propagation to truly transient problems in space and time. Practically, it includes plane-wave enrichment functions into the h-version time-domain boundary element procedure. It is the first work on enriched methods for time-dependent integral equation methods.

A main challenge is the accurate assembly of the Galerkin matrix. Using the quadrature method described in [8], we propose a carefully-chosen plane-wave enrichment and provide a preliminary numerical analysis of this scheme. The theoretical analysis of [2,9] proves that our method is stable and converges.

As for the structure of this article: In Section 2 we recall the initial-boundary problem for the acoustic wave equation which we consider and reformulate it as an integral formulation on the boundary of the scatterer. The partition-of-unity TDBEM is introduced in Section 3 and shown to lead to an explicit time-stepping scheme. Section 4 provides some details on the computation of the Galerkin matrix. After discussing different notions of convergence and error in Section 5, Section 6 presents preliminary numerical results for both the

partition-of-unity method and the h-method obtained by turning off the enrichment. The results are put into perspective in Section 7.

2. THE WAVE EQUATION AND ITS INTEGRAL FORMULATION

We consider transient sound radiation problems in the exterior of a scatterer Ω^-, where Ω^- is a bounded polygon with connected complement $\Omega := \Omega^+ = \mathbb{R}^3 \setminus \Omega^-$. Let **n** be the outer normal vector on the boundary $\Gamma := \partial\Omega$.

Figure 1. Ω^- and outer normal **n**.

The acoustic pressure field $u(t,\mathbf{x})$ induced by an incident field u^{inc} from the exterior domain or from sources on Γ, fulfills the linear wave equation:

$$\frac{1}{c^2}\frac{\partial^2 u(t,\mathbf{x})}{\partial t^2} - \Delta u(t,\mathbf{x}) = 0 \qquad (1)$$

where $\mathbf{x} \in \Omega$, $t \in \mathbb{R}$ and c is the wave velocity. We always set c=1 to simplify the notation.

We impose the initial conditions:

$$u(0,\mathbf{x}) = \frac{\partial}{\partial t}u(0,\mathbf{x}) = 0 \qquad \text{for } \mathbf{x} \in \Omega \qquad (2)$$

and boundary conditions:

$$u(t,\mathbf{x}) = f(t,\mathbf{x}) \qquad \text{in } \mathbb{R} \times \Gamma. \qquad (3)$$

We can represent the solution to the Dirichlet problem using a single-layer ansatz for $\mathbf{x} \notin \Gamma$:

$$u(t,\mathbf{x}) = \frac{2}{4\pi}\int_\Gamma \frac{\phi(t-|\mathbf{x}-\mathbf{y}|,\mathbf{y})}{|\mathbf{x}-\mathbf{y}|}\, ds_y \qquad (4)$$

The single-layer operator is continuous when passing with **x** to the boundary, hence (3) yields the boundary integral equation:

$$V\phi(t,\mathbf{x}) = f(t,\mathbf{x}) \qquad (5)$$

for the single layer operator:

$$V\phi(t,\mathbf{x}) = \frac{2}{4\pi}\int_\Gamma \frac{\phi(t-|\mathbf{x}-\mathbf{y}|,\mathbf{y})}{|\mathbf{x}-\mathbf{y}|}\, ds_y. \qquad (6)$$

Multiplying (6) by the time derivative of a test function Ψ and integrating over Γ, a coercive weak formulation of the integral equation is:

$$\int_0^\infty \exp(-2\sigma t)\int_\Gamma \left(V\phi(t,\mathbf{x})\right)\dot{\psi}(t,\mathbf{x})\, ds_x dt = \int_0^\infty \exp(-2\sigma t)\int_\Gamma f(t,\mathbf{x})\dot{\psi}(t,\mathbf{x})\, ds_x dt \qquad (7)$$

In later computations we set $\sigma = 0$ [2,8].

3.PARTITION OF UNITY TDBEM

We use a time-dependent boundary element method to solve (7). A numerical approximation is sought of the form:

$$\phi = \sum c_j \phi_j \qquad (8)$$

where φ_j are suitable basis functions in space and time. We denote the space of all such functions S.

We use a plane wave basis enrichment to better approximate the oscillatory nature of solutions at large frequency. In the frequency domain, such partition-of-unity methods are discussed by Trevelyan et al. in [5,6] for boundary elements, and in [7] for finite elements.

A first work by Ham and Bathe in the time-domain [10] discusses the enrichment for wave propagation problems in two dimensions. They choose φ_j as:

$$\phi_i = \tilde{\Lambda}_i(t)\Lambda_i(\mathbf{x})\cos(\omega_i t - \mathbf{k}_i\mathbf{x}_i + \sigma_i) \qquad (9)$$

where $\Lambda_j(t)$ is a piecewise polynomial hat function in space, and $\Lambda_i(\mathbf{x})$ a corresponding hat function in space. **K** denotes the spatial and ω the temporal frequency $\omega = |\mathbf{k}|$ of the plane wave. $\sigma_i \in \{0, \pi/2\}$ allows to include both sine and cosine enrichments.

We use the basis functions (9) in a partition-of-unity TDBEM in 3 dimensions, with both piecewise constant shape functions $\Lambda_j(t)$ and $\Lambda_i(\mathbf{x})$. We also use piecewise linear shape functions in time. The resulting discretised numerical scheme for the Dirichlet problem (7) is:

Find $\varphi_{h,\Delta t}$ such that for all $\Psi_{h,\Delta t} \in$ S:

$$\langle V\phi_{h,\Delta t}, \dot{\psi}_{h,\Delta_t}\rangle = \langle f, \dot{\psi}_{h,\Delta_t}\rangle \qquad (10)$$

Because of the piecewise constant shape functions, the space-time equation (10) takes a lower triangular form, where each block corresponds to one time step.

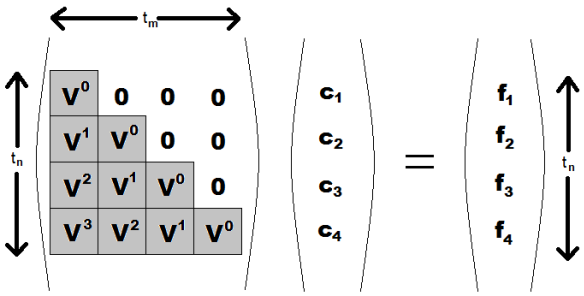

Figure 2. The "Marching on in Time" (MOT) matrix system.

The matrix $\mathbf{V}^j$ and right hand side $\mathbf{f}_j$ are calculated at time t_j. The solution vector $\mathbf{c}_j$ gives the coefficients in (8) at time t_j. More explicitly:

$\mathbf{V}^0\mathbf{c}_1 = \mathbf{f}_1$
$\mathbf{V}^0\mathbf{c}_2 = \mathbf{f}_2 - \mathbf{V}^1\mathbf{c}_1$
$\mathbf{V}^0\mathbf{c}_3 = \mathbf{f}_3 - \mathbf{V}^2\mathbf{c}_1 - \mathbf{V}^1\mathbf{c}_2 \ldots$

Solving the system in this way, is a "marching on in time" (MOT) algorithm for time-stepping.

In each time step, we solve a block-linear algebraic system as below:

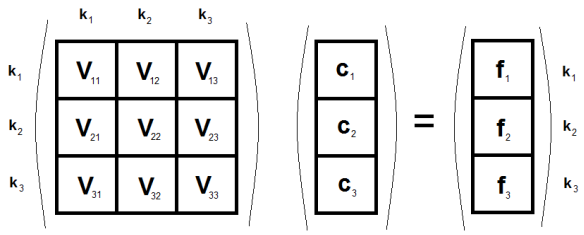

Figure 3. The PUBEM system for each time step.

Each $\mathbf{V}_{mn}$ is a matrix of size (#nodes) x (#nodes), which relates to two **k** vectors - one for the ansatz function φ, and one for the test function Ψ. These **k** are determined by the row and column number of each matrix. For example, matrix $\mathbf{V}_{21}$ relates to $\mathbf{k}_2$ (taken from the row, and used in the test function) and $\mathbf{k}_1$ (taken from the column, and used in the ansatz function).

The numerical scheme (10) minimises the energy:

$$E := \frac{1}{2}\phi \cdot (\mathbf{V}\phi) - F \cdot \phi \qquad (11)$$

As a Galerkin method, the stability and convergence of the numerical method (10) are guaranteed [9,2].

4. ALGORITHMIC ASPECTS

Up to a constant pre-factor, as in [8] each element of the Galerkin matrix $\mathbf{V}_{m,n}$ is given by:

$$V_{m,n} := \int_0^\infty \int_\Gamma \underbrace{\int_\Gamma \frac{\phi_m(t-|\mathbf{x}-\mathbf{y}|,\mathbf{y})}{|\mathbf{x}-\mathbf{y}|}\, dS_y}_{V\phi} \dot{\psi}_n(t,\mathbf{x})\, dS_x \quad dt \qquad (12)$$

We first evaluate the time integral analytically, resulting in an analytic expression for $\mathbf{V}_{m,n}$ which has the form:

$$\begin{aligned} V_{m,n} = \int_\Gamma \int_\Gamma \frac{1}{|\mathbf{x}-\mathbf{y}|} \Lambda_m(\mathbf{y})\Lambda_n(\mathbf{x}) \Big\{ & \\ F_1(\mathbf{y},\mathbf{x},\omega_m,\omega_n) \cdot & \cos(\mathbf{k}_m\cdot\mathbf{y})\cos(\mathbf{k}_n\cdot\mathbf{x}) \\ + F_2(\mathbf{y},\mathbf{x},\omega_m,\omega_n) \cdot & \cos(\mathbf{k}_m\cdot\mathbf{y})\sin(\mathbf{k}_n\cdot\mathbf{x}) \\ - F_3(\mathbf{y},\mathbf{x},\omega_m,\omega_n) \cdot & \cos(\mathbf{k}_m\cdot\mathbf{y})\omega_n\cos(\mathbf{k}_n\cdot\mathbf{x}) \\ + F_4(\mathbf{y},\mathbf{x},\omega_m,\omega_n) \cdot & \cos(\mathbf{k}_m\cdot\mathbf{y})\omega_n\sin(\mathbf{k}_n\cdot\mathbf{x}) \\ + F_5(\mathbf{y},\mathbf{x},\omega_m,\omega_n) \cdot & \sin(\mathbf{k}_m\cdot\mathbf{y})\cos(\mathbf{k}_n\cdot\mathbf{x}) \\ + F_6(\mathbf{y},\mathbf{x},\omega_m,\omega_n) \cdot & \sin(\mathbf{k}_m\cdot\mathbf{y})\sin(\mathbf{k}_n\cdot\mathbf{x}) \\ - F_7(\mathbf{y},\mathbf{x},\omega_m,\omega_n) \cdot & \sin(\mathbf{k}_m\cdot\mathbf{y})\omega_n\cos(\mathbf{k}_n\cdot\mathbf{x}) \\ + F_8(\mathbf{y},\mathbf{x},\omega_m,\omega_n) \cdot & \sin(\mathbf{k}_m\cdot\mathbf{y})\omega_n\sin(\mathbf{k}_n\cdot\mathbf{x}) \Big\}\, dS_y\, dS_x \end{aligned} \qquad (13)$$

The functions F_j vanish outside a light cone – a spherical shell whose inner and outer radii relate to the time steps t_m *and* t_n, see Figure 4:

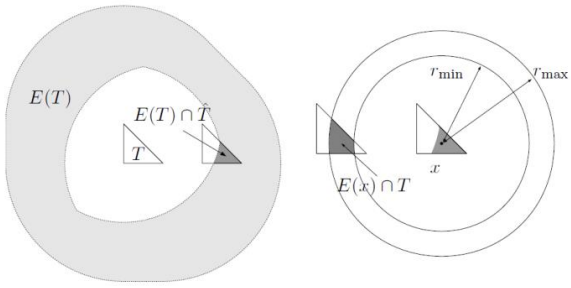

Figure 4. Light cone and domain of influence [8].

Here, triangle T is the ansatz element, and triangle T is the test element. The rightmost diagram shows the light cone around a point **x** in T represents the inner integral in (13). The leftmost diagram shows the union of all light cones around points in T, as needed for the outer integral in (13).

Because of the denominator |**x**-**y**| in (12) and the singularities of F_j at the boundary of the light cone, a main challenge in the TDBEM is the accurate computation of the matrix elements $\mathbf{V}_{m,n}$.

For the inner integration (shown on the right in Figure 4), we consider the grey area on triangle T.

We first project the point of observation **x** onto the ansatz triangle plane, as shown in Figure 5.

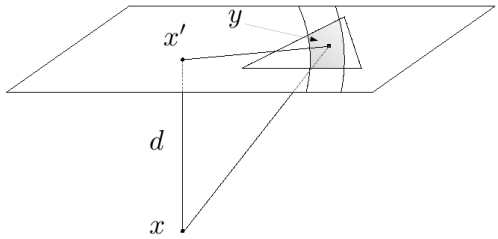

Figure 5. The projection of **x** onto the triangle plane, which we call **x**' [8].

In the two-dimensional plane, we change to polar coordinates around **x**' and partition the region into sectors D_l as in Figure 6.

$$(P\phi)(\mathbf{x}) := \sum_{l=1}^{n_d} \int_{D_l} \frac{\phi(\mathbf{y})}{|d^2 + r^2|} \, ds_y. \tag{14}$$

where d = |**x**-**x'**|. The integrals over D_l have simple descriptions in polar coordinates and may be accurately evaluated with a geometrically graded hp-Gauss quadrature [8].

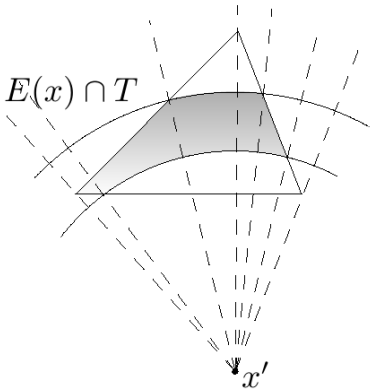

Figure 6. A partitioned element/light cone intersection, in polar coordinates [8].

5. MEASURING THE ERROR

We quantify the numerical errors in three ways:

1. By comparing $\varphi_{h,\Delta t}$ to the density obtained from standard h-TDBEM with a fine mesh.
2. By comparing $u_{h,\Delta t}$ to the sound pressure from standard h-TDBEM with a fine mesh.
3. By considering the energy (see below).

The first two methods require varying degrees of post-processing. We compute $\varphi_{h,\Delta t}$ from formulas (8) and (9). To compute $u_{h,\Delta t}$ requires more work:

The condition:

$$t_i \quad \leq \quad \left[t - |\mathbf{x} - \mathbf{y}|\right] \quad \leq \quad t_{i+1} \tag{15}$$

generally holds for some time step *i*. For a linear basis in time, we use the linear interpolation formula to compute φ at retarded times:

$$\begin{aligned}\phi_j(t - |\mathbf{x} - \mathbf{y}|, \mathbf{y}) = \sum_{h=1}^{N_h} \Bigg\{ & C_{i,j}\left[1 - \left(\frac{\left[t - |\mathbf{x} - \mathbf{y}|\right] - t_i}{t_{i+1} - t_i}\right)\right] \\ & \cos\left(\omega_h\left[t - t_i - |\mathbf{x} - \mathbf{y}|\right] - \mathbf{k}_h \cdot \mathbf{y} + \sigma_h\right)\Lambda_j(\mathbf{y}) \\ & + C_{i+1,j}\left(\frac{\left[t - |\mathbf{x} - \mathbf{y}|\right] - t_i}{t_{i+1} - t_i}\right) \\ & \cos\left(\omega_h\left[t - t_{i+1} - |\mathbf{x} - \mathbf{y}|\right] - \mathbf{k}_h \cdot \mathbf{y} + \sigma_h\right)\Lambda_j(\mathbf{y}) \Bigg\}\end{aligned} \tag{16}$$

where *i* indexes the time step, *j* indexes the element, and *h* indexes the enrichment functions. The position vector **y** is the spatial Gauss point where the function is evaluated on the element, and **x** is a point of evaluation outside Γ, where *u* is to be evaluated from.

We can now use this to calculate *u*:

$$\begin{aligned} u(t, \mathbf{x}) &= \frac{2}{4\pi} \int_\Gamma \frac{\phi(t - |\mathbf{x} - \mathbf{y}|, \mathbf{y})}{|\mathbf{x} - \mathbf{y}|} \, ds_y \\ &= \frac{2}{4\pi} \sum_{i=1}^{N} \int_{E(\mathbf{x})_i} \frac{\phi(t - |\mathbf{x} - \mathbf{y}|, \mathbf{y})}{|\mathbf{x} - \mathbf{y}|} \, ds_y \\ &= \frac{2}{4\pi} \sum_{i=1}^{N} J(E(\mathbf{x})_i) \sum_{j=1}^{15} \frac{\phi(t - |\mathbf{x} - \mathbf{p}_j|, \mathbf{p}_j)}{|\mathbf{x} - \mathbf{p}_j|} \end{aligned} \tag{17}$$

where we decompose Γ into its natural covering of elements and use a projection to the reference triangle to calculate the Gauss points $\mathbf{p}_j$ on the reference triangle. $J(E(\mathbf{x})_i)$ is the Jacobian for element $E(\mathbf{x})_i$.

A Galerkin method seeks a minimiser for the corresponding energy functional, here given by

$$E := \frac{1}{2}\phi \cdot (\mathbf{V}\phi) - F \cdot \phi \tag{18}$$

V is the full space-time Galerkin matrix, and F the full space-time right hand side vector. We compute each part component-wise,

$$\mathbf{V}\phi = \begin{bmatrix} \mathbf{V}^0\phi^0 \\ \mathbf{V}^1\phi^0 + \mathbf{V}^0\phi^1 \\ \mathbf{V}^2\phi^0 + \mathbf{V}^1\phi^1 + \mathbf{V}^0\phi^2 \\ etc... \end{bmatrix} \tag{19}$$

and

$$F\phi = F^0 \cdot \phi^0 + F^1 \cdot \phi^1 + F^2 \cdot \phi^2 + ... \tag{20}$$

where numerals index the time steps.

6. PRELIMINARY NUMERICAL RESULTS

To analyse the convergence of our algorithm, we first consider a wave problem with known exact solution φ when Γ is the sphere of radius 1. If $f(t,\mathbf{x}) = \sin(t)^5$, $\varphi(t) = 5\sin(t)^4\cos(t)$ (for $t < 2$) [11].

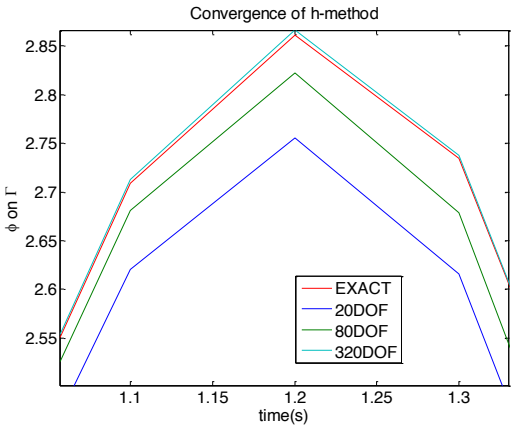

Figure 7. Convergence everywhere, as we increase the degrees of freedom, for t<2s.

Figure 7 shows the numerical results for $\varphi_{h,\Delta t}$ with 20, 80 resp. 320 triangles and constant ratio of h and the time step for our implementation of the partition-of-unity TDBEM, with **k**=0.

A plot of degrees of freedom vs. the absolute error in the centroid of a triangle is shown in Figure 8. We thereby recover the convergence of h-TDBEM, with almost linear order of convergence.

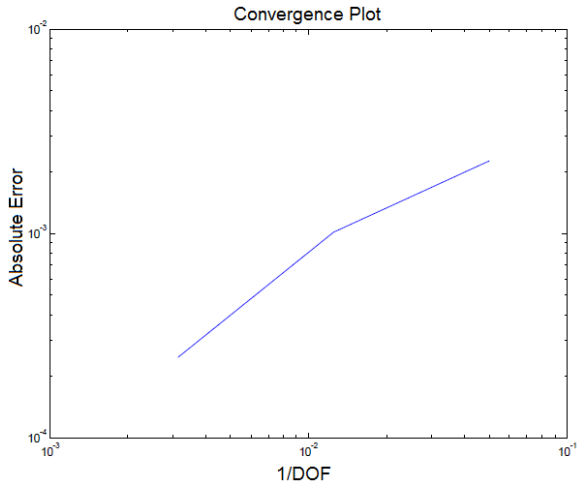

Figure 8. The absolute error at t = 1.2s.

The following plot shows some preliminary results for the piecewise linear shape functions in time with enrichment |**k**|>0.

For Γ, a regular convex icosahedron (20 triangular faces) of diameter 2 and centered in (0, 0, 0), we use the right hand side: $f(t,x)=\exp(-4/t^2)\cos(\omega_f t - \mathbf{k}_f\mathbf{x})$, a plane wave with $\mathbf{k}_f$ =(1, 0.5, 0.1) which is smoothly turned on for small times. An h-TDBEM approximation with 320 triangles serves as replacement for an 'exact' solution. We compare with a partition-of-unity TDBEM based on 20 triangles and n enrichment functions in each triangle. The approximations $\varphi_{h,\Delta t}$ and $u_{h,\Delta t}$ show similar convergence. Figure 9 shows the numerical PU-TDBEM solution for the sound pressure $u_{h,\Delta t}$ in the point (1.2, 0.5, 0.4) outside Γ.

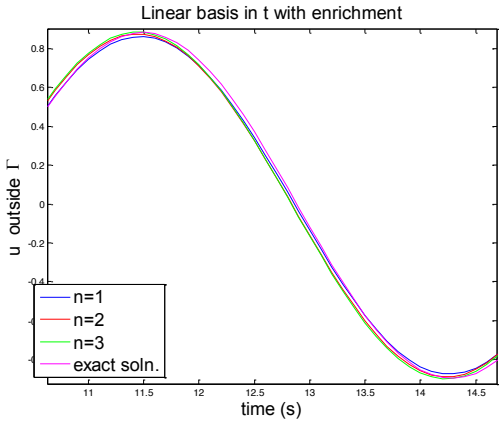

Figure 9. Plot of *u vs t* with our linear basis, using a varying number of enrichment functions.

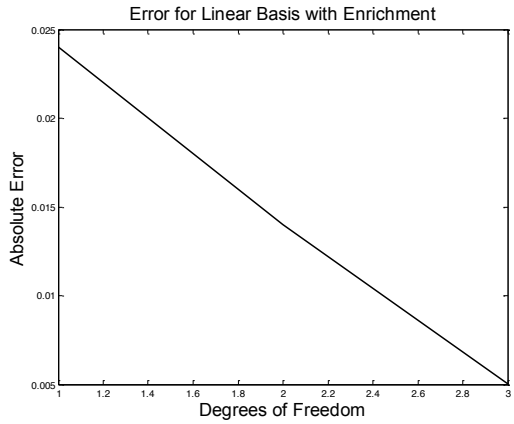

Figure 10. Plot of absolute error vs degrees of freedom for the linear basis. Taken at t = 11.6s.

The corresponding absolute errors are exhibited in Figure 10.

7. CONCLUSIONS AND OUTLOOK

This work presents a first step towards enriched time-domain methods, here for boundary elements. Even for finite elements such methods are just beginning to be explored in time-domain. They present a promising approach to take large time steps even for rapidly oscillating solutions, with applications from imaging to the numerics of concert halls.

Our plots indicate that we have implemented a partition-of-unity method which converges for low numbers of suitably chosen enrichment functions.

We hope to extend our numerical experiments to more realistic geometries and data, where 20 or more enrichment functions would be required. For large numbers of enrichments the Galerkin matrix is known to be badly conditioned for time-independent problems.

One motivation comes from the sound radiation of truck tyres [1]. Here, the boundary of the tyre is meshed and treated as an emitter. Figure 9 shows snapshots from the corresponding time evolution.

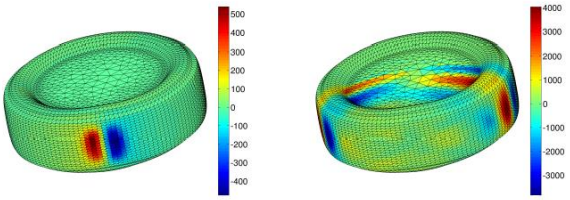

Figure 9. Time evolution of the density for a vibrating tyre [1].

A longer-term outlook might compare a working time-domain PUBEM method with hp-adaptivity as competing approaches to deal with numerical pollution at high frequency.

REFERENCES

[1] L. Banz, H. Gimperlein, Z. Nezhi, E. P. Stephan, Time domain BEM for sound radiation of tires, preprint.

[2] T. Ha Duong. On retarded potential boundary integral equations and their discretisations. Topics in computational wave propagation, Lect. Notes Comput. Sci. Eng., Vol. 31 (2003). Springer: Berlin, 301-336.

[3] A. E. Yilmaz, J.-M. Jin, E. Michielssen, Time domain adaptive integral method for surface integral equations, IEEE Trans. Antennas Propagation **52** (2004); 2692-2708.

[4] H. Gimperlein, M. Maischak, E. P. Stephan, Adaptive time-domain boundary element methods and engineering applications, invited survey, Journal of Integral Equations and Applications, to appear (2016).

[5] E. Perrey-Debain, J. Trevelyan, P. Bettess, Wave Boundary Elements: A Theoretical Overview Presenting Applications in Scattering of Short Waves, Engineering Analysis with Boundary Elements 28 (2004) 131-141.

[6] E. Perrey-Debain, J. Trevelyan, P. Bettess, On Wave Boundary Elements for Radiation and Scattering, IEEE Transactions on Antennas and Propagation, vol. 53, no. 2, (Feb 2005).

[7] O. Laghrouche, P. Bettess, E. Perrey-Debain, J. Trevelyan, Wave Interpolation Finite Elements for Helmholtz Problems with Jumps in the Wave Speed, Comput. Methods Appl. Mech. Engrg. 194 (2005) 367-381.

[8] E. Ostermann, Numerical Methods for Space-Time Variational Formulations of Retarded Potential Boundary Integral Equations, Ph.D. thesis, Leibniz Universität Hannover, 2009.

[9] A. Bamberger, T. Ha Duong, Formulation variationnelle espace-temps pour le calcul par potentiel retard de la diffraction d'une onde acoustique. Math. Methods in the Appl. Sciences 8 (1986); 405-435 and 598-608.

[10] S. Ham, K.J. Bathe, A Finite Element Method Enriched For Wave Propagation Problems, Computers And Structures 94-95 (2012), 1-12.

[11] S. Sauter, A. Veit, Retarded boundary integral equations on the sphere: exact and numerical solution, IMA J. Numer. Anal. 34 (2014); 675-699.

Infrastructure and Environment Scotland 3rd Postgraduate Conference
9th December 2015
Heriot-Watt University, Edinburgh

An Immittance spectroscopy study of cementitious materials during early hydration

H.M. TAHA,
Institute for Infrastructure and Environment,
HERIOT-WATT UNIVERSITY
(e-mail: hmt4 @hw.ac.uk)

ABSTRACT

The electrical response during the early hydration process (setting and hardening) for different water to cement ratios cement pastes has been characterized .Different electrical conductance stages have shown to be existed through the first 24 hours of the samples age. The electrical capacitance response has shown to be affected by the used measuring electrical frequency, as different polarization signals have been clearly identified at a.c. frequencies which are larger than 1kHz .The electrical response which has been obtained through the early hydration period has been related and explained according to the physiochemical processes which take place through the monitoring period.

1. INTRODUCTION

Portland cement hydration is a complex process which involves several physical and chemical processes taking place simultaneously during the hydration reaction.
The minerals which compose the Portland cement, all contribute to the hydration reaction, however the influence of the C_3S phase on the early hydration stage kinetics is more prominent which has led many researchers to study this particular phase in order to reduce the complexity exerted by the chemical contribution of other cement minerals (Alizadeh *et al.*, 2009; Bellmann *et al.*, 2010; Bellmann *et al.*, 2012).However, the influence from the other minerals phases (C_2S, C_3A, C_4AF) has shown to have a significant influence on the reaction kinetics of cement which should not be neglected when studying hydration (Minard *et al.*, 2007).

By utilising the exothermal nature of the cement hydration reaction, isothermal conduction calorimeter (ICC) tests are widely used to monitor the hydration kinetics of the early stages for cement pastes. In addition to the ICC test, auxiliary tests such as scanning electron microscopy (SEM) ,back scatter electron microscopy (BSE) have been used to explain and to support the features which are observed on the ICC results. However, due to the destructive nature of these mentioned tests as well as the sample scale which is normally used, limitations in the accuracy as well as in the continuous monitoring ability normally are encountered.

Electrical impedance spectroscopy measurements and electrical measurements in general, have proved to be simple, easy to use and none destructive which allows them to be used routinely as quality control tests.
The similarity which exists between the movement of ions under the effect of electrical potential and the movement under the effect of chemical potential allows electrical measurements to be used as a durability indicator regarding the ability of aggressive ions to diffuse through the cementitious materials (Christensen *et al.*, 1994; McCarter, Starrs and Chrisp, 2000).

Despite the advantages of electrical measurement techniques, especially the non-destructive nature of these tests, there is a paucity in early hydration studies which utilize a wide frequency range to characterize the electrical response through the setting and early hardening process. Therefore, this study utilizes an electrical impedance monitoring technique in order to characterise the Portland cement paste early hydration reaction.

2. Materials and Methods:

In this study, three Portland cement pastes with different water to cement ratios have been used. The water to cement ratios are (0.3, 0.35 and 0.45).The cement is (52.5N) CEM I from Lafarge which complies with the EN197-1: 2011.
A Perspex mould with the dimension of (50mm×50mm×50mm) has been used for casting the samples. A pair of stainless steel electrodes of 2.4mm diameter and 100cm length have been embedded inside the samples to a depth of 25mm from the samples surface.

A Solartron 1260 electrical impedance analyzer were used to perform a continuous electrical impedance measurements in the frequency range between 1Hz - 10MHz through the first 24- hours since mixing the samples with water. The impedance measurements were repeated three times for each mix to assess the repeatability of the data. Due to the low electrical impedance of the samples during this early age, the procedure adopted by (Edwards *et al.*, 1997) has used to correct the data from leads inductive effect.

3. Results:

3.1 Portland cement conductance response:

Error! Reference source not found. shows both the electrical conductance graphs at 100 kHz frequency and the derivative graphs for the Portland cement pastes with different water /Cement ratios.

With reference to figure 2 , the electrical conductance graph for all the cement pastes shows similar distinctive stages which could be described as follow:

I. An early increasing region in the conductance graphs which appears as soon as the samples are mixed with water figure1 (a). A distinctive feature in this region is the dG/dt curve underwent a progressive decreasing trend through this stage which is evident from figure1 (b).

II. The conductance peaked and the time of this peak depends on the used water to cement ratio. It is clear that as the water to cement ratio in the samples increases the time at which this peak occurs delayed.

During the mentioned early increase region and prior to the first peak in the conductance graph, the slope of the electrical conductance shows noticeable variation between an initial rapidly decreasing slope (which is represented by ***Stage I***),followed by a relatively constant slope region prior reaching the peak and defined as (***Stage II***). (**Stage I)** region is noticed very clearly at the derivative graphs as a rapidly decreasing slope; (**Stage II)** manifests itself as a plateau of relatively constant slope appears before the appearance of the early conductance peak. It should be mentioned, that for some conductance graphs such as the 0.35 W/C PC paste, the constant slope period, which appears during **(Stage II)**, is not as noticeable as in the other W/C ratio pastes.

III. After the early conductance peak, a decreasing region on the electrical conductance graphs appears. This is accompanied with a variation in decreasing rates through time as is evident from the derivative graphs. After the early conductance peak, a short lived period appears on the dG/dt curve whose duration in all the mixes does not last more than (10 minutes).

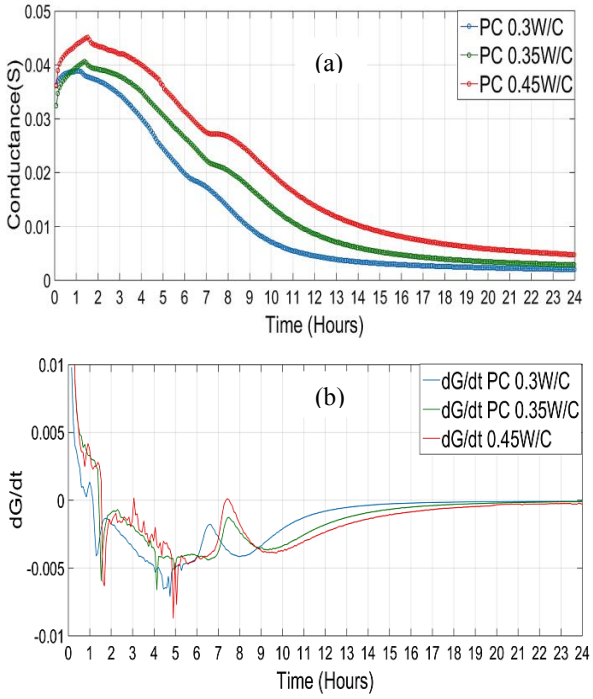

Figure1: (a)Electrical conductance for (0.3,0.35,0.45) Water to cement ratio Portland cement paste (b) Electrical conductance derivative graphs for (0.3,0.35,0.45)Water to cement ratio Portland cement paste.

IV. Thereafter, the dG/dt values start to increase again indicating a supressed increase on the mixes electrical conductance values. This region of increase in the dG/dt curve shows a dependency on the used water to cement ratio; for the 0.3W/C paste ratio; this rising period starts at 78mins, and for the 0.45W/C ratio paste it begins at 101 minutes.

V. After the increasing slope region, it then starts to decrease before reaching a relatively constant negative slope region. Then there follows a rapid increase in the slope. Regarding the latter, it should be noticed that, this peak in the derivative graph is marginally affected by the water to cement ratio with regards to its time appearance, as, indeed, it appears earlier on the derivative curve for the 0.3 W/C ratio paste in comparison to the to the 0.35W/C paste and the 0.45 W/C PC mix. However, the 0.35 & 0.45 PC pastes show the same time for this peak on their derivative curves.

VI. After this peak in the derivative graph, the conductance graph gradually decreases with

time till reaches a value of almost zero at the age of 24 hours.

Error! Reference source not found. presents a typical conductance vs time response and six regions have been identified for the different water to cement ratios Portland cement mixes.

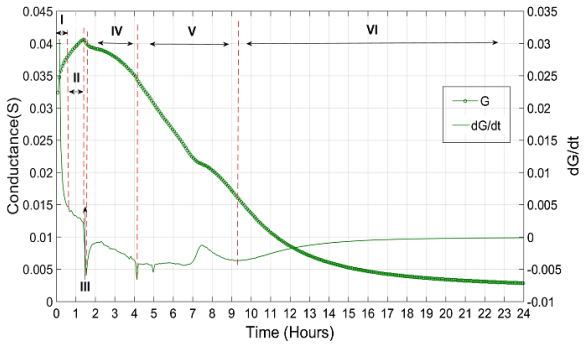

Figure 2: Electrical Conductance stages through the first 24 hours after mixing the samples with water

3.2 Portland cement pastes capacitive response:

In order to assess the electric polarization effect which takes place during this first 24 hours of the samples age, the normalised capacitances for the pastes are plotted through the mentioned time period by using different measuring electrical frequencies(1kHz,100kHz,200kHz,500kHz and1MHz)(See Figure3).

As it can be noticed from the capacitance response for the samples during the first 24 hours, the change in the capacitance measuring frequencies affects the capacitance response markedly. It is worth noting that at lower a.c. frequency measurements the capacitance response (in terms of their features) is virtually similar to the conductance response discussed above , hence the capacitance response could be divided in to the same six regions

By increasing the measurement frequency, the features which are noticed for the (1kHz) capacitance repose change dramatically, as some of the features which are witnessed at the 1kHz capacitive response disappear and others emerge. Also it could be noticed that , at the early hours of the samples age and in the (1kHz) capacitance response , all the samples show a similar early peak as the one which has been witnessed on the conductance response for the samples. However as the a.c. frequency increases a relaxation process occurs to the polarization process induced by the (1kHz) alternative current, and consequently this relaxation process reveals other polarization mechanisms which have been masked by the former induced polarization processes.

It is very noticeably by increasing the measuring frequency from (1kHz) to (100kHz), a capacitive peak at the age between (4-6 hours) appears (See Figure3), and by comparing the same time period in which this capacitive feature appears with the capacitive response for the (1kHz) , the (1kHz) capacitive response does not show this feature

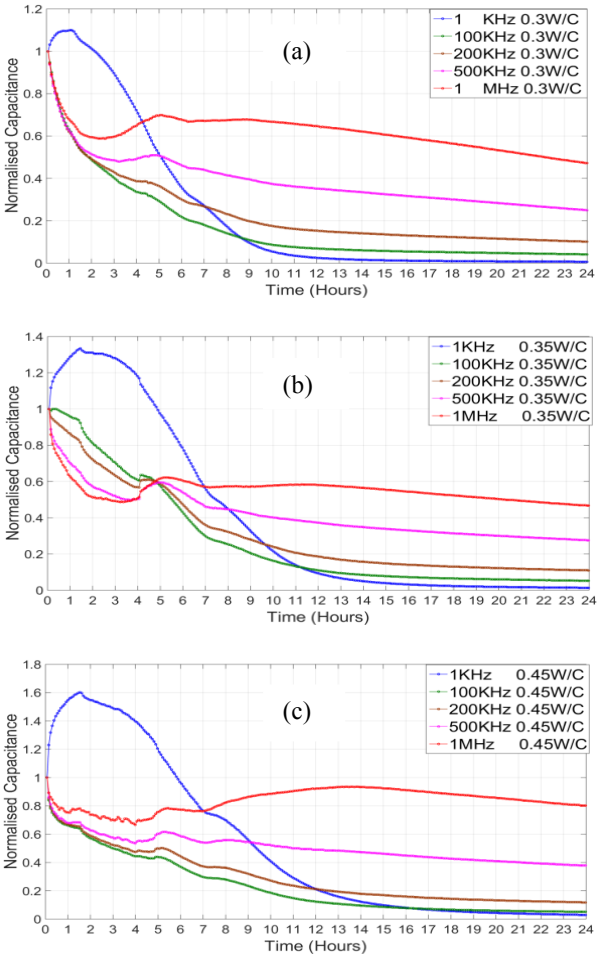

Figure3: Normalise Capacitance response at(1kHz,100kHz,200kHz,500kHz and 1MHz)for (a) 0.3W/C Portland Cement paste(b) 0.35W/C Portland Cement paste (c) 0.45 W/C Portland Cement paste.

By increasing the frequency up to (1MHz) it could be noticed that the mentioned resemblance between the conductance response and the capacitance response decreases, and the mentioned intermediate capacitive peak becomes well defined.

Also it could be noticed that the peak of the mentioned intermediate capacitive signal when considering the (1MHz) capacitive response ,have got a noticeable relation with the used water to cement ratio. The 0.3W/C ratio, the 0.35W/C ratio and the 0.45 W/C paste mixes show this peak at the ages of (303 , 316 min) and (326 mins) respectively . By comparing the starting time for the same capacitive signal for the 0.3 W/C, 0.35W/C and the 0.45W/C cement pastes, it is noticeable that the relation between the starting time and the W/C ratio is also evident; as the three mentioned mixes record a starting time of (150 min ,195min and 240 min) respectively. Therefore it is

very clear that increasing the water to cement ratio for the pastes delays the time of the intermediate capacitive increase region.

It could be noticed that another late third capacitive peak which is more flat in comparison to the early hour's capacitive peak exists. This third peak takes place in the time between (7 hours to 23 hours) of the samples age. This later polarization signal shows a more pronounced starting time at the (1kHz) frequency capacitive response. However by increasing the Ac frequency measurement to a frequency value of (1MHz) it appears that this later polarization signal extends to almost (23 hours) since mixing the samples with water (SeeFigure 4).

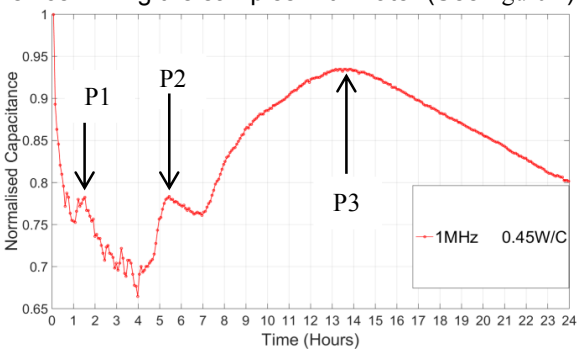

Figure 4: Identified Capacitive peaks (P1,P2,P3) on the capacitive response for Portland cement samples

4. Discussion:

As it has shown, the electrical response for the different tested cement pastes through the first 24 hours of the samples age, shows different stages which are easily distinguished.

Both the electrical conductance response as well as the capacitance response for the samples give an indication about the exiting ions ease of move by assessing the conductance response, as well as give an indication about the 'on surfaces activities' which are attributed for the formation of hydration products by assessing the produced capacitive response.

In the following section the discussed electrical response is going to be characterized taking in consideration the possible reaction activities which may give a rise for the noticed electrical feature.

Stage I:

As it has been noticed on the electrical conductance response at (Stage I), a continuous increase in the electric conductance is witnessed during this stage.
As the samples are mixed with water, a rapid exothermic dissolution of ions from the surface of the moist cement particles to the contact solution takes place. This dissolution processes manly takes place on the surfaces of the different minerals which compose the cement grains such as the Alite phase , the aluminate phase (C_3A) and the ferrite phase (C_4AF).The Belite phase is also contributing on the hydration process however in later stages and not expected to contribute significantly in this early age. Other cement components such as , alkali sulphates (C,N,K)S ,Calcium sulphates , and free lime (CaO) also contribute in this early hydration reaction stage by reacting with the cement interstitial minerals either to precipitate some early hydration products such as ettringite (Aft) ,or by increasing the mix concentration by liberating alkali ions in to the solution .
Due to the rapid dissolution process of the mentioned cement phases, the ions concentration in the solution increases rapidly. This mainly due to the contribution of theNa^+, K^+, Ca^{+2} and OH^-.This increase in the ions concentration affects the electrical conductance of the mixes, hence an increasing trend in the electrical conductance is witnessed.

Stage II:

It could be noticed that the electrical conductance's slope for **(Stage I)** records a continuous decreasing trend, till an almost a plateau area appears which indicates a relatively constant positive increasing rate before reaching the early conductance peak.

The dissolution of the cement particles has been subjected to many theories, as it is well known that the dissolution process does not proceed in the same rate through the whole hydration period.
Different suggestions and theories have been proposed to account for the dormant period which occurs after the first rapid dissolution stage. It has been noticed that during this mentioned dormant period the slope of the heat emission diagram produced by the calorimetric devices witnesses a constant slope value.

One of the most common theories which has been proposed to explain the dormant period in the cement hydration process as well as in pure tricalcium silicate phases , is the impermeable layer theory in which an impermeable layer has been suggested to cover the active cement sites which consequently hinders further dissolution for the allite phase(Gartner *et al.*, 2002). However one of the main criticism for this theory is that, the direct visual tests such as the SEM have not proven the existence of such a layer during this early stage of the cement hydration process(Bullard *et al.*, 2011). Recently (Juilland *et al.*, 2010) have suggested a dissolution theory which suggests different energy barriers which should be overcome in order to change the dissolution rates and the type of the crystallographic defects on the surfaces of the cement grains.

By comparing the conductance rate trends during (Stage I & II), and by assessing these stages with the two mentioned hydration theories, it is very clear that the cement grains dissolution rate starts to decrease since **(Stage I)** which affects the electrical conductance slope values before (**Stage II)**. At **(Stage II)** the ions dissolution follows a relatively constant rate. Therefore from this it could be notice that the dormant stage which already known to exists after the rapid dissolution stage ,starts to impact the hydration process gradually till it reaches its peak effect at **(Stage II)**, in which the conductance rate level off on a relatively constant value.

Stage III:

Despite the relatively constant positive slope for the electrical conductance at **(Stage II)**, the conductance values continue to rise. This suggests a continuous repletion of ions to the solution from the cement grains. The increase on the conductance graph proceeds till reaching the end of **(Stage II)** in which a conductance peak appears.

The Alite dissolution process leads to the early nucleation of C-S-H product which is one of the main products of the hydration process .As the solution reaches a super saturation level with respect to the C-S-H ,C-S-H starts to precipitate leading to a decrease in the ionic content in the solution.However due to the difference in the stoichiometry between the Alite phase and the early formed C-S-H hydration product (Ca/Si<2)(Taylor, 1997) , the calcium ions concentration increases in the solution till reaching a super saturation level with respect to the portlandite. Therefore the latter starts to precipitate (Garrault, 2005).These mentioned changes in the solution concentrations effects the electrical response especially the conductance response. During this stage the participated ions have different equivalent ionic conductivities which impact the ions relative contribution towards the electrical conductance.

Table 1shows the equivalent ionic conductivity for some of the contributing ions during the hydration reaction ions (Snyder *et al*., 2003):

Table 1: Product of the equivalent ionic activity (λ_0) and valance (z) for different ions.

Species)	$z\lambda_0$ $(cm^2 S/mol)$
OH^-	198
K^+	73.5
Na^+	50.1
Ca^{+2}	59

From Table 1it is clear that the hydroxyl ions have a significant impact on the electrical conductance value during this early hydration stage ,as their equivalent ionic conductivity is almost more than twice the equivalent ionic conductivity of other existed participating ions. Therefore as the portlandite starts to precipitate, hydroxyl ions as well as the calcium ions are removed from the solution leading to a quick drop in the electrical conductance.

Interestingly during this stage **(Stage III)** the capacitance response for the mixes shows a peak which matches the portlandite precipitation timing, which indicates this precipitation process increases the polarizability of the mix due to the adsorption of the portlandite sheets on the surface of the cement grains.

Stage IV:

After **Stage (III)**, the electrical conductance graph witnesses a continuous decreasing trend through time, as the slope of the conductance graph turns to a negative value. Immediately after **(Stage III)** ,the conductance slope shows an increase in its values indicating an increase in the ionic activities during this stage .This is attributed to the renewed reactivity of the silicate phase in the mix.(Damidot, Nonat and Barret, 1990) have shown the appearance of this renewed reactivity stage in a diluted (C_3S) suspension immediately after an endothermic peak which has been related to the portlandite precipitation process.

Stage V:

Two very noticeable features are presented in this stage, which are the electrical capacitance peak (P2), as well as the electric conductance derivative peak which appears after the capacitance peak. (See figure3& figure 4).

As a result for the renewed reactivity for the silicate phase ,the growth of the C-S-H starts to take place by forming an outer product on the ettringite outer network , leaving a void of almost in the micro meter range which is filled subsequently by the same product. Between the inner product and the outer product, the presence of a thin C-S-H layer which acts as a supportive shell for the deposition of the two mentioned inner and outer products has been reported. The first detection time for this growth mechanism structure for the C-S-H hydration product has been recorded at the age of 4 hours in the study which has been performed by (Gallucci, Mathur and Scrivener, 2010) on a 0.35W/C ratio cement pastes, which is comparable to the age in which the electrical capacitance values at **(Stage V)** starts to increase for the 0.35 W/C ratio Portland cement samples in this study. This increase in the capacitance continues till the hydration product of the mentioned structure

becomes difficult to oscillate with the electrical field due to the ongoing hardening process for the cement paste matrix.

Regarding the sudden rise in the derivative graph in this stage, this could be attributed to the renewed reactivity of the aluminate phase in the mix, as during this stage low level of sulphate ions has been reported to take place in the mix(Rothstein *et al.*, 2002) .This latter affects the already formed ettringite phase stability which consequently transforms to the monosulphoaluminate product (Afm).
The same later reaction increases the polarizability of the mixes therefore a clear peak (P3) on the capacitance response appears at the same stage.

Stage VI:

This stage could be distinguished by its gradual electrical conductance decreasing trend, which also could be noticed from its corresponding derivative graph. This gradual decrease in the electrical conductance indicates an increase in the electrical resistance in the cement matrix. By this age the gradual formation of the pore structure starts to affect the movement of the charges carriers, therefore the conductance repose at this stage gives both the pore structure response as well as the pore solution response.
Interesting to notice that at this stage of the electrical conductance response, the higher water to cement ratio samples 0.45W/C exhibit higher electrical conductance which indicates particularly in this age more continuous pore structure which do not impede the movement of the ions through the mix, and this of course could be regarded as low performance paste if it is compared with the other low water to cement ratios mixes.

4. Conclusion:

The electrical conductance, as well as the capacitance, has been used to characterise the first 24 hours of the hydration process for three different cement pastes.
The electrical response showed six distinctive stages which have been indicated on both the electrical conductance graph as well as the derivative graph. These six stages have been explained in terms of the through solution process which are more affected by the repletion and depletion of ions to and from the solution.
The polarization processes which take place during the test period also have been monitored by extracting the capacitance response of the samples at different electrical frequencies. It has been shown that utilising wide frequency range to characterize the polarization processes which take place through the early hydration period, gives more information about the on surface processes which their polarizability could be easily detected in certain frequency ranges in opposed to other frequency ranges.
Three polarization peaks have been detected through the test period , an early hydration polarization peak, an intermediate polarization peak and late age polarization peak .These polarization signals have been explained in terms of the precipitated phases during each stage.
The early hydration polarization signal has been related to the precipitation of the portlandite phase from the solution, the intermediate polarization signal has been related to the growth mechanism of the C-S-H on the cement grains and the last polarization signal has been attributed to the transformation of the ettringite phase(Aft) to monosulphoaluminate (Afm) .

REFERENCES :

Alizadeh, R., Raki, L., Makar, J. M., Beaudoin, J. J. and Moudrakovski, I. (2009) 'Hydration of tricalcium silicate in the presence of synthetic calcium-silicate-hydrate', *Journal of Materials Chemistry*, 19(42), pp. 7937-7946.

Bellmann, F., Damidot, D., Möser, B. and Skibsted, J. (2010) 'Improved evidence for the existence of an intermediate phase during hydration of tricalcium silicate', *Cement and Concrete Research*, 40(6), pp. 875-884.

Bellmann, F., Sowoidnich, T., Ludwig, H. M. and Damidot, D. (2012) 'Analysis of the surface of tricalcium silicate during the induction period by X-ray photoelectron spectroscopy', *Cement and Concrete Research*, 42(9), pp. 1189-1198.

Bullard, J. W., Jennings, H. M., Livingston, R. A., Nonat, A., Scherer, G. W., Schweitzer, J. S., Scrivener, K. L. and Thomas, J. J. (2011) 'Mechanisms of cement hydration', *Cement and Concrete Research*, 41(12), pp. 1208-1223.

Christensen, B. J., Coverdale, T., Olson, R. A., Ford, S. J., Garboczi, E. J., Jennings, H. M. and Mason, T. O. (1994) 'Impedance Spectroscopy of Hydrating Cement-Based Materials: Measurement, Interpretation, and Application', *Journal of the American Ceramic Society*, 77(11), pp. 2789-2804.

Damidot, D., Nonat, A. and Barret, P. (1990) 'Kinetics of Tricalcium Silicate Hydration in Diluted Suspensions by Microcalorimetric Measurements', *Journal of the American Ceramic Society*, 73(11), pp. 3319-3322.

Edwards, D. D., Hwang, J. H., Ford, S. J. and Mason, T. O. (1997) 'Experimental limitations in impedance spectroscopy:: Part V. Apparatus

contributions and corrections', *Solid State Ionics*, 99(1–2), pp. 85-93.

Gallucci, E., Mathur, P. and Scrivener, K. (2010) 'Microstructural development of early age hydration shells around cement grains', *Cement and Concrete Research*, 40(1), pp. 4-13.

Garrault, S. (2005) 'Study of C-S-H growth on C3S surface during its early hydration', *Materials and Structures*, 38(278), pp. 435-442.

Gartner, E., Young, J., Damidot, D. and Jawed, I. (2002) 'Hydration of Portland cement', *Structure and performance of cements*, 13, pp. 978-0.

Juilland, P., Gallucci, E., Flatt, R. and Scrivener, K. (2010) 'Dissolution theory applied to the induction period in alite hydration', *Cement and Concrete Research*, 40(6), pp. 831-844.

McCarter, W. J., Starrs, G. and Chrisp, T. M. (2000) 'Electrical conductivity, diffusion, and permeability of Portland cement-based mortars', *Cement and Concrete Research*, 30(9), pp. 1395-1400.

Minard, H., Garrault, S., Regnaud, L. and Nonat, A. (2007) 'Mechanisms and parameters controlling the tricalcium aluminate reactivity in the presence of gypsum', *Cement and Concrete Research*, 37(10), pp. 1418-1426.

Rothstein, D., Thomas, J. J., Christensen, B. J. and Jennings, H. M. (2002) 'Solubility behavior of Ca-, S-, Al-, and Si-bearing solid phases in Portland cement pore solutions as a function of hydration time', *Cement and Concrete Research*, 32(10), pp. 1663-1671.

Snyder, K. A., Feng, X., Keen, B. D. and Mason, T. O. (2003) 'Estimating the electrical conductivity of cement paste pore solutions from OH−, K+ and Na+ concentrations', *Cement and Concrete Research*, 33(6), pp. 793-798.

Taylor, H. F. (1997) *Cement chemistry*. Thomas Telford.

.

Infrastructure and Environment Scotland 3rd Postgraduate Conference
9th December 2015
Heriot-Watt University, Edinburgh

Consideration of a new hydrological index: Macroinvertebrate community response to multiannual flow indicators

Annie Visser,
Institute for Infrastructure and Environment,
Heriot-Watt University, Edinburgh
(e-mail: av96@hw.ac.uk)

ABSTRACT

There is a growing need and demand for tools to aid in the setting of environmental flow allocations in rivers. Work done to date has concentrated on the development of generic empirical models linking ecosystem health to antecedent flows, not applicable to individual rivers suffering from severe stresses. Presented here is a case study upon the River Nar, a chalk river in Norfolk, subject to over-abstraction, sediment ingress and extensive physical habitat modification. A methodology modifying and advancing upon those pre-existing has been applied across four scenarios to determine the influence that flows beyond the immediately preceding antecedent have on macroinvertebrate response. It is found that these multiannual antecedent flow indicators significantly correspond with, and can account for, up to 68.7% (i.e. maximum R^2 = 0.687) of macroinvertebrate response. The relative simplicity of the approach represents an opportunity to replace presently unsophisticated methods (Arthington et al., 2006), such as look-up tables, in common use. However, there is still a need for further work to improve the statistical robustness of the models.

1. INTRODUCTION

Freshwater aquatic ecosystems provide many key services, principally clean (drinking) water, flood protection, food, recreation, wild species habitat and support for interconnected systems (UK NEA, 2011). Physical processes such as flow, morphology, water quality and sediment transport underpin these ecosystems which are incredibly vulnerable, particularly to drought. The effects of over-abstraction are similar to drought: lowering the entire flow regime and perturbing the riverine community. The effect is made worse when drought caused extreme low-flows are further exacerbated by abstraction. (Acreman, 2001)

Knowledge of drought based changes in ecosystem processes, and subsequent ecosystem response, for flowing waters is limited. Macroinvertebrates are particularly sensitive to changes in water chemistry and quality, physical habitat, flow regime, and exhibit clear responses to environmental perturbations, making them ideal biological indices (Acreman et al., 2008). Further, macroinvertebrates are a vital freshwater food source, operating at intermediate trophic levels (the middle of the food web) and are generally the primary in-stream food source of fish (Wallace and Webster, 1996). They therefore occupy a niche making them ideal proxies for the assessment of the threat posed to the wider ecosystem.

Extensive anthropological influences have placed significant and often unsustainable pressures upon rivers. Increasingly resolution is sought via better environmental management, frequently including flow limits known as 'environmental flows' (Acreman et al., 2014, Dunbar et al., 2012). The World Bank defines environmental flows as "the quality, quantity and [temporal distribution] of flows required to maintain the components, functions, processes, and resilience of aquatic ecosystems" (Hirji and Davis, 2009, p. 13-14). At present, there are hundreds of approaches in use for the determination of environmental flow requirements (Acreman and Dunbar, 2004). Frequently limits are based upon primitive methods such as 'look up tables' with no empirical basis (Arthington et al., 2006). If these pressures are to be redressed then there is a real need for scientifically credible flow guidelines tailored to individual regions and rivers.

Water scarcity is an increasing threat in the United Kingdom, particularly in the south. Further, many of the rivers in the south are groundwater fed, their waters originating deep within the bands of porous rock covering the region. Climate variability, changes in runoff and high levels of abstraction threaten both the vital aquifer recharge (which shapes the annual flow regime – a dry winter can result in a summer drought) and normal flow levels.

The focus of this study is the River Nar, Norfolk, England (Figure 1), one of southern England's rare and highly valued chalk streams (a type of groundwater fed river). Despite this, over-

abstraction is one of the major causes in degradation of the riverine ecosystem and the services it provides (NRT, 2012). This is commonplace, with over 47% of the water in East Anglia is abstracted from the chalk aquifers (EA, 2013). This study seeks to begin the process of defining environmental flow guidelines for the River Nar. It builds upon existing work, which has looked at relationships between immediately preceding antecedent flow and macroinvertebrate response. Here the long-term impacts of flow, for up to five years prior, are investigated. Strong relationships may necessitate environmental flow limits encompassing a number of seasons and/or years.

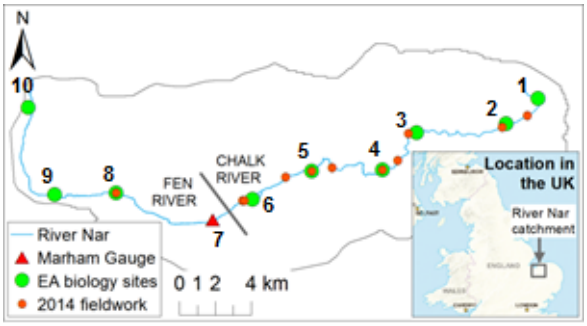

Figure 1. The River Nar and its; the river flows east to west. The EA biology sites and locations of the 2014 sediment sampling are detailed; EA site 7 is considered to be at the same location as the Marham Gauge.

2. METHODOLOGY

The methodology developed for the River Nar applies and develops previous work by Dunbar et al. (2006) and Dunbar and Mould (2009) in the DRIED-UP studies. These studies use linear regression modelling to determine links between antecedent flows and macroinvertebrate response. Boulton (2003) observed that macroinvertebrate response to drought is variable, and that there is the potential for delays in recolonisation; such delays appear to be present in the River Nar. This lag in response serves as the focus of this study, leading to the inclusion of time-offset flows as explanatory variables.

2.1 Case study – River Nar

The River Nar rises in the Norfolk Chalk Hills 60 m above sea level; from here the river flows west for some 42 km, transitioning from steep to a far gentler gradient. This topography and underlying geology give rise to two very different ecosystems. Upstream of Narborough the Nar flows as a chalk river, thereafter the chalk has been eroded forming a fen basin (Figure 1). This distinctive change at the river's midpoint has led to its designation as a Site of Special Scientific Interest (SSSI). The Nar has a high BFI (Base Flow Index) of 0.91 (CEH, 2012), typical of pure chalk streams. This reliance on groundwater results in a highly seasonal flow regime (Figure 2); aquifer recharge primarily occurs in autumn, producing a progressive rise in river flow until March/April.

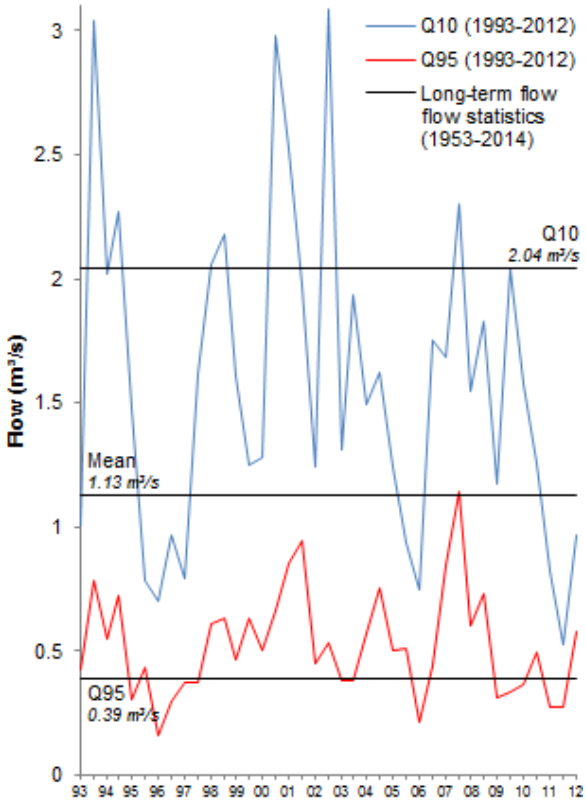

Figure 2. Flow hydrograph at the Marham Gauge for 1993-2012 overlaid with long-term flow statistics (1953-2014). Every second data point represents the flow in the winter season (see 2.2 Data). Data source: CEH (2012)

2.2 Data

Macroinvertebrate assessment data was provided by the Environment Agency (EA) (1993-2012) for 10 biology sites on the River Nar (Figure 1) (EA, 2012). The data was incorporated into the regression modelling (to species level) through the biotic index LIFE: the Lotic-invertebrate Index for Flow Evaluation. LIFE links benthic macroinvertebrates to flow regime (Extence et al., 1999). Data from both the spring (April-June) and autumn (October-December) seasons, where macroinvertebrate activity peaks (Lenz, 1997), were considered. The biotic data was standardised by the biological site mean for each season.

Daily mean flow data from 1993-2012 was extracted from the National River Flow Archive (NRFA) for the Marham Gauge (TF723119) (CEH, 2012). Daily flow is converted into seasonal flow indices, Q10 and Q95, using flow duration analysis. Where Q10 and Q95 are the daily streamflow values exceeded 10% and 95% of the time respectively (i.e. high and low flow); these flows represent the

hydrological 'extremes'. Standard hydrological seasons of summer (April to September) and winter (October to March) were used. Flow indices are statistically standardised (normalised).

Anomalous data is known to prevent the detection of relationships between antecedent flow and LIFE (Clarke and Dunbar, 2005). Therefore, those sites affected by sampling issues or other sources of variability were excluded from this work. The criterion for removal was in line with Exley (2006) and the DRIED-UP studies (Dunbar et al., 2006, Dunbar and Mould, 2009). Sites 1, 2 and 5 were excluded from the analysis.

The hydrological dataset was paired with the ecological (macroinvertebrate) to produce two river-wide regression models: one for the chalk (sites 3-6) and one for the fen (sites 7-10). It was expected that these two 'distinct river units' would produce differing responses.

2.3 Regression modelling

Four scenarios relating LIFE to antecedent flow were explored (Table 1) using through stepwise linear multiple linear regression. Within each scenario LIFE is related to both antecedent high and low (Q10 and Q95 respectively) flows in both summer and winter (Table 2). In order to explore the lag in macroinvertebrate response the explanatory variable, flow, is time-offset. This begins with the immediately preceding antecedent flow up to 5 years previous antecedent flow. In stepwise regression the variables are added in steps. For example, scenario A, model run 5, combination 2 (featuring two years antecedent flow for summer Q10 ($Q_{S10}(t)$) and the immediately preceding antecedent flow for summer Q95 ($Q_{S95}(t)$)) would be expressed as:

$$y = (a_1 \cdot Q_{S10}(t)) + (a_2 \cdot Q_{S10}(t-1)) + (a_3 \cdot Q_{S95}(t)) + b_1$$

where y is LIFE, a_i is the explanatory coefficient, b_i is the intercept and t is the antecedent flow.

Table 1. Scenarios assessed in the regression modelling. Seasons are as discussed in 2.2 Data.

Scenario	River section	LIFE data
A	Chalk	Spring
B	Chalk	Autumn
C	Fen	Spring
D	Fen	Autumn

Similar studies assessing links between antecedent flows and macroinvertebrate response have made use of more bespoke, esoteric software. In this study all regression modelling and additional analysis, is performed using R (software environment for statistical programming and graphical analysis), thereby making it more accessible for use by agencies and river managers.

Table 2. Multiple regression combinations considered for each scenario; a total of 240 were considered for each scenario (Table 1). Seasons are as discussed in 2.2 Data.

Model run	Explanatory variables (EV)		No. combinations
	EV1	EV2	
1	Summer Q10	-	6
2	Summer Q95	-	6
3	Winter Q10	-	6
4	Winter Q95	-	6
5	Summer Q10	Summer Q95	36
6	Winter Q10	Winter Q95	36
7	Winter Q10	Summer Q95	36
8	Winter Q95	Summer Q10	36
9	Winter Q95	Summer Q95	36
10	Winter Q10	Summer Q10	36

3. RESULTS AND DISCUSSION

In total, multiple regression analysis was performed for 960 potential models. It is therefore not possible to present all of the results. Provided here is a synthesis of those (statistically significant) models with the highest R^2 (level of explanatory power provided by the models) only (Table 3). Note that the significance threshold was set at p-value = 0.05, the standard arbitrary value used (Biau et al., 2010). Future (ongoing) work includes the selection of the highest quality models through statistical methods (AIC/BIC).

3.1 Chalk river

3.1.1 Scenario A – Spring LIFE

As can be seen from Table 3, no models required input of more than four years of flow data (i.e. models featuring a 3 year antecedent flow time-offset). This is due to the fact that not all potential explanatory variables add value to the predictive power of the model; addition of certain variables contributes only to the error term.

Model runs 1-4 feature only one seasonal flow index and may be thought to represent the 'base' models (Table 3). These in turn, indicate the relative strength of the relationships in the subsequent model runs featuring more than one seasonal flow index (runs 5-10). From Table 3 it can be seen that of the base models, summer flow indicators (runs 1 and 2) provide considerably greater explanatory power. It should therefore follow that those modelling runs which include summer flow indicators would also report higher R^2 values. Whilst this does hold true, the modelling runs (number 8) featuring a combination of winter

low flows and summer high flows actually produces the model with the greatest explanatory power.

Table 3. Models (with p-value >0.05) with the highest R^2 for each model run as well as the number of years of flow data required. The highest R^2 for each scenario is highlighted in red. Results from scenario C and D discussed in 3.2 Fen river.

Model run	EV	R^2	p-value	Years flow data
Scenario A – Spring LIFE				
1	Summer Q10	0.465	0.008	4
2	Summer Q95	0.453	0.002	3
3	Winter Q10	0.286	0.009	2
4	Winter Q95	0.202	0.042	2
5	Summer Q10 + Q95	0.541	0.005	4
6	Winter Q10 + Q95	0.301	0.046	2
7	Winter Q10 + Summer Q95	0.510	0.009	4
8	Winter Q95 + Summer Q10	0.687	0.004	4
9	Winter Q95 + Summer Q95	0.506	0.010	4
10	Winter Q10 + Summer Q10	0.470	0.040	4
Scenario B – Autumn LIFE				
1	Summer Q10	0.538	0.0004	2
2	Summer Q95	0.518	0.0007	2
3	Winter Q10			
4	Winter Q95			
5	Summer Q10 + Q95	0.590	0.002	2
6	Winter Q10 + Q95			
7	Winter Q10 + Summer Q95	0.518	0.003	2
8	Winter Q95 + Summer Q10	0.552	0.001	2
9	Winter Q95 + Summer Q95	0.570	0.003	2
10	Winter Q10 + Summer Q10	0.560	0.004	2

These findings strongly suggest that there is a significant lagged response of the macroinvertebrate community to flow indicators in the River Nar. In reality, this demand for four years antecedent flow data impedes the practical use of these models. The requirement of two years of antecedent flow data for the models featuring winter flows only (run 6) improves the usability of such models for river managers.

Spring and summer months tend to be a very active period for macroinvertebrates (Lenz, 1997), therefore it follows that summer flows have the most influence over spring LIFE and by extension ecosystem health. Further, in the Nar, sediment mobility occurs only at high flows (Sear et al., 2005), which allow the cleansing of fines from the gravel substrate thereby promoting greater biological activity. This relationship could explain the low level of explanatory power of models including winter Q10 flow (when highest flows occur).

Model run 8 produced the model with the greatest explanatory power, featuring both summer Q10 (high) and winter Q95 (low) flows:

$$LIFE = (0.01Q_{WQ5}(t)) - (0.015Q_{WQ5}(t-1)) + (0.031Q_{WQ5}(t-2)) - (0.009Q_{WQ5}(t-3)) - (0.029Q_{SQ0}(t)) + (0.0002Q_{SQ0}(t-1)) - (0.002Q_{SQ0}(t-2)) - (0.033Q_{SQ0}(t)) + 1.003$$

Two broad conclusions are possible. Firstly, very high summer flows, i.e. spate, negatively affect LIFE scores. However, it appears that this acts as a moderating influence, with LIFE scores increasing in subsequent years. Secondly, winter low flows prove critical and cannot be offset by summer high flows; this presumably follows from the winter aquifer recharge, which if insufficient, cannot give rise to high summer flows.

3.1.2 Scenario B – Autumn LIFE

For autumn LIFE, similar to the spring LIFE results, the base models (runs 1 to 4) suggest that the summer flow indicators represent the strongest relationship (Table 3). This is again reflected in the results from the models featuring combinations of seasonal flow indicators. Interestingly the base winter models (runs 3 and 4) feature no significant models, subsequently producing no relationships for model run 6 either.

As for scenario A, model runs 5, and 7-10 feature the highest R^2 values. Notably, for autumn LIFE, the data requirements are consistently lower than spring but at no cost to explanatory. From a management perspective models which use only minimal flow data have a significant advantage over more complex ones. It can therefore be concluded that these models are sufficiently robust to provide meaningful results for river managers.

For autumn, model run 5 produced the model with the greatest explanatory power, featuring summer Q10 (high) and Q95 (low) flows:

$$LIFE = (0.007Q_{SQ0}(t)) + (0.017Q_{SQ0}(t-1)) - (0.015Q_{SQ5}(t)) + (0.011Q_{SQ5}(t-1)) + 1.002$$

Here, in contrast to spring macroinvertebrate response, summer high flows have a strongly positive effect. This suggests that autumn macroinvertebrates have an overall preference for higher flows. Corresponding summer low flows appear to be slightly less influential here.

Scenarios A and B share similarities in terms of the level of explanatory power of the models. However, the results are not identical, and therefore it is clear that the macroinvertebrate responses in both seasons must be taken into consideration in the chalk river section of the River Nar.

3.2 Fen river

In the fen river very few statistically significant relationships were output. It was concluded that this could be the result of a number factors which relate to the physical habitat.

Firstly, the fen river section is the most modified (for historical navigational purposes). River Habitat Surveys (RHS) performed on the fen river section reveal the extent of the modification, where the majority of sites are considered 'severely modified' (Figure 4). Varied morphology is known to provide refugia and help to sustain habitats, thereby reducing the overall drought impact (Wood and Petts, 1994). Previous studies incorporating RHS data in the statistical modelling (Dunbar et al., 2006, Dunbar and Mould, 2009) have found that a modified physical habitat can mask relationships with low flow specifically. Therefore, further work should look to include physical. While this is imperative for the fen section of the river, there may also be benefit in extending this work to the chalk section too (see Figure 4).

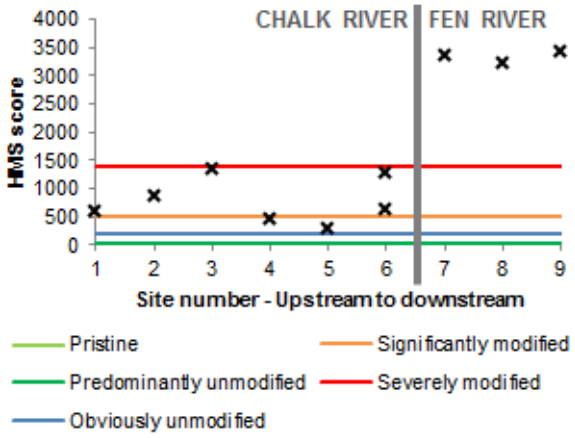

Figure 4. River Nar RHS scores for Habitat Modification (site numbers as per Figure 1). Data source: EA (2008)

Secondly, fine sediments in the lotic environment have a deleterious effect on habitat quality (Wood and Armitage, 1997). This is particularly true of chalk rivers, as clogging of the characteristic chalk gravel beds inhibits macroinvertebrate and plant growth; in consequence fish reliant on these are also affected. Dredge sampling fieldwork was undertaken on the River Nar in 2014 (Figure 1) (Visser, 2014). This work revealed that a high proportion of the Nar substrate consisted of fine materials, findings which agreed with previous surveys (Sear et al., 2005). One method of accounting for this influence would be the inclusion of Pressure-Specific Invertebrate biotic index as an explanatory variable in future modelling efforts.

4. CONCLUSIONS

Clarity has been brought to the response of macroinvertebrates, and thus by extension ecosystem health, to extreme flow events. The models produced exhibit a clear lagged response to flows, suggesting that flows must be considered continually, and not as individual events in time. Further, by exploring all possible combinations of high (Q10) and low flow (Q95), it has been possible to identify those which influence the biological health of the river system most. This analysis has shown, overall, summer flows to be the most critical to sustaining riverine macroinvertebrate health. Environmental flow limits on the River Nar could thus have serious implications for water supply in the region in the summer months (when abstraction is highest (NRT, 2012)).

Examining the results with a view to greater resolution revealed that (in the chalk river section) the models for spring and autumn LIFE are significantly different. This strongly suggests that there are notable differences in the composition of the macroinvertebrate community inter-seasonally. Any environmental flow allocations then, must allow for the resulting difference in response and flow preferences through the year. It has also been shown that when managing a river under stress, such as the Nar, a bespoke modelling effort is required both for understanding and management.

Further work, expanding upon the findings to date, is underway, with a view to bringing clarity and optimisation of the models produced to this point. This work includes the addition of more data, thereby improving model robustness, as well as variable and model selection through Principal Component Analysis, Akaike Information Criterion (AIC) and Bayesian Information Criterion (BIC).

These findings have broader implications beyond the River Nar (although restricted to groundwater fed rivers). It is clear that environmental flow requirements are subject to seasonal variation, therefore, limits should avoid being inflexible if they are to best protect the riverine ecosystem and its associated services. This flexibility is further essential, as it is clear that macroinvertebrates are influenced by more than just the immediately preceding antecedent flow. The need for time-offset antecedent flow could represent a significant constraint due to the high data input requirements. Fortunately, the findings suggest that two years of flow data may be sufficient; this will be determined in future work through the application of AIC and BIC. The relative simplicity of the modelling, coupled with the use of open source software,

promises to provide a more sophisticated, and yet accessible, method for the determination of environmental flows (rather than look-up tables).

Beyond this, a greater understanding and accounting for other parameters flagged up by the modelling efforts thus far is vital:

- The relationship between physical habitat and low flows for highly modified channels needs to be accounted for.
- Accounting for the influence of fine sediments through the inclusion of the PSI biotic index as a regression variable, accounting for the response of taxa based upon silt tolerance. Dependent on the findings, headwater sites 1 and 2 may be reinstated in the modelling efforts.

5. ACKNOWLEDGEMENTS

This study has been undertaken as part of the TWSTT transforming water scarcity through trading project (EP/K013661/1). The author gratefully acknowledges the Environment Agency for the provision of the macroinvertebrate data and Ms Jenny Garbe and Ms Isabel Scherer for their assistance in the data gathering.

REFERENCES

Acreman, M. (2001). Ethical aspects of water and ecosystems. *Water Policy,*3(3): 257-265.
Acreman, M., Dunbar, M., Hannaford, J., Mountford, O., Wood, P., Holmes, N., Wx, I. C., Noble, R., Extence, C., Aldrick, J., King, J., Black, A. & Crookall, D. (2008). Developing environmental standards for abstractions from UK rivers to implement the EU Water Framework Directive. *Hydrological Sciences Journal,* 53(6): 1105-1120.
Acreman, M. & Dunbar, M. J. (2004). Methods for defining environmental flow requirements. *Hydrology and Earth System Sciences,* 8(5): 861-876.
Acreman, M. C., Overton, I. C., King, J., Wood, P. J., Cowx, I. G., Dunbar, M. J., Kendy, E. & Young, W. J. (2014). The changing role of ecohydrological science in guiding environmental flows. *Hydrological Sciences Journal,* 59(3-4): 433-450.
Arthington, A. H., Bunn, S. E., Poff, N. L. & Naiman, R. J. (2006). The challenge of providing environmental flow rules to sustain river ecosystems. *Ecological Applications,* 16(4): 1311-1318.
Biau, D., Jolles, B. & Porcher, R. (2010). P Value and the Theory of Hypothesis Testing: An Explanation for New Researchers. *Clinical Orthopaedics and Related Research®,* 468(3): 885-892.
Boulton, A. J. (2003). Parallels and contrasts in the effects of drought on stream macroinvertebrate assemblages. *Freshwater Biology,* 48(7): 1173-1185.
CEH (2012). Flow at Marham Gauge: Extracted from NRFA database. Centre for Environment and Hydrology.
Clarke, R. & Dunbar, M. (2005). Producing Generalised LIFE Response Curves. Environment Agency.
Dunbar, M. J., Alfredsen, K. & Harby, A. (2012). Hydraulic-habitat modelling for setting environmental river flow needs for salmonids. *Fisheries Management and Ecology,* 19(6): 500-517.
Dunbar, M. J. & Mould, D. J. (2009). Distinguishing the Relative Importance of Environmental Data Underpinning flow pressure assessment 2 (DRIED-UP 2). Centre for Ecology and Hydrology.
Dunbar, M. J., Young, A. R. & Keller, V. (2006). Distinguishing the Relative Importance of Environmental Data Underpinning flow pressure assessment (DRIED-UP). Centre for Ecology and Hydrology.
EA (2008). River Nar RHS data. (Available upon request from the Environment Agency).
EA (2012). River Nar macro-invertebrate data. (Avai-lable upon request from the Environment Agency).
EA (2013). Groundwater protection: Principles and practice (GP3). Bristol: Environment Agency.
Exley, K. P. (2006). River Itchen macro-invertebrate community relationship to river flow changes. Winchester: Environment Agency Report.
Extence, C. A., Balbi, D. M. & Chadd, R. P. (1999). River flow indexing using British benthic macroinvertebrates: a framework for setting hydroecological objectives. *Regulated Rivers: Research & Management,* 15(6): 545-574.
Hirji, R. & Davis, R. (2009). *Environmental Flows in Water Resources Policies, Plans, and Projects: Findings and Recommendations,* Washington DC, World Bank Publications.
Lenz, B. N. (1997). Feasibility of Combining Two Aquatic Benthic Macroinvertebrate Community Databases for Water-Quality Assessment. *National Water-Quality Assessment.* USGS.
NRT (2012). The River Nar A WFD Local Catchment Plan. Norfolk Rivers Trust.
Sear, D. A., Newson, M., Old, J. C. & Hill, C. 2005. Geomorphological appraisal of the River Nar Site of Special Scientific Interest. English Nature.
UK NEA (2011). *UK NEA Technical Report,* Cambridge, UNEP-WCMC.
Visser, A. 2014. *Developing a model relating antecedent low flows and macro-invertebrate health (using LIFE) in the River Nar.* MEng Civil Engineering, Heriot-Watt University.
Wallace, J. B. & Webster, J. R. (1996). The Role of Macroinvertebrates in Stream Ecosystem Function. *Annual Review of Entomology,* 41(1): 115-139.
Wood, P. J. & Armitage, P. D. (1997). Biological Effects of Fine Sediments in the Lotic Environment. *Environmental Management,* 21(2): 203-217.
Wood, P. J. & Petts, G. E. (1994). Low flows and recovery of macroinvertebrates in a small regulated chalk stream. *Regulated Rivers: Research & Management,* 9(4): 303-316.